

Constitutive and numerical modeling of anisotropic quasi-brittle shales

THÈSE N° 7053 (2016)

PRÉSENTÉE LE 28 JUIN 2016

À LA FACULTÉ DE L'ENVIRONNEMENT NATUREL, ARCHITECTURAL ET CONSTRUIT
LABORATOIRE DE MÉCANIQUE DES SOLS - CHAIRE GAZ NATUREL PETROSIBRI
PROGRAMME DOCTORAL EN MÉCANIQUE

ÉCOLE POLYTECHNIQUE FÉDÉRALE DE LAUSANNE

POUR L'OBTENTION DU GRADE DE DOCTEUR ÈS SCIENCES

PAR

Francesco PARISIO

acceptée sur proposition du jury:

Prof. C. Ancey, président du jury
Prof. L. Laloui, directeur de thèse
Prof. S. Pietruszczak, rapporteur
Dr P. Bossart, rapporteur
Dr J. Cugnoni, rapporteur



ÉCOLE POLYTECHNIQUE
FÉDÉRALE DE LAUSANNE

Suisse
2016

To my center.

Der Aphorismus deckt sich nie mit der Wahrheit; er ist entweder eine halbe Wahrheit oder
anderthalb.

An aphorism can never be the whole truth; it is either a half-truth or a truth-and-a-half.

Karl Kraus

TABLE OF CONTENTS

ABSTRACT	I
RIASSUNTO	III
ACKNOWLEDGEMENTS	VII
1. INTRODUCTION	1
1.1. <i>Background and objectives</i>	1
1.2. <i>Thesis layout</i>	8
1.3. <i>References</i>	10
2. STRENGTH EVOLUTION OF GEOMATERIALS IN THE OCTAHEDRAL PLANE UNDER NON- ISOTHERMAL AND UNSATURATED CONDITION	13
<i>Abstract</i>	13
2.1. <i>Introduction</i>	13
2.2. <i>Model formulation</i>	14
2.3. <i>Evolution of the strength with temperature, suction and stress path direction</i>	26
2.4. <i>Conclusions</i>	35
2.5. <i>Acknowledgments</i>	36
2.6. <i>References</i>	36
3. CONSTITUTIVE ANALYSIS OF SHALE: A COUPLED DAMAGE PLASTICITY APPROACH	39
<i>Abstract</i>	39
3.1. <i>Introduction</i>	39
3.2. <i>Rheological evidence concerning shale</i>	41
3.3. <i>Constitutive framework of the model</i>	44
3.3.1. <i>Plasticity</i>	46
3.3.2. <i>Damage</i>	47
3.4. <i>Coupled plastic-damage model</i>	47
3.5. <i>Thermodynamic consistency</i>	54
3.6. <i>Numerical integration</i>	56
3.6.1. <i>Stress return algorithm</i>	56
3.7. <i>Results of numerical analyses</i>	57
3.7.1. <i>Determination of parameters</i>	57
3.7.2. <i>Triaxial tests on Opalinus Clay from the Mont Terri site</i>	58
3.7.3. <i>Triaxial tests on LaBiche Shale</i>	61
3.8. <i>Conclusions</i>	63
3.9. <i>Acknowledgments</i>	64
3.10. <i>References</i>	65

4. PLASTIC-DAMAGE MODELING OF SATURATED QUASI-BRITTLE SHALES 69

Abstract 69

4.1. *Foreword*..... 69

4.2. *Introduction* 71

4.3. *Poroelastic coupled hydro-mechanical formulation* 76

4.4. *Plastic damage model*..... 77

 4.4.1. *Isotropic plastic yield surface and hardening internal variables*..... 77

 4.4.2. *The plastic yield surface with isotropic hardening* 78

 4.4.3. *Non-associated plastic potential* 83

 4.4.4. *Isotropic damage model*..... 85

4.5. *Numerical integration*..... 90

4.6. *Example of the calibration procedure*..... 91

4.7. *Validation of the constitutive behavior against experimental findings* 95

 4.7.1. *Mechanical behavior* 95

 4.7.2. *Hydro-mechanical undrained behavior* 99

4.8. *Conclusions* 100

4.9. *Acknowledgements*..... 101

4.10. *References*..... 101

5. A GENERALIZED FAILURE SURFACE FOR THE STRENGTH OF GEOMATERIALS ACCOUNTING FOR INTRINSIC ANISOTROPY AND TRUE TRIAXIAL CONDITIONS 107

Abstract 107

5.1. *Introduction* 107

5.2. *True triaxial behavior of geomaterials*..... 108

5.3. *Intrinsic anisotropic behavior of sedimentary geomaterials*..... 112

5.4. *Van-Eekelen type formulation to model strength dependency on Lode's angle*..... 114

5.5. *Anisotropic extension of the constitutive model*..... 118

5.6. *Material parameters calibration*..... 121

 5.6.1. *Calibration of the modified Van Eekelen formulation* 121

 5.6.2. *Calibration of the anisotropic extension of the yield criteria* 124

5.7. *Selected failure criteria for the comparative study*..... 126

 5.7.1. *Failure criteria for the true triaxial extension*..... 126

 5.7.2. *Failure criteria for comparison in anisotropic conditions*..... 129

5.8. *Analyses and results*..... 131

 5.8.1. *True triaxial conditions* 131

 5.8.2. *Anisotropic conditions*..... 135

5.9. *Conclusions* 139

5.10. *Acknowledgements*..... 140

5.11. *References*..... 140

6. COMBINING MICRO-DILATANT CONTINUA FRAMEWORK WITH PLASTIC-DAMAGE CONSTITUTIVE MODEL FOR THE REGULARIZATION OF LOCALIZED STRAIN.....	145
<i>Abstract</i>	145
6.1. <i>Introduction</i>	145
6.2. <i>Strain localization and regularization techniques</i>	147
6.3. <i>Micropolar continua and the second gradient of dilatancy</i>	150
6.4. <i>Numerical model in plane strain conditions</i>	153
6.5. <i>Numerical analyses</i>	154
6.5.1. <i>Comparison between homogeneous, non-regularized and regularized solution</i>	155
6.5.2. <i>Effects of the second gradient of dilatancy regularization</i>	157
6.5.3. <i>Element size influence</i>	161
6.5.4. <i>Non-associativity effect</i>	162
6.5.5. <i>Confinement effect</i>	166
6.5.6. <i>Anisotropy effect</i>	167
6.5.7. <i>Upscaling size</i>	169
6.6. <i>Conclusions</i>	172
6.7. <i>Acknowledgements</i>	173
6.8. <i>References</i>	173
7. HYDRO-MECHANICAL MODELING OF TUNNEL EXCAVATION IN ANISOTROPIC SHALE WITH COUPLED DAMAGE-PLASTICITY AND MICRO-DILATANT REGULARIZATION	179
<i>Abstract</i>	179
7.1. <i>Introduction</i>	179
7.2. <i>The Mont Terri Project and the FE-Experiment</i>	182
7.3. <i>Numerical model of the FE-Tunnel</i>	188
7.4. <i>Hydro-mechanical formulation of the second gradient of dilatancy model</i>	191
7.5. <i>Calibration of material parameters</i>	192
7.6. <i>Simulation results of the FE-Tunnel</i>	195
7.6.1. <i>Analysis of the pore pressure field</i>	196
7.6.2. <i>Damage distribution</i>	199
7.6.3. <i>Comparison of tunnel wall radial convergence with in-situ measurements</i>	202
7.7. <i>Conclusions</i>	206
7.8. <i>Acknowledgements</i>	207
7.9. <i>References</i>	207
8. CONCLUSIONS AND PERSPECTIVES	211
8.1. <i>General conclusions</i>	211
8.2. <i>Future perspectives</i>	213
8.2.1. <i>Experimental perspectives and recommendations</i>	214
8.2.2. <i>Constitutive and numerical perspectives and recommendations</i>	214
APPENDIX A. PLASTIC MULTIPLIERS OF THE THERMO-MECHANICAL MODEL.....	217

APPENDIX B. PLASTIC MULTIPLIER OF THE WATER RETENTION MODEL	225
APPENDIX C. DATA TABLES OF TRUE TRIAXIAL FAILURE OF ROCKS.....	227
APPENDIX D. DATA TABLES OF ANISOTROPIC FAILURE OF ROCKS	233
APPENDIX E. <i>CODE_ASTER</i> SCRIPTS OF THE CONSTITUTIVE MODEL.....	243
APPENDIX F. COMMAND FILE OF THE 2D TUNNEL ANALYSIS.....	263
APPENDIX G. SUMMARY OF MODEL PARAMETERS CALIBRATION	281
<i>References.....</i>	<i>283</i>

Abstract

Understanding the hydro-mechanical behavior of shale is fundamental to assess the safety of deep geological nuclear repository sites. Several countries have adopted argillaceous formations as host geological media for the repository. In Switzerland, the candidate for hosting the deep geological repository site is Opalinus Clay. This thesis aims at improving the current predicting and modeling capabilities of the hydro-mechanical behavior of shale by: (1) developing proper constitutive models tailor fitted to the purpose; (2) validating the developed models against experimental findings at the small (laboratory) and medium scale (rock mass).

First, thermo-hydro-mechanical (THM) couplings at the constitutive level are addressed. A constitutive model that accounts for suction and temperature dependent failure is presented. Additionally, the model accounts for the true triaxial nature of strength, a feature that has not yet been extensively investigated in literature in case of THM couplings. Two numerical case studies related to nuclear waste storage and CO₂ sequestration are presented. Results of the case studies showed that not accounting for true triaxial strength of geomaterials in unsaturated and non-isothermal conditions can lead to an overestimation of its strength and a reduced global safety factor.

The employed model accounts for purely plastic strains, and as Opalinus Clay and many other shales have a quasi-brittle mechanical behavior, the solution is the formulation of a new model extended to damage. Attention is focused on the hydro-mechanical behavior in water saturated conditions, as limited experimental data is available on the full thermo-hydro-mechanical behavior in unsaturated and non-isothermal conditions of Opalinus Clay in general, and shale in particular. A new constitutive model combining damage and plasticity theory for quasi-brittle geomaterials is developed. The damage variable evolves as a function of the elastic strain energy taken as a tensile split of the elastic strain tensor. To ensure uniqueness of the solution, plasticity is formulated in the damage effective stress space and the constitutive model is implemented numerically with an implicit scheme. A posteriori checks reveal the thermodynamic consistency of the model. Numerical results at material point level are compared with experimental results in triaxial compression tests. Good agreement between predictions and experimental values is found.

The constitutive model is furtherly developed and modified to improve the calibration scheme and to represent a wider range of confinements. The coupling between damage and plasticity is such that the damage variable is a scalar function of the plastic strain increment and the plastic yield surface represents the strength envelope of the material. A non-associated plastic potential is formulated. The constitutive model is implemented with an implicit scheme in the Finite Element solver *Code_Aster*. Validation examples include the comparison with results

of pure mechanical behavior in triaxial compression of two shales and the coupled hydro-mechanical behavior in undrained conditions of a third shale. The comparison gives good results and the model proves to be a powerful tool to describe the hydro-mechanical behavior of shale in saturated conditions.

The developed constitutive model is furtherly extended to account for anisotropy and true triaxial strength, both typical features of shale. Both extensions are compared separately against experimental data on several materials, in true triaxial conditions first and in conventional triaxial compression conditions with anisotropic materials second. The performance of the constitutive model in terms of failure stress predictions is compared, for the different set of materials, against the performances of other failure criteria common in geomechanics. Results demonstrate how the proposed model gives a global smaller error between predictions and data compared to the other criteria.

To avoid pathological mesh dependency and excessive localization of the solution, the Finite Element analyses must be carried out with a proper regularization technique. The one employed in this study is the second gradient of dilatancy formulation, which was available in *Code_Aster*. A series of numerical examples are presented to highlight the main characteristics of the structural response of the proposed constitutive model in combination with a second gradient of dilatancy formulation. Results demonstrate how the parameter controlling the non-associated plastic potential, the softening response, the anisotropic failure surface and the size of the problem play a major role in the final solution in presence of localized inelastic strains. Results show as well that the pathological mesh dependency is removed and the objectivity of the solution restored.

A Finite Element analysis of tunnel excavation in coupled hydro-mechanical conditions is presented. The developed anisotropic plastic-damage model is employed along with the second gradient of dilatancy. The parameters are partly calibrated on laboratory experimental results and partly retrieved from literature and were not adjusted to fit the excavation results. Pore water pressure, tunnel walls displacement and damage around the tunnel are compared with in-situ recorded data during the excavation of the FE-tunnel at the Mont Terri site, Switzerland. The comparison between numerical predictions and recorded data is consistent and validates the concepts developed in the thesis.

Keywords: constitutive modeling, shale mechanics, the Mont Terri Project, Opalinus Clay, plasticity and damage couplings, *Code_Aster*, anisotropic plasticity, fabric tensor anisotropy, true triaxial strength, Lode's angle, localization, second gradient of dilatancy, FE-tunnel, tunnel excavation analysis, Excavation Damaged Zone (EDZ), unsaturated plasticity, non-isothermal plasticity, thermo-hydro-mechanical couplings, nuclear waste storage, CO₂ sequestration.

Riassunto

La comprensione del comportamento idro-meccanico di scisti ed argilliti (shale nella letteratura anglosassone) è necessaria al fine di valutare la sicurezza dello stoccaggio di scorie altamente radioattive. In diversi paesi le argilliti sono state identificate come possibili formazioni geologiche per ospitare i siti di stoccaggio. In Svizzera, la formazione indenticata per ospitare il sito di stoccaggio è l'Opalinus Clay. L'obiettivo della tesi è mirato al miglioramento delle attuali capacità di modellazione costitutiva e numerica del comportamento idro-meccanico delle argilliti tramite: (1) lo sviluppo di modelli costitutivi pensati specificatamente per le argilliti; (2) la validazione dei modelli sviluppati attraverso il confronto dei risultati numerici con i risultati sperimentali in piccola e media scala (rispettivamente, scala di laboratorio e dell'ammasso roccioso).

In primo luogo, viene presentato uno studio relativo agli accoppiamenti termo-idro-meccanici a livello costitutivo. Viene presentato un modello costitutivo plastico in cui la superficie di rottura dipende dalla suzione e dalla temperatura. Inoltre, la resistenza è una funzione dell'angolo di Lode (comportamento triassiale vero), una caratteristica che finora è stata scarsamente investigata in letteratura per modelli termo-idro-meccanici. Vengono presentati due casi studio numerici relativi allo stoccaggio sotterraneo di rifiuti nucleari e allo stoccaggio sotterraneo di CO₂. I risultati ottenuti mostrano l'importanza, nei processi sopracitati, che rivestono i percorsi di carico in cui sono fatti variare simultaneamente temperatura, suzione e stato tensionale nel piano ottaedrico. Viene mostrato come la mancata presa in considerazione della vera natura triassiale della resistenza (dipendenza della resistenza dall'angolo di Lode) possa dare origine a previsioni a sfavore di sicurezza.

Il modello impiegato prevede un comportamento puramente plastico, mentre in generale le argilliti hanno un comportamento meccanico quasi-fragile rappresentabile tramite la teoria della meccanica del danno. Lo sviluppo di nuovi modelli costitutivi è concentrato sul comportamento idro-meccanico in condizioni sature, in quanto la disponibilità di dati sperimentali sul comportamento accoppiato termo-idro-meccanico in condizioni non sature e non isoterme delle argilliti è limitata. Sulla base di tali riflessioni è stato sviluppato un nuovo modello costitutivo che unisce le teorie del danno e della plasticità per geomateriali quasi-fragili. La variabile interna che descrive il danno è una funzione dell'energia di deformazione elastica, a sua volta una funzione del tensore della deformazione elastica di trazione. Al fine di garantire l'unicità della soluzione, la funzione plastica è stata formulata nello spazio delle tensioni efficaci del danno. Il modello costitutivo è stato implementato numericamente attraverso uno schema di tipo implicito. La consistenza termodinamica del modello costitutivo è stata successivamente analizzata, rivelando risultati positivi. I risultati numerici a livello del punto materiale sono stati confrontati con i risultati sperimentali presi da letteratura

e ottenuti in prove di compressione triassiale. Si riscontra accordo tra i valori relativi alle previsioni numeriche e i dati sperimentali.

Il modello costitutivo è stato ulteriormente sviluppato e modificato per migliorarne la calibrazione dei parametri ed i risultati numerici su uno spettro più ampio di confinamenti. In questo caso, l'accoppiamento tra il danno e la plasticità è tale per cui la variabile danno è una funzione scalare dell'incremento di deformazione plastica e la funzione plastica rappresenta il limite di resistenza del materiale. Il potenziale plastico è non associato ed il modello costitutivo è stato implementato numericamente con uno schema implicito nel risolutore ad elementi finiti *Code_Aster*. Esempi di validazione del modello costitutivo comprendono il confronto tra i risultati numerici e sperimentali relativi al comportamento meccanico puro in condizioni di compressione triassiale di due argilliti e il comportamento idro-meccanico in condizioni non drenate di una terza argillite. Dai risultati del confronto si evince come il modello costitutivo sviluppato sia un potente strumento per descrivere il comportamento idro-meccanico delle argilliti.

Il modello costitutivo è stato ulteriormente esteso per tenere conto dell'anisotropia e del comportamento in condizioni triassiali vere della resistenza. Entrambe le caratteristiche sono peculiari delle argilliti. Le due estensioni sono state confrontate separatamente con i dati sperimentali presi da letteratura e relativi a diversi geomateriali, in vere condizioni triassiali prima e in condizioni di compressione triassiale classica per quanto riguarda l'estensione dell'anisotropia. Le prestazioni del modello costitutivo, in termini di errore tra risultati numerici e dati sperimentali, sono state confrontate, per la diversa serie di materiali presi in considerazione, con le prestazioni fornite da altri criteri di rottura comunemente utilizzati in geomeccanica. I risultati mostrano come il modello proposto fornisca un errore globale inferiore rispetto a quello relativo agli altri criteri di rottura.

Al fine di evitare una dipendenza della soluzione dalla discretizzazione spaziale e dunque una eccessiva localizzazione, le analisi agli elementi finiti, in presenza di comportamento rammollente che può dare origine a soluzioni biforcute, devono essere eseguite impiegando una tecnica di regolarizzazione adeguata. In questo caso, tale tecnica è costituita dal secondo gradiente della dilatanza, la cui implementazione è disponibile in *Code_Aster*. Una serie di esempi numerici sono stati svolti per evidenziare le principali caratteristiche della risposta strutturale del modello costitutivo di plasticità e danno in abbinamento al secondo gradiente della dilatanza. I risultati ottenuti mostrano come il parametro che controlla l'evoluzione del potenziale plastico non associato, i parametri che controllano la risposta nella fase di rammollimento, l'anisotropia della resistenza e la scala del problema svolgano un ruolo di primo piano nel definire le caratteristiche della soluzione in presenza di localizzazione. I risultati mostrano infine che la dipendenza della soluzione dalla discretizzazione spaziale viene rimossa e l'obiettività della soluzione ripristinata.

Infine, viene presentata l'analisi agli elementi finiti relativa allo scavo di una galleria in condizioni idro-meccaniche. Il modello costitutivo di plasticità e danno sviluppato è stato impiegato in combinazione al secondo gradiente della dilatanza. I parametri sono stati in parte calibrati sulla base di risultati sperimentali ed in parte ottenuti a partire dalla letteratura e non sono stati fatti variare per ottenere risultati più fedeli relativi allo scavo di tunnel. I risultati numerici relativi alla pressione interstiziale, alla convergenza delle pareti del tunnel e al danno intorno allo scavo sono stati confrontati con i dati registrati in-situ durante lo scavo del FE-tunnel presso il sito del Mont Terri, Svizzera. Il confronto tra le previsioni numeriche e i dati sperimentali mostra la coerenza del modello sviluppato nel fornire previsioni numeriche accurate.

Parole chiave: modellazione costitutiva, meccanica delle argilliti, Mont Terri Project, Opalinus Clay, plasticità e danno, *Code_Aster*, plasticità anisotropica, tensore strutturale anisotropo, resistenza in condizioni triassiali vere, angolo di Lode, localizzazione, secondo gradiente di dilatanza, FE-tunnel, analisi di scavo di gallerie, Excavation Damaged Zone (EDZ), plasticità in condizioni non sature, plasticità in condizioni non isoterme, accoppiamenti termo-idro-meccanici.

Acknowledgements

Several people had an impact on a personal and professional level during my studies as a Ph.D. student, and I will like to take this opportunity to thank them.

My gratitude goes to Prof. Lyesse Laloui, my thesis supervisor, for the trust he placed on me, for the opportunity that I received, for his guidance and for the countless advices, professional and personal, that he gave me. I will always be grateful for the liberty he entrusted me with, for the several opportunities to present my work in international conferences I received, for having the possibility of taking an active role in the scientific community and for the strong support I received in all the initiatives I engaged.

I would like to express my gratitude to swisstopo, ENSI (Eidgenössisches Nuklearsicherheitsinspektorat) and the Mont Terri Project for financing this research. In particular, I would like to thank Dr. Paul Bossart, Dr. Christophe Nussbaum and Dr. David Jaeggi of swisstopo and Dr. Erik Frank of ENSI for their exceptional support with highly valuable scientific and professional advices and discussions and for providing support with data and reports from the Mont Terri Project. I wish also to thank Dr. Werner Gräsle of BGR for providing experimental data on the triaxial behavior of Opalinus Clay.

I wish to thank Prof. Stan Pietruszczak, Dr. Paul Bossart and Dr. Joël Cugnoni for accepting to review my Ph.D. thesis and to take part to the examination jury and Prof. Christophe Ancy for accepting to chair the committee on behalf of the doctoral school.

A special thanks goes to Dr. Victor Vilarrasa, for the highly valuable support, advices and revisions he gave me during the last phases of this thesis. I wish to thank the senior scientists and post-docs at the LMS laboratory, Dr. Sergio Samat, with whom I share authorship of part of this work, Dr. Alessio Ferrari, Dr. Fabrice Dupray and Dr. Roman Makhnenko. Their advices and the scientific discussions I highly enjoyed having with them constituted a fundamental added value to the thesis.

I would like to thank Dr. Sylvie Granet, Dr. Roméo Fernandes, Dr. Sam Cuvilliez and Dr. Simon Raude of EDF for the important support I received in the implementation of the constitutive model in *Code_Aster* and for the hospitality they gave me during my stay at the EDF R&D department in Clamart.

I wish to thank Prof. Frédéric Collin of Université de Liège for the important advices in numerical modeling I received from him. I will like to thank as well Prof. Milan Jiràsek of Charles University Prague for the inspirational lectures I assisted to during the attendance of the course “Modeling localized inelastic deformations”.

I had the wonderful opportunity of supervising the final master work of Thibaut Le Gac, an exceptional student that I shall thank for his professional attitude and for the friendship we shared.

I wish to thank Prof. Benoît Girardin and his wife Ms. Claire Falcay for the long discussions we shared (I call them “the Swiss talks”) in front of some amazing bottles of aged Bordeaux and homemade apple pies.

Writing a Ph.D. thesis requires long hours of work sitting, so I wish to take this occasion to thank Monica Deferre and Andrea Orvieto, my friends and personal physiotherapists, who were responsible for my wellness in the last period of my Ph.D. studies.

I wish to express my gratitude to the staff of LMS and LMR laboratories, Gilbert Gruaz, Patrick Dubey, Laurent Gastaldo, Barbara Tinguely, Rosana Turielle and Dr. Federica Sandrone.

The benefits I received from studying in an international environment at EPFL are incalculable. I had the opportunity of meeting several wonderful people, colleagues and friend, to whom I am deeply grateful. I shall consider myself lucky if I made half the impact they did on me. Their names, which I will never forget, are Alessandro Rotta Loria, Donatella Manca, Felipe Orellana Espinoza, Alberto Minardi (for long my personal driver!), Timur Gökok, Alice Di Donna, Étienne Cassini, Ali Seiphoori, Chao Li, Erika Paltrinieri, Andrea Delisio, Abdusalam Aili, Yafei Qiao, Belinda Bates, Mathias Nagel, Wladislav Mantic, Dimitrios Terzis, Samuel Maceda, John Eichenberger, Thomas Mimouni, Valentina Favero, Giovanni Schicchi, Eleonora Crisci, Andrea Salmi, Gaia Rodriquez and Danila Mylnikov.

A special thanks goes to my family, my father, my mother, my brother and my cousin, who were simply “always there”.

Last but not least (!), I am thankful to Valentina, my beloved, who supported me unconditionally during the darker and lighter times.

1. Introduction

1.1. Background and objectives

Since the mid 1950's, the exploitation of nuclear energy for civil purposes of electric power generation became a reality in different countries. At the time speaking, 442 reactors are operative in 30 countries and 66 are under construction in 15 countries (www.iaea.org). Countries like Switzerland, Germany, Belgium and Italy have opted for phase-out policies of the national nuclear power program, i.e., have opted for an interruption of energy production from nuclear reactors and a decommissioning of the related infrastructures. High-level radioactive wastes originate from operation and decommissioning of nuclear power plants and necessitate proper storage and isolation, given the dangers for living beings related to high doses of radiations exposure. In a 2015 report from the International Atomic Energy Agency (International Atomic Energy Agency, 2015), a global inventory of 2'745'000 m³ storage and 72'000 m³ cumulative disposal of high-level radioactive wastes was estimated. Whether future global nuclear power production policies will lead to an increase or a decrease of installed capacity^a, the safe disposal of high-level nuclear spent fuel will remain an important issue to address.

It is currently accepted by the international community that deep geological storage is the safest solution for long-term management of high-level nuclear spent fuel (Feiveson et al., 2011). The spent nuclear fuel is placed in metal canisters surrounded by engineered buffer materials made of swelling bentonite mixture. Everything is emplaced in tunnels excavated in the host geological formation. All the components of this concept, called multiple barrier system, are essential to the final safety of the disposal. Host geological formations should be located at depth of several hundred meters and will consist in low-permeable crystalline, argillaceous or salty rocks. While the concept in countries like Sweden, Canada and Finland contemplates the disposal in granite rocks, in countries like Switzerland, Belgium and France argillaceous formations are taken into consideration as disposal sites.

More precisely, in Switzerland, Opalinus Clay (OPA), a sedimentary low-permeable argillaceous rock with schistosity planes originated from marine deposition and which is extensively present in the north of the country, is currently considered as the potential host formation. The Mont Terri Project started in 1996 with the precise aim of studying and

^a Actual trends indicate a future increase in installed nuclear capacity. Current projections estimate that installed nuclear power capacity should grow from 372 GW(e) in 2014 to 401 GW(e) and 699 GW(e) in 2030, for the low and high estimates, respectively (International Atomic Energy Agency, 2015).

gathering information on the mechanical, hydrogeological and geochemical behavior of OPA (Thury and Bossart, 1999). An Underground Research Laboratory (URL) was since then opened in the Jura mountains, at the Mont Terri anticline, inside an OPA formation. Currently, 15 international partners take an active role in the project with the Swiss Federal office of Topography (swisstopo) running the URL and holding responsibility for the safety of the laboratory (www.mont-terri.ch). As it is intended exclusively as a research project, no radioactive material will ever be stored in the URL (Bossart and Thury, 2007).

Several experiments took place at the Mont Terri URL since its creation in 1996, principally aimed at characterizing the hydrogeological, geochemical and rock mechanical properties of OPA, the effects of tunnel excavation on OPA, the formation and evolution of the excavation damaged zone (EDZ) and demonstration experiments to test, e.g., the tunnel excavation, canister and bentonite emplacement, sealing and heating (Bossart and Thury, 2007). Since 2012, a 1:1 scale demonstration experiment called FE Full-scale Emplacement experiment is running at the Mont Terri URL. Its goal is to simulate a real emplacement case with heated canisters, which simulate the heat released by high-level nuclear waste, surrounded by bentonite buffer inside OPA. The collected data will serve many purposes, including early stage assessment and evolution of the EDZ and hydrogeological and thermo-hydro-mechanical response of the system from the short to the medium term (up to 15 to 20 years).

The formation and evolution of the EDZ was characterized in detail at the Mont Terri URL by collecting data during several excavations that include Gallery 98, Gallery 04, Gallery 08 which are excavated perpendicular to schistosity (also called bedding planes) of OPA and MB-tunnel and FE-tunnel which are excavated parallel to the schistosity of OPA (Lisjak et al., 2015). A detailed investigation of the principal hydro-mechanical characteristics of the EDZ around Gallery 98 was carried out in Bossart et al. (2002) by analyzing resin injected overcores and by performing hydraulic permeability tests. Figure 1-1 shows the conceptual model of the excavation damaged zone, which can be divided into two subzones: an inner zone with connected fractures and an outer zone with non-connected fracture network (Bossart et al., 2002). Permeability tests have shown an increase of hydraulic conductivity of several orders of magnitude in the EDZ (Bossart et al., 2002). Furthermore, geophysical measurements from boreholes drilled around FE-tunnel showed a decrease in elastic wave velocity in the EDZ, which corresponds to a degradation of elastic moduli (Jaeggi et al., 2014). The hydraulic conductivity increase and elastic degradation in the EDZ, both caused by unloading fractures that form during and after the excavation process, can constitute a weak link in the global safety of the repository (Bossart et al., 2002). Radionuclides and other harmful substances could leak from opened preferential paths in the EDZ.

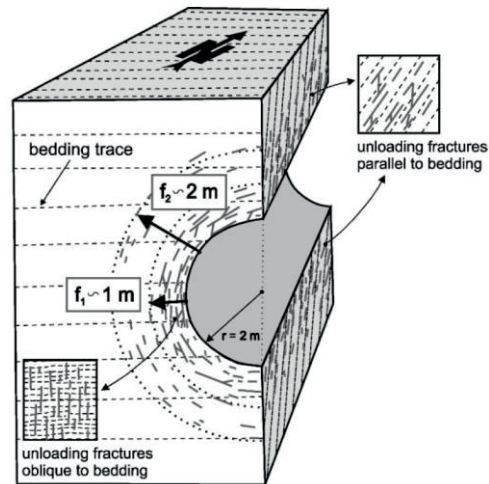


Figure 1-1: EDZ conceptual model from Bossart et al. (2002).

Reliable numerical predictions of the formation and evolution of EDZ, crucial for the global safety of repository conditions, lay their bases on the understanding of the related hydro-mechanical processes. These complex processes are multi-physics in nature, i.e., they result from the combined effects of mechanical stress redistribution and pore pressure decreasing around the excavated tunnel. Integrated campaigns to investigate the hydro-mechanical behavior of OPA at both the laboratory and field scale were carried out to assess properly the knowledge of these processes. Analogously, numerical predictions must integrate both scales to be successfully employed. In this context, the overall focus and back-bone of this thesis consists in the prediction of the hydro-mechanical characteristics of OPA at the laboratory and field scale in the short-term. At field scale, this corresponds to the response during the excavation and subsequent ventilation phase (up to several months).

Multiphysics conditions are often encountered not only in nuclear wastes repository applications, but also in unconventional oil and gas operations or carbon capture and storage (CCS) in deep geological formations. The true triaxial strength of geomaterials is a feature that must be considered to obtain reliable and realistic predictions. This applies as well when non-isothermal and unsaturated conditions are found. Few studies are dedicated to this topic, which remains at present widely unexplored. No integrated experimental campaign was undertaken to highlight strength dependency in non-isothermal and unsaturated conditions when all three components of the principal stress tensor are controlled simultaneously (true triaxial conditions). The first objective of this thesis is to explore an important characteristic of geomaterials from a purely numerical point of view: the true triaxial strength in coupled thermo-hydro-mechanical (THM) conditions.

Since few experimental data on the coupled THM behavior of OPA in particular, and shale in general, are available, attention is drawn toward the hydro-mechanical behavior in water saturated conditions. From a purely mechanical point of view, OPA can be considered as a quasi-brittle geomaterial. Figure 1-2a shows the evolution of deviatoric stress as a function of vertical strain in a triaxial test on OPA (Gräsle and Plischke, 2011). The definition of quasi-brittleness implies that, in triaxial compression conditions, failure is accompanied by a stress drop (softening) in which inelastic permanent strains accumulate as the elastic characteristics are degraded. Prior to the stress peak (failure stress), the permanent strains are small and comparable to the elastic ones and, at the onset of inelasticity, dilatancy is observed. In this phase, micro-cracks form and grow inside the material. In the post-peak phase, the response becomes brittle, softening appears and dilation continues until residual conditions are reached. In this last phase, the material deformation is localized and constant shear stresses are observed. Loading-unloading cycles evidence degradation of the elastic moduli. This behavior is common to many shales and was observed, e.g., in La Biche shale (Wong, 1998) and Tournemire shale (Abdi et al., 2015; Niandou et al., 1997).

Carrying out triaxial undrained tests evidences the coupled hydro-mechanical behavior of OPA. Figure 1-2b shows undrained triaxial tests on OPA with pore water pressure measurements from the Schlattingen site, Switzerland (Jahns, 2013). Initial pore water pressure is 4.9 MPa and confinement 7.8 MPa. The pore water pressure increases in the pre-peak compression phase as a result of the imposed no-flow conditions (undrained). At the onset of dilatancy, the pore water pressure increase is damped as the pore space increases and can even change its sign and decrease. From these results, non-associativity of the post-peak plastic behavior of OPA is deduced. Otherwise, the pressure drop in the associated case would lead to negative values of the pore pressure. Similar behavior was observed, e.g., in North Sea shale (Horsrud et al., 1998).

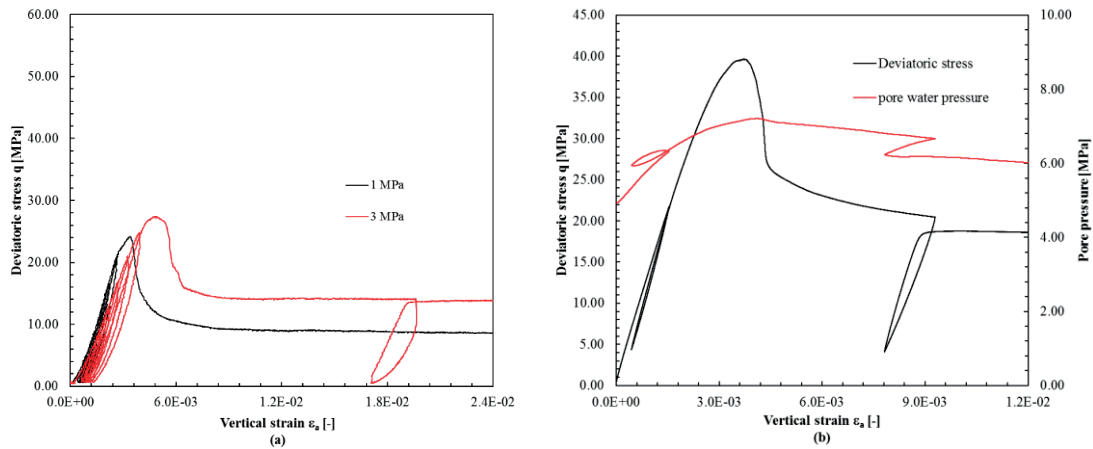


Figure 1-2: Experimental results on OPA sandy facies from Mont Terri in conventional undrained triaxial tests with bedding planes oriented parallel to the maximum principal stress (a). Data obtained from Gräsle and Plischke (2010). Experimental results on OPA from Schlattingen in conventional undrained triaxial tests with bedding planes oriented parallel to the maximum principal stress and pore pressure measurement (b). Data obtained from Jahns (2013).

As some of the peculiar aspects of OPA are in reality common features of several shales, the analyses and interpretation will be, in these cases, not solely restricted to OPA but expanded to other shales. Constitutive models that couple the theories of plasticity and damage are the most effective to represent the main characteristics of the mechanical behavior of OPA in particular, and shale in general (Chen et al., 2010; Chen et al., 2012; Chiarelli et al., 2003). Continuum damage mechanics (CDM) is a powerful mathematical tool to represent at the continuum level the formation, growth and coalescence of microcracks in a solid and was successfully employed to describe failure characteristics of metals, ceramics, concrete, geomaterials and composites (Lemaitre et al., 2009). From a phenomenological point of view, CDM accounts for the reduction of elastic moduli and the hardening/softening response (depending on the formulation). No permanent strain development can be incorporated in the constitutive description by purely damage models, so that it is necessary to couple it with plastic theory to successfully represent the experimental characteristics of the mechanical behavior of shales. Both purely plastic or purely damage models suffer shortcomings in the description of the constitutive response of quasi-brittle geomaterials. Several possible choices can be made in the way that plasticity and damage are coupled together, and the discriminant is often given by what is the final goal to be achieved by the constitutive model. This constitutes the second objective of the thesis developed in Chapters 3 and 4, where two possible combinations of plasticity and damage to describe the isotropic constitutive mechanical response of shales are explored. The effects of pore water pressure in undrained tests are also explored in a coupled hydro-mechanical formulation in Chapter 4.

OPA contains bedding planes as a result from the process of marine sedimentation of clay particles. Most of the physical properties of OPA are anisotropic and, more precisely, transversely isotropic. These include the mechanical properties of deformability and strength. A laboratory characterization of the anisotropic strength of OPA at the Mont Terri site can be found in Gräsle and Plischke (2011) and in Gräsle and Plischke (2010). Results concerning anisotropic behavior of OPA from Schlattingan site, Switzerland, are found in Jahns (2013). In a conventional triaxial compression test, the stress at failure depends on the orientation of the bedding planes with respect to the maximum principal stress (Gräsle and Plischke, 2011). The minimum is found at 45° degrees of inclination, although the tested inclinations are exclusively 0°, 45° and 90° for OPA at Mont Terri. OPA at Shlattingen site was tested at an additional inclination of 30° between maximum principal stress (vertical) and bedding planes (Jahns, 2013). In this set of experimental tests, the minimum strength is found at 30°, which is closer to experimental findings related to other shales (e.g., Penrhyn slate (Attewell and Sandford, 1974)). Strength anisotropy is a feature peculiar of many other shales that contain bedding planes, like Tournemire shale (Abdi et al., 2015; Niandou et al., 1997). As an example, Figure 1-3a shows the linear deviatoric strength envelope as a function of minimum principal stress for Penrhyn slate (Attewell and Sandford, 1974). The anisotropic nature of strength of OPA, and shales in general, must be taken into account in the constitutive response. Several failure criteria for anisotropic geomaterials were proposed in the literature and an extensive review can be found in Dubeau et al. (1998). The extension to include anisotropic strength in the constitutive plastic-damage description is the third objective of the thesis and is developed in Chapter 5.

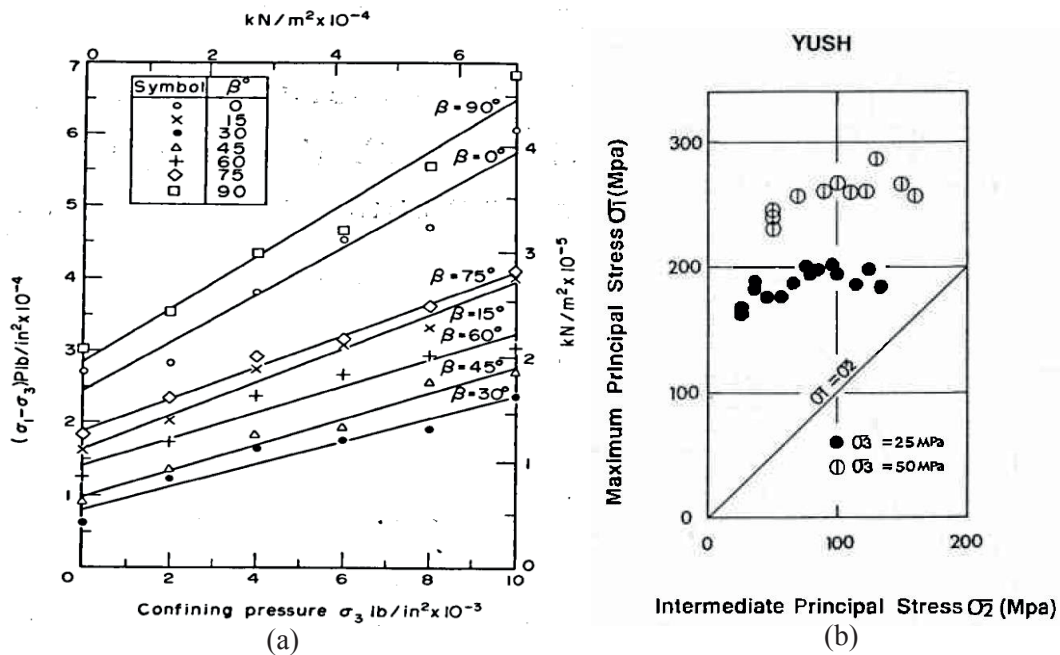


Figure 1-3: Experimental results on Penrhyn Slate anisotropic strength envelopes (a) (Attewell and Sandford, 1974) and on the true triaxial strength of Yuubari Shale (b) (Takahashi and Koide, 1989).

Although no data exists for OPA, it can be assumed that, like many other geomaterials, strength characteristics depend as well on all three components of the stress tensor. This, referred to as true triaxial strength, is illustrated for Yuubari shale in Figure 1-3b, where true triaxial compression tests were performed by controlling the three components of the principal stress tensor independently (Takahashi and Koide, 1989). Accounting for true triaxial strength is of particular importance when performing FEM analyses of boundary value problems, as the three components of the principal stress tensor are usually different from each other. The extension to account for true triaxial strength of shale is the fourth objective of the thesis and Chapter 5 is partly devoted to this.

It is commonly known that softening constitutive models (like the one developed) employed for the description of quasi-brittle materials suffer from spurious mesh dependency in FEM analyses. This is caused by the so-called loss of ellipticity of the governing equations and translates into instabilities of the solution in terms of localized inelastic strain (Jirásek, 2007). Upon mesh refinement, the size of the localization band will decrease as it is usually the size of the smallest elements in the spatial discretization. Dissipation will reduce as well and the global response can degenerate into snap-back type phenomenon. The global mechanical response is affected by the discretization, which is unphysical and therefore unacceptable. To overcome this issue, proper regularization techniques need to be employed (Jirásek and

Bazant, 2002). This leads to the fifth objective of the thesis developed in Chapter 6, i.e., exploring the structural response in presence of localization with the proposed plastic-damage model and a second gradient of dilatancy model available in *Code_Aster*.

The work flow takes its start from the experimental behavior of OPA at the URL field scale. The coupled hydro-mechanical behavior is then analyzed in detail based on laboratory scale observations, mainly from triaxial compression tests. The result is a proper constitutive model designed for OPA, although its results can be well applied to a wider range of shale and sedimentary geomaterials. Numerical issues are addressed so that the resulting constitutive model can be employed to perform FEM analysis of problems at the field scale. Current numerical studies of excavation problems in argillaceous material for nuclear storage application are either based on purely plastic approaches (Pardoen et al., 2015), or lack the possibility of performing medium to long-term analyses as they are based on a purely mechanical approach, which is representative for short-term conditions (Lisjak et al., 2015). This leads to the sixth objective of the thesis, which is developed in Chapter 7: employing all of the concepts developed from Chapter 3 to 6 in a numerical study of the medium term hydro-mechanical response during the FE-tunnel excavation at the Mont Terri site.

1.2. Thesis layout

The thesis is composed of 6 chapters that each constitute the material of articles prepared for publication in international peer-reviewed journals. At present, one is already published, one is under review and the remaining 4 are to be submitted. Each chapter is structured as a paper and contains its own introduction, literature review, methods, results, conclusions and bibliography. The last chapter presents general conclusions and future perspectives based on the results of the previous ones. The thesis is structured as follows:

- Chapter 2 addresses the problem of true triaxial strength in coupled thermo-hydro-mechanical conditions from a constitutive point of view. A constitutive model based on the work of Francois and Laloui (2008) and extended to account for true triaxial strength is presented. Two case studies are addressed with simulations at the Gauss point level of THM stress paths with the presented model. The first case deals with a hypothetical CO₂ injection case in OPA and the second one with the combined saturation and heating in bentonite during a hypothetical canister post emplacement situation. The content of this chapter was submitted to the International Journal of Geomechanics and is currently under review.
- Chapter 3 presents the development steps of a first coupled plastic-damage model in isotropic conditions called MS1. The damage law is of the Marigo type (Marigo, 1981) and its evolution depends on a strain decomposition of the tensile principal stress tensor. Plasticity is formulated in the effective stress space and controls the

residual part of the stress-strain curve. The model is tested against laboratory experimental triaxial compression data from Opalinus Clay and LaBiche shale. The content of this chapter was published in the International Journal of Solids and Structures (Parisio et al., 2015).

- Chapter 4 deals with the evolution and improvement of the first plastic-damage model MS1 by exploring a different combination of the two theories. It results in a new constitutive model called MS2, which is better fitted for a wider range of confinements and easier to calibrate with respect to the most common laboratory experimental tests available. The constitutive model is implemented in the FEM open source solver *Code_Aster* (www.code-aster.org). The model is once again validated against experimental triaxial compression tests from Opalinus Clay at the Mont Terri site and LaBiche shale. An additional validation example is presented. It consists of coupled hydro-mechanical undrained triaxial compression tests results from Opalinus Clay at Schlattingen site. The contents of this chapter are planned to be published in the scientific journal Computers and Geotechnics.
- Chapter 5 presents the extension of the coupled damage-plasticity constitutive model MS2 to include true triaxiality and anisotropy of strength. True triaxiality is implemented with a modified Van Eekelen formulation (Van Eekelen, 1980) and anisotropy is introduced by employing the theory of mix invariants of stress and fabric tensor proposed by Pietruszczak and Mroz (2000). It results in a new constitutive model called MS3 with an updated failure surface. The failure surface is validated against five different sedimentary geomaterials for the true triaxial extension and against ten different shales for the anisotropic extension. To assess the performances of the new failure surface, results given by model MS3 on the different sets of experimental behavior are compared against results given by 3 other failure surfaces for the true triaxial extension and against 2 other failure surfaces for the anisotropic extension. The contents of this chapter constitute the material that will be submitted to the scientific journal Rock Mechanics and Rock Engineering for publication.
- Chapter 6 addresses the problems of strain localization and pathological mesh dependency for the anisotropic plastic-damage model MS3. *Code_Aster* offers the possibility of employing a second gradient of dilatancy formulation for the regularization of localized strains (Fernandes, 2009). The combination of the plastic-damage model and this regularization technique are explored with a series of numerical examples. The principal factors that control the structural behavior are highlighted. The contents of this chapter will be submitted for publication in the scientific journal Geomechanics for the Energy and the Environment.

- Chapter 7 deals with the numerical simulation of the FE-tunnel excavation at the Mont Terri site. The simulation is carried out in hydro-mechanical coupled conditions with the proposed anisotropic plastic-damage model MS3 implemented in *Code_Aster*. To avoid pathological mesh-dependency, the second gradient of dilatancy formulation is employed. The predicted pore water pressure evolution, tunnel walls displacements and damage are compared against data collected in-situ. Considerations regarding the anisotropic deformation mode are presented. The contents of this chapter will constitute the material for a publication in the scientific journal *Engineering Geology*.
- Chapter 8 presents the general conclusions of the work and some perspectives for future research are addressed based on the results obtained in the thesis.

1.3. References

- Abdi, H., Labrie, D., Nguyen, T.S., Barnichon, J.D., Su, G., Evgin, E., Simon, R., Fall, M., 2015. Laboratory investigation on the mechanical behaviour of Tournemire argillite. *Can Geotech J* 52, 268-282.
- Attewell, P.B., Sandford, M.R., 1974. Intrinsic shear strength of a brittle, anisotropic rock—I: experimental and mechanical interpretation, *International Journal of Rock Mechanics and Mining Sciences & Geomechanics Abstracts*. Elsevier, pp. 423-430.
- Bossart, P., Meier, P.M., Moeri, A., Trick, T., Mayor, J.-C., 2002. Geological and hydraulic characterisation of the excavation disturbed zone in the Opalinus Clay of the Mont Terri Rock Laboratory. *Eng Geol* 66, 19-38.
- Bossart, P., Thury, M., 2007. Research in the Mont Terri Rock laboratory: quo vadis? *Physics and Chemistry of the Earth, Parts A/B/C* 32, 19-31.
- Chen, L., Shao, J.F., Huang, H.W., 2010. Coupled elastoplastic damage modeling of anisotropic rocks. *Comput Geotech* 37, 187-194.
- Chen, L., Shao, J.F., Zhu, Q.Z., Duveau, G., 2012. Induced anisotropic damage and plasticity in initially anisotropic sedimentary rocks. *Int J Rock Mech Min* 51, 13-23.
- Chiarelli, A.S., Shao, J.F., Hoteit, N., 2003. Modeling of elastoplastic damage behavior of a claystone. *Int J Plasticity* 19, 23-45.
- Duveau, G., Shao, J.F., Henry, J.P., 1998. Assessment of some failure criteria for strongly anisotropic geomaterials. *Mech Cohes-Frict Mat* 3, 1-26.
- Feiveson, H., Mian, Z., Ramana, M., von Hippel, F., 2011. Managing nuclear spent fuel: Policy lessons from a 10-country study. *Bulletin of the Atomic Scientists* 27.
- Fernandes, R., 2009. Modélisation numérique objective des problèmes hydromécaniques couplés dans le cas des géomatériaux. Thèse de doctorat à l'école doctorale Université jean Fourier (Grenoble1), 107-136.

- Francois, B., Laloui, L., 2008. ACMEG-TS: A constitutive model for unsaturated soils under non-isothermal conditions. *Int J Numer Anal Met* 32, 1955-1988.
- Gräsle, W., Plischke, I., 2010. Laboratory Testing (LT) Experiment: Mechanical Behavior of Opalinus Clay, Final report from Phases 6 – 14. Mont Terri Technical Note TN 2009-07.
- Gräsle, W., Plischke, I., 2011. LT-A Experiment: Mechanical Behavior of Opalinus Clay, Data report from Phase 15. Mont Terri Technical Note TN 2010-86.
- Horsrud, P., Sonstebo, E.F., Boe, R., 1998. Mechanical and petrophysical properties of north sea shales. *Int J Rock Mech Min* 35, 1009-1020.
- International Atomic Energy Agency, 2015. Nuclear Technology Review 2015.
- Jaeggi, D., Wymann, L., Burrus, F., Becker, J., P, B., 2014. FE-E (EDZ-characterization in the vicinity of the FE-gallery) Experiment Synthesis of the excavation damaged zone (EDZ) (Draftversion). Mont Terri Technical Note TN 2014-33.
- Jahns, E., 2013. Geomechanical laboratory tests on Opalinus Clay cores from the bore hole Schlattingen SLA-1. Nagra Work Report NAB.
- Jirásek, M., 2007. Mathematical analysis of strain localization. *Revue Européenne de Génie Civil* 11, 977-991.
- Jirásek, M., Bazant, Z.P., 2002. Inelastic analysis of structures. John Wiley & Sons.
- Lemaitre, J., Chaboche, J.-L., Benallal, A., Desmorat, R., 2009. *Mécanique des matériaux solides-3eme édition*. Dunod.
- Lisjak, A., Garitte, B., Grasselli, G., Müller, H., Vietor, T., 2015. The excavation of a circular tunnel in a bedded argillaceous rock (Opalinus Clay): short-term rock mass response and FDEM numerical analysis. *Tunn Undergr Sp Tech* 45, 227-248.
- Marigo, J., 1981. Formulation d'une loi d'endommagement d'un matériau élastique. *CR Acad. Sci. Paris II* 292, 1309-1312.
- Niandou, H., Shao, J.F., Henry, J.P., Fourmaintraux, D., 1997. Laboratory investigation of the behaviour of Tournemire shale. *Int J Rock Mech Min* 34, 3-16.
- Pardoen, B., Seyedi, D., Collin, F., 2015. Shear banding modelling in cross-anisotropic rocks. *Int J Solids Struct* 72, 63-87.
- Parisio, F., Samat, S., Laloui, L., 2015. Constitutive analysis of shale: a coupled damage plasticity approach. *Int J Solids Struct* 75-76, 88-98.
- Pietruszczak, S., Mroz, Z., 2000. Formulation of anisotropic failure criteria incorporating a microstructure tensor. *Comput Geotech* 26, 105-112.
- Takahashi, M., Koide, H., 1989. Effect of the intermediate principal stress on strength and deformation behavior of sedimentary rocks at the depth shallower than 2000 m, ISRM international symposium. International Society for Rock Mechanics.

1.3 References

- Thury, M., Bossart, P., 1999. The Mont Terri rock laboratory, a new international research project in a Mesozoic shale formation, in Switzerland. *Eng Geol* 52, 347-359.
- Van Eekelen, H., 1980. Isotropic yield surfaces in three dimensions for use in soil mechanics. *Int J Numer Anal Met* 4, 89-101.
- Wong, R., 1998. Swelling and softening behaviour of La Biche shale. *Can Geotech J* 35, 206-221.

2. Strength evolution of geomaterials in the octahedral plane under non-isothermal and unsaturated condition

Authors: V Vilarrasa, F. Parisio and L. Laloui.

Status: under review at International Journal of Geomechanics.

Contributions: V. Vilarrasa and F. Parisio co-wrote the manuscript, decided the modeling strategies to adopt and interpreted the results. Model implementation and calculating model derivatives was performed by V. Vilarrasa. Numerical analyses were performed by F. Parisio. L. Laloui supervised the work, contributed to the decision of modeling strategies, edited the manuscript and will be the senior responsible author (SRA) of the publication.

Abstract

Current geomechanical applications imply non-isothermal processes of unsaturated geomaterials, in most cases following stress paths different than the classical triaxial compression often used in laboratory testing. Though the effects of temperature, suction and stress path direction (Lode's angle) on the strength of geomaterials have been investigated independently, the integrated analysis combining the three effects has not been performed yet. In this paper, we formulate a thermo-plastic constitutive model for unsaturated conditions that accounts for the Lode's angle on the strength of geomaterials. The yield surface evolves shrinking for increasing temperature, expanding for increasing suction and has its maximum strength for triaxial compression and the minimum for triaxial extension. We highlight the importance of accounting for temperature, suction and Lode's angle on the evolution of the strength through examples that can be related to geo-energy applications. Numerical results show that not considering these effects may give rise to misleading predictions of the strength of geomaterials.

Keywords: Lode's angle, plane strain, thermo-plasticity, constitutive modeling, thermo-hydro-mechanical couplings

2.1. Introduction

The strength of geomaterials is known to be dependent on the stress path direction in the octahedral plane, i.e., on the Lode's angle (Potts and Gens, 1984). The Lode's angle can be accounted for in existing constitutive models using, for example, the Van Eekelen formulation (Van Eekelen, 1980). However, deriving the parameters that describe the strength of geomaterials as a function of Lode's angle is difficult because the strength of soils is usually derived from conventional triaxial tests at the laboratory scale. Despite their appellative, most of the times conventional triaxial tests are to be intended as biaxial, since only two components are controlled simultaneously (vertical stress and the horizontal stress, equal in all direction and applied through confinement). To account for plane strain conditions, 'true triaxial' tests, in which the three principal stresses, σ'_1 , σ'_2 and σ'_3 , are controlled simultaneously, are required (e.g., Makhnenko and Labuz, 2015). Since the actual strength is lower for all stress paths different than a compressive triaxial stress path

($\sigma'_2 = \sigma'_3$) (Lee, 1970; Peric et al., 1992; Alshibli et al., 2003; Wanatowski and Chu, 2007; Makhnenko and Labuz, 2014), strength is usually overestimated in many geo-engineering problems that involve stress paths different than triaxial compression (Potts and Gens, 1984), such as landslides, shallow foundations and tunnel excavations.

In recent years, new geomechanical applications, including high-level nuclear waste disposal, energy piles and geologic carbon storage, which imply temperature and suction variations, have arisen because of the growing interest in geo-energies. This adds further complexity to the strength evolution of geomaterials because, apart from the effect of Lode's angle, the strength also evolves with temperature and suction changes. On the one hand, the yield limit is enhanced as suction increases (Gens et al., 2006; Sheng, 2011) and on the other hand, the yield surface shrinks for increasing temperatures (Hueckel and Baldi, 1990; Hueckel and Borsetto, 1990; Laloui and Cekerevac, 2003). Though some efforts have been devoted to determining the strength of soils for stress paths different than triaxial compression (e.g., Nanda and Patra, 2015), the integrated analysis of the combined effect of temperature, suction and stress path direction on the strength of geomaterials has not been performed (e.g., Xie and Shao, 2012; Zhang et al., 2012).

This lack of integrated analysis of the strength of non-isothermal unsaturated geomaterials represents a big limitation to accurately predict the behavior of geomaterials in the current applications that are of interest. The objective of this paper is to provide a qualitative understanding of the effects of temperature, suction and stress path direction on the strength of geomaterials. To do so, a non-isothermal constitutive model for unsaturated geomaterials that accounts for the stress path direction is first presented. Next, we determine the evolution of the strength as a function of temperature, suction and stress path direction considering several examples that can be related to geo-energy applications. Finally, we discuss the implications of this study and draw some conclusions.

2.2. Model formulation

We describe a sophisticated constitutive model that captures the main characteristics of the non-isothermal behavior of unsaturated geomaterials. This constitutive model is based on the work of Hujeux (1979) and its extensions to unsaturated non-isothermal conditions (Laloui and François, 2009; François and Laloui, 2008; Di Donna and Laloui, 2015). The thermo-hydro-mechanical equations of the model were introduced in the original work of Laloui and François (2008, 2009) and the water retention curve with hysteresis is taken after the work of Laloui and Nuth (2009). While the thermo-mechanical equations taking into account the true triaxial nature of strength (Lode's angle dependency) were introduced in the work of Di Donna and Laloui (2015), the present work aims at integrating all of the previous

developments in a single constitutive model that takes into account the true triaxial nature of strength in a full thermo-hydro-mechanical framework. It not only integrates non-linear thermo-elasto-plasticity with a water retention curve model that includes hysteresis between the drying and wetting paths, but also incorporates the Lode's angle to account for a stress path dependent strength in the octahedral plane.

This constitutive model for unsaturated geomaterials under non-isothermal conditions is formulated in terms of the generalized effective stress approach (Nuth and Laloui, 2008; Kim et al., 2013)

$$\boldsymbol{\sigma}' = (\boldsymbol{\sigma} - p_g \mathbf{I}) + S_l (p_g - p_l) \mathbf{I} = \boldsymbol{\sigma} - \alpha_b (S_g p_g + S_l p_l) \mathbf{I}, \quad (2.1)$$

where $\boldsymbol{\sigma}'$ is the effective stress tensor, $\boldsymbol{\sigma}$ is the total stress tensor, $s = p_g - p_l$ is suction, p_l is liquid pressure, p_g is gas pressure, \mathbf{I} is the identity matrix, α_b is Biot coefficient, S_l is the liquid saturation degree and S_g is the gas saturation degree. The degrees of saturation of the two phases present in the pore volume satisfy that

$$S_g + S_l = 1. \quad (2.2)$$

Changes in the effective stress will induce deformation of the geomaterial. Deformation can be either elastic or plastic, where the classical decomposition of the incremental total strain holds valid

$$d\boldsymbol{\varepsilon} = d\boldsymbol{\varepsilon}^e + d\boldsymbol{\varepsilon}^p, \quad (2.3)$$

where $d\boldsymbol{\varepsilon}$ is the total strain increment tensor, $d\boldsymbol{\varepsilon}^e$ is the non-linear thermo-elastic strain increment tensor and $d\boldsymbol{\varepsilon}^p$ is the thermo-plastic strain increment tensor. Elastic strain will occur when the stress state falls inside the yield surface. Additionally, plastic strain will occur when the stress state lays on the yield surface. We adopt the sign convention of geomechanics, i.e., stress and strain are positive in compression and negative in extension.

The rate of elastic strain is given by

$$d\boldsymbol{\varepsilon}^e = \mathbf{E}^{-1} d\boldsymbol{\sigma}' - \boldsymbol{\beta}_T dT, \quad (2.4)$$

where \mathbf{E} is the mechanical stiffness tensor, $\boldsymbol{\beta}_T$ is the thermal expansion coefficient tensor and T is temperature. Thus, elastic strain can be due to changes in the total stress and/or fluid pressure (first term of Eq. (2.4)) and in temperature (second term of Eq. (2.4)).

A non-linear elastic theory is employed and the elastic moduli that compose the mechanical stiffness tensor \mathbf{E} (Appendix A) depend on the effective stress state as

$$K = K_{ref} \left(\frac{p'}{p'_{ref}} \right)^{n_e}, \quad (2.5)$$

$$G = G_{ref} \left(\frac{p'}{p'_{ref}} \right)^{n_e}, \quad (2.6)$$

where K and G are the bulk and shear moduli, respectively, K_{ref} and G_{ref} are the reference bulk and shear moduli, respectively, measured at the reference mean effective stress p'_{ref} , p' is the mean effective stress and n_e is a material parameter controlling the non-linearity of the elastic law.

The thermal expansion coefficient tensor $\beta_{\mathbf{T}}$ depends on both temperature and effective stress state, which, assuming an isotropic thermal expansion, reads

$$\beta_{\mathbf{T}} = \frac{1}{3} \beta'_s \mathbf{I}, \quad (2.7)$$

where the volumetric thermal expansion coefficient of the solid skeleton β'_s is given by

$$\beta'_s = \beta'_{s_0} \left(1 - \frac{T - T_0}{100} \right) \frac{p'_{cr_0}}{p'}, \quad (2.8)$$

where β'_{s_0} is the reference thermal expansion coefficient at a reference temperature T_0 and p'_{cr_0} is the initial critical state pressure at reference temperature T_0 .

If the effective stress state reaches the yield surface, plastic strain occurs. This irreversible strain is induced by two coupled dissipative processes

$$d\boldsymbol{\varepsilon}^p = d\boldsymbol{\varepsilon}^{p,iso} + d\boldsymbol{\varepsilon}^{p,dev}, \quad (2.9)$$

where $d\boldsymbol{\varepsilon}^{p,iso}$ and $d\boldsymbol{\varepsilon}^{p,dev}$ are the components of the plastic strain tensor deriving from the isotropic and deviatoric plastic mechanisms, respectively. Each of these mechanisms are activated when their respective yield surface is reached, its magnitude is proportional to a plastic multiplier and its direction is given by the flow rule as

$$d\boldsymbol{\varepsilon}^{p,iso} = \lambda_{iso}^p \frac{\partial \mathbf{g}_{iso}}{\partial \boldsymbol{\sigma}'}, \quad (2.10)$$

$$d\boldsymbol{\varepsilon}^{p,dev} = \lambda_{dev}^p \frac{\partial \mathbf{g}_{dev}}{\partial \boldsymbol{\sigma}'}, \quad (2.11)$$

where λ_{iso}^p and λ_{dev}^p are the plastic multipliers of the isotropic and deviatoric mechanisms, respectively, and \mathbf{g}_{iso} and \mathbf{g}_{dev} are the plastic potential functions of the isotropic and deviatoric mechanisms, respectively.

The yield surface of each mechanism is given by

$$f_{iso} = p' - p'_c r_{iso} = 0, \quad (2.12)$$

$$f_{dev} = q - Mp' \left(1 - b \ln \left(\frac{p'd}{p'_c} \right) \right) r_{dev} = 0, \quad (2.13)$$

where f_{iso} and f_{dev} are the yield surface of the isotropic and deviatoric mechanisms, respectively, r_{iso} and r_{dev} are the degrees of plastification of the isotropic and deviatoric mechanisms, respectively, p'_c is the preconsolidation pressure, q is the deviatoric stress, M is the slope of the critical state line in the $(q - p')$ plane, b is a material parameter and d is

$$d = \frac{p'_{c_0}}{p'_{cr_0}}, \quad (2.14)$$

where p'_{c_0} is the preconsolidation pressure at the reference temperature T_0 and p'_{cr_0} is the initial critical pressure at the reference temperature T_0 .

The mean effective stress and the deviatoric stress read

$$p' = \frac{1}{3} (\sigma'_{11} + \sigma'_{22} + \sigma'_{33}), \quad (2.15)$$

$$q = \sqrt{3J_{2D}} = \sqrt{\sigma'^2_{11} + \sigma'^2_{22} + \sigma'^2_{33} - \sigma'_{11}\sigma'_{22} - \sigma'_{22}\sigma'_{33} - \sigma'_{33}\sigma'_{11} + 3(\sigma'^2_{12} + \sigma'^2_{23} + \sigma'^2_{13})}, \quad (2.16)$$

respectively, where $J_{2D} = 1/2 \text{tr}(\mathbf{s} : \mathbf{s})$ is the second invariant of the deviatoric effective stress tensor $\mathbf{s} = \boldsymbol{\sigma}' - p'\mathbf{I}$ and σ'_{ij} is the ij th component of the effective stress tensor, where $i, j = 1, 2, 3$.

The preconsolidation pressure couples the two plastic mechanisms because it appears in both yield surfaces (recall Equations (2.12) and (2.13)). The preconsolidation pressure, which is the main hardening parameter, depends on the volumetric plastic strain, ε_v^p , temperature and suction as

$$p'_c = \begin{cases} p'_{c_0} \exp(\beta \varepsilon_v^p) [1 - \gamma_T \log(T/T_0)], & \text{if } s < s_{eH} \\ p'_{c_0} \exp(\beta \varepsilon_v^p) [1 - \gamma_T \log(T/T_0)] [1 + \gamma_s \log(s/s_{eH})], & \text{if } s \geq s_{eH} \end{cases}, \quad (2.17)$$

where β is the plastic compressibility modulus, i.e., the slope of the linear relationship $\varepsilon_v^p - \ln p'_c$, γ_T and γ_s are two material parameters for the thermal and suction evolution, respectively, s is suction and s_{eH} is the entry pressure, i.e., the value of suction at which desaturation starts. The plastic compressibility modulus β is a function of suction

as $\beta = \beta_0 + \omega(s - s_{eH})$, if $s > s_{eH}$, where β_0 is the value of β at suction equal or lower than the entry value and ω is a material parameter. Thus, the yield surfaces expressed in Equations (2.12) and (2.13) should be expressed as a function of the variables $q, p', \varepsilon_v^p, T$ and s (Figure 2-1).

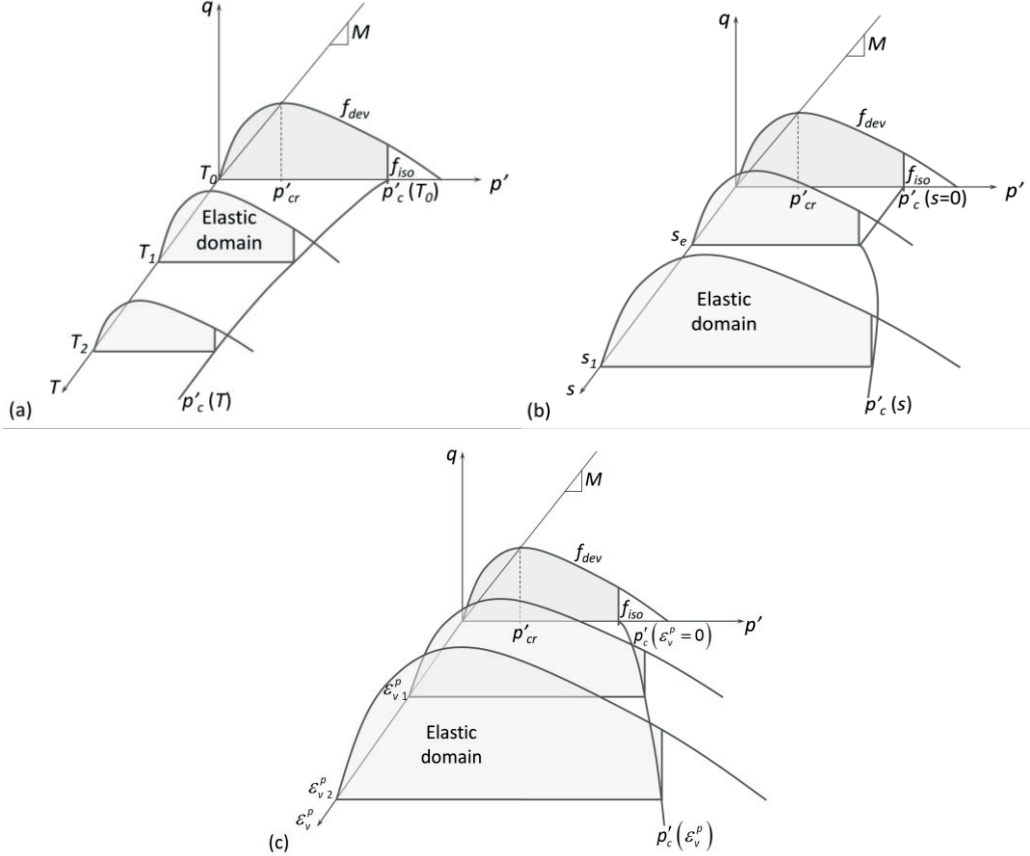


Figure 2-1: Effect of (a) temperature, (b) suction and (c) volumetric plastic strain on the shape of the yield surface of the non-isothermal constitutive model for unsaturated geomaterials.

The degrees of plastification allow a progressive evolution of the yield surfaces during loading as implied in the bounding surface plasticity theory. Their expressions are

$$r_{iso} = r_{iso}^e + \frac{\varepsilon_v^{p,iso}}{c + \varepsilon_v^{p,iso}}, \quad (2.18)$$

$$r_{dev} = r_{dev}^e + \frac{\varepsilon_d^p}{a + \varepsilon_d^p}, \quad (2.19)$$

where a and c are material parameters, r_{iso}^e and r_{dev}^e define the size of the elastic nuclei of the isotropic and deviatoric mechanisms, respectively, $\varepsilon_v^{p,iso}$ is the isotropic part of the volumetric plastic strain and ε_d^p is the deviatoric plastic strain. Previous to reaching the final yield surface, the model produces plastic hardening, while the softening behavior can be observed once the state of stress reaches the final yield surface on the “dry” side and the volumetric plastic strain becomes negative.

The deviatoric yield surface was formulated in Equation (2.13) as depending on two invariants of the effective stress tensor, q and p' . This implies assuming that the projection of the yield surface on the octahedral plane is circular. Such a circular yield surface in the octahedral plane involves that yield conditions are reached at the same deviatoric stress regardless of the direction of the stress path (Lode’s angle). However, plasticity is stress path dependent both for granular (e.g. Lade and Duncan, 1973) and fine-grained soils (e.g. Lade and Musante, 1978) as well as for rocks (e.g., Colmenares and Zoback, 2002; Makhnenko et al., 2015). To overcome such limitations, the yield surface can be formulated in terms of three invariants of stress. The new invariant is the circular coordinate in the deviatoric plane and it is known as Lode’s angle, ϑ , and it varies from -30° to 30° . The Lode’s angle is defined as

$$\sin(3\vartheta) = \frac{3\sqrt{3}}{2} \frac{J_{3D}}{J_{2D}^{3/2}}, \quad (2.20)$$

where $J_{3D} = 1/3 \text{tr}(\mathbf{s}^3) = 1/3 \left(\sum_{i=1,2,3} (\sigma'_{ii} - p')^3 + (\sigma'_{11} - p')(\sigma'_{12} + \sigma'_{13} - 2\sigma'_{23}) + (\sigma'_{22} - p')(\sigma'_{12} + \sigma'_{23} - 2\sigma'_{13}) + (\sigma'_{33} - p')(\sigma'_{13} + \sigma'_{23} - 2\sigma'_{12}) + 6\sigma'_{12}\sigma'_{13}\sigma'_{23} \right)$ is the third invariant of the deviatoric effective stress tensor.

According to the given definition, Lode’s angle equals 30° if the stress path is triaxial in compression, -30° if the stress path is triaxial in extension and an intermediate value for plane strain and plane stress conditions. Though a circular yield surface works well for triaxial stress paths in compression, it generally overestimates the strength for other stress paths. The Mohr-Coulomb yield surface, which shape is an irregular hexagon, is more accurate than the circular surface, but the corners are difficult to handle numerically (Potts and Gens, 1984) if an associated flow rule is employed (the direction of the plastic strain is non defined in the corners and proper techniques must be employed to overcome this issue). Among the different models proposed to reproduce experimental results providing a smooth yield surface, we adopt the Van Eekelen (1980) formulation to define the coefficient M due to its versatility and consistency

$$M = 3\sqrt{3}a_L(1 + b_L \sin(3\vartheta))^{n_L}, \quad (2.21)$$

where a_L , b_L and n_L are three material parameters defined as (Barnichon, 1998)

$$a_L = \frac{r_c}{(1 + b_L)^{n_L}}, \quad (2.22)$$

and

$$b_L = \frac{(r_c/r_e)^{1/n_L} - 1}{(r_c/r_e)^{1/n_L} + 1}, \quad (2.23)$$

where

$$r_c = \frac{1}{\sqrt{3}} \frac{2 \sin \phi'_c}{(3 - \sin \phi'_c)} \text{ and } r_e = \frac{1}{\sqrt{3}} \frac{2 \sin \phi'_e}{(3 + \sin \phi'_e)}, \quad (2.24)$$

where ϕ'_c and ϕ'_e are the friction angles in triaxial compression and extension, respectively. These friction angles may vary with temperature and if they are equal, the Van Eekelen surface coincides with the inscribed Mohr-Coulomb yield surface at Lode's angle equal to $\pm 30^\circ$, yielding a M coefficient of $M = 6 \sin \phi' / (3 - \sin \phi')$ for compression and $M = 6 \sin \phi' / (3 + \sin \phi')$ for extension. If no experimental data of triaxial tests in extension is available, a good approximation could be assuming the extension friction angle equal to the one in compression because it generally leads to small errors (Di Donna, 2014). The parameter a_L must be positive, $-1 < b_L < 1$ and $b_L n_L > 0$. As in the original work of Van Eekelen (1980), the following conditions ensure convexity of the curve in the octahedral plane

$$\begin{aligned} |b_L| &\leq \frac{1}{|9n_L + 1|} && \text{if } n_L \geq 0 \text{ or } n_L \leq -\frac{3}{11} \\ |b_L| &\leq \frac{1}{2} \left[\frac{4 + 13n_L}{(1 + n_L)(1 - 9n_L^2)} \right]^{1/2} && \text{if } -\frac{3}{11} \leq n_L \leq 0, \end{aligned} \quad (2.25)$$

The parameter n_L , in order to ensure the convexity of the surface, has its optimum value of -0.229 (Van Eekelen, 1980) (see Figure 2-2, where the M parameter is plotted in the octahedral plane for a compression angle of 30° and several extension angles).

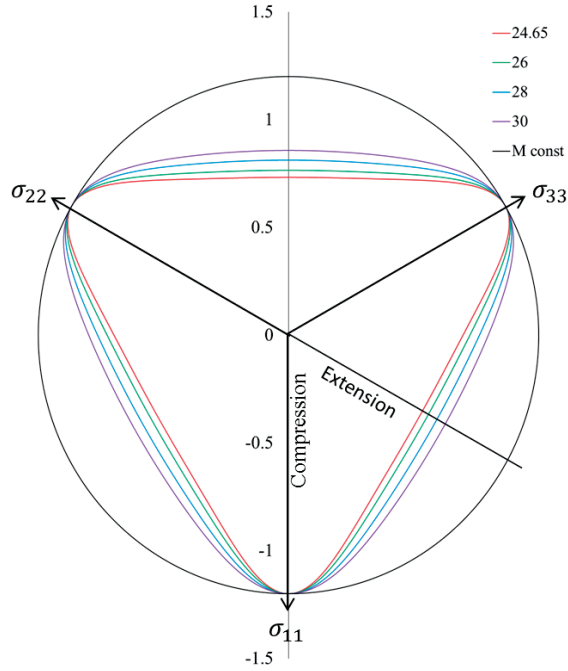


Figure 2-2: Yield surface accounting for the Lode's angle in the octahedral plane for $n_L = -0.229$, a friction angle in compression of 30° and several friction angles in extension.

With this value of n_L , the second condition implies that

$$|b_L| \leq \frac{1}{2} \left[\frac{4 + 13n_L}{(1 + n_L)(1 - 9n_L^2)} \right]^{1/2} = 0.7925, \quad (2.26)$$

therefore, imposing restrictions on the values that the friction angle in extension and in compression can take (recall Equation (2.23)). Furthermore, from Equation (2.26) and assuming that $n_L = -0.229$, it is found that the ratio between coefficients r_c and r_e must satisfy the following condition

$$r_c / r_e \leq 1.6385. \quad (2.27)$$

Figure 2-3 shows the limiting values of the friction angle in extension as a function of the value of the friction angle in compression. To ensure convexity, all possible combinations of the two parameters must lie above the limiting curve and below the bisection line of the plane, where $\phi'_c = \phi'_e$. For values of ϕ'_c above 46.55° the yield surface becomes non-convex and at this point, to ensure convexity, one must have $\phi'_c = \phi'_e$. Above such limit the friction angle

in extension would need to be greater than the one in compression. The maximum strength difference between compression and extension is reached when ϕ'_c is between 20° and 30°.

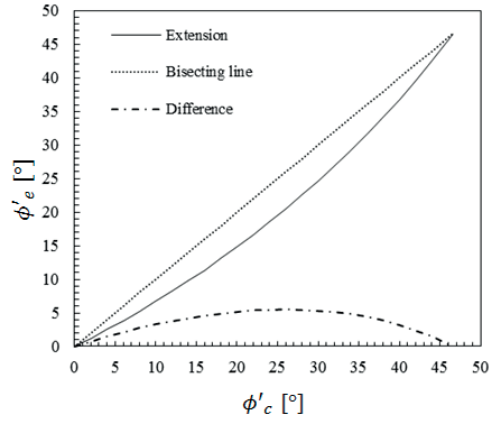


Figure 2-3: Range of possible values of the friction angle in extension as a function of the value of the friction angle in compression to guarantee convexity of the yield surface.

Figure 2-4 and Figure 2-5 illustrate the yield surface in the octahedral plane as a function of temperature and suction, respectively. The yield surface does not have a circular shape due to the strength dependency on Lode's angle. While the yield surface shrinks as temperature increases (Figure 2-4), it maintains a constant size while the suction is lower than the entry pressure, but it expands for higher values of suction.

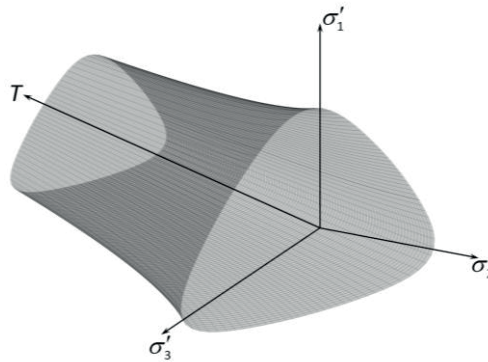


Figure 2-4: 3D representation of the yield surface in the octahedral plane as a function of temperature. The yield surface shrinks for increasing temperatures.

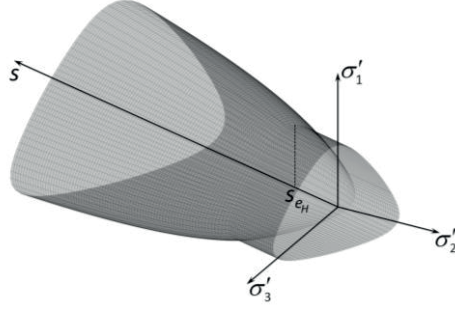


Figure 2-5: 3D representation of the yield surface in the octahedral plane as a function of suction. The yield surface maintains its size while suction is lower than the entry pressure, but it expands for higher values of suction.

The flow rule of the isotropic mechanism is associated, i.e., the plastic potential equals the yield surface, while the deviatoric flow rule is non-associated. The plastic potentials have the following expressions

$$g_{iso} = p' - p'_c r_{iso} = 0 \quad (2.28)$$

$$g_{dev} = q - \frac{\alpha}{\alpha - 1} M p' \left[1 - \frac{1}{\alpha} \left(\frac{p'd}{p'_c} \right)^{\alpha - 1} \right] = 0, \quad (2.29)$$

where α is a non-associativity parameter. Nevertheless, the form of the plastic potentials is unimportant and what matters is their derivative with respect to stress because it determines the flow rules

$$d\boldsymbol{\varepsilon}^{p,iso} = \lambda_{iso}^p \frac{\partial g_{iso}}{\partial \boldsymbol{\sigma}'} = \frac{\lambda_{iso}^p}{3} \mathbf{I}, \quad (2.30)$$

$$d\boldsymbol{\varepsilon}^{p,dev} = \lambda_{dev}^p \frac{\partial g_{dev}}{\partial \boldsymbol{\sigma}'} = \lambda_{dev}^p \left[\frac{\partial q}{\partial \boldsymbol{\sigma}'} + \frac{\alpha}{3} \left(M - \frac{q}{p'} \right) \mathbf{I} - \frac{\partial M}{\partial \boldsymbol{\sigma}'} \frac{\alpha}{\alpha - 1} p' \left[1 - \frac{1}{\alpha} \left(\frac{p'd}{p'_c} \right)^{\alpha - 1} \right] \right]. \quad (2.31)$$

The plastic multipliers λ_{iso}^p and λ_{dev}^p are determined from the Prager's consistency condition, which reads

$$\begin{cases} d\mathbf{F} = \frac{\partial \mathbf{F}}{\partial \boldsymbol{\sigma}'} : d\boldsymbol{\sigma}' + \frac{\partial \mathbf{F}}{\partial \boldsymbol{\pi}} \cdot \frac{\partial \boldsymbol{\pi}}{\partial \boldsymbol{\lambda}^p} \cdot \boldsymbol{\lambda}^p \leq \mathbf{0}, \\ d\mathbf{F}' \cdot \boldsymbol{\lambda}^p \geq 0, \quad \boldsymbol{\lambda}^p \geq \mathbf{0} \end{cases}, \quad (2.32)$$

where $d\mathbf{F}$ is the differential yield surface vector, \mathbf{F} is the yield surfaces vector, $\boldsymbol{\pi}$ is the internal variable vector and $\boldsymbol{\lambda}^p$ is the plastic multiplier vector. The internal variables of the isotropic and deviatoric mechanisms are the preconsolidation pressure p'_c through the volumetric

plastic strain ε_v^p and the degree of plastification of each mechanism, r_{iso} and r_{dev} , respectively. All the derivatives, as well as the plastic multipliers, are detailed in Appendix A. Once the thermo-mechanical stress-strain model is defined, we define the water retention model. This water retention model includes a hysteretic retention curve (Figure 2-6) and a yield surface (Laloui and Nuth, 2009).

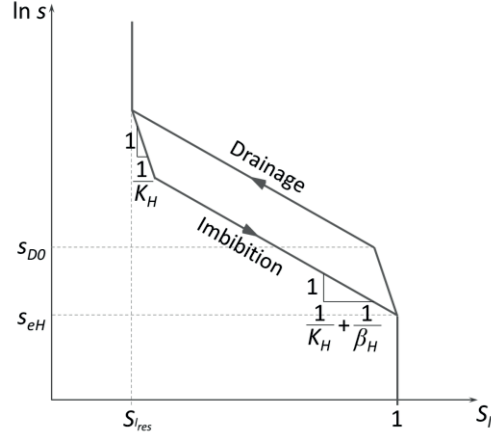


Figure 2-6: Hysteretic retention curve used in the water retention model.

Changes in suction will induce changes in the degree of saturation, which can be either elastic or plastic

$$dS_l = dS_l^e + dS_l^p, \quad (2.33)$$

where dS_l^e and dS_l^p are the elastic and plastic increments in liquid saturation degree, respectively. The elastic part is defined as

$$dS_l^e = \frac{ds}{K_H s/s_{eH}}, \quad (2.34)$$

where K_H is the elastic modulus associated with suction strain and s_{eH} is the updated entry pressure. The entry pressure is a function of the volumetric strain and temperature as

$$s_{eH} = s_e \left(1 - \theta_T \log \left(\frac{T}{T_0} \right) \right) (1 + c_H \varepsilon_v), \quad (2.35)$$

where s_e is the reference entry pressure, ε_v is the volumetric strain and θ_T and c_H are material parameters describing the evolution of the entry pressure with respect to temperature and volumetric deformation, respectively.

The yield surface of the degree of saturation for both the drying and wetting paths is expressed as (Nuth and Laloui, 2008)

$$f_H = \left\| \ln\left(\frac{s}{s_D}\right) + \frac{1}{2} \ln\left(\frac{s_{D_0}}{s_{e_H}}\right) \right\| - \frac{1}{2} \ln\left(\frac{s_{D_0}}{s_{e_H}}\right), \quad (2.36)$$

where s_D is the actual drying yield suction and s_{D_0} is the reference yield suction. s_D is analogous to the preconsolidation pressure of the mechanical stress-strain model. Thus, s_D evolves with suction and its initial value is s_{D_0} . $1/2 \ln(s_{D_0}/s_{e_H})$ is the radius of the yield surface, which is assumed to be constant, and controls the distance between the main drying and wetting curves. Since s_{e_H} evolves with the volumetric strain, the reference yield suction has to be updated to keep the hysteresis of the retention curve constant

$$s_{D_0} = s_{D_i} \frac{s_{e_H}}{s_e}, \quad (2.37)$$

where s_{D_i} is the initial reference yield suction. The actual drying yield suction is given by

$$s_D = s_{D_0} \exp(\beta_H dS_i^p), \quad (2.38)$$

where β_H is the coefficient of compressibility for the plastic part of the degree of saturation.

If the yield surface is reached, plastic increment of degree of saturation occurs. Since the flow rule is associated, this increment reads

$$dS_i^p = \lambda_H^p \frac{\partial f_H}{\partial s}, \quad (2.39)$$

where λ_H^p is the plastic multiplier for the water retention model. The plastic multiplier is derived from the consistency equation

$$\begin{cases} df_H = \frac{\partial f_H}{\partial s} ds + \frac{\partial f_H}{\partial \pi_H} \cdot \frac{\partial \pi_H}{\partial \lambda_H^p} \cdot \lambda_H^p \leq 0 \\ df_H \cdot \lambda_H^p \geq 0, \quad \lambda_H^p \leq 0 \end{cases}, \quad (2.40)$$

where π_H are the internal variables for the water retention model, i.e., dS_i^p . The derivation of the plastic multiplier is detailed in Appendix B.

If the soil is saturated, i.e., $s \leq s_{e_H}$, or the degree of saturation equals its residual value, i.e., $S_l = S_{l_{res}}$, then the degree of saturation remains constant and equals 1 or $S_{l_{res}}$, respectively.

2.3. Evolution of the strength with temperature, suction and stress path direction

We present some examples of the evolution of the strength with temperature, suction and stress path direction (recall Figure 2-4 and Figure 2-5). In the first set of examples, we consider a clay rich shale which properties are shown in Table 2-1. From a purely mechanical point of view, shales are usually approached with combined plastic-damage models (as in e.g. Chen et al., 2010; Shojaei et al., 2014; Parisio et al., 2015), although the theory of plasticity itself was employed as well in modelling their deformation behavior (Salager et al., 2013). In the present work focus is addressed toward the purely plastic models that could be representative of a range of geomaterials that not necessarily include damageable behavior. Further extensions in the framework of Continuum Damage Mechanics are possible and foreseeable when focus is placed toward quasi-brittle materials like shale or other sedimentary rocks.

Table 2-1: Material parameters of a clay rich shale based on properties of Opalinus clay adapted from Salager et al. (2013).

Property	Value
Reference bulk modulus, K_{ref} (MPa)	1500
Reference shear modulus, G_{ref} (MPa)	1250
Material parameter n_e (-)	0.15
Reference thermal expansion coefficient, β'_{s_0} ($^{\circ}\text{C}^{-1}$)	$2.0 \cdot 10^{-5}$
Initial critical state pressure, p'_{cr_0} (MPa)	25.0
Parameter d (-)	1.2
Parameter b (-)	0.8
Plastic compressibility modulus at zero suction β_0 (-)	43
Material parameter ω (MPa^{-1})	0
Material parameters for the thermal evolution γ_T (-)	0.7
Material parameters for the suction evolution γ_s (-)	0.25
Material parameter a (-)	0.003
Material parameter c (-)	0.02
Size of the elastic nucleus of the isotropic mechanism, r_{iso}^e (-)	1.0
Size of the elastic nucleus of the deviatoric mechanism, r_{dev}^e (-)	1.0
Non-associativity parameter, α (-)	1.0
Friction angle in triaxial compression, ϕ'_c ($^{\circ}$)	25
Friction angle in triaxial extension, ϕ'_e ($^{\circ}$)	23
Lode's angle parameter n_L (-)	-0.229

The initial stress state, fluid pressure and temperature are assumed to be those at In Salah, Algeria, i.e., $\sigma'_v = 26.5$ MPa, $\sigma'_H = 31.9$ MPa, $\sigma'_h = 12.7$ MPa, $p_l = 18.0$ MPa and $T = 95$ $^{\circ}\text{C}$ (Morris et al., 2011). We consider two cases, one in which a water pressure increment of up to 12 MPa at constant temperature is applied and another in which, simultaneously, a water pressure increment of up to 12 MPa and a temperature decrease of up to 45 $^{\circ}\text{C}$ are applied. For this particular example, saturated conditions are maintained during the whole analysis, so temperature effects on shale strength are emphasized. In both cases, we analyze the effect of considering or not Lode's angle.

Figure 2-7 clearly illustrates the difference in the size of the yield surface when considering or not Lode's angle. Failure conditions are reached for a fluid pressure increase of 2.3 MPa if the effect of Lode's angle on the strength is taken into account. However, not considering Lode's angle leads to safe geomechanical conditions even for an increase in fluid pressure of 12 MPa. This significant difference in the overpressure necessary to reach failure conditions highlights the importance of using formulations that take into account Lode's angle, especially when the stress path is far from triaxial compression (see Figure 2-8). Thus, polyaxial triaxial tests at the laboratory scale including temperature and suction changes should also be employed for a full characterization of the geomechanical behavior of reservoir rocks, given the implications for safety analyses.

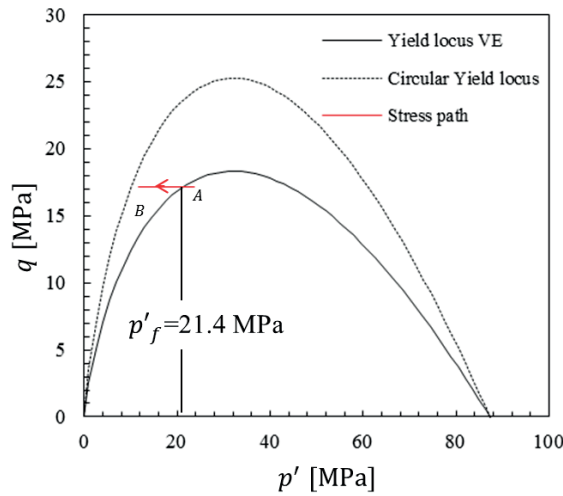


Figure 2-7: Stress path due to a fluid pressure increase of 12 MPa in the deviatoric stress – mean effective stress plane. Both the yield surface when not considering (circular yield) and when considering Lode's angle (yield locus VE, referring to van Eekelen (1980) formulation) are plotted.

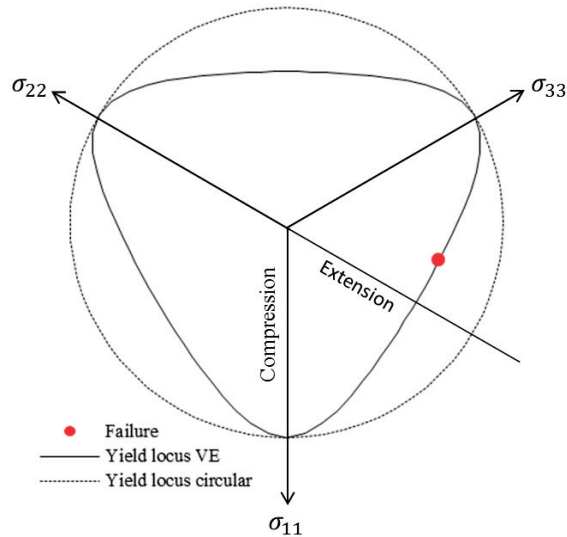


Figure 2-8: Yield surface in the octahedral plane that causes failure when considering Lode's angle (VE: van Eekelen (1980) formulation) at a mean effective stress of 21.4 MPa (see Figure 7). The circular yield surface, which does not consider Lode's angle, is shown for comparison.

Figure 2-9 shows the effect of cooling on the strength of the considered geomaterial. The strength increases as temperature drops and thus, a higher overpressure can be induced before reaching the yield surface. For the case in which Lode's angle is taken into account (Figure 2-9b), the yield surface is reached for an overpressure of 4.9 MPa, instead of the 2.3 MPa in the isothermal case. When not considering Lode's angle effect on the strength, the overpressure that could be reached is even higher, which may lead to the false impression that injection conditions are safe. These examples could be representative of the processes that occur in geologic carbon storage. The caprock, which is a low permeability formation with high entry pressure will experience a pressure buildup that will progressively increase during the duration of the CO₂ injection (Rutqvist et al., 2010), which will last several decades. This pressure buildup will be due to water flow, but not CO₂ flow, because if the caprock integrity is maintained, CO₂ will not be able to penetrate into the caprock due to capillarity (Vilarrasa and Carrera, 2015). Furthermore, CO₂ reaches the storage formation at a lower temperature than that corresponding to the geothermal gradient, which will eventually cool down the caprock (Paterson et al., 2008).

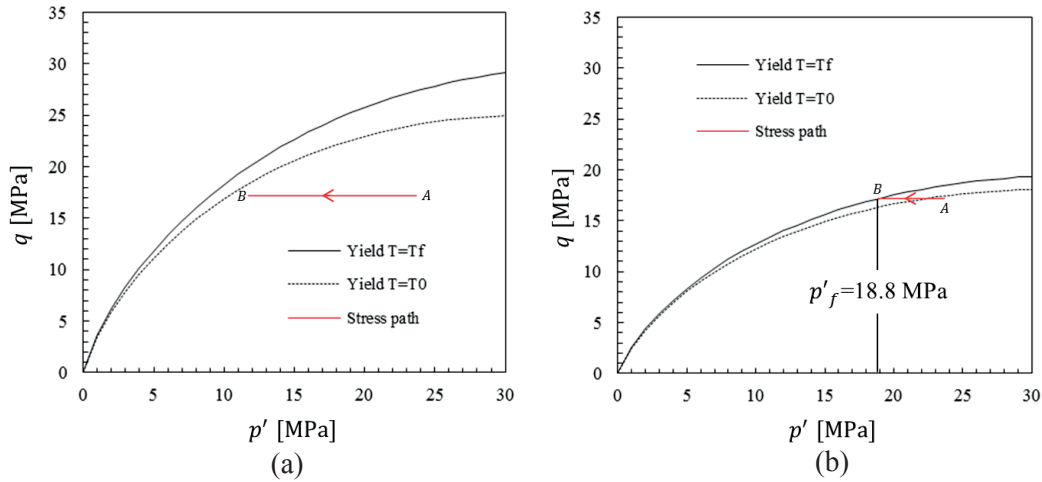


Figure 2-9: Stress path due to a fluid pressure increase of 12 MPa and a temperature decrease of 45 °C in the deviatoric stress – mean effective stress plane when (a) not considering Lode’s angle and (b) considering Lode’s angle. Cooling increases the size of the yield surface. The initial yield surface (before cooling) is shown for comparison.

Since cooling increases the size of the yield surface, the reduction in the strength caused by the stress path direction is partially compensated (Figure 2-9). Thus, in the vicinity of the injection well, where cooling will occur, a larger overpressure may be sustained without undergoing yielding. However, cooling will induce a thermal stress reduction that should be considered in rock stability analysis (Vilarrasa et al., 2015a). Farther away, outside of the cooled region, the overpressure induced by injection will be smaller and thus, failure conditions will be less likely to occur even though the strength will not be increased by cooling.

In the second set of examples, we consider an expansive soil with the properties shown in Table 2-2. We consider an initial stress state with $\sigma'_v = 7.0$ MPa, $\sigma'_H = 1.0$ MPa, $\sigma'_h = 0.5$ MPa. We assume that the initial temperature equals 20 °C and that the initial suction of the soil is 3 MPa, which equals the initial entry pressure and thus, the initial water saturation degree is 1.0. We consider the effect of considering or not Lode’s angle in two situations. One in which the suction remains constant while temperature progressively increases (temperature increment of 100 °C) and another in which both suction and temperature increase (suction and temperature increment of 3 MPa and 100 °C, respectively). The problem is solved in plane strain conditions at the material point level, with the out of plane direction coinciding with the maximum horizontal stress. The initial stress state is close to triaxial compression (Lode’s angle of 26°). However, the symmetry of the problem causes an increase of the intermediate stress due to induced thermal and suction stresses that progressively brings the stress state far from triaxial compression.

Table 2-2: Material parameters of an expansive clay adapted from François and Laloui (2008).

Property	Value
Reference bulk modulus, K_{ref} (MPa)	16.0
Reference shear modulus, G_{ref} (MPa)	3.5
Material parameter n_e (-)	1.0
Reference thermal expansion coefficient, β'_{s_0} ($^{\circ}\text{C}^{-1}$)	$6.8 \cdot 10^{-4}$
Initial critical state pressure, p'_{cr_0} (MPa)	12.0
Parameter d (-)	1.5
Parameter b (-)	1.0
Plastic compressibility modulus at zero suction β_0 (-)	14.3
Material parameter ω (MPa^{-1})	10^{-6}
Material parameters for the thermal evolution γ_T (-)	0.87
Material parameters for the suction evolution γ_s (-)	1.1
Material parameter a (-)	0.001
Material parameter c (-)	0.02
Size of the elastic nucleus of the isotropic mechanism, r_{iso}^e (-)	0.99
Size of the elastic nucleus of the deviatoric mechanism, r_{dev}^e (-)	0.99
Non-associativity parameter, α (-)	1.0
Friction angle in triaxial compression, ϕ'_c ($^{\circ}$)	30
Friction angle in triaxial extension, ϕ'_e ($^{\circ}$)	25
Lode's angle parameter n_L (-)	-0.229
Reference entry pressure, s_e (MPa)	3.0
Elastic modulus associated with suction strain, K_H (MPa)	∞
Coefficient of compressibility for the plastic part of the degree of saturation, β_H (MPa)	8.64
Material parameter θ_T (-)	0.1
Material parameter c_H (-)	1.15

Figure 2-10 and Figure 2-11 plot the stress path in the temperature – mean effective stress plane and suction – mean effective stress plane, respectively, for the two cases, i.e., temperature increment and simultaneous increment in temperature and suction. The mean effective stress slightly increases due to the thermal stress induced by heating (Figure 2-10a and Figure 2-11a). When suction increases along with temperature (Figure 2-10b and Figure 2-11b), an additional increase in the mean effective stress takes place (recall Equation (2.1)). In both cases, the stresses induced by heating and drying become larger in the out of plane direction than in the other two principal directions because of the symmetry of the problem, which causes a reduction of Lode’s angle. The Lode’s angle becomes -5° and 11° when only heating occurs and when both temperature and suction increase, respectively. The larger reduction in Lode’s angle when only heating occurs is due to the fact that the maximum and minimum principal stresses remain constant, while the intermediate increases due to the induced thermal stress. By contrast, all stresses become higher when suction also increases (recall Equation (2.1)), so the relative difference between the principal stresses remains smaller in this case.

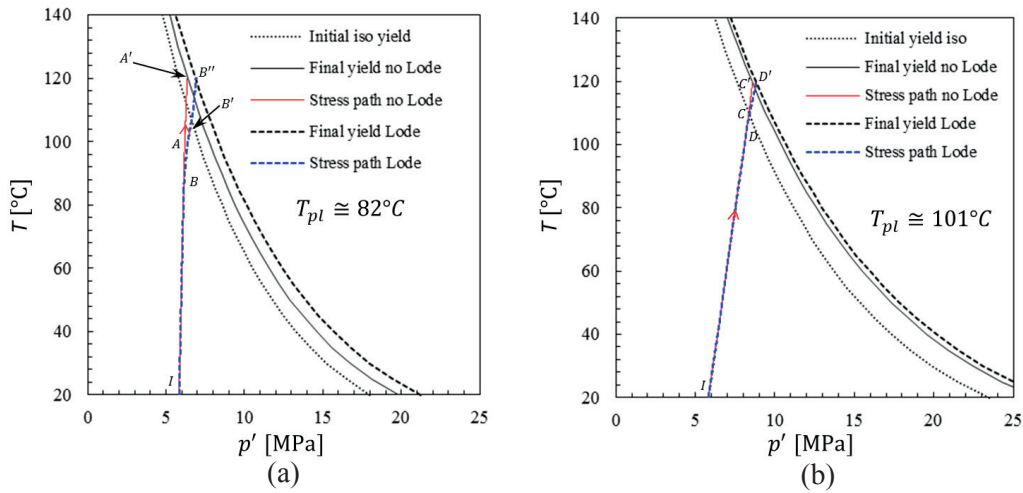


Figure 2-10: Stress path in the temperature – mean effective stress plane for (a) a 100 $^\circ\text{C}$ increment in temperature and (b) a simultaneous 100 $^\circ\text{C}$ and 3 MPa increment in temperature and suction, respectively. Both the isotropic yield surface at the onset of failure and the final isotropic yield surface are indicated.

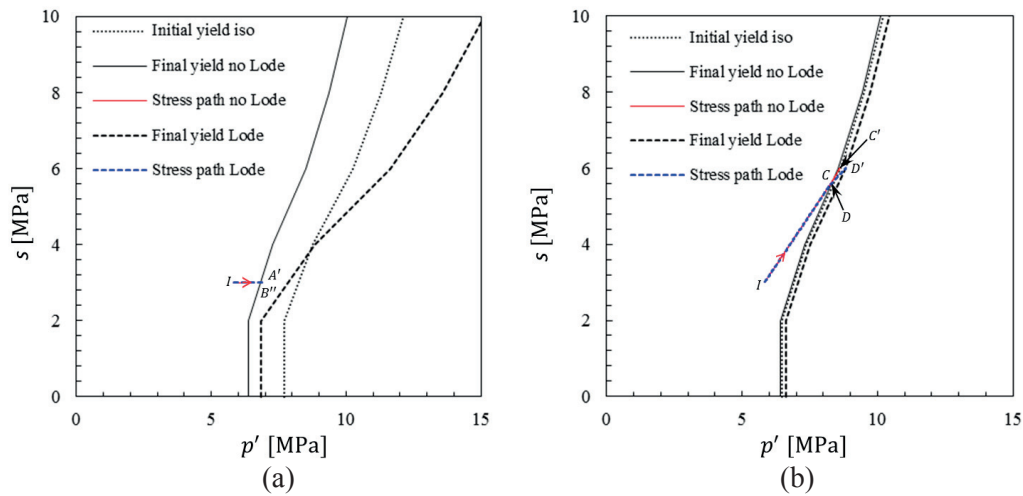


Figure 2-11: Stress path in the suction – mean effective stress plane for (a) a 100 °C increment in temperature and (b) a simultaneous 100 °C and 3 MPa increment in temperature and suction, respectively. Both the isotropic yield surface at the onset of failure and the final yield surface are indicated.

Figure 2-10a shows that, when there are no suction changes, the yield surface is first reached around 82 °C when considering Lode's angle, but around 92 °C when not considering Lode's angle. Thus, not considering Lode's angle may result in an overestimation of the maximum reachable temperature before failure occurs. Note that the yield surface shrinks as temperature increases (recall Figure 2-1 and Figure 2-4). This shrinkage is the reason why the expansive soil eventually yields. The deviatoric yield surface is first reached (points A and B). Furthermore, the isotropic yield surface is also reached around 110 °C when considering Lode's angle (point B'). For temperatures higher than the yield temperature, the yield surface moves following the stress path with hardening while plastic strain accumulates. Figure 2-10a and Figure 2-10b show the isotropic yield surface when the deviatoric yield surface is first reached (point B at 82 °C and point A at 92 °C), the isotropic yield surface when it is first reached when considering Lode's angle (point B' at 109 °C) and the final isotropic yield surface (points A' and B'' at 120 °C).

Figure 2-10b illustrates the isotropic yield surface when suction increases together with temperature in the temperature – mean effective stress plane at the onset of plasticity, which occurs around 101 °C when considering Lode's angle (point D) and around 109 °C when not considering Lode's angle (point C), and the final isotropic yield surfaces (points C' and D'). The initial yield surface (at point I) coincides with the one shown in Figure 2-10a for the initial yield. However, suction strengthens the geomaterial, increasing the size of the yield surface (recall Figure 2-1 and Figure 2-5). Thus, the onset of failure occurs at a higher mean effective stress. Nevertheless, since the mean effective stress increases with suction, if the suction increment is very pronounced, plasticity could start at a lower temperature than when

suction remains constant because the resulting stress path points more directly towards the yield surface.

Figure 2-12 represents the volumetric strain as a function of temperature for the two analyzed examples. The expansive soil dilates as it is heated. For the case where suction remains constant, this dilation is elastic until the onset of plasticity (points A and B). Between A and A' and B and B'' , in addition to the elastic expansion, there is a thermal consolidation that causes an irreversible volume decrease of the soil, which reduces the rate of expansion and even causes compaction (between B' and B''). When both suction and temperature increase, the expansion of the expansive soil is smaller because the soil shrinks as suction increases, i.e., water saturation degree decreases. Furthermore, strain evolution is not linear because the soil becomes stiffer as suction increases (recall Equations (2.5) and (2.6)). In both cases, considering Lode's angle leads to larger plastic strain than when not considering Lode's angle, which again highlights the importance of accounting for the combined effect of temperature, suction and Lode's angle on the strength of geomaterials.

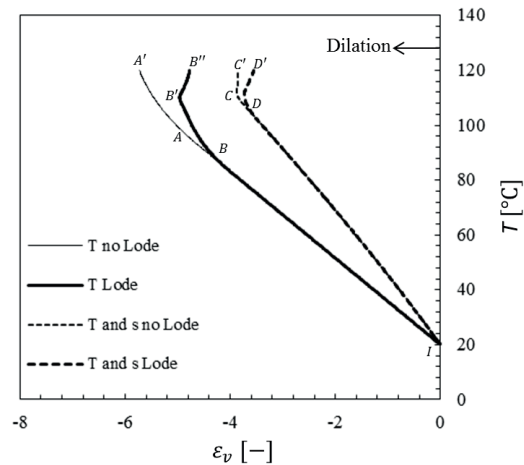


Figure 2-12: Volumetric strain as a function of temperature considering (Lode) and not considering (no Lode) Lode's angle for the case in which only temperature increment of 100°C is applied (T) and for the case in which a simultaneous temperature increment of 100 °C and suction increment of 3 MPa are applied (T and s). The letters in the Figure can be correlated to the letters appearing in Figure 2-10 and Figure 2-11.

Another interesting process is that when the soil is heated at constant suction, the degree of saturation slightly decreases. This decrease is due to the coupling between the thermo-mechanical stress-strain model and the water retention model, in which the entry pressure is a function of temperature and soil deformation (recall Equation (2.35)). A temperature increase and a dilation of the soil cause a decrease of the entry pressure. Since the initial suction of the soil coincides with the initial entry pressure, the heating of the soil at constant suction leads to a decrease in the entry pressure that causes the desaturation of the soil.

This last set of examples could be related to the processes that will occur in nuclear waste disposal. The high-level nuclear waste will release heat over hundreds of thousands of years as a result of the continuing nuclear decay of the radioactive material that it contains. This heat will cause expansion of the bentonite buffer, which, if not fully allowed to increase its volume, will generate thermally induced stresses. Furthermore, the temperature rise will initially dry the bentonite surrounding the canisters, increasing suction (Sanchez et al., 2012; Vilarrasa et al., 2015b). In the long-term, groundwater will eventually saturate the whole backfill, but this saturation process may take decades or even longer due to the dual structure nature of expansive soils (Sanchez et al., 2012; Vilarrasa et al., 2015b) and to the low rate of water inflow coming from the low permeability host rock.

The absolute values of temperature and overpressure that lead to failure conditions in the presented examples should be interpreted qualitatively because we are not modeling the whole 3D problem. However, the relative effect of temperature, suction and stress path direction on strength evolution is clearly highlighted by these examples. To properly model whether failure conditions may be reached or not in practical applications, a complete characterization of geomaterials, including the combined effect of temperature, suction and stress path direction should be carried out. Such testing programs represent new challenges for the entire geomechanics community, as clearly one can understand the difficulties of performing laboratory investigations with proper combinations of the mentioned effects. However complicated and challenging, such testing programs constitute the starting point towards increasing safety margins and reducing uncertainties related with the most demanding geomechanical applications, such as, e.g., nuclear waste storage, geologic carbon storage, unconventional reservoir and deep geothermal exploitation.

2.4. Conclusions

A constitutive model for unsaturated geomaterials that includes non-isothermal effects and the effect of the stress path direction on the strength has been presented. The yield surface shrinks for increasing temperature, expands for increasing suction and has its maximum value for triaxial compression and its minimum value for triaxial extension. Temperature and suction changes and a stress path direction different than triaxial compression are usually found in most geo-energy and geo-engineering applications. All these effects affect the strength of geomaterials. We have shown through examples that can be related to geologic carbon storage and nuclear waste disposal that not considering the combined effect of temperature, suction and stress path direction may originate misleading results that are far from what will actually happen. We conclude that constitutive models for geomaterials that include the combined effect of temperature, suction and stress path direction on the yield

surface evolution should be used to obtain realistic results and accurately describe coupled thermo-hydro-mechanical processes.

2.5. Acknowledgments

V.V. acknowledges support from the 'EPFL Fellows' fellowship programme co-funded by Marie Curie, FP7 Grant agreement no. 291771. We would also like to acknowledge financial support from NAGRA (Swiss National Cooperative for the Disposal of Radioactive Waste).

2.6. References

- Alshibli, K.A., Batiste, S.N., Sture, S., 2003. Strain localization in sand: plane strain versus triaxial compression. *J Geotech Geoenviron Eng*, 129(6), 483-494.
- Barnichon, J.D., 1998. Finite element modeling in structural and petroleum geology. PhD thesis, University of Liege, Faculte des Sciences Appliquees.
- Chen, L., Shao, J.F., Huang, H.W., 2010. Coupled elastoplastic damage modeling of anisotropic rocks. *Comp Geotech*, 37(1), 187-194.
- Colmenares, L.B., Zoback, M.D., 2002. A statistical evaluation of intact rock failure criteria constrained by polyaxial test data for five different rocks. *Int. J of Rock Mec Min Sci*, 39(6), 695-729.
- Di Donna, A., 2014. Thermo-mechanical aspects of energy piles. PhD Thesis, École Polytechnique Fédérale de Lausanne.
- Di Donna A., Laloui, L., 2015. Numerical analysis of the geotechnical behaviour of energy piles. *Int J Num Analyt Meth Geomech*, 39(8), 861-888.
- François, B., Laloui, L., 2008. ACMEG-TS: A constitutive model for unsaturated soils under non-isothermal conditions. *Int J Num Analyt Meth Geomech*, 32(16), 1955-1988.
- Gens, A., Sánchez, M., Sheng, D., 2006. On constitutive modelling of unsaturated soils. *Acta Geotech*, 1, 137-147.
- Hueckel, T., Baldi, G., 1990. Thermoplasticity of saturated clays: experimental constitutive study. *J Geotech Eng*, 116(12), 1778-1796.
- Hueckel, T., Borsetto, M., 1990. Thermoplasticity of saturated soils and shales: constitutive equations. *J Geotech Eng*, 116(12), 1765-1777.
- Hujeux, J.C., 1979. Calcul numérique de problèmes de consolidation elastoplastique. Ecole Centrale, Paris.
- Kim, J., Tchalepi, H.A., Juanes, R., 2013. Rigorous coupling of geomechanics and multiphase flow with strong capillarity. *SPE Journal*, 18(06), 1123-1139.
- Lade, P.V., Duncan, J.M., 1973. Cubical triaxial tests on cohesionless soil. *J Soil Mech Found Div*, 99(SM10), 793-812.

- Lade, P.V., Musante, H.M., 1978. Three-dimensional behavior of remolded clay. *J Geotech Eng Div*, 104(2), 193-209.
- Laloui L., Cekerevac. C., 2003. Thermo-plasticity of clays: an isotropic yield mechanism. *Comp Geotech*, 30(8), 649-660.
- Laloui, L., François, B., 2009. ACMEG-T: A Soil Thermo-Plasticity Model. *J Eng Mech*, 135(9), 932-944.
- Laloui, L., Nuth, M., 2009. On the use of the generalised effective stress in the constitutive modelling of unsaturated soils. *Comp Geotech*, 36(1), 20-23.
- Lee, K.L., 1970. Comparison of plane strain and triaxial tests on sand. *J Soil Mech Found Div*, 96(3), 901-923.
- Makhnenko, R.Y., Labuz, J., 2014. Plane strain testing with passive restraint. *Rock Mech Rock Eng*, 47(6), 2021-2029.
- Makhnenko, R.Y., Labuz, J., 2015. Dilatant hardening of fluid-saturated sandstone. *J Geophys Res: Solid Earth*, 120.
- Makhnenko, R.Y., Harvieux, J., Labuz, J., 2015. Paul-Mohr-Coulomb Failure Surface of Rock in the Brittle Regime. *Geophys Res Lett*.
- Morris, J.P., Hao, Y., Foxall, W., McNab, W., 2011. A study of injection-induced mechanical deformation at the In Salah CO₂ storage project. *Int J Greenhouse Gas Cont* 5(2), 270-280.
- Nanda, S., Patra, N.R., 2015. Determination of soil properties for plane strain condition from the triaxial tests results. *Int J Num Analyt Meth Geomech*.
- Nuth M., Laloui L., 2008. Effective Stress Concept in Unsaturated Soils: Clarification and Validation of a Unified Framework. *Int J Num Analyt Meth Geomech*, 32(7), 771-801.
- Nuth, M., Laloui, L., 2008. Advances in modelling hysteretic water retention curve in deformable soils. *Comp Geotech*, 35(6), 835-844.
- Paterson, L., Lu, M., Connell, L., Ennis-King, J.P., 2008. Numerical modeling of pressure and temperature profiles including phase transitions in carbon dioxide wells. In *SPE Annual Technical Conference and Exhibition*, Denver, 21-24 September 2008.
- Parisio, F., Samat, S., Laloui, L., 2015. Constitutive analysis of shale: a coupled damage plasticity approach. *Int J Solids Struct*.
- Peric, D., Runesson, K., Sture, S., 1992. Evaluation of plastic bifurcation for plane strain versus axisymmetry. *J Eng Mech*, 118(3), 512-524.
- Potts, D.M., Gens, A., 1984. The effect of the plastic potential in boundary value problems involving plane strain deformation. *Int J Num Analyt Meth Geomech*, 8(3), 259-286.

- Rutqvist, J., Vasco, D.W., Myer, L., 2010. Coupled reservoir-geomechanical analysis of CO₂ injection and ground deformations at In Salah, Algeria. *Int J Greenhouse Gas Cont*, 4(2), 225-230.
- Salager, S., François, B., Nuth, M., Laloui L., 2013. Constitutive analysis of the mechanical anisotropy of Opalinus Clay. *Acta Geotech*. 8(2), 137-154.
- Sánchez, M., Gens, A., Olivella, S., 2012. THM analysis of a large-scale heating test incorporating material fabric changes. *Int J Num Analyt Meth Geomech*, 36, 391–421.
- Sheng, D., 2011. Review of fundamental principles in modelling unsaturated soil behaviour. *Comp Geotech*, 38(6), 757-776.
- Shojaei, A., Taleghani, A.D., Li, G., 2014. A continuum damage failure model for hydraulic fracturing of porous rocks. *Int J Plast*, 59, 199-212.
- Van Eekelen, H.A.M., 1980. Isotropic yield surfaces in three dimensions for use in soil mechanics. *Int J Num Analyt Meth Geomech*, 4(1), 89-101.
- Vilarrasa, V., Carrera, J., 2015. Geologic carbon storage is unlikely to trigger large earthquakes and reactivate faults through which CO₂ could leak. *Proceedings of the National Academy of Sciences*, 112(19), 5938-5943.
- Vilarrasa, V., Rutqvist, J., Rinaldi, A.P., 2015a. Thermal and capillary effects on the caprock mechanical stability at In Salah, Algeria. *Greenhouse Gases: Sci Tech*, 5: 449-461.
- Vilarrasa, V., Rutqvist, J., Blanco Martin, L., Birkholzer, J., 2015b. Use of a dual structure constitutive model for predicting the long-term behavior of an expansive clay buffer in a nuclear waste repository. *ASCE Int J Geomech*.
- Wanatowski, D., Chu, J., 2007. Drained behaviour of Changi sand in triaxial and plane-strain compression. *Geomech Geoeng*, 2(1), 29-39.
- Xie, S.Y., Shao, J.F., 2012. Experimental investigation and poroplastic modelling of saturated porous geomaterials. *Int J Plast*, 39, 27-45.
- Zhang, S., Leng, W., Zhang, F., Xiong, Y., 2012. A simple thermo-elastoplastic model for geomaterials. *Int J Plast*, 34, 93-113.

3. Constitutive analysis of shale: a coupled damage plasticity approach

Authors: F. Parisio, S. Samat and L. Laloui.

Status: published in International Journal of Solids and Structures.

Reference: Parisio, F., Samat, S., Laloui, L., 2015. Constitutive analysis of shale: a coupled damage plasticity approach. Int J Solids Struct 75-76, 88-98.

Contributions: The manuscript was written by F. Parisio, who developed the constitutive model, performed the numerical implementation and performed the analysis. S. Samat overviewed the thermodynamic consistency and furnished the general FORTRAN 77 routine for the numerical analyses. L. Laloui overviewed the work, edited the manuscript and is the senior responsible author (SRA) of the publication.

Abstract

Shales have become increasingly important because they play key roles in modern energy and environmental geomechanics applications, such as nuclear waste storage, non-conventional oil and gas operations and CO₂ geological storage. Shale behaves in a quasi-brittle manner, often exhibiting linear elasticity before reaching its peak stress. Furthermore, softening of the material leads to a residual state in which pure plastic flow is observed under constant values of deviatoric stress. Degradation of the elastic moduli and the accumulation of irreversible strains are believed to be primarily caused by the debonding and decohesion mechanisms in the structure, as well as the growth of microcracks. To capture these features, a constitutive model that couples elastic, plastic and damage theories is developed. The isotropic damage model is based on the Weibull probabilistic theory and describes the failure of brittle materials. This model is coupled with a modified version of the Lade-Duncan criterion to account for non-linear dependency of shear resistance with a mean stress typical of geomaterials. The two surfaces of damage and plasticity and the rate equations for the internal variables are postulated and thermodynamic consistency is subsequently investigated. The coupled plastic-damage constitutive model is integrated with an implicit stress return algorithm for the plastic part, while the damage part can be integrated implicitly. Numerical back-calculations of experimental results from two quasi-brittle shales demonstrate the ability of the model to reproduce the primary features of their mechanical behavior.

Keywords: plastic-damage couplings, shale mechanics, Weibull damage model, Lade-Duncan plasticity, energy and environmental geomechanics.

3.1. Introduction

Attaining a deeper understanding of the mechanical behavior of shale has become one of the predominant challenges in energy and environmental geomechanics. These materials have a prominent place in present-day research because they are often part of strategic applications, such as deep geological nuclear waste storage, un-conventional hydrocarbon exploitation in the form of shale gas and CO₂ sequestration in deep aquifers (Ferrari and Laloui, 2013). For deep geological nuclear waste repositories, shales are often selected as a host formation due to their low hydraulic permeability that guarantees proper isolation of harmful substances

from their surroundings. Geomechanical predictions are of crucial importance because major modifications that take place during the construction of the repository site are expected to substantially alter the hydro-mechanical properties of the host rock (Bossart et al., 2002). The increasing interest in shale gas reservoirs has focused much attention on understanding the mechanical behavior of shale. In such applications, the study of strength and stiffness of the material allows for predictions of its brittleness, which defines its behavior with respect to hydraulic fracture propagation (Josh et al., 2012). Recent research efforts that examined the characterization of shale were carried out to find suitable solutions to the problem of subsurface CO₂ storage in geological formations. Shales are considered to be good candidates as efficient cap formations above potential CO₂ storage reservoirs (Busch et al., 2008).

Concerning the constitutive modeling of shale, geomaterials have been often approached with purely plastic behavior with eventually softening laws to account for the brittle or quasi-brittle modes of failure. Shale usually behaves as a brittle or quasi-brittle material (i.e., when “dissipation prior to cracking exists with no or negligible permanent strains” (Lemaître and Desmorat, 2005)), in which the decohesion mechanisms and growth of microcracks are primarily responsible for the accumulation of inelastic strains. Therefore, suitable models are usually formulated following the framework of Continuum Damage Mechanics (CDM), which can effectively represent microcrack and microvoid formation and growth. Although CDM theories can predict elastic degradation of materials and softening behavior, they cannot account for the accumulation of irreversible plastic strains. Therefore, the most suitable models to study the constitutive behavior of shale are coupled plastic-damage models. In these models, the plastic dissipation mechanism controls the accumulation of irreversible strains and the damage dissipation mechanism is responsible for the degradation of elastic parameters and the softening of the material. A number of models coupling plasticity and damage theories that were applied to stiff geomaterials in general and to shales in particular have been presented in the literature (Chazallon and Hicher, 1998; Chen et al., 2010; Chen et al., 2012; Chiarelli et al., 2003; Einav et al., 2007; Hu et al., 2013; Jia et al., 2007; Salari et al., 2004; Shao et al., 2006). The complexity of the mechanical behavior of quasi-brittle geomaterials necessitates the inclusion of features such as elastic degradation, softening, irreversible strains, anisotropy in strength and deformability into the formulation of the constitutive model. This often results in constitutive models that have a large number of parameters and are sometimes difficult to calibrate.

Typically, plastic-damage models are developed following a full thermodynamic approach (Einav et al., 2007), in which the whole mechanical behavior is derived from thermodynamic potentials. One of the main difficulties for such approaches lays in finding proper expressions for the thermodynamic potentials that are adequate to the material behavior. Despite the importance of thermodynamics in the formulation of constitutive models, alternative

approaches propose the postulation of yield surfaces and rate equations (Grassl and Jirásek, 2006). In this type of approach, thermodynamic consistency is investigated afterwards.

Another critical component of the formulation of coupled plastic-damage theories is the uniqueness of the solution to the coupled problem, which can be interpreted as a Linear Complementary Problem (LCP) and poses further restrictions to the parameters of the model. When two yield surfaces are employed to describe the behavior of the material (one for damage and one for plasticity), it is important to define the space in which they are formulated. Different choices will lead to different restrictions on the model parameters. From a numerical perspective, the advantage of implementing implicit schemes for the integration of non-linear constitutive models is clear (Simo and Hughes, 1998) and contributes to the robustness of the numerical solution.

The original contribution of this work relies in the choice of modeling shale behavior with a combination of proper damage and plasticity theories instead of purely plastic theories that account for softening. It is shown how it is possible to combine existing theories of plasticity and damage, usually developed for quasi-brittle materials like concrete, to account for the principal features of the complex non-linear mechanical behavior of shale such as pre-peak hardening, quasi-brittle softening, accumulation of irreversible strains and damage and constant shear stress in the post-peak phase.

The goal of this work is to develop a plastic-damage model that is able to capture the constitutive behavior of quasi-brittle shale while also aiming for simplicity in formulation. To meet such a challenge, it is necessary to formulate the model making assumptions about the yield surfaces. A thermodynamic check is later carried out to verify the consistency of the model. The challenge becomes more difficult when considering that the goal of simplicity should not disregard the fidelity of the model in capturing the physics that control the behavior of the material. Therefore, the importance of selecting proper expressions for plastic and damage formulations that rely on a sound physical basis is clear. The proposed plastic formulation is implemented in the damage effective stress space. The damage model is specific to quasi-brittle materials, such as shale, and is derived from a probabilistic approach to the failure of materials (as reported in Lemaître and Desmorat (2005)). The constitutive equations are developed and a proper thermodynamic framework for non-linear materials, e.g., the work of Lubliner (1972) is employed to investigate the consistency of the formulation and to check the validity of the assumptions. The proposed model is integrated numerically with an implicit scheme in coupled plastic-damage conditions.

3.2. Rheological evidence concerning shale

Shale is defined in different ways in the literature and its definition ultimately depends on which properties are to be emphasized. In a general way, shale can be defined as

“sedimentary rock... characterized by fine grains and lamination. [...] Carbonates and evaporates may be present as cement and inter beds. [...] any rock type containing at least 30% clay minerals is known as an engineering shale” (Farrokhrouz and Asef, 2014). From a geomechanical point of view it is very difficult to give a unique and satisfactory definition of shale because its properties are highly dependent on many factors. Microstructural features, inter and intra-granular porosity, static deformability and failure properties, anisotropy degree, petrophysical characteristics, mineralogy (clay content and mineral type), thermal history and organic matter content are just some of the most important properties that influence the mechanical behavior of shale. To validate the constitutive model that is proposed in the following sections, the focus of this paper is directed toward the mechanical behavior of two different shales. Both shales exhibit similar features that are typical of quasi-brittle geomaterials: Opalinus Clay from the Mont Terri underground rock laboratory in northern Switzerland and La Biche shale from Alberta, Canada.

According to Bossart et al. (2002) Opalinus Clay (OPA) can be viewed as a “stiff, over-consolidated clay with a hydraulic conductivity less than 10^{-12} m/s, a Young’s modulus varying between 4000 and 10,000 MPa (large range due to bedding anisotropy) and a cohesion greater than 2 MPa”. Some typical features can be clearly distinguished such as intrinsic structural anisotropy, quasi-brittle behavior, strength dependency on mean pressure and degradation of stiffness. The formation and growth of microcracks can be considered to be responsible for both the softening behavior observed in the post-peak stress-strain curve and the development of irreversible plastic strains. Different conventional triaxial compression tests to explore the mechanical behavior of OPA are reported in the literature e.g., Gräsle and Plischke (2011) and Salager et al. (2013b)^b. According to the bedding plane orientation with respect the vertical stress direction in a triaxial configuration, Opalinus Clay samples can be divided into P-Samples, S-Samples and Z-Samples, as shown in Figure 3-1.

The rheology of Opalinus Clay can be observed as representative of the behavior of quasi-brittle shale (test reported from Gräsle and Plischke (2011)). The stress-strain response of a triaxial compression test performed at a confinement of 3 MPa for P-Samples is illustrated in Figure 3-2 and can be characterized by three phases: during phase I the material behaves almost linear-elastically and irreversible strains are small but comparable to the elastic ones; in phase II microcracks start to grow rapidly and carbonate bonds are broken, damage accumulates and after the peak is reached the materials shows a softening response; in phase

^b In the present work we refer to conventional triaxial compression test as a test in which a cylindrical sample is isotropically compressed to the desired confinement pressure and then sheared by applying a vertical load (by displacement control) while keeping the lateral pressure constant (applied by the confining fluid).

III microcracks are believed to be stable and the material plastically flows, exhibiting the accumulation of permanent strains at constant values of deviatoric stress.

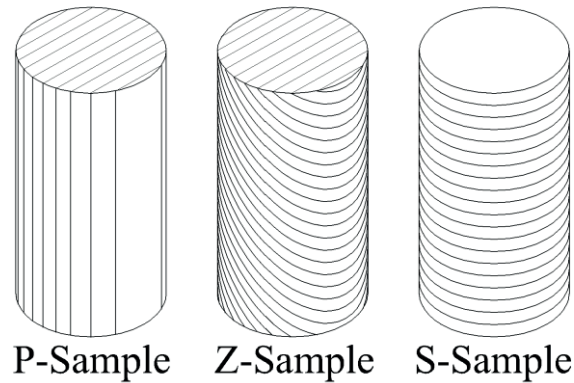


Figure 3-1: Bedding orientation in samples of Opalinus Clay subjected to triaxial compression tests.

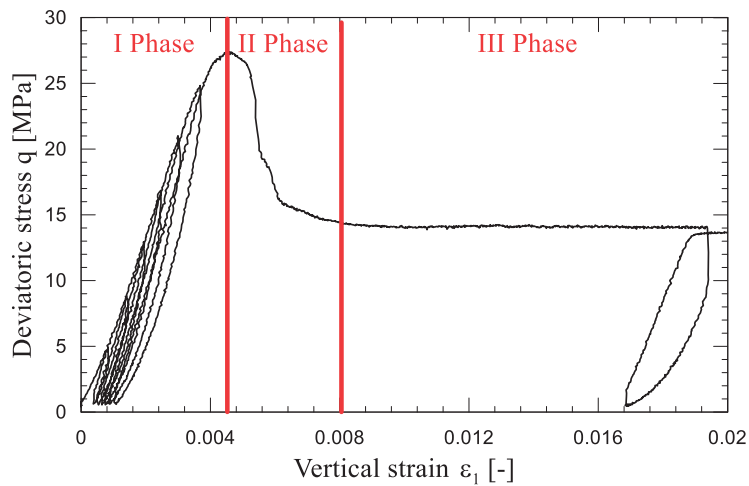


Figure 3-2: Typical rheology of P-Sample of Opalinus Clay in triaxial compression conditions at a confinement pressure of 3 MPa (Gräsle and Plischke, 2011).

The tests performed on La Biche shale considered in this paper are reported in a study by Wong (1998), in which the material was described as consisting of “...thinly bedded, dark grey to black bentonitic and concretionary shale, together with thin beds of medium to light grey siltstone, argillaceous sandstone, laminae of bentonite, and coal.” From a mechanical point of view it can be observed as a quasi-brittle material because it exhibits a linear elastic behavior until reaching its peak stress (in this phase the irreversible deformations are

expected to be negligible, although this is not confirmed by unloading cycles) and follows a softening phase that eventually leads to constant values of deviatoric stress in residual conditions.

The main features observed from these tests results are the brittleness of shale, in terms of its post peak softening response, and the residual conditions of constant deviatoric stress, in which the material is plastically flowing and exhibits a plateau. The loading-unloading tests performed on Opalinus Clay showed an interesting feature. Before the peak of stress is reached, permanent strains are comparable to the elastic ones. After the softening phase, the degradation of the elastic moduli manifests itself and an increase in the values of permanent strains is observed. This can be attributed to the quasi-brittle nature of the material and be explained by the progressive breakage of the bonds in the first phase prior to the peak of stress (accumulation of plastic strain is mainly due to decohesion of the carbonate bonds and the growth and coalescence of microcracks). In the second phase, the behavior of the material seems to be dominated by the clayey components and results in plastic flow at constant deviatoric stress conditions and an accumulation of permanent inelastic strains. Elastic moduli degradation is a result of the damage process. Therefore, it is possible to assert that in the first phase the material is behaving elastically brittle with negligible accumulated plastic strains. Then, the accumulation of microcracks is responsible for irreversible strains, the peak of stress is reached and the accumulation of damage drives the stress response toward a brittle softening phase. In the last phase, the material does not develop any more damage and instead exhibits plastic flow at constant stress.

3.3. Constitutive framework of the model

The coupling between the theories of Continuum Damage Mechanics and the theory of plasticity is particularly useful for the representation of the mechanical behavior of quasi-brittle materials that exhibit both decohesion, microcrack formation, inelastic strains and post peak softening. A vast number of damage models have been proposed in the literature. The basis of damage mechanics was developed in the early 1970s. Rigorous developments to this literature based on the framework of non-equilibrium and irreversible thermodynamics for different classes of materials started in the 1980s but applied to the constitutive modeling of concrete (Nguyen, 2005). Damage models for brittle and ductile materials have been presented in many works (Kattan and Voyiadjis, 1990; Krajcinovic, 1983; Marigo, 1981; Maugin, 1992; Ortiz, 1985). As mentioned above, damage alone is not suitable for predicting inelastic permanent strains. To overcome this issue, it can be coupled with plasticity. A series of constitutive models that couple plasticity and isotropic damage for concrete, and in general geomaterials, were proposed in the literature (Bourgeois et al., 2003; Gatuingt and Pijaudier-Cabot, 2002; Jason et al., 2006; Kratzig and Polling, 2004; Salari et al., 2004). Couplings

between plasticity and damage can be defined by accounting for one or more dissipation mechanism (e.g., damage + plasticity), or by defining one unique dissipative mechanism and deriving the rate evolution equations for the thermodynamic internal variables of the model (Einav et al., 2007). For example, models can be built by only specifying a damage criterion as in Faria et al. (1998) and Voyiadjis and Kattan (1992), or a plastic criterion as in Lee and Fenves (1998) and Lemaitre (1985).

When specifying two or more yield functions, as is the case for multi-dissipative materials, the couplings are implicitly embedded in the formulations of the plastic yield function and damage criteria. Two possible choices arise, and the stress based plastic yield function can either be formulated in terms of effective stress (Jason et al., 2006; Ju, 1989; Lee and Fenves, 1998) or in terms of nominal stress (Ananiev and Ožbolt, 2004; Imran and Pantazopoulou, 2001; Lubliner et al., 1989). In the work of Grassl and Jirásek (2006), both approaches are developed and compared for the formulation of an isotropic damage-plasticity model for concrete. In the case of nominal stress space based plasticity, the results show that the plastic part should exhibit a strong hardening to fulfill local uniqueness conditions (Grassl and Jirásek, 2006). Therefore, for brittle materials that behave in a softening manner, effective stress based plasticity should be considered as more appropriate.

Another approach for coupling plasticity and damage was proposed in the work of Einav et al. (2007) based on a hyperplastic theory. Geomaterials are often considered to not belong to this class of generalized standard materials because the prediction of realistic values of dilatancy often requires the non-associated flow rule. For this class of materials, some authors have proposed a different approach to thermodynamic consistency in which both yield surfaces and rate equations of internal variables are simply postulated and subsequently checked for thermodynamic compatibility (Grassl and Jirásek, 2006). In the present work, we follow the latter approach because it generates models that can be readily extended to non-associated frameworks. The stress and strain sign conventions applied are the ones commonly used in geomechanics literature, i.e., compressions are considered positive and tensions negative. Shear components are oriented such that on positive faces, positive components are directed in the negative frame axes direction. The constitutive equation that relates stresses σ_{ij} to strains ε_{ij}^e can be written as

$$\sigma_{ij} = (1 - d) D_{ijkl}^e \varepsilon_{kl}^e, \quad (3.1)$$

where D_{ijkl}^e is the rate independent elastic stiffness tensor and d is the damage internal variable. The strain decomposition between plastic ε_{ij}^p and elastic ε_{ij}^e is

$$\varepsilon_{ij} = \varepsilon_{ij}^e + \varepsilon_{ij}^p, \quad (3.2)$$

and the concept of effective stress $\tilde{\sigma}_{ij}$ is described by

$$\sigma_{ij} = (1-d) \tilde{\sigma}_{ij}. \quad (3.3)$$

The stress strain equation can be rewritten as

$$\sigma_{ij} = (1-d) \tilde{\sigma}_{ij} = (1-d) D_{ijkl}^e (\varepsilon_{kl} - \varepsilon_{kl}^p), \quad (3.4)$$

which in its rate form becomes

$$\dot{\sigma}_{ij} = (1-d) D_{ijkl}^e (\dot{\varepsilon}_{kl} - \dot{\varepsilon}_{kl}^p) - \dot{d} D_{ijkl}^e (\varepsilon_{kl} - \varepsilon_{kl}^p). \quad (3.5)$$

In this work, references to “effective stress” are equivalent to the concept of “damage effective stress”. Damage effective stress is the stress that acts on the intact (undamaged) part of the material (if damage is observed as the reduction of the area A_s on which stresses act, then by external equilibrium consideration the effective stress $\tilde{\sigma}_{ij}$ acting on the reduced area \tilde{A}_s is equal to nominal stress acting on the area according to $\tilde{\sigma}_{ij} \tilde{A}_s = \sigma_{ij} A_s$). For a complete derivation of the concept of effective stress, the reader can refer to Lemaître and Desmorat (2005).

3.3.1. Plasticity

The plastic response of the model is formulated in the effective stress space and includes the definition of the yield surface, the flow rule and the rate equation of the internal variable that governs the hardening. The plastic yield function f^p is expressed as

$$f^p(\tilde{\sigma}_{ij}, h_r) = 0, \quad (3.6)$$

where f^p is formulated in the damage effective stress space and h_r is the variable that controls the hardening of the plastic yield surface. The authors of Grassl and Jirásek (2006) have demonstrated the advantage of formulating plasticity in the damage effective stress space: by investigating the uniqueness of the solution in such coupled approach they concluded that this type of combination does not introduce any further restriction than the ones already valid for uncoupled plasticity and damage. The evolution of the hardening variable is a function of the rate of plastic strain and is determined by

$$h_r = g(k_p), \quad (3.7)$$

where k_p is a plastic hardening internal variable that depends on plastic strain. The plastic strain rate, whose magnitude is controlled by the plastic multiplier $\dot{\lambda}^p$, is given by the plastic flow rule

$$\dot{\varepsilon}_{ij}^p = \dot{\lambda}^p \partial_{\tilde{\sigma}_{ij}} f^p. \quad (3.8)$$

The loading-unloading problem is represented by the Karush-Kuhn-Tucker complementarity conditions (Simo and Hughes, 1998)

$$\dot{\lambda}^p \geq 0 \quad f^p \leq 0 \quad \dot{\lambda}^p f^p = 0. \quad (3.9)$$

3.3.2. Damage

The damage response is formulated in the elastic strain space so that the yield surface, analogous to plasticity, can be expressed in the following way

$$f^d(Y, d) = 0, \quad (3.10)$$

where f^d is the damage criterion formulated in terms of the elastic energy density Y and an internal damage variable d . The rate of damage of the internal variable d is normal to the damage criterion through the damage associated variable Y (often called damage thermodynamic force), therefore

$$\dot{d} = \dot{\lambda}^d \partial_Y f^d, \quad (3.11)$$

where $\dot{\lambda}^d$ is the damage multiplier that controls the magnitude of the damage rate. Similarly to plasticity, the loading unloading problem is once again represented by the Karush-Kuhn-Tucker conditions applied to the damage formulation

$$\dot{\lambda}^d \geq 0 \quad f^d \leq 0 \quad \dot{\lambda}^d f^d = 0. \quad (3.12)$$

3.4. Coupled plastic-damage model

The formulation of the complete elasto-plastic-damage model requires appropriate plastic and damage criteria as well as rate equations for the respective internal variables. The implemented plastic yield surface is a non-linear extension of the Lade-Duncan model as proposed by Lai et al. (2010). The advantage of such a choice is that Opalinus Clay has demonstrated a strong non-linear dependence of the yield locus to the mean stress and has often been interpreted with bi-linear Mohr-Coulomb type models (e.g., Bock (2009)). The following formulation of the three-dimensional effective stress space is implemented

$$f^p = \tilde{q} - f_{q-p}^p(\tilde{p}, h_r) f_{\pi}^p(\tilde{g}), \quad (3.13)$$

where \tilde{q} is the deviatoric stress, \tilde{p} the mean stress. The yield surface is a combination of functions in the $\tilde{q} - \tilde{p}$ plane and in the octahedral plane $\tilde{\pi}$ that accounts for a complete three-dimensional formulation of class C^1 in the stress space. This formulation depends on three invariants of the stress tensor defined as

$$\tilde{p} = \frac{\tilde{I}_1}{3}, \quad (3.14)$$

$$\tilde{q} = \sqrt{3\tilde{J}_2}, \quad (3.15)$$

$$\tilde{g} = \frac{1}{3} \arcsin \left(\frac{3\sqrt{3}}{2} \frac{\tilde{J}_3}{(\tilde{J}_2)^{3/2}} \right), \quad (3.16)$$

where $\tilde{I}_1 = \tilde{\sigma}_{ii}$ is the first invariant of the stress tensor, $\tilde{J}_2 = 1/2 \tilde{s}_{ij} \tilde{s}_{ij}$ is the second invariant of the deviatoric stress tensor, $\tilde{J}_3 = \det \tilde{s}_{ij}$ is the third invariant of the deviatoric stress tensor, \tilde{g} is the Lode's angle, $\tilde{s}_{ij} = \tilde{\sigma}_{ij} - \tilde{p} \delta_{kk}$ is the deviatoric stress tensor and δ_{ij} is the Kronecker's delta. The value of the function in the octahedral plane can be taken from the literature (Van Eekelen, 1980), and the complete formulation can be written as

$$f^p = \tilde{q} - \left(\alpha \frac{\tilde{p}^2}{c} + \beta \tilde{p} + h_r c \right) a_{\tilde{g}} \left(1 - b_{\tilde{g}} \sin 3\tilde{g} \right)^{-0.229}, \quad (3.17)$$

where $\alpha, \beta, c, a_{\tilde{g}}$ and $b_{\tilde{g}}$ are material parameters. This formulation ensures regularity and convexity of the yield surface and can account for the strength dependency on Lode's angle, which is a typical feature of geomaterials (the strength in the triaxial extension is lower than the strength available in triaxial compression conditions). In this paper, only simulations in triaxial compression conditions are considered. Therefore, only the function in the $\tilde{q} - \tilde{p}$ plane $f^p = \tilde{q} - f_{q-p}^p(\tilde{p})$ is retained because in such conditions $\tilde{g} = 30^\circ$ and $f_{\pi}^p(\tilde{g}) = 1$. In the proposed model, the parameter c represents the cohesive component of the material in the effective stress space. Figure 3-3a illustrates the plastic yield surface for different values of the hardening variable h_r ($0 < h_r \leq 1$). Negative values of \tilde{p} correspond to tensile components.

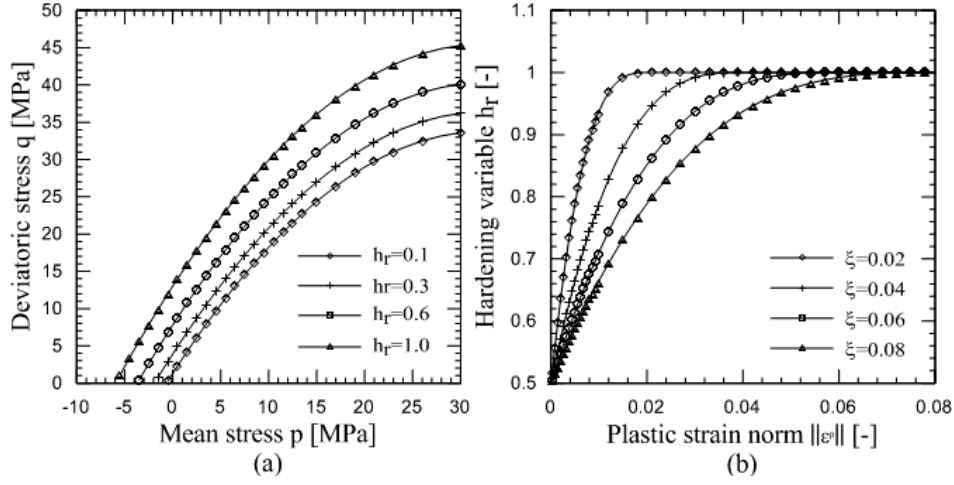


Figure 3-3: Plastic yield function in the plane $\tilde{q} - \tilde{p}$ for different values of the hardening parameter h_r . (a). Evolution of the hardening variable with the plastic strain norm for different values of the parameter ξ (b).

The hardening of the yield function is governed by the parameter h_r , which depends on the internal variable k_p defined in rate form as $\dot{k}_p = \sqrt{\dot{\varepsilon}_{ij}^p \dot{\varepsilon}_{ij}^p}$. The expression of h_r is taken from Grassl and Jirásek (2006)

$$h_r = \begin{cases} h_{r0} + (1 - h_{r0}) \frac{k_p}{\xi} \left[\left(\frac{k_p}{\xi} \right)^2 - 3 \frac{k_p}{\xi} + 3 \right] & \text{if } k_p \leq \xi \\ 1 & \text{if } k_p > \xi \end{cases}, \quad (3.18)$$

where ξ is the value of the plastic strain norm at which the hardening variable becomes equal to one and plastic saturation occurs. The dependence of the hardening function on the plastic strain norm is shown in Figure 3-3b. The material parameters to be determined are α , β , c , h_{r0} and ξ . To represent the damage response, the model proposed by Marigo (1981) has been followed. This model is particularly suitable for brittle materials. The yield surface for damage can therefore be represented in the elastic strain space as

$$f^d(\varepsilon_{ij}, \varepsilon_{ij}^p, d) = Y_- - k(d), \quad (3.19)$$

where

$$Y_- = \frac{1}{2} D_{ijkl}^e \bar{\varepsilon}_{ij}^e \bar{\varepsilon}_{kl}^e, \quad (3.20)$$

is the elastic energy density associated with principal negative (tensile) elastic strains. The definition of the tensor of tensile strains is based on a spectral decomposition proposed by Ortiz (1985) as

$$\bar{\varepsilon}_{ij}^e = \sum_{\alpha=1}^3 \langle \lambda_{\alpha} \rangle_- V_i^{\alpha} V_j^{\alpha}, \quad (3.21)$$

where λ_{α} and V_i^{α} are respectively the eigenvalues and eigenvectors of the elastic strain tensor ε_{ij}^e , while the negative Macaulay brackets has the following meaning

$$\langle \lambda_{\alpha} \rangle_- = \frac{\lambda_{\alpha} - |\lambda_{\alpha}|}{2}. \quad (3.22)$$

Damage eventually results from the accumulation of principal tensile strains. Another advantage of such a choice is the implicit accounting of confining stress dependency.

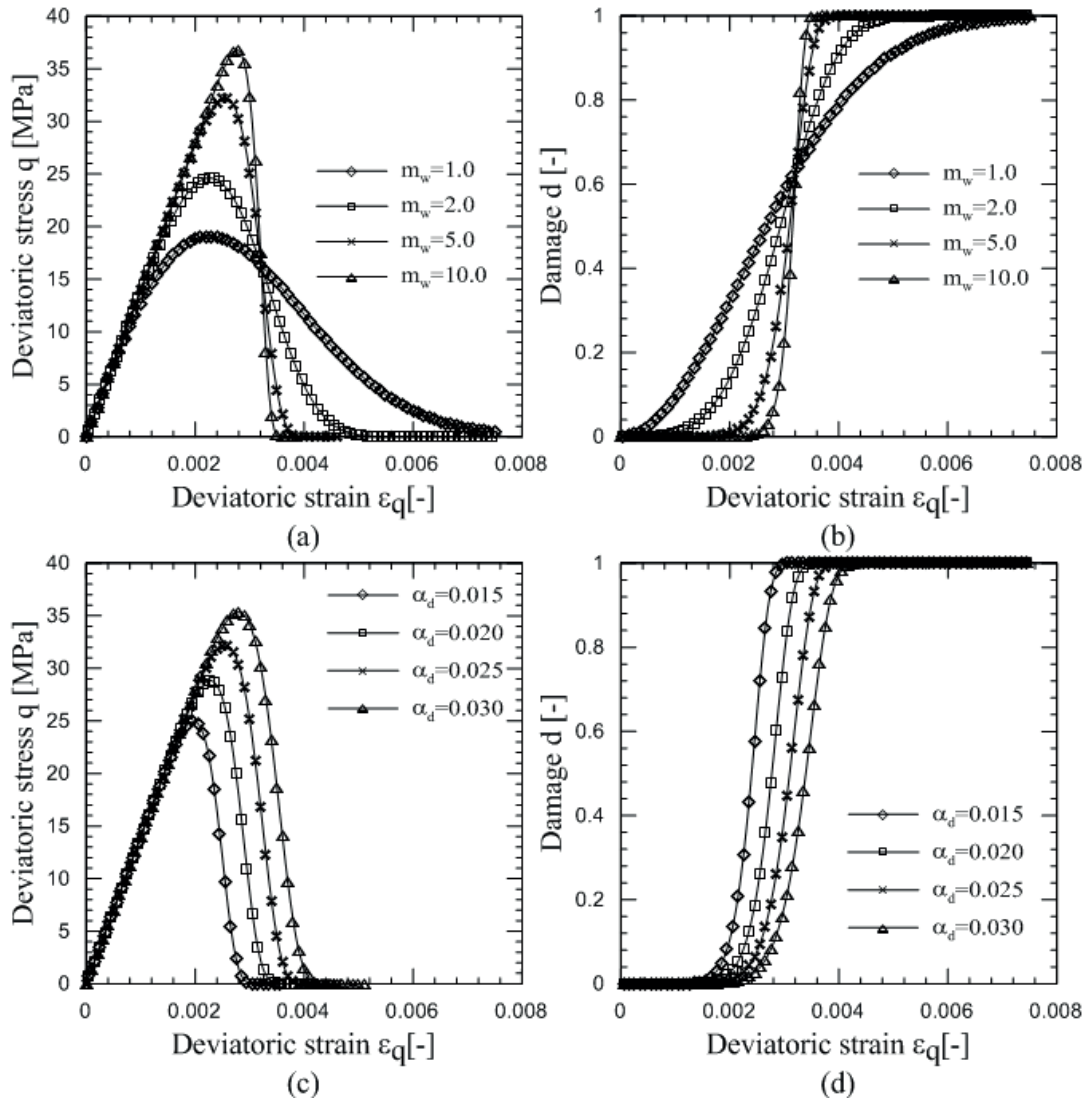


Figure 3-4: Dependence on the response of the pure damage model in terms of the material parameters: shape parameter for (a) stress-strain response and (b) damage evolution ($\alpha_d=0.025$); Weibull modulus for (c) stress-strain response and (d) damage evolution ($m_w=5$).

The expression of $k(d)$ follows from the work of Weibull as reported in Lemaître and Desmorat (2005). This model originates from a probabilistic approach to the fracture of brittle materials and results in the following expression for $k(d)$

$$k(d) = \alpha_d \left[\log \left(\frac{1}{1-d} \right) \right]^{1/m_w}, \quad (3.23)$$

where α_d and m_w are material parameters. m_w is the shape parameter and controls the brittleness of the material and α_d is the scale parameter (Weibull modulus). The Weibull damage model has been applied to model debonding effects in fiber reinforced composites (Kabir et al., 2006; Kim and Lee, 2011; Lee, 2001). Despite the fact that shale can be viewed as a geomaterial with a clay rich matrix and brittle bonds inclusion as a result of diagenetic processes, in the present work the damage model is introduced as purely phenomenological and no connection between micro-structure and the damage evolution function is asserted. Figure 3-4 shows plots of the stress-strain behavior along with the evolution of the damage variable with different values of the material parameters.

The relationship between the damage parameters and the uniaxial compressive strength (UCS) can be found by considering the nominal stress rate equation

$$\dot{\sigma}_{ij} = (1-d) D_{ijkl}^e \dot{\epsilon}_{kl}^e - \dot{d} D_{ijkl}^e \epsilon_{kl}^e. \quad (3.24)$$

The right hand side of (3.24) is positive during hardening and becomes negative during softening. From this consideration, the peak of stress is the condition in which (3.24) changes its sign. Therefore, the condition $\dot{\sigma}_{ij} = 0$ can be used to find the values of the damage parameters at peak stress. This condition can be written as

$$(1-d) D_{ijkl}^e \dot{\epsilon}_{kl}^e - \dot{d} D_{ijkl}^e \epsilon_{kl}^e = 0. \quad (3.25)$$

In unconfined compression, after eliminating the elastic matrix on both members of (3.25) and by writing the equation along direction of compression, equation (3.25) can be rewritten as

$$\frac{\dot{\epsilon}_{11}^e}{\epsilon_{11}^e} = \frac{\dot{d}}{(1-d)}. \quad (3.26)$$

From equation (3.23) the postulated damage law can be written as

$$d = 1 - \exp \left\{ - \left[\frac{K (\epsilon_{11}^e)^2}{\alpha_d} \right]^{m_w} \right\}, \quad (3.27)$$

so that the rate evolution of damage reads

$$\dot{d} = \frac{2Km_w \varepsilon_{11}^e \dot{\varepsilon}_{11}^e \exp \left\{ - \left[\frac{K (\varepsilon_{11}^e)^2}{\alpha_d} \right]^{m_w} \right\} \left[\frac{K (\varepsilon_{11}^e)^2}{\alpha_d} \right]^{m_w-1}}{\alpha_d}, \quad (3.28)$$

where

$$K = \nu^2 \left[\frac{E_e (1-\nu)}{(1+\nu)(1-2\nu)} + \frac{E_e \nu}{(1+\nu)(1-2\nu)} \right], \quad (3.29)$$

where E_e is Young's modulus and ν is Poisson's ratio. Equation (3.26) can be rewritten as

$$\frac{\dot{\varepsilon}_{11}^e}{\varepsilon_{11}^e} - \frac{2Km_w \varepsilon_{11}^e \dot{\varepsilon}_{11}^e \left[\frac{K (\varepsilon_{11}^e)^2}{\alpha_d} \right]^{m_w-1}}{\alpha_d} = 0, \quad (3.30)$$

and after simplification as

$$\frac{1 - 2m_w \left[\frac{K (\varepsilon_{11}^e)^2}{\alpha_d} \right]^{m_w}}{\varepsilon_{11}^e} = 0. \quad (3.31)$$

A positive real solution of (3.31) is

$$\varepsilon_{11}^{e,f} = \sqrt{\frac{\alpha_d}{K} \left(\frac{1}{2m_w} \right)^{\frac{1}{2m_w}}}, \quad (3.32)$$

which represents the strain along the direction of compression at maximum stress in function of the two damage parameters. At the peak stress, in a uniaxial compression test, the negative energy writes

$$Y_-^f = (\varepsilon_{11}^{e,f})^2 K = \alpha_d \left(\frac{1}{2m_w} \right)^{\frac{1}{m_w}}, \quad (3.33)$$

while the damage

$$d^f = 1 - \exp \left(- \frac{1}{2m_w} \right), \quad (3.34)$$

and the nominal stress

$$\sigma_{11}^f = \left[\exp\left(-\frac{1}{2m_w}\right) \right] E_e \sqrt{\frac{\alpha_d}{K}} \left(\frac{1}{2m_w}\right)^{\frac{1}{2m_w}}. \quad (3.35)$$

From equation (3.35) it can be asserted that, for a given set of elastic parameters, UCS is a unique function of the damage material parameters α_d and m_w . By choosing an appropriate value of m_w , which controls the softening branch of the curve, the parameter α_d can be determined as a function of the unconfined compressive strength σ_{11}^f as

$$\alpha_d = K \left(\sigma_{11}^f\right)^2 \left\{ \left[\exp\left(-\frac{1}{2m_w}\right) \right] E_e \left(\frac{1}{2m_w}\right)^{\frac{1}{2m_w}} \right\}^{-2}. \quad (3.36)$$

3.5. Thermodynamic consistency

The thermodynamic compatibility of the proposed formulation follows at all times the first and second laws of thermodynamics. As previously mentioned, the model is not derived from a dissipation potential. Therefore, the need to examine its thermodynamic consistency is clear (one of the dangers often encountered is that spurious energy generation might arise during simulations). The framework is based on the work of Lubliner on the thermodynamics of non-linear solids (Lubliner, 1972). In this sense, the local thermodynamic state of a solid body is assumed to be uniquely determined by the strain tensor ε_{ij} , the entropy per unit volume S and a set of the so-called internal variables α_i (in the local state method, the latter represents the history of the material, i.e., it is representative of dissipative phenomena (Lemaitre and Chaboche, 1990)). Therefore, the internal energy of the solid is a function of the variables mentioned above, $E = E(\varepsilon_{ij}, S, \alpha_i)$ and the local equation of energy conservation is expressed as the following

$$\dot{E} = \partial_S E \dot{S} + \partial_{\varepsilon_{ij}} E \dot{\varepsilon}_{ij} + \partial_{\alpha_i} E \dot{\alpha}_i = \sigma_{ij} \dot{\varepsilon}_{ij} - \partial_{x_k} h_k, \quad (3.37)$$

where h_k is the heat flow vector and x_k is the vector of spatial coordinates. The Clausius-Duhem inequality, which is representative of the second law of thermodynamics, can be written as

$$\dot{S} + \partial_{x_k} \left(\frac{h_k}{T} \right) = \dot{S} + \frac{1}{T} \partial_{x_k} h_k - \frac{h_k}{T^2} \partial_{x_k} T \geq 0, \quad (3.38)$$

where T is the temperature. Alternatively

$$T\dot{S} + \partial_{x_k} h_k - \frac{h_k}{T} \partial_{x_k} T = d_m + d_T \geq 0, \quad (3.39)$$

where $d_m = T\dot{S} + \partial_{x_k} h_k$ is the mechanical dissipation and $d_T = -h_k/T \partial_{x_k} T$ is the thermal dissipation. For isothermal processes, in which the temperature is assumed constant ($\dot{T} = 0$) and uniform ($\partial_{x_k} T = 0$), thermal dissipation becomes zero $d_T = -h_k/T \partial_{x_k} T = 0$. The Clausius-Duhem inequality reads therefore

$$T\dot{S} + \partial_{x_k} h_k = d_m \geq 0. \quad (3.40)$$

Equation (3.37) can be rewritten as

$$\partial_{x_k} h_k = \sigma_{ij} \dot{\varepsilon}_{ij} - \partial_S E \dot{S} - \partial_{\varepsilon_{ij}} E \dot{\varepsilon}_{ij} - \partial_{\alpha_i} E \dot{\alpha}_i, \quad (3.41)$$

and substitution of right hand side of (3.41) into (3.40) leads to

$$(T - \partial_S E) \dot{S} + (\sigma_{ij} - \partial_{\varepsilon_{ij}} E) \dot{\varepsilon}_{ij} - \partial_{\alpha_i} E \dot{\alpha}_i \geq 0. \quad (3.42)$$

By definition of the state equations $T = \partial_S E$ and $\sigma_{ij} = \partial_{\varepsilon_{ij}} E$, it results the mechanical dissipation

$$d_m = -\partial_{\alpha_i} E \dot{\alpha}_i \geq 0. \quad (3.43)$$

For coupled plastic-damage models, and based on the assumption of isothermal conditions and uniform temperature, the internal energy can be expressed as a function of the total strain, and the damage d and plastic ε_{ij}^p internal variables as

$$E(\varepsilon_{ij}, \varepsilon_{ij}^p, d) = \frac{1}{2} (1-d) D_{ijkl}^e (\varepsilon_{ij} - \varepsilon_{ij}^p) (\varepsilon_{kl} - \varepsilon_{kl}^p), \quad (3.44)$$

which yields to the constitutive equation

$$\sigma_{ij} = \partial_{\varepsilon_{ij}} E = (1-d) D_{ijkl}^e (\varepsilon_{kl} - \varepsilon_{kl}^p). \quad (3.45)$$

The damage associated variable Y , which represents the elastic energy density inside the material, is

$$Y = -\partial_d E = \frac{1}{2} D_{ijkl}^e (\varepsilon_{ij} - \varepsilon_{ij}^p) (\varepsilon_{kl} - \varepsilon_{kl}^p), \quad (3.46)$$

and the associated variable for plasticity

$$\sigma_{ij} = -\partial_{\varepsilon_{ij}^p} E = (1-d) D_{ijkl}^e (\varepsilon_{kl} - \varepsilon_{kl}^p). \quad (3.47)$$

The dissipation equation in isothermal conditions for an elasto-plastic-damage model is

$$-\partial_{\varepsilon_{ij}^p} E \dot{\varepsilon}_{ij}^p - \partial_d E \dot{d} = \sigma_{ij} \dot{\varepsilon}_{ij}^p + Y \dot{d} \geq 0, \quad (3.48)$$

in which the first term accounts for the plastic dissipation and the second term for damage dissipation.

The Clausius-Duhem inequality must be valid globally, although a sufficient but non-necessary condition is that each term is non-negative. In this case, $Y\dot{d} \geq 0$ is always valid because the elastic energy density is expressed in quadratic form and the damage rate is always positive by definition. By applying the normality rule to plastic dissipation mechanism, one can write

$$\sigma_{ij} \dot{\varepsilon}_{ij}^p = \dot{\lambda}^p (1-d) \tilde{\sigma}_{ij} \partial_{\tilde{\sigma}_{ij}} f^p \geq 0, \quad (3.49)$$

which means that the scalar product between the damage effective stress $\tilde{\sigma}_{ij}$ and the plastic flow rule must be non-negative. This is always true if normal flow rules are applied and the plastic yield surface is convex. In the proposed model, an associated flow rule is applied.

3.6. Numerical integration

The proposed model has been integrated with an implicit Newton-Raphson scheme to ensure convergence and stability of the solution independently from the step size. The problem can be observed as strain driven; therefore, the objective is to find a correct solution for the internal variables of plasticity ε_{ij}^p and for the effective stress $\tilde{\sigma}_{ij}$ of a given value of the total strain increment $\varepsilon_{ij}^{n+1} - \varepsilon_{ij}^n$. To do so, a stress return algorithm which minimizes the residuals has been implemented. The problem solution consists in obtaining the values of the effective stress and the plastic multiplier while the plastic strains can be explicitly computed via the flow rule with the normality condition as

$$\dot{\varepsilon}_{ij}^p = \dot{\lambda}^p \partial_{\tilde{\sigma}_{ij}} f^p. \quad (3.50)$$

The evolution of the damage internal variable is computed explicitly since it depends exclusively on the plastic and total strain components.

3.6.1. Stress return algorithm

The stress return algorithm for the plastic part is based on a minimization of the residuals $R(\Xi)$ and represents the discretized form of the problem at the load step $n+1$ (in this case, the engineering notation is used instead of tensorial notation)

$$R(\Xi) = \left\{ \begin{array}{c} f_{n+1}^p \\ \tilde{\sigma}_{i,n+1} - \tilde{\sigma}_{i,n} - E_{ij} (\varepsilon_{j,n+1} - \varepsilon_{j,n}) + \Delta \lambda_{n+1}^p E_{ij} \partial_{\tilde{\sigma}_j} f_{n+1} \end{array} \right\}, \quad (3.51)$$

which are functions of the variables that represent the unknowns of the problem

$$\Xi = \begin{Bmatrix} \Delta \lambda_{n+1}^p \\ \tilde{\sigma}_{i,n+1} \end{Bmatrix}. \quad (3.52)$$

Plastic strain tensor can then be computed explicitly by applying the flow rule condition, which in discretized form reads

$$\varepsilon_{i,n+1}^p = \varepsilon_{i,n}^p + \Delta \lambda_{n+1}^p \partial_{\tilde{\sigma}_i} f_{n+1}^p. \quad (3.53)$$

Writing the rate problem equation of the residuals in a discretized form leads to

$$R(\Xi_{n+1}^{m+1}) = R(\Xi_{n+1}^m) + J_{n+1}^m (\Xi_{n+1}^{m+1} - \Xi_{n+1}^m), \quad (3.54)$$

where the matrix J is the Jacobian matrix of the problem and contains the second derivatives of the constitutive model, (i.e., the derivatives of the residual vector with respect to the unknowns of the problem). New values of the unknowns are computed by setting $R(\Xi_{n+1}^{m+1}) = 0$, which leads to

$$\Xi_{n+1}^{m+1} = \Xi_{n+1}^m - (J_{n+1}^m)^{-1} R(\Xi_{n+1}^m). \quad (3.55)$$

The process is iterated through the m index until the norm of the residuals is less than a

given value of tolerance $\|R(\Xi_{n+1}^{m+1})\| = \sqrt{\sum_{i=1}^{nres} [R_i(\Xi_{n+1}^{m+1})]^2} \leq \theta_{tol}$ and the solution Ξ_{n+1}^{m+1} is

obtained. Once the algorithm reaches convergence and the plastic solution is found, the damage internal variable can be updated explicitly when the damage surface is active, and computed as

$$d = 1 - \exp \left[- \left(\frac{Y_-}{\alpha_d} \right)^{m_w} \right]. \quad (3.56)$$

3.7. Results of numerical analyses

3.7.1. Determination of parameters

The procedure for the determination of model parameters starts with the determination of the elastic parameters. The parameters to be determined are Young's modulus E_e and Poisson's ratio ν , which can be easily computed from the results of the standard triaxial compression tests. For the damage model, a rigorous procedure to determine the values of the parameters requires the probabilistic analysis of a consistent number of tests (between 10 and 20 according to Lemaître and Desmorat (2005)). Therefore, it is hardly applicable unless such a number of tests are available. Alternatively, the parameters of the Weibull distribution can be

calibrated according to the procedure illustrated in Section 3.4. Because plasticity governs the present model's values of stress at steady states, the points at this state can be plotted in the $q - p$ plane, as in Figure 3-5a. The data can be interpolated with a second degree polynomial function, which gives the values of the three coefficients a_{pol} , b_{pol} and c_{pol} that are related to the plastic parameters via the following equations

$$\begin{cases} a_{pol} = \alpha/c \\ b_{pol} = \beta \\ c_{pol} = c \end{cases}, \quad (3.57)$$

so the plastic parameters can be obtained by solving this simple system. The remaining parameters $h_{r,0}$ and ξ control the evolution of the plastic yield surface (plastic hardening). It is difficult to obtain their values from direct measurements because one would have to directly measure the onset of plastic irreversible deformation. Therefore, we propose to calibrate these parameters by a numerical back-analysis of experimental results.

3.7.2. Triaxial tests on Opalinus Clay from the Mont Terri site

The proposed constitutive model is used to numerically simulate the experimental findings reported in Gräsle and Plischke (2011), in which a series of undrained triaxial compression tests on Opalinus Clay were performed to investigate the strength resistance of the material. Three different tests at 1, 3 and 6 MPa of confining pressure were used to validate the proposed elasto-plastic-damage formulation. The interpretation is carried out in terms of total stresses in a geomechanical sense, since pore water pressure increase is not known. The parameters were determined based on literature values, interpretation of triaxial tests and numerical calibration against the experimental findings. The elastic parameters for OPA are taken from the literature (Bock, 2009) and Young's modulus is adjusted based on the experimental evidence considered in this work. These values are shown in Table 4-1. Based on experimental evidences, the value of the shape parameter in the Weibull damage model is set to $m_w = 10$. The order of magnitude of α_d can be roughly estimated as (considering that plastic deformations prior to the peak are difficult to estimate precisely, the purely elastic-damage analysis is used here)

$$\alpha_d = K (\sigma_{11}^f)^2 \left\{ \left[\exp\left(-\frac{1}{2m_w}\right) \right] E_e \left(\frac{1}{2m_w} \right)^{\frac{1}{2m_w}} \right\}^{-2} = 0.012, \quad (3.58)$$

where $\sigma_{11}^f = 25 \text{ MPa}$ is an estimated value of the unconfined compressive strength (no UCS tests are available in this series for OPA, so the estimate is based on the test at low values of confinement of 1 MPa). The parameter is then further adjusted to better fit the experimental data. The determination of the plastic yield locus can be approximated by plotting in the $q - p$ plane the points at a residual state, as shown in Figure 3-5a. By interpolating the data with a second degree polynomial, it is possible to directly obtain the values of the three coefficients that characterize the plastic yield locus. Since based on the experimental data the points show opposite curvature (which can be attributed to the scatter obtained from experimental tests on natural material as Opalinus Clay), the plastic yield surface is built by quadratic interpolation with the restraint that the yield surface is convex (which means $\alpha \leq 0$) and intersects the \tilde{q} axis at positive values. Keeping in mind that plasticity is formulated in terms of damage effective stress, the surface should be translated to account for those values of stress (it is not possible to predict the damage effective stress a-priori from analyses, given the highly non-linear behavior and the strict coupling between damage evolution and plastic deformation). Therefore, the cohesive component c is increased to the value of 11.25 MPa to better represent the experimental behavior, which gives then $\alpha = a_{pol} \times c = -0.0324 \times 11.25 = -0.365$. The set of parameters used to simulate the triaxial behavior of Opalinus Clay is illustrated in Table 4-1. The value of $h_{r,0}$ is quite difficult to measure from experimental data. Hence in this case, the assigned value has been calibrated to better reproduce low values of irreversible strains shown before the peak of stress is reached. To calibrate ξ , one would require complete measurements of all the plastic strain components, which is practically impossible to perform. As a result, the parameter has to be adjusted in numerical simulations.

3.7 Results of numerical analyses

Table 3-1: Set of parameters used for the simulation of triaxial tests on Opalinus Clay.

Parameter	Values	Units
E_e	9800	MPa
ν	0.3	-
α	-0.365	-
β	1.9804	-
c	11.25	MPa
h_{r0}	0.35	-
ξ	0.01	-
m_w	10	-
α_d	0.014	MPa

The simulation of triaxial tests has been carried out by first applying an isotropic pressure to reach the values of confinement, and then vertical displacement has been applied to simulate the shearing phase. The samples are the so-called P samples, in which the bedding planes that confer anisotropy to Opalinus Clay are parallel to the direction of the applied maximum principal stress (Salager et al., 2013b). Therefore, the results can be interpreted as representative of the shale matrix. The comparison between the numerical results and the experimental findings is shown in Figure 3-5. From this, it is clear that the proposed model can satisfactorily predict the main characteristics of the investigated material. The damage formulation is responsible for the post peak softening that represents the brittleness of the material. One of the hypotheses is that before the peak of stress is reached, the response shows values of irreversible strains that are comparable to the elastic ones. In this phase, the microcracks inside the material are growing and are responsible for the accumulation of irreversible plastic strains. Low values of irreversible strain before the stress peak is reached can be predicted by the model. After the softening response, the material exhibits constant values of deviatoric stress. In the final part of the stress-strain curve, after the softening branch, it is possible to assert that the material is plastically flowing in this phase, as confirmed by the occurrence of unloading. In the proposed model this happens because damage is coupled to the elastic energy density, therefore once plastic saturation occurs and no more hardening takes place, the evolution of the damage internal variable is stopped. Saturation and hardening are referred to the plastic part of the model, which is formulated in the space of damage effective stresses $\tilde{\sigma}_{ij}$. The elastic unloading is accurately predicted in the pre peak phase as shown in Figure 3-5b, Figure 3-5c and Figure 3-5d. In the post peak the scatter between numerical and experimental unloading elastic modulus is higher at 3 MPa of confinement (Figure 3-5c), while good agreement between experimental data and numerical predictions can be found at 6 MPa of confinement (Figure 3-5d). An overall good agreement

between the proposed model and experimental evidence is shown, which validates the hypothesis made in the formulation of this study.

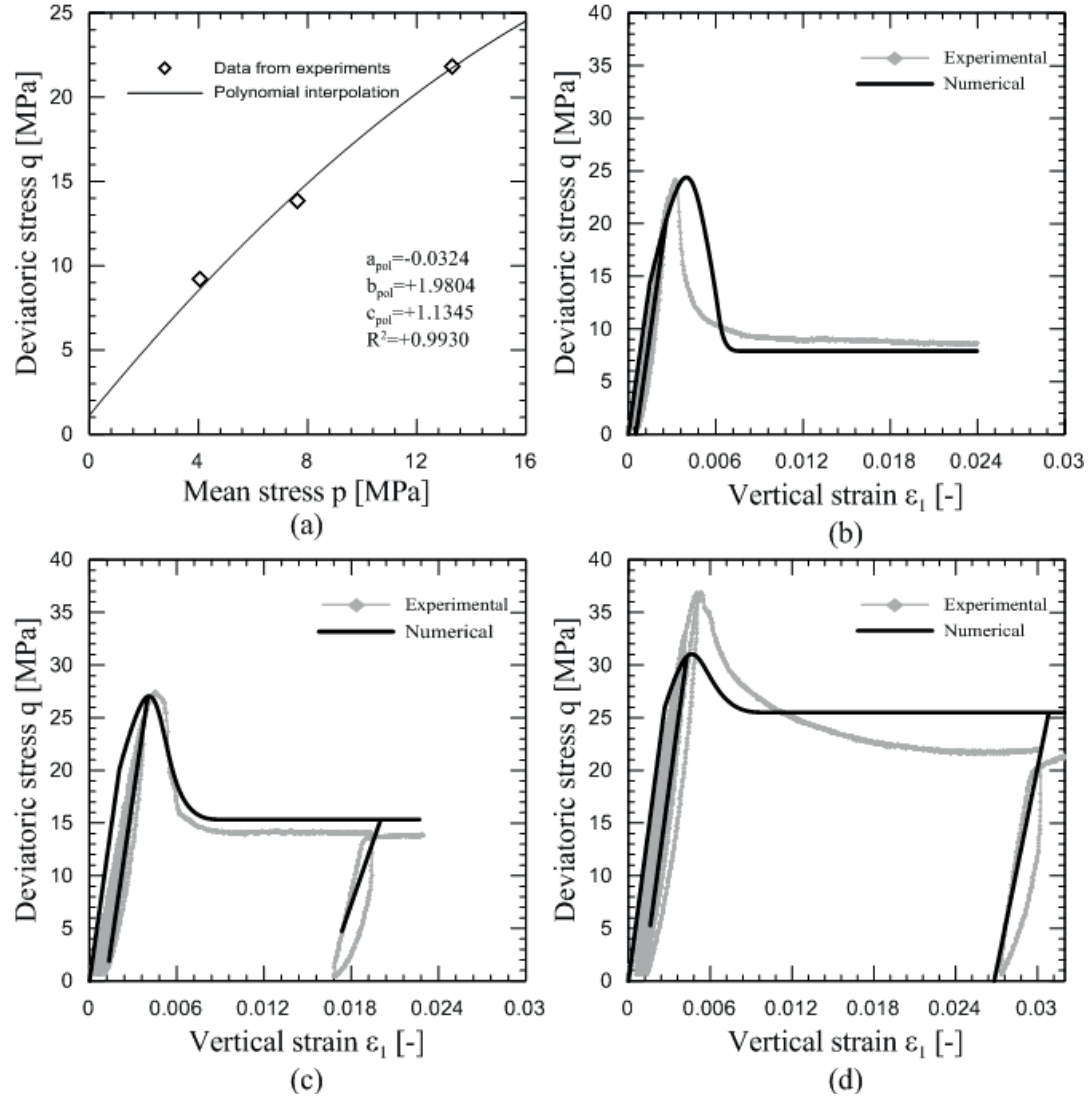


Figure 3-5: Plastic calibration of the parameters with the values obtained for the second degree polynomial (a). Numerical simulations of triaxial experimental tests performed on Opalinus Clay: experimental-vs-numerical results in classic triaxial compressive tests at 1 MPa of confinement (b), 3 MPa of confinement (c) and 6 MPa of confinement (d).

3.7.3. Triaxial tests on LaBiche Shale

To establish the general validity of the constitutive model in the reproduction of the mechanical behavior of quasi-brittle shale, it was decided to perform a second set of numerical analyses to simulate the behavior of La Biche shale, from Alberta, Canada. Three

3.7 Results of numerical analyses

drained triaxial tests performed by Wong (1998) on La Biche shale and reported in literature were considered for numerical analyses. The testing procedure starts with isotropic consolidation of the intact samples at up to three different investigated confinements (50 kPa, 250 kPa and 500 kPa), which were then sheared until failure. The volumetric deformation of the sample was computed by the author after measuring the volume change of the pore fluid. The procedure for the determination of parameters illustrated previously was applied to this case. Table 3-2 illustrates the whole set of parameters used for these simulations.

For the proposed case, the model is able to sufficiently capture the main features of the mechanical behavior. In Figure 3-6, the peaks of stress and the residuals in the post-peak phase are accurately reproduced. A slight discrepancy can be observed for the residual stress of test at 500 kPa of lateral confinement. The volumetric behavior of the numerical analyses was compared to the experimental results in Figure 3-7, and a good agreement is observed. In this case, both the initial compression and the dilatant phase are adequately reproduced by the numerical model.

Table 3-2. Set of parameters used for the simulation of triaxial tests on La Biche shale.

Parameter	Values	Units
E_e	85000	kPa
ν	0.3	-
α	-0.434	-
β	2.124	-
c	940	kPa
h_{r0}	0.75	-
ξ	0.02	-
m_w	10	-
α_d	12.0	kPa

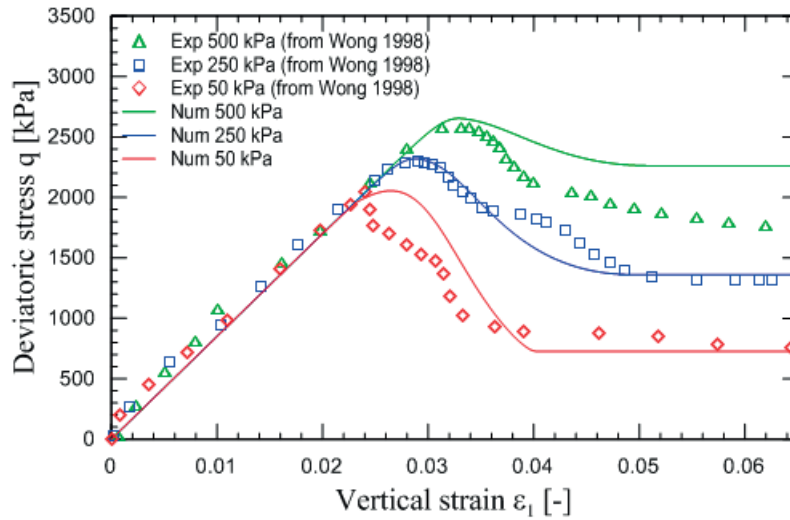


Figure 3-6. Comparison of deviatoric stress vs vertical strain between experimental results and numerical simulations in drained triaxial compression tests on La Biche shale.

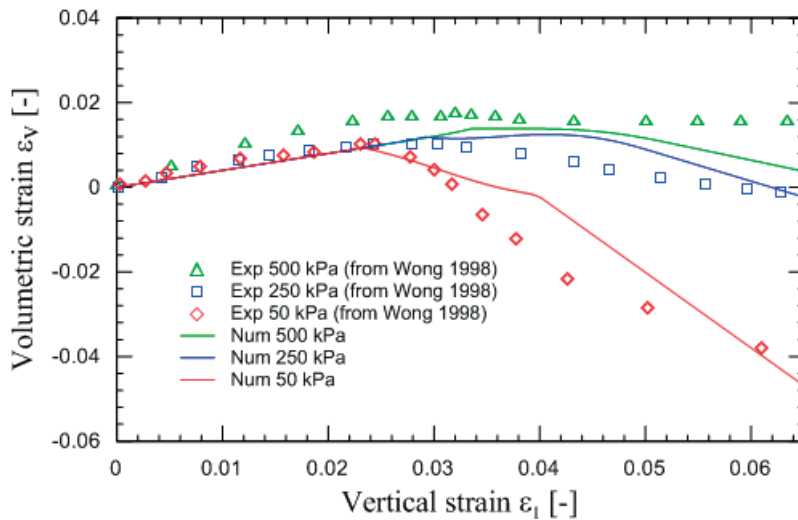


Figure 3-7. Comparison of volumetric strain vs vertical strain between experimental results and numerical simulations in drained triaxial compression tests on La Biche shale.

3.8. Conclusions

Based on the experimental results of mechanical behavior in triaxial conditions, a coupled plastic-damage constitutive model for shale was presented. The selected framework for the development of the constitutive model allowed for the couplings between damage and

plasticity to be made without employing additional restrictions compared to those imposed in the uncoupled versions of the models. The associated framework that was selected required no further restrictions that would have arisen from the second principle of thermodynamics. A non-linear yield function was adopted for the plastic portion of the model, as was a specific hardening rule. The damage model implemented allowed for an accurate representation of the quasi-brittle nature of shale. The total number of parameters was limited to nine, and their determination procedure was thoroughly detailed. The constitutive model was integrated numerically into a fully coupled implicit scheme to compute the plastic internal variable, while damage can be computed explicitly.

The proposed model was validated by back-predictions of experimental results on two compacted shales: Opalinus Clay from Mont Terri, Switzerland and La Biche shale from Alberta, Canada. This set of numerical simulations showed that the model can correctly reproduce the mechanical behavior of shale and its principal features, namely, softening behavior, elastic degradation and constant stress residual conditions. The volumetric deformation behavior was captured quite well by the model, although more data on OPA will be necessary to further validate the proposed formulation. This is not intended as a blind prediction exercise from a set of experimentally based parameters but as a back-calculation showing that the proposed model is able to predict the main features of the mechanical behavior of the selected materials. All of the developments are analyzed in an isotropic framework so that the proposed model is representative of the matrix behavior.

The main innovation in the proposed model is the coupling of two specific theories for certain types of nonlinear solids. On one hand, the plasticity function proposed was specifically developed and tested for geomaterials, and its nonlinear extension allows for a better representation of the behavior of some shales. On the other hand, the damage model that was coupled was specifically developed for quasi-brittle materials, such as shale. The choice of a suitable framework has also allowed a strong and consistent interpretation of the parameters of the model with physical quantities, such that only a few of them will need numerical calibration. This model represents an efficient tool to answer problems related to the mechanical behavior of shale and to model associated geomechanical problems, such as nuclear waste storage problems, unconventional oil and gas exploitation and CO₂ sequestration.

3.9. Acknowledgments

The authors would like to acknowledge Swisstopo, ENSI and the Mont Terri Project for the financial support to this work. The authors would like also to thank Dr. Werner Gräsle from BGR, Germany, for providing the triaxial test data in the framework of the Mont Terri LT experiment.

3.10. References

- Ananiev, S., Ožbolt, J., 2004. Plastic-damage model for concrete in principal directions, in: Li, V., Leung, C.K.Y., Willam, K.J., Billington, S.L. (Eds.), *Fracture Mechanics of Concrete Structures*, pp. 271–278.
- Bock, H., 2009. RA Experiment: Updated Review of the Rock Mechanics Properties of the Opalinus Clay of the Mont Terri URL based on Laboratory and Field Testing. Mont Terri Project, Technical Report 2008-04.
- Bossart, P., Meier, P.M., Moeri, A., Trick, T., Mayor, J.-C., 2002. Geological and hydraulic characterisation of the excavation disturbed zone in the Opalinus Clay of the Mont Terri Rock Laboratory. *Eng Geol* 66, 19-38.
- Bourgeois, F., Burlion, N., Duveau, G., Shao, J.-F., 2003. Mise en œuvre d'une modélisation élasto-plastique endommageable du béton: Calculs numériques dans le cadre d'un benchmark EDF. *Revue française de génie civil* 7, 583-594.
- Busch, A., Alles, S., Gensterblum, Y., Prinz, D., Dewhurst, D.N., Raven, M.D., Stanjek, H., Krooss, B.M., 2008. Carbon dioxide storage potential of shales. *International Journal of Greenhouse Gas Control* 2, 297-308.
- Chazallon, C., Hicher, P.Y., 1998. A constitutive model coupling elastoplasticity and damage for cohesive-frictional materials. *Mech Cohes-Frict Mat* 3, 41-63.
- Chen, L., Shao, J.F., Huang, H.W., 2010. Coupled elastoplastic damage modeling of anisotropic rocks. *Comput Geotech* 37, 187-194.
- Chen, L., Shao, J.F., Zhu, Q.Z., Duveau, G., 2012. Induced anisotropic damage and plasticity in initially anisotropic sedimentary rocks. *Int J Rock Mech Min* 51, 13-23.
- Chiarelli, A.S., Shao, J.F., Hoteit, N., 2003. Modeling of elastoplastic damage behavior of a claystone. *Int J Plasticity* 19, 23-45.
- Einav, I., Houlsby, G.T., Nguyen, G.D., 2007. Coupled damage and plasticity models derived from energy and dissipation potentials. *Int J Solids Struct* 44, 2487-2508.
- Faria, R., Oliver, J., Cervera, M., 1998. A strain-based plastic viscous-damage model for massive concrete structures. *Int J Solids Struct* 35, 1533-1558.
- Farrokhrouz, M., Asef, M., 2014. *Shale Engineering: Mechanics and Mechanisms*. CRC Press.
- Ferrari, A., Laloui, L., 2013. Advances in the Testing of the Hydro-mechanical Behaviour of Shales, in: Laloui, L., Ferrari, A. (Eds.), *Multiphysical Testing of Soils and Shales*. Springer, pp. 57-68.
- Gatuingt, F., Pijaudier-Cabot, G., 2002. Coupled damage and plasticity modelling in transient dynamic analysis of concrete. *Int J Numer Anal Met* 26, 1-24.

- Gräsle, W., Plischke, I., 2011. LT-A Experiment: Mechanical Behavior of Opalinus Clay, Data report from Phase 15. Mont Terri Technical Note TN 2010-86.
- Grassl, P., Jirásek, M., 2006. Damage-plastic model for concrete failure. *Int J Solids Struct* 43, 7166-7196.
- Hu, D., Zhou, H., Shao, J., 2013. An anisotropic damage–plasticity model for saturated quasi-brittle materials. *Int J Numer Anal Met* 37, 1691-1710.
- Imran, I., Pantazopoulou, S.J., 2001. Plasticity model for concrete under triaxial compression. *J Eng Mech-Asce* 127, 281-290.
- Jason, L., Huerta, A., Pijaudier-Cabot, G., Ghavamian, S., 2006. An elastic plastic damage formulation for concrete: Application to elementary tests and comparison with an isotropic damage model. *Comput Method Appl M* 195, 7077-7092.
- Jia, Y., Song, X.C., Duveau, G., Su, K., Shao, J.F., 2007. Elastoplastic damage modelling of argillite in partially saturated condition and application. *Phys Chem Earth* 32, 656-666.
- Josh, M., Esteban, L., Delle Piane, C., Sarout, J., Dewhurst, D., Clennell, M., 2012. Laboratory characterisation of shale properties. *J Petrol Sci Eng* 88, 107-124.
- Ju, J.W., 1989. On Energy-Based Coupled Elastoplastic Damage Theories - Constitutive Modeling and Computational Aspects. *Int J Solids Struct* 25, 803-833.
- Kabir, M.R., Lutz, W., Zhu, K., Schmauder, S., 2006. Fatigue modeling of short fiber reinforced composites with ductile matrix under cyclic loading. *Comp Mater Sci* 36, 361-366.
- Kattan, P.I., Voyiadjis, G.Z., 1990. A Coupled Theory of Damage Mechanics and Finite Strain Elastoplasticity .1. Damage and Elastic Deformations. *Int J Eng Sci* 28, 421-435.
- Kim, B.R., Lee, H.K., 2011. Elastic-damage modeling for particulate composites considering cumulative damage. *Int J Damage Mech* 20, 131-158.
- Krajcinovic, D., 1983. Constitutive-Equations for Damaging Materials. *J Appl Mech-T Asme* 50, 355-360.
- Kratzig, W.B., Polling, R., 2004. An elasto-plastic damage model for reinforced concrete with minimum number of material parameters. *Comput Struct* 82, 1201-1215.
- Lai, Y., Yang, Y., Chang, X., Li, S., 2010. Strength criterion and elastoplastic constitutive model of frozen silt in generalized plastic mechanics. *Int J Plasticity* 26, 1461-1484.
- Lee, H.K., 2001. A computational approach to the investigation of impact damage evolution in discontinuously reinforced fiber composites. *Computational Mechanics* 27, 504-512.
- Lee, J.H., Fenves, G.L., 1998. Plastic-damage model for cyclic loading of concrete structures. *J Eng Mech-Asce* 124, 892-900.

- Lemaitre, J., 1985. Coupled Elasto-Plasticity and Damage Constitutive-Equations. *Comput Method Appl M* 51, 31-49.
- Lemaitre, J., Chaboche, J., 1990. *Mechanics of solid materials*. Cambridge University Press, Cambridge.
- Lemaître, J., Desmorat, R., 2005. *Engineering damage mechanics : ductile, creep, fatigue and brittle failures*. Springer, Berlin ; New York.
- Lubliner, J., 1972. On the thermodynamic foundations of non-linear solid mechanics. *Int J Nonlin Mech* 7, 237-254.
- Lubliner, J., Oliver, J., Oller, S., Onate, E., 1989. A Plastic-Damage Model for Concrete. *Int J Solids Struct* 25, 299-326.
- Marigo, J., 1981. Formulation d'une loi d'endommagement d'un matériau élastique. *CR Acad. Sci. Paris II* 292, 1309-1312.
- Maugin, G.A., 1992. *The thermomechanics of plasticity and fracture*. Cambridge University Press.
- Nguyen, G.D., 2005. A thermodynamic approach to constitutive modelling of concrete using damage mechanics and plasticity theory. PhD Thesis.
- Ortiz, M., 1985. A Constitutive Theory for the Inelastic Behavior of Concrete. *Mech Mater* 4, 67-93.
- Salager, S., François, B., Nuth, M., Laloui, L., 2013. Constitutive analysis of the mechanical anisotropy of Opalinus Clay. *Acta Geotech*, 1-18.
- Salari, M.R., Saeb, S., Willam, K.J., Patchet, S.J., Carrasco, R.C., 2004. A coupled elastoplastic damage model for geomaterials. *Comput Method Appl M* 193, 2625-2643.
- Shao, J.F., Jia, Y., Kondo, D., Chiarelli, A.S., 2006. A coupled elastoplastic damage model for semi-brittle materials and extension to unsaturated conditions. *Mech Mater* 38, 218-232.
- Simo, J., Hughes, T., 1998. *Computational inelasticity*. Springer, New York.
- Van Eekelen, H., 1980. Isotropic yield surfaces in three dimensions for use in soil mechanics. *Int J Numer Anal Met* 4, 89-101.
- Voyiadjis, G.Z., Kattan, P.I., 1992. A Plasticity-Damage Theory for Large Deformation of Solids .1. Theoretical Formulation. *Int J Eng Sci* 30, 1089-1108.
- Wong, R., 1998. Swelling and softening behaviour of La Biche shale. *Can Geotech J* 35, 206-221.

4. Plastic-damage modeling of saturated quasi-brittle shales

Authors: F. Parisio and L. Laloui.

Status: to be submitted to Computers and Geotechnics.

Contributions: The development of the constitutive model, its numerical implementation, the calibration against the experimental results, the validation with numerical analyses and results interpretation were carried out by F. Parisio. The manuscript was written by F. Parisio and edited by L. Laloui, who overruled the work and will also be the senior responsible author (SRA) of the publication.

Abstract

The constitutive modeling of shales is an important topic in the geomechanics community as it is often encountered in most advanced applications such as nuclear waste storage, CO₂ sequestration and unconventional oil and gas exploitation. The goal of this work is to describe, within a unique framework, the full deformation process of shales along with the main features of their mechanical behavior, such as pre-peak hardening plasticity, non-linearity in the onset of inelastic strains, dilatancy, post-peak softening and degradation of the elastic parameters. To do so, we propose a constitutive model that couples plasticity and damage theories in a consistent hydro-mechanical framework and is developed as an improvement of the model presented in Chapter 3. The proposed model is numerically implemented within the Finite Element open source solver *Code_Aster*. We propose a detailed calibration procedure that involves all the material parameters of the formulation, which is developed within the constraints of being successful for practical use in engineering applications. To validate the proposed model, we provide a comparison between numerical analyses and experimental results in conventional triaxial compression tests for a set of three shales. Additionally, the model is validated in coupled hydro-mechanical conditions, by comparing it with saturated undrained triaxial tests with pore pressure measurements. Results show that the model can successfully reproduce the main deformation characteristics of shales in both purely mechanical and hydro-mechanically coupled conditions.

Keywords: shale modeling, plastic and damage mechanics, hydro-mechanics of saturated shales.

4.1. Foreword

The aim of the present chapter is to develop a new constitutive model for the mechanical behavior of shale by coupling damage and plasticity theories. The constitutive framework of the model is the same one adopted in Chapter 3 (Parisio et al., 2015) for coupled plastic damage theories. The model presented there constitutes the basis of the following new developments. For clarity, we will refer to the constitutive model presented in Chapter 3 as MS1, while the one that will be presented here as MS2. There are several reasons that lead to the necessity for new developments in the constitutive model. The first one is to include in the capabilities of the constitutive model the representation of the mechanical behavior under a wider range loading conditions. Specifically, a better representation of the deformation and strength under higher mean stresses. The second one is to formulate a new model with a

simpler identification process of the material parameters involved in the formulation. Thirdly, the model was extended to cover non-associated plasticity, which allows more flexibility and, as it will be shown in Chapter 6, will constitute an important advantage in the modeling of localization bands.

Despite the fact that the two models share similarities concerning the formulation of the plastic yield surface equation and hardening rule, substantial differences exist in the effect that the hardening variable evolution has on the shape of the yield surface. The other fundamental difference consists in the way damage is coupled to the plastic part of the model. In model MS1 damage yield function was based on a Marigo's approach (Marigo, 1981) with a Weibull formulation (Lemaître and Desmorat, 2005) of damage evolution that represents the statistical distribution of cracks at the macro level and is characteristic of the failure of brittle material. This formulation bases damage evolution on the evolution of the elastic energy of the solid, which in turn is a function of negative strain decomposition proposed by Ortiz (1985).

Tensile elastic strains are therefore responsible for the evolution of damage and the failure of the material. This idea has strong physical meaning in terms of the deformation behavior of quasi-brittle material. It also allows the implicit accounting of mean stress dependency of the material's strength. Damage develops along with plasticity and the damage yield surface constitutes a strength envelope of the material. When plastic saturation is reached, elastic strain increments are null and damage remains constant (elastic strain energy does not grow anymore). This well represents the post-peak residual conditions with constant deviatoric stress.

Plasticity is therefore acting firstly, as the responsible mechanism for inelastic permanent strains, which damage alone cannot account for, and secondly, as a limiter of damage developments and is representative of post-peak residual conditions. This formulation MS1 has proven effective in modeling the mechanical behavior of shale under a given range of mean stresses. Discrepancies between model predictions and experimental results grow larger with increasing mean stress. It can therefore be seen as a strong physical model able to capture well the behavior of shale under low confinement values (roughly up a confinement of 25% the unconfined compressive strength). As damage yield function represents, in this case, the strength envelope of the material, and it is formulated on a negative split of the elastic strain tensor, it is not always trivial to calibrate damage parameters in the strain space (or alternatively the elastic energy space). Furthermore, the dependency of the yield locus on mean stress is accounted implicitly but can hardly be controlled, making the formulation of model MS1 not particularly suited for higher ranges of loading conditions in multiaxial behavior.

For these reasons, a new model called MS2 was formulated, starting from the results of model MS1. The main difference between the two models resides on the way that damage was coupled to plasticity. The new coupling can somehow be seen as a “weaker” coupling between the theories of continuum damage mechanics and plasticity. Weaker in this sense refers to the fact that while for model MS1 plasticity and damage were highly superposed during the deformation of the material and the two yield surfaces could be ideally separated and act independently in the pre-peak phase and damage was blocked by plasticity in residual conditions, for model MS2, the deformation process is more clearly distinct in two phases, i.e., a first phase until the stress peak where only hardening plasticity is active, and a second phase post-peak where both mechanisms are active, damage is responsible for strain softening and elastic degradation. Plasticity controls the developments of permanent inelastic strains. To achieve this, damage evolution depends for model MS2 on a cumulative measure of plastic strain that starts at peak of stress. This has a strong implication on the global behavior of the constitutive model, as well as on the physical meaning of the parameters involved in the formulation. Specifically, for MS2, plastic yield surface is the maximum strength envelope of the model and damage controls post-peak stress behavior and final residual conditions. This is, somehow, the opposite of model MS1, where the strength envelope was controlled by damage yield function and residual conditions by its coupling with plasticity. Additionally, the extension to non-associated plasticity for model MS2 allows a better representation of the post-peak dilatant behavior of shale and will prove to be an important tool to control localization band expansion in FEM analyses.

4.2. Introduction

Shale is a clay rich material usually identified by the feature of having more than 35% of clay mineral content with bonding between the clay particles that can be stronger or weaker depending on mineralogy (Nauroy, 2011). Because of deposition and sedimentation processes, many shales have a layered structure in which the clay particles are oriented, conferring initial orthotropic properties to the material. Given this broad classification, common features of the constitutive behavior of shales are not always clearly identifiable. The rheological base is similar to the one presented in Chapter 3, i.e., the behavior of shale is assumed to belong to the class of quasi-brittle geomaterials. In quasi-brittle materials the accumulation of plastic strains during the inelastic phase prior to cracking is small compared to the total strains after failure (Lemaitre and Chaboche, 1990). While the clay rich matrix confers plasticity properties to the materials, the bonding breakage during loading can be associated with damageable-like behavior. Experimental results on Opalinus Clay (Amann et al., 2015; Corkum and Martin, 2007; Gräsle and Plischke, 2011; Jahns, 2013; Popp and Salzer, 2007; Popp et al., 2008), LaBiche Shale (Wong, 1998), Tournemire Shale (Abdi et al.,

2015; Niandou et al., 1997b), Callovo-Oxfordian Shale (Sarout et al., 2007), North Sea Shale (Horsrud et al., 1998) and Dotternhausen shale (Rybacki et al., 2015) evidence that: (1) the complete deformation process in conventional triaxial compression tests can be resumed as a first phase of linear elastic deformation with no dissipation, followed by the accumulation of small permanent strains originated by microcracking and bonding breakage (same order of magnitude as the elastic ones) until the peak of stress is reached; (2) peak conditions are followed by a softening phase in which the breaking of brittle bonding accumulates, permanent strain becomes significant, the material is dilating and a reduction of elasticity is usually observed until a final residual deviatoric stress plateau is reached. A comparison of deformation and strength characteristics of different shales can be found in (Vilarrasa et al., 2013).

Figure 4-1 to Figure 4-4 illustrate a series of experimental evidences at the laboratory scale on the mechanical behavior of different shales. Figure 4-1 plots the results of the compressive behavior of OPA in undrained conditions in terms of axial stress as a function of axial and radial strains at different levels of confinements (Amann et al., 2012). Figure 4-2a shows experimental results on the deviatoric stress evolution as a function of the axial strain in triaxial compression tests at different confinements on LaBiche shale (Wong, 1998) and Figure 4-2b shows for the same set the evolution of volumetric strains as a function of the axial strain. Figure 4-3a shows experimental results on the deviatoric stress evolution as a function of the axial strain in triaxial compression tests at different confinements on Tournemire shale (Abdi et al., 2015) and Figure 4-3b shows for the same set the evolution of deviatoric stress as a function of the volumetric strain. Figure 4-4a shows experimental results on the deviatoric stress evolution as a function of the axial strain in triaxial compression tests at different confinements of a weak shale (Josh et al., 2012). Figure 4-4b illustrates the evolution of vertical stress and pore water pressure during the shearing phase of an undrained triaxial compression test during the shearing phase on North Sea shale at 5 MPa confinement (Horsrud et al., 1998).

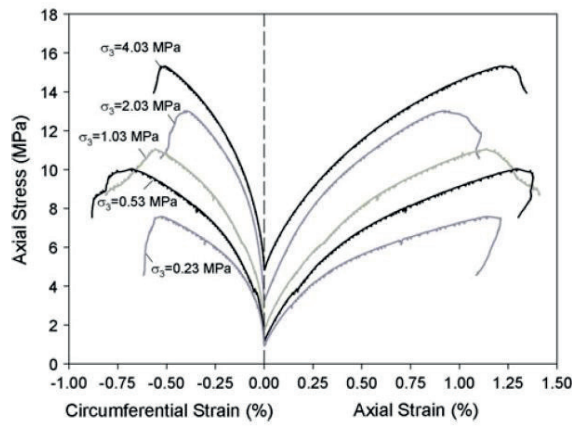


Figure 4-1: Experimental results in triaxial compression conditions at different confinements of Opalinus Clay. Image taken from Amann et al. (2012).

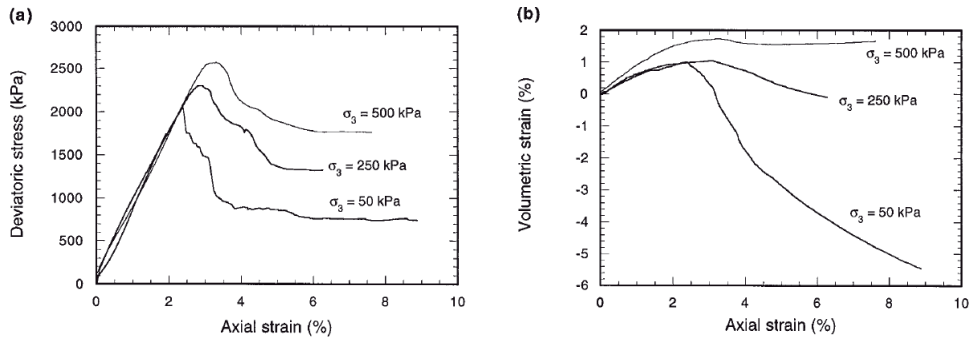


Figure 4-2: Experimental behavior of La Biche shale at different confining pressures in terms of stress-strain behavior (a) and volumetric strain behavior (b). Image taken from Wong (1998).

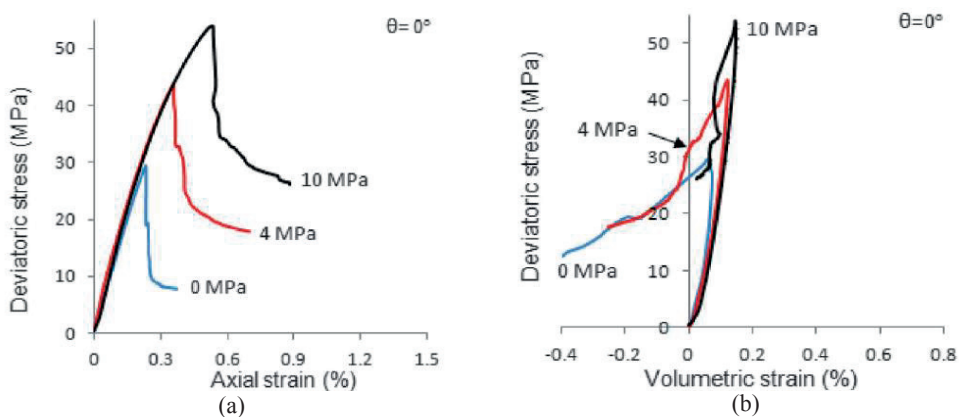


Figure 4-3: Experimental behavior of Tournemire shale samples with vertical bedding planes at different confining pressures in terms of stress-strain behavior (left) and volumetric strain behavior (right). Image taken from Abdi et al. (2015).

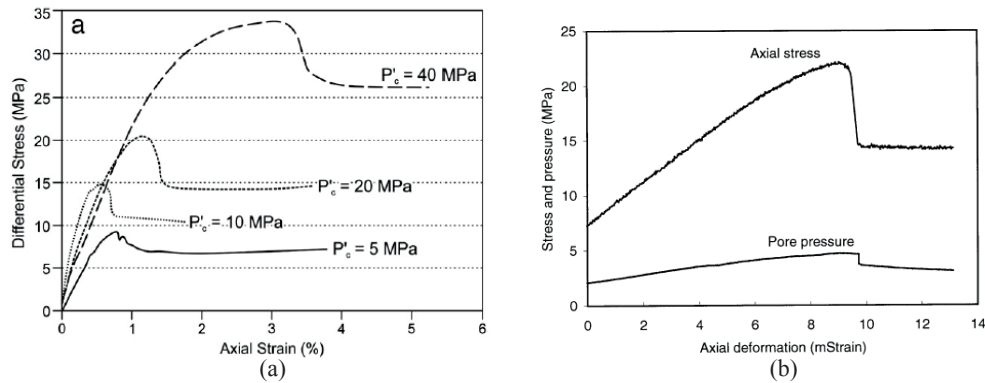


Figure 4-4: Experimental behavior of weak shale samples in terms of stress-strain behavior at different confining pressures (a). Image taken from Josh et al. (2012). Experimental behavior of North Sea shale sample in terms of stress-strain behavior and induced increase of pore water pressure during the undrained shearing phase at an initial confining pressure of 5 MPa (b). Image taken from Horsrud et al. (1998).

From the experimental evidences, linear elasticity is valid in a certain range of confining pressure (see Figure 4-2a, Figure 4-3a and Figure 4-4). Plastic compressibility prior to the peak of stress is usually small, while the quasi-brittle nature is best evidenced by the softening post-peak behavior that lead to residual constant deviatoric stress conditions (Figure 4-2a, Figure 4-3a, and Figure 4-4). The onset of dilatant behavior can be observed slightly prior to the stress peak, confirming the hypothesis of pre-peak inelastic permanent strain development, while dilatancy seems to be pressure-dependent (Figure 4-1, Figure 4-2b and Figure 4-3b). In quasi-brittle materials brittleness might be expected to decrease by increasing confinement. This is not always the case for shale in the brittle regime, as shown in Figure 4-2a, Figure 4-3a, and Figure 4-4. At high levels of confinement stress, a transition into cataclastic compressive deformation was shown in (Rybacki et al., 2015). Although this feature has been widely investigated in other sedimentary geomaterials like sandstones (Wong and Baud, 2012) and limestones (Baud et al., 2000; Renner and Rummel, 1996; Wong and Baud, 2012), in shale still few and limited data exist (Nauroy, 2011). In undrained conditions, the shear phase is performed by not allowing water to migrate out of the sample. This generates an increase in the pore water pressure (see Figure 4-4b). The magnitude of the pore water pressure increase depends on the poromechanical properties, i.e. solid and water compressibility, as well as on the volumetric strain behavior. Dilatancy in the inelastic phase generates volumetric expansion, i.e., additional pore space. The result is a decrease in pore water pressure in the sample.

Given these peculiar features, as widely discussed in Chapter 3, shale has been often modelled with coupled damage-plasticity constitutive models (Chazallon and Hicher, 1998; Chen et al., 2010; Chen et al., 2012; Chiarelli et al., 2003; Einav et al., 2007; Hu et al., 2013; Jia et al., 2007; Salari et al., 2004; Shao et al., 2006). More recently, discrete damage

evolution was proposed by Haghghat and Pietruszczak (2015). The plastic part is usually responsible for the permanent inelastic strain accumulation, while damage confers the brittleness to the material, i.e., softening and degradation of elastic moduli. Given the layered structure of the material, many shales exhibit anisotropic deformation and strength properties (Abdi et al., 2015; Ambrose, 2014; Gräsle and Plischke, 2011; McLamore and Gray, 1967; Niandou et al., 1997b). This subject will be presented and developed in detail in Chapter 5.

The main goal of the present work is the development and validation of a plastic-damage constitutive model in an isotropic framework. The proposed model is a direct extension of the previous constitutive model MS1 developed in the work of Parisio et al. (2015), where plasticity was formulated in the effective stress space as in Jason et al. (2006), Ju (1989) and Lee and Fenves (1998). Details on the advantages of a model that couples plasticity in the damage effective stress space can be found in the work of Grassl and Jirásek (2006). While the plastic formulation is improved, along with the calibration of its parameters, the damage driving variable depends on a measure of the accumulation of plastic strain. In this way, the plastic yield surface constitutes a real strength envelop of the material, so that no damage accumulates prior to the peak and therefore, strength is dissociated from elastic characteristics. Although no damage accumulates prior the peak of stress (as evidenced in Figure 4-15, where loading-unloading cycles, prior the peak of stress, show no elastic degradation), it is known how inelastic processes begin in this phase as micro cracks start to accumulate. An example of this phenomenon is given by Amann et al. (2011), where cumulative acoustic emissions count shows that inelasticity starts before the peak of stress is reached. In the current formulation of model MS2, such pre-peak inelastic processes are implicitly accounted for by the accumulation of plastic strains.

The model is furtherly extended to include true triaxial behavior. The equation of the yield surface in the octahedral plane is here simply presented and will be analyzed in details in Chapter 5. A non-associated plastic potential is developed in order to avoid over-estimation of the dilatant strain in the inelastic phase. The model is implemented into the open source FEM code *Code_Aster*, developed by Électricité de France (EDF) (www.code-aster.org). Validation examples are focused mainly on Opalinus Clay from Switzerland (Mont Terri site for undrained and Schlattingen site for undrained with pore pressure measurements), although, given the accuracy of the volumetric strain measurements, LaBiche shale from Canada was selected as well. Results demonstrate the ability of the proposed model to account for the prominent characteristics of the deformation process in shales in pure mechanical as well as hydro-mechanical coupled conditions.

4.3. Poroelastic coupled hydro-mechanical formulation

We present here the poroelastic theory implemented in *Code_Aster* as described in the work of Plassart et al. (2013), which constitutes here the problem formulation solved in numerical analyses. As the sign convention in *Code_Aster* is the one of solid mechanics, i.e., compressions are negative and tensions positive, in this section only, this convention is applied. In the rest of the Chapter, the geomechanics convention is applied. The elastic strain increment is driven by the water effective stress increment in saturated conditions with the effective stress equation that writes

$$\sigma_{ij} = \sigma'_{ij} - b p_w \delta_{ij}, \quad (4.1)$$

where σ_{ij} is the total stress tensor, σ'_{ij} is the effective stress tensor, p_w is the pore water pressure and b is Biot's coefficient defined as

$$b = 1 - \frac{K_o}{K_s}, \quad (4.2)$$

with K_o being the undrained modulus of the porous material and K_s the bulk elasticity modulus of the solid skeleton. The variation of porosity $\dot{\phi}$ is a function of the volumetric strain increment $\dot{\varepsilon}_{kk}$ defined as

$$\dot{\phi} = (b - \phi) \left(\dot{\varepsilon}_{kk} + \frac{P_w}{K_s} \right), \quad (4.3)$$

where ϕ is the porosity of the medium, i.e., the ratio between pore volume and total one. The fluid mass m_w is related to fluid mass density ρ_w , initial fluid mass density ρ_w^0 and initial porosity ϕ^0 as

$$m_w = \rho_w (1 + \varepsilon_{kk}) \phi - \rho_w^0 \phi^0. \quad (4.4)$$

The water mass flow rate M_i^w is related to the pore water pressure geometrical gradient $\partial p_w / \partial x_i$ via Darcy's law for fluid flow as

$$M_i^w = - \frac{k_{ij}}{\mu_w} \left(\frac{\partial p_w}{\partial x_i} - \rho g_i \right), \quad (4.5)$$

where k_{ij} is the intrinsic permeability in tensorial form, μ_w is the water dynamic viscosity and g_i is the gravity vector. Neglecting the volumetric terms, the momentum balance equation of

the mixture is defined for a kinematic admissible field $(\bar{\varepsilon}_{ij}, \bar{u}_i, \bar{p}_i)$, in the spirit of the principle of virtual work, as

$$\int_{\Omega} \sigma'_{ij} \bar{\varepsilon}_{ij} dv = \int_{d\Omega} p_i \bar{u}_i ds, \quad (4.6)$$

while the fluid mass balance as

$$-\int_{\Omega} \frac{dm_w}{dt} \bar{p}_w dv + \int_{\Omega} M_j^w \frac{\partial \bar{p}_w}{\partial x_j} dv = \int_{d\Omega} M^{w,ext} \bar{p}_w ds, \quad (4.7)$$

where $M^{w,ext}$ is the incoming fluid mass per unit area at the boundaries while p_i is a given traction at boundaries.

4.4. Plastic damage model

4.4.1. Isotropic plastic yield surface and hardening internal variables

In the following section the constitutive framework is presented and discussed, along with the yield surface and the hardening equation. The constitutive equation relates stresses with elastic strains as

$$\sigma'_{ij} = (1-d) D_{ijkl}^e \varepsilon_{kl}^e, \quad (4.8)$$

where σ'_{ij} is the nominal water effective stress, d is the damage internal variable, D_{ijkl}^e is the rate independent linear elastic stiffness tensor and ε_{ij}^e is the elastic strain. The split in the rate total strain tensor $\dot{\varepsilon}_{ij}$ between elastic $\dot{\varepsilon}_{ij}^e$ and plastic $\dot{\varepsilon}_{ij}^p$ strain rate is valid and writes

$$\dot{\varepsilon}_{ij} = \dot{\varepsilon}_{ij}^e + \dot{\varepsilon}_{ij}^p. \quad (4.9)$$

The damage effective stress $\tilde{\sigma}'_{ij}$ is defined as

$$\sigma'_{ij} = (1-d) \tilde{\sigma}'_{ij}. \quad (4.10)$$

Effective stress $\tilde{\sigma}'_{ij}$ is in this case is referred to as damage effective stress and is the stress acting in the undamaged part of the solid, where the damage represents the creation of microvoids inside the material. For further clarification on the physical meaning of damage effective stress and for its derivation, the reader is referred to the work of Lemaître and Desmorat (2005). The constitutive relation can be written as

$$\sigma'_{ij} = (1-d) \tilde{\sigma}'_{ij} = (1-d) D_{ijkl}^e (\varepsilon_{kl} - \varepsilon_{kl}^p), \quad (4.11)$$

and in rate form becomes

$$\dot{\sigma}'_{ij} = (1-d)D_{ijkl}^e (\dot{\varepsilon}_{kl} - \dot{\varepsilon}_{kl}^p) - \dot{d}D_{ijkl}^e (\varepsilon_{kl} - \varepsilon_{kl}^p). \quad (4.12)$$

It can be demonstrated that equation (4.11) can be derived from thermodynamic potentials. The internal energy E at a given point of the solid can be represented as a function of the strain tensor ε_{ij} , the entropy per unit volume S and a set of internal variables α_i representative of the events sequence in the material, and can be written as

$$E = E(\varepsilon_{ij}, S, \alpha_i). \quad (4.13)$$

In case of damage-plastic models, under isothermal conditions, the following expression for internal energy function can be used

$$E(\varepsilon_{ij}, \varepsilon_{ij}^p, d) = \frac{1}{2}(1-d)D_{ijkl}^e (\varepsilon_{ij} - \varepsilon_{ij}^p)(\varepsilon_{kl} - \varepsilon_{kl}^p), \quad (4.14)$$

and by definition of the state equation $\sigma'_{ij} = \partial_{\varepsilon_{ij}} E$, one can retrieve the constitutive equation expressed in equation (4.11)

$$\sigma'_{ij} = \partial_{\varepsilon_{ij}} E = (1-d)D_{ijkl}^e (\varepsilon_{kl} - \varepsilon_{kl}^p). \quad (4.15)$$

4.4.2. The plastic yield surface with isotropic hardening

The plastic yield surface is formulated in the effective stress space, so that uniqueness of the solution is always guaranteed independently of the values of the hardening modulus as demonstrated in the work of Grassl and Jirásek (2006). Such a surface is defined in terms of three stress invariants. The first invariant of stress \tilde{I}_1 is defined as

$$\tilde{I}_1 = \tilde{\sigma}'_{11} + \tilde{\sigma}'_{22} + \tilde{\sigma}'_{33}, \quad (4.16)$$

while the second invariant \tilde{J}_2 as

$$\tilde{J}_2 = \frac{1}{6} \left[(\tilde{\sigma}'_{11} - \tilde{\sigma}'_{22})^2 + (\tilde{\sigma}'_{22} - \tilde{\sigma}'_{33})^2 + (\tilde{\sigma}'_{33} - \tilde{\sigma}'_{11})^2 \right] + \tilde{\sigma}'_{12}^2 + \tilde{\sigma}'_{23}^2 + \tilde{\sigma}'_{31}^2. \quad (4.17)$$

The mean stress \tilde{p} is defined as

$$\tilde{p} = \frac{\tilde{I}_1}{3}, \quad (4.18)$$

and the third invariant \tilde{J}_3 reads

$$\tilde{J}_3 = (\tilde{\sigma}'_{11} - \tilde{p})(\tilde{\sigma}'_{22} - \tilde{p})(\tilde{\sigma}'_{33} - \tilde{p}). \quad (4.19)$$

The deviatoric stress \tilde{q} is given by

$$\tilde{q} = \sqrt{3\tilde{J}_2}, \quad (4.20)$$

and Lode's angle as

$$\tilde{g} = \frac{1}{3} \arcsin \left(\frac{3\sqrt{3}}{2} \frac{\tilde{J}_3}{(\tilde{J}_2)^{3/2}} \right). \quad (4.21)$$

The plastic yield function expression was formulated as an extension of the plastic yield function of model MS1 to allow a better representation of the material behavior, and, although it maintains the same second order polynomial structure, the hardening variable acts in a different way in the various coefficients, making it more fit and well designed to reproduce the pre-peak hardening. The new plastic yield surface has the following expression in terms of invariants of stress

$$f_p = \tilde{q} - \left\{ (1 - r_{ha}) \alpha \tilde{p}^2 + [(1 - \delta) r_{ha} + \delta] \beta \tilde{p} + r_{ha} \gamma \right\} r_{\tilde{\theta}}, \quad (4.22)$$

where α , β , γ and δ are material parameters, r_{ha} is a plastic hardening internal variable and $r_{\tilde{\theta}}$ is a function of Lode's angle to account for a different strength in the octahedral plane. To ensure convexity of the yield surface $\alpha \leq 0$, where α represents the curvature of the yield surface in the \tilde{p} - \tilde{q} plane. For null values of α , a linear surface is retrieved. The coefficient β can be seen as the frictional coefficient, and, e.g., can be expressed as function of the internal friction angle ϕ at peak as

$$\beta = \frac{6 \sin \phi}{3 - \sin \phi}. \quad (4.23)$$

γ is the intercept of the yield surface with the effective deviatoric stress axis, i.e., $\tilde{p} = 0$. It can also be expressed as a function of the equivalent Mohr-Coulomb internal friction angle ϕ and cohesion c as

$$\gamma = \frac{6c \cos \phi}{3 - \sin \phi}. \quad (4.24)$$

Both parameters, alternatively, can be expressed as functions of the tensile σ^t and compressive σ^c strength as

$$\beta = \frac{3(\sigma^c - \sigma^t)}{\sigma^c + \sigma^t}, \quad (4.25)$$

$$\gamma = \frac{2\sigma^c \sigma^t}{\sigma^c + \sigma^t}$$

or in the inverse way as

$$\begin{aligned}\sigma^c &= \frac{\gamma}{3-\beta} \\ \sigma^t &= \frac{\gamma}{3+\beta}\end{aligned}\quad (4.26)$$

The plastic loading-unloading conditions, often referred to as the Karush-Kuhn-Tucker conditions (Simo and Hughes, 1998), are written as

$$\dot{\lambda}^p \geq 0 \quad f^p \leq 0 \quad \dot{\lambda}^p f^p = 0, \quad (4.27)$$

while the hardening function r_{ha} is a function of the plastic hardening variable k_p defined as follows

$$\dot{k}_p = \|\dot{\epsilon}_{ij}^p\|, \quad (4.28)$$

so that

$$r_{ha} = \begin{cases} (r_{ha0} - 1)(k_p/\chi_h)^2 - 2(r_{ha0} - 1)(k_p/\chi_h) + r_{ha0} & k_p \leq \chi_h \\ 1.0 & k_p > \chi_h \end{cases}, \quad (4.29)$$

with $0 \leq r_{ha} \leq 1$ and r_{ha0} and χ_h as material parameters. Figure 4-5 displays the evolution of the internal variable r_{ha} for different values of the material parameters. Figure 4-5a plots the evolution for different values of r_{ha0} , which controls the initial value of the hardening variable when plastic strain is null. This material parameter, as it will be seen, has a direct influence on the initial yield surface. The parameter χ_h , instead, can be seen as a measure of plastic deformability, i.e., it is the value of the plastic strain norm at which the hardening function r_{ha} equals one and then hardening stops (Figure 4-5b). Higher values of χ_h mean more plastic deformation during hardening, while smaller values have the opposite effect.

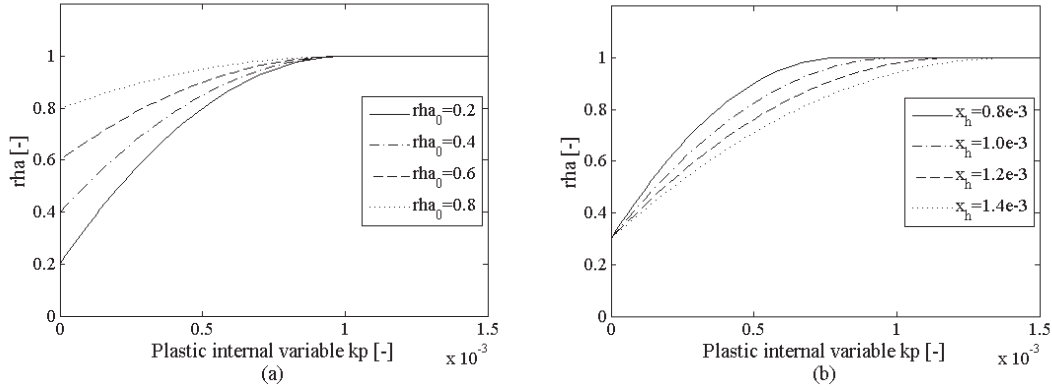


Figure 4-5: Evolution of the hardening function r_{ha} for different values of the parameters r_{ha0} (a) and χ_h (b).

The effect of the plastic hardening variable on the yield surface can be most easily explained if each parameter on which acts r_{ha} is examined separately. The quadratic term, which confers a curvature to the yield surface, has an initial value of $(1 - r_{ha0})\alpha$ at $r_{ha} = r_{ha0}$ and becomes null when plastic saturation is reached (i.e., when $r_{ha} = 1$ and no more hardening takes place), collapsing the quadratic surface into a linear one. The second term, called here the friction coefficient, ranges from $[(1 - \delta)r_{ha0} + \delta]\beta$ when $r_{ha} = r_{ha0}$, to β at $r_{ha} = 1$. Therefore, the coefficient δ is a parameter useful to control the evolution of the friction coefficient β during hardening by controlling its values at the onset of inelasticity. The third term, $r_{ha}\gamma$, simply ranges from $r_{ha0}\gamma$ at the onset of inelasticity to γ at the end of the hardening process. Thus, the yield surface at the onset of plasticity takes therefore the following form

$$f_p = \tilde{q} - \left\{ (1 - r_{ha0})\alpha \tilde{p}^2 + [(1 - \delta)r_{ha0} + \delta]\beta \tilde{p} + r_{ha0}\gamma \right\} r_{\tilde{\theta}}, \quad (4.30)$$

while at plastic saturation will have the form of a classical Drucker-Prager type formulation

$$f_p = \tilde{q} - (\beta \tilde{p} + \gamma) r_{\tilde{\theta}}. \quad (4.31)$$

The advantage of the curved second degree plastic yield surface consists in the implicit inclusion of a cap surface into the plastic formulation. Furthermore, as shown in Figure 4-6a, the hardening is more pronounced for higher values of the mean effective stress \tilde{p} . When $\alpha = 0$, the second degree yield surface degenerates into a linear one and the hardening variable has an effect on the frictional β and cohesive γ coefficients (Figure 4-6b). When $\alpha = 0$ and $\delta = 1$ the hardening function r_{ha} has a hardening effect only on the cohesive coefficient. Therefore, the yield surface translates without rotation during the inelastic process

as shown in Figure 4-6c. The concept of a loading surface representing a cap of the material that opens toward a final yield of the cohesive-frictional type (either linear or non-linear) was proposed for the modeling of concrete by, e.g., Grassl and Jirásek (2006) and Imran and Pantazopoulou (2001).

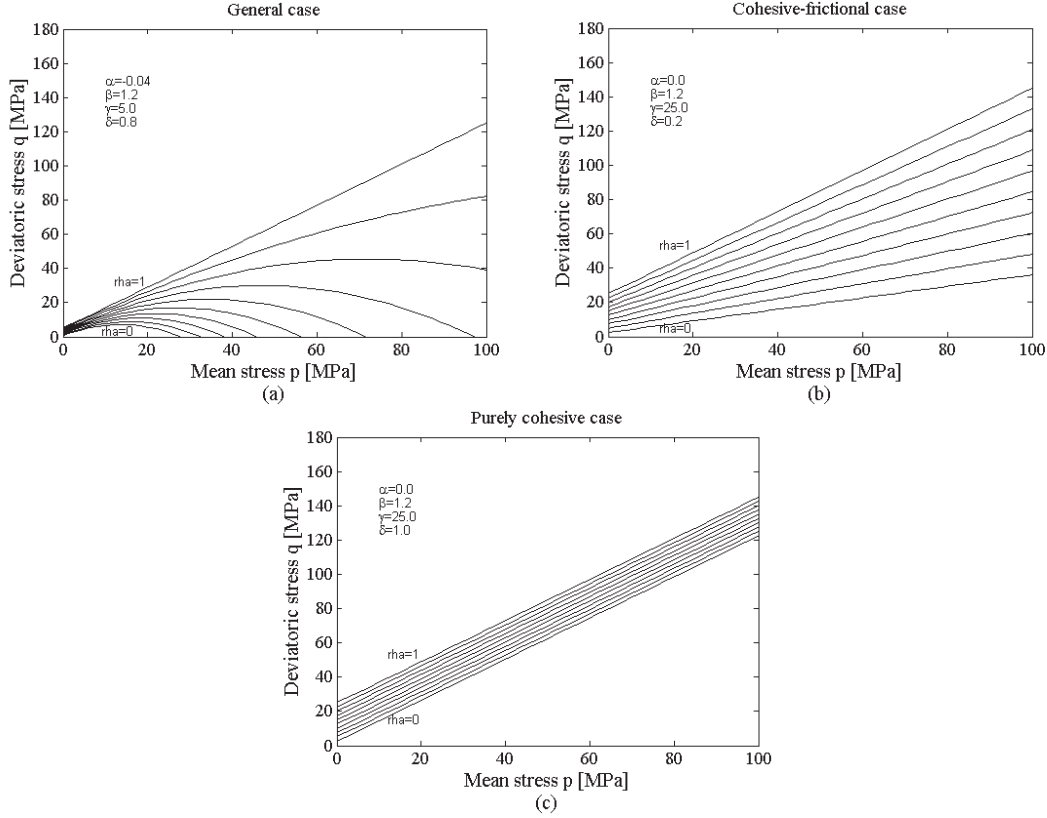


Figure 4-6: Evolution of the plastic yield surface during hardening for three different cases: the general case in which the initial curved shape will open toward higher values of mean effective stress (a); cohesive-frictional case in which the surface remains linear and the effect of plastic hardening is to increase values of cohesive and frictional coefficients (b); purely cohesive case in which plastic hardening has an effect only on the intercept which increases and translates the initial yield surface, which keeps the same slope (c).

For comparison, the yield function of model MS1 presented in (Parisio et al., 2015) reads

$$f^P = \tilde{q} - \left(\alpha \frac{\tilde{p}^2}{c} + \beta \tilde{p} + r_{ha} c \right) r_{\tilde{\theta}}, \quad (4.32)$$

which implies translational hardening, as the effect of r_{ha} was exclusively on the cohesive parameter c , while the final yield surface remained non-linear. In the new formulation MS2, all the plastic yield surface parameters show a dependency on the hardening function r_{ha} .

While the final yield is linear, the hardening has a roto-translational effect as well as an opening of the cap part of the surface toward higher mean stresses. MS2 allows a better description of the plastic behavior toward higher mean stresses, as well as additional degree of freedom in all conditions.

To account for the difference in strength in the octahedral plane, the deviatoric strength is multiplied by a function that accounts for Lode's angle dependency r_l and writes

$$r_l(\theta) = \left(\frac{1 - \beta_\theta \frac{3\sqrt{3}}{2} \frac{J_3}{J_2^{3/2}}}{1 - \beta_\theta} \right)^{-0.229}, \quad (4.33)$$

where β_θ is a material parameters defining the shape of the yield function in the octahedral plane. This formulation is taken after Van Eekelen (1980) and modified here. In a given range of values of the material parameter, it ensures convexity in the octahedral plane. Its effect will be studied and further discussed in Chapter 5.

4.4.3. Non-associated plastic potential

It is known how associativity of the plastic potential leads to overestimating the dilatancy in both dry and fluid saturated geomaterials, as the dilatancy angle must be smaller than the friction angle (Maier and Hueckel, 1979; Makhnenko and Labuz, 2015; Rudnicki and Rice, 1975b; Vardoulakis and Sulem, 1995). In order to correctly predict the volumetric plastic behavior, the plastic potential is therefore non-associated and is defined as

$$g_p = \tilde{q} - \left\{ (1 - r_{ha}) \alpha \tilde{p}^2 + [(1 - \delta)r_{ha} + \delta](1 - s_h) \beta \tilde{p} \right\}, \quad (4.34)$$

where s_h is an internal variables defining the evolution of the dilatant coefficient $[(1 - \delta)r_{ha} + \delta](1 - s_h) \beta$ and depends on the plastic internal variable k_{ps} , which in turn is defined as

$$k_{ps} = \begin{cases} k_p - \chi_h & k_p > \chi_h \\ 0 & k_p \leq \chi_h \end{cases}. \quad (4.35)$$

Plastic strain evolution is given by the flow rule

$$\dot{\varepsilon}_{ij}^p = \dot{\lambda}^p \frac{\partial g^p}{\partial \tilde{\sigma}'_{ij}}, \quad (4.36)$$

where the plastic multiplier $\dot{\lambda}^p$ gives the magnitude of plastic strain rates, while direction is given by the gradient of the plastic potential in the effective stress space. The formulation of

the non-associated plastic internal variable postulated in equation (4.35) implies that non-associativity of the behavior appears when plastic hardening terminates and perfect plasticity conditions are reached. This means that prior the peak of stress the model is associated and the equivalent Mohr-Coulomb dilatancy angle will be equal to the equivalent Mohr-Coulomb friction angle. In the post-peak phase, the volumetric behavior deviates from associativity and the coefficient s_h takes the form

$$s_h = \begin{cases} -\left(k_{ps}/\psi_h\right)^2 + 2\left(k_{ps}/\psi_h\right) & k_{ps} < \psi_h, \\ 1 & k_{ps} \geq \psi_h \end{cases}, \quad (4.37)$$

where ψ_h is a material parameter defining the value of post-peak plastic strain norm (i.e., the total plastic strain norm minus the plastic strain norm at peak) at which plastic dilation is nullified and deformative plastic behavior is purely deviatoric. Figure 4-7a illustrates the evolution of the non-associated coefficient $1-s_h$ with the internal variable k_{ps} for different values of the parameter ψ_h . When plastic internal variable k_{ps} is equal to ψ_h , the non-associated coefficient $1-s_h$ nullifies as well as the volumetric plastic strain increment while the inelastic strain is purely deviatoric. The dilatancy coefficient can be associated to the dilation angle ψ via the following equation

$$(1-s_h)\beta = \frac{6 \sin \psi}{3 - \sin \psi}, \quad (4.38)$$

and combining it with equation (4.23), which relates the friction coefficient β to the friction angle ϕ , the evolution of dilatancy angle ψ as a function of the non-associated plastic variable k_{ps} and of the friction angle ϕ will result in the following

$$\psi = \begin{cases} \arcsin \left[\frac{3\left(1+k_{ps}^2/\psi_h^2-2k_{ps}/\psi_h\right)\frac{6 \sin \phi}{3-\sin \phi}}{6+\left(1+k_{ps}^2/\psi_h^2-2k_{ps}/\psi_h\right)\frac{6 \sin \phi}{3-\sin \phi}} \right] & k_{ps} < \psi_h \\ 0 & k_{ps} \geq \psi_h \end{cases}. \quad (4.39)$$

Figure 4-7b shows the evolution of the dilatancy angle as a function of the non-associated plastic internal variable k_{ps} for different values of the friction angle and $\psi_h = 1 \times 10^{-2}$. The dilatancy equals the friction angle at the peak of stress, when perfect plasticity in the damage effective stress space starts. In contrast, the dilatancy becomes null for the rest of the deformative process once $k_{ps} = \psi_h$.

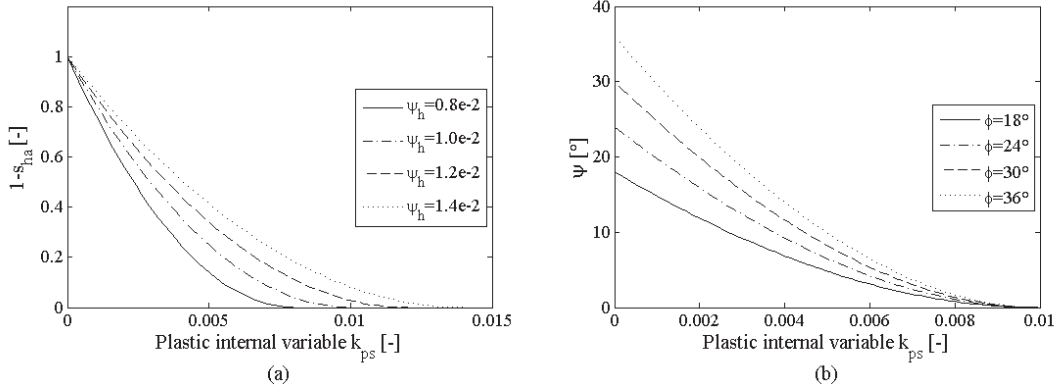


Figure 4-7: Evolution of the non-associated coefficient $1 - S_h$ (a) and of the dilatancy angle (b) with the plastic internal variable k_{ps} .

In model MS1 the plastic yield surface remained associated, and although it could account for dependency of dilatancy on mean stress because of non-linearity, it did not allow control in the dilatant behavior in the post-peak range as the new model does. A non-associated potential allows a better description of the decreased dilatancy and, as it will be shown in Chapter 1, will prove to be a strong tool in controlling unphysical shear band expansions.

For what concerns thermodynamic consistency of the current formulation, for Durcker-Parager perfect plasticity (and for cohesive-frictional plasticity in general) it is demonstrated how non-associativity is thermodynamically consistent as normality is always satisfied in the generalized stress space for hyperplastic formulations (Puzrin, 2012).

4.4.4. Isotropic damage model

The damage model can be expressed in the same formalism of plasticity, by introducing a damage loading function of the type

$$f_d(\widehat{\varepsilon}, k_d) = \widehat{\varepsilon} - k_d, \quad (4.40)$$

that defines the limit of the damage domain, where $\widehat{\varepsilon}$ is an equivalent strain and k_d is an internal variable that contains the history of damage evolution. Loading-unloading conditions can be postulated in the form of the Karush-Kuhn-Tucker conditions as

$$\dot{k}_d \geq 0 \quad f_d \leq 0 \quad \dot{k}_d f_d = 0, \quad (4.41)$$

where the first condition implies positiveness of the rate of the damage internal variable k_d , the second one implies that k_d is the upper bound of $\widehat{\varepsilon}$, while the third one states that the

evolution of k_d is possible only if the current value of k_d and $\widehat{\varepsilon}$ are equal. The evolution of the damage variable can be expressed as a function of the damage internal variable k_d

$$d = h(k_d). \quad (4.42)$$

In the current model, the equivalent strain $\widehat{\varepsilon}$ writes

$$\dot{\widehat{\varepsilon}}(\dot{\varepsilon}_{ij}^p) = \begin{cases} \dot{\tilde{\varepsilon}}_d^p & k_p > \chi_h \\ 0 & k_p \leq \chi_h \end{cases}, \quad (4.43)$$

where $\dot{\tilde{\varepsilon}}_d^p$ is a measure of the plastic deviatoric strain increment defined as

$$\dot{\tilde{\varepsilon}}_d^p = \sqrt{\frac{2}{3}} \left\{ \frac{1}{6} \left[(\dot{\varepsilon}_{11}^p - \dot{\varepsilon}_{22}^p)^2 + (\dot{\varepsilon}_{11}^p - \dot{\varepsilon}_{33}^p)^2 + (\dot{\varepsilon}_{22}^p - \dot{\varepsilon}_{33}^p)^2 \right] + (\dot{\varepsilon}_{12}^p)^2 + (\dot{\varepsilon}_{13}^p)^2 + (\dot{\varepsilon}_{23}^p)^2 \right\}, \quad (4.44)$$

and therefore damage grows when

$$k_d = \widehat{\varepsilon}. \quad (4.45)$$

The damage evolution law $d = h(k_d)$ has the following form

$$d = h(k_d) = (1 - \beta_d) \left[1 - \exp\left(-\frac{k_d}{\alpha_d}\right) \right], \quad (4.46)$$

where $0 \leq \beta_d \leq 1$ controls the residual values of damage and $\alpha_d > 0$ defines the initial slope of the softening curve. Both are dimensionless parameters. A direct implication of the proposed formulation is that damage will develop when the plastic internal variable $k_p > \chi_h$, i.e., when the behavior is perfectly plastic and hardening has reached saturation. Therefore, damage will be responsible for the softening branch of the stress-strain curve, along with the degradation of elasticity.

The meaning of the parameter α_d can be better explained by introducing the intacticity parameter $i = 1 - d$ in equation (4.46), which will lead to

$$i = 1 - d = \beta_d + (1 - \beta_d) \exp\left(-\frac{k_d}{\alpha_d}\right). \quad (4.47)$$

The intacticity parameter will have the same shape of the softening curve. Deriving equation (4.47) with respect to k_d , we obtain

$$\frac{\partial i}{\partial k_d} = -\frac{(1 - \beta_d)}{\alpha_d} \exp\left(-\frac{k_d}{\alpha_d}\right), \quad (4.48)$$

which is the slope evolution of the softening branch along damage internal variable k_d . At $k_d = 0$, equation (4.48) becomes

$$\frac{\partial i}{\partial k_d}(k_d = 0) = -\frac{(1 - \beta_d)}{\alpha_d}, \quad (4.49)$$

so that the line with such a slope and that passes through the point $(0,1)$ in the (k_d, i) space has equation

$$i = -\frac{(1 - \beta_d)}{\alpha_d} k_d + 1. \quad (4.50)$$

Such line intercepts the k_d axis at

$$k_d = \frac{\alpha_d}{(1 - \beta_d)}. \quad (4.51)$$

Finally, for $\beta_d = 0$ the intercept with k_d axis is equal to α_d . This better illustrates the meaning of the α_d parameter (Figure 4-9b), which represents the intercept of the derivative of the softening curve computed with k_d axis at zero damage when damage can fully develop ($\beta_d = 0$). When the residual damage parameter β_d is not equal to zero, the value of this intercept is given by equation (4.51).

The parameter β_d controls the residual values of damage, or alternatively the residual values of stress in the softening post-peak phase. When $\beta_d = 0$, damage can fully develop and stress is allowed to drop to zero, while, for $\beta_d = 1$, damage will equal zero at all time and the resulting behavior will be purely elasto-plastic. Figure 4-8a and Figure 4-8b display the evolution of damage and intacticity parameter with internal variable k_d for different values of β_d and for $\alpha_d = 1 \times 10^{-2}$. Figure 4-8c and Figure 4-8d show the same evolution but when α_d varies for a constant value of $\beta_d = 0.3$. Figure 4-9a shows intacticity parameter along with its derivative at null values of damage for different values of α_d and for $\beta_d = 0.3$. Figure 4-9b illustrates the same concept but for $\beta_d = 0$, clearly underlining the meaning of α_d .

The advantages of coupling damage with measures of plastic strains that develop after hardening saturation consist in the fact that the plastic yield surface becomes a real strength envelope, defining the peak of stress of the global model. While plastic hardening controls the

pre-peak behavior, damage controls the post-peak behavior, without overlaps. In model MS1, the damage evolution was controlled by the elastic energy function

$$Y_- = \frac{1}{2} D_{ijkl}^e \bar{\varepsilon}_{ij}^e \bar{\varepsilon}_{kl}^e, \quad (4.52)$$

obtained with the negative split of the elastic strain tensor

$$\bar{\varepsilon}_{ij}^e = \sum_{\alpha=1}^3 \langle \lambda_{\alpha} \rangle_- V_i^{\alpha} V_j^{\alpha}, \quad (4.53)$$

where λ_{α} and V_i^{α} are the eigenvalues and eigenvectors of the elastic strain tensor ε_{ij}^e , respectively, and $\langle * \rangle_-$ the negative Macaulay brackets. The damage evolution equation of model MS1 reads

$$d = h(k_d) = 1 - \exp \left[- \left(\frac{Y_-}{\alpha_d^{MS1}} \right)^{m_w} \right], \quad (4.54)$$

with α_d^{MS1} and m_w as model parameters. The substantial and important difference between the two models is that in model MS1 the damage formulation allowed damage evolution prior the peak of stress, whereas in model MS2 only plastic strains develop prior the peak of stress. The most important implication is that in model MS1 the combination of damage and plasticity yield criteria governed the strength envelope, while in model MS2 only plasticity formulated in the stress space controls the strength envelope, making it: (1) valid for wider range of loading conditions, (2) easier for the constitutive parameter to be calibrated and finally, (3) more flexible in the description of the strength of the material.

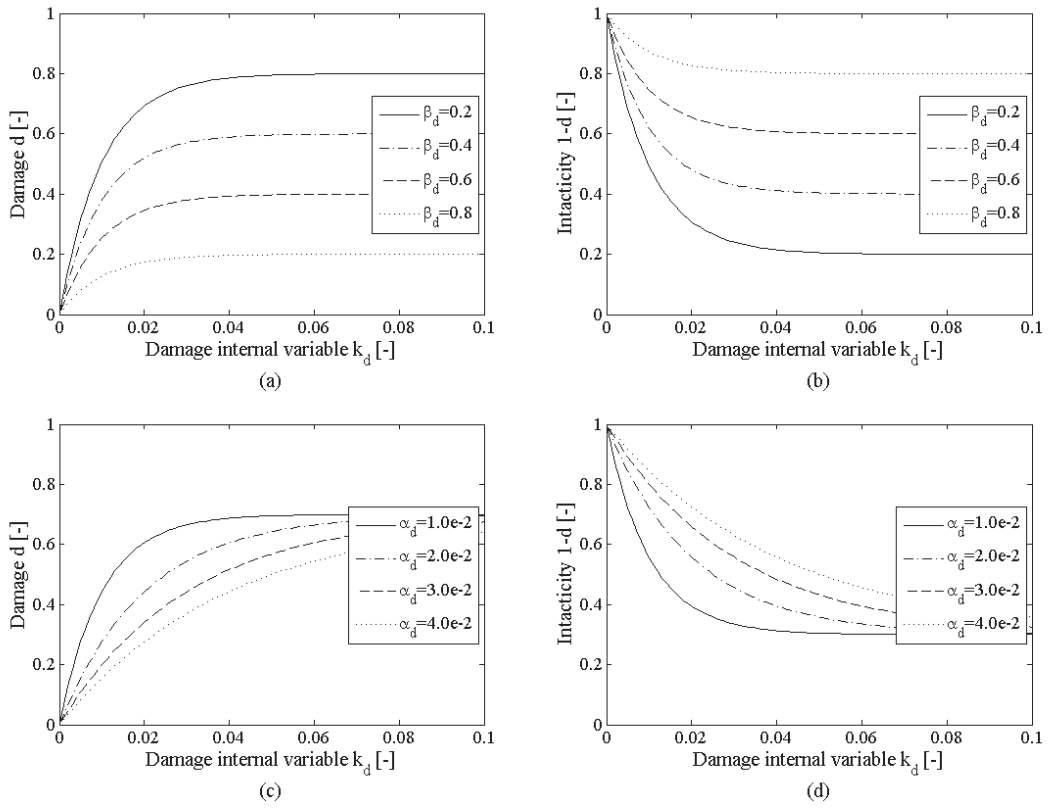


Figure 4-8: Evolution of damage (left) and equivalent intacticity parameter (right) for different values of damage parameters. (a) and (b) β_d varies for a fixed $\alpha_d=1e^{-2}$, while (c) and (d) $\beta_d=0.3$ is fixed and α_d varies.

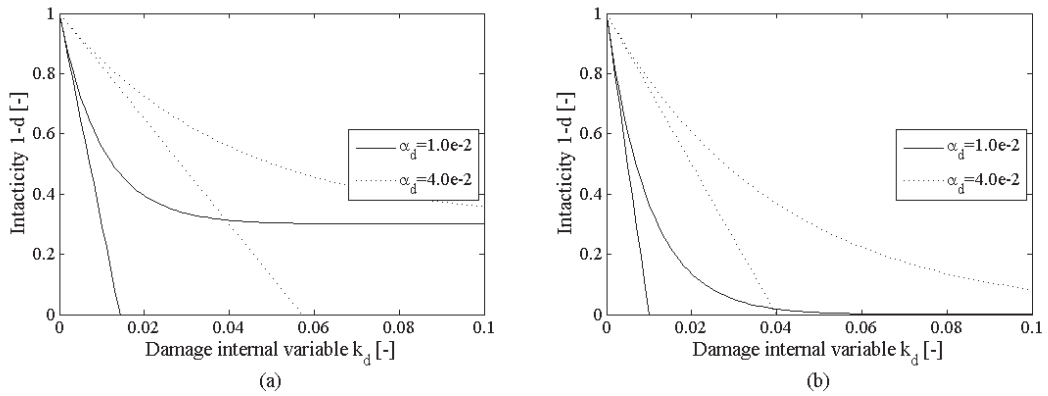


Figure 4-9: Evolution of intacticity parameter and slope of the softening curve at the initial point of the curve. (a) Parameter $\beta_d=0.3$ and (b) $\beta_d=0$.

4.5. Numerical integration

The proposed constitutive model is implemented within the Finite Element Method in the code *Code_Aster*, developed by Électricité de France (EDF) and distributed freely under a general public license. Further information on the code can be found at www.code-aster.com. The numerical implementation is performed with an implicit integration scheme to ensure stability, robustness and speed of the stress return algorithm ([D5.04.01]). The algorithm is based on the minimization of the residual vector of the plastic component of the model, defined as

$$R(\Delta y) = \begin{pmatrix} g(\Delta y) \\ l(\Delta y) \\ f(\Delta y) \end{pmatrix} = 0, \quad (4.55)$$

where the associated variables are

$$\Delta y = \begin{pmatrix} \Delta \tilde{\sigma} \\ \Delta va \\ \Delta p \end{pmatrix} = 0. \quad (4.56)$$

The first component of R contains the stress equations defined as

$$g(\Delta y) = \tilde{\sigma}_i^{n+1} - \tilde{\sigma}_i^n - E_{ij} \left(\varepsilon_j^{n+1} - \varepsilon_j^n - \lambda_p^{n+1} \partial_{\sigma_j} \mathbf{g}_p \right) = 0, \quad (4.57)$$

while the second components contain the rate equation of the internal variable for plasticity

$$k_p^{n+1} - k_p^n - \left\| \lambda_p^{n+1} \partial_{\sigma_j} \mathbf{g}_p \right\| = 0, \quad (4.58)$$

and the third component is relative to the plastic yield function and reads

$$f_p^{n+1} = 0. \quad (4.59)$$

The vector of the associated variables is defined as

$$\begin{aligned} \tilde{\sigma} &= \tilde{\sigma}_i^{n+1} \\ va &= k_p^{n+1} \\ p &= \lambda_p^{n+1} \end{aligned} \quad (4.60)$$

By differentiation, and assuming engineering notation instead of the tensorial one, we can express the rate equation of the residuals as

$$R(y_{n+1}^{m+1}) = R(y_{n+1}^m) + J_{n+1}^m (y_{n+1}^{m+1} - y_{n+1}^m), \quad (4.61)$$

where J_{n+1}^m is the Jacobian matrix that contains the derivatives of the residual vector with respect to the associated variables. In this case the Jacobian is computed by numerical

perturbation technique. Updated values of the associated variables can be computed by setting $R(y_{n+1}^{m+1}) = 0$ so that

$$y_{n+1}^{m+1} = y_{n+1}^m - (J_{n+1}^m)^{-1} R(y_{n+1}^m), \quad (4.62)$$

the process is iterated until the norm of the residual is smaller than a given tolerance

$$\|R(y_{n+1}^{m+1})\| = \sqrt{\sum_{i=1}^{nres} [R_i(y_{n+1}^{m+1})]^2} \leq \theta_{tol}, \quad (4.63)$$

and the solution y_{n+1}^{m+1} is obtained. The advantage of formulating plasticity in the damage effective stress space is that the damage variable can be computed explicitly, after the plastic return algorithm has reached convergence.

4.6. Example of the calibration procedure

The meaning of the plastic and damage parameters was thoroughly illustrated and their calibration is somehow straight forward. In the following, an example of calibration of plastic and damage parameters on LaBiche Shale from Wong (1998) is shown. The complete knowledge of the stress and strain in a triaxial configuration is necessary to calibrate the model. LaBiche shale is an outcrop from Canada and drained triaxial tests at different confinements were reported in the work of Wong (1998). Figure 4-10a shows the experimental results in terms deviatoric stress as function of vertical strain and Figure 4-10b in terms volumetric strain as function vertical strain.

The calibration of the plastic yield surface parameters α , β , γ , δ and r_{ha0} can be retrieved if the state of stress at the onset of plasticity and at the stress peak is known. The onset of plasticity is not always trivial to detect. Ideally acoustic measurements could constitute a valuable mean of doing so, as the onset of acoustic emissions usually coincides with the beginning of inelastic strains (Lemaitre et al, 2009). Alternatively, loading-unloading cycles before the peak of stress could highlight the accumulation of permanent inelastic strains in the elastic unloading phase. Unfortunately, these measurements are not always available, and shall this be the case, the onset of plasticity can be determined as the deviation from linearity of the behavior in the stress-strain space. The peak of stress, on the contrary, is usually trivial to determine for softening and brittle materials.

Three triaxial tests are necessary to calibrate the initial yield surface, given the fact that is a second degree function with three parameters. In cases where only two tests are available, only a linear yield function could be use. In Figure 4-10a the points of the plastic onset and the ones of the final failure (peak stress) are shown respectively in green and red.

4.6 Example of the calibration procedure

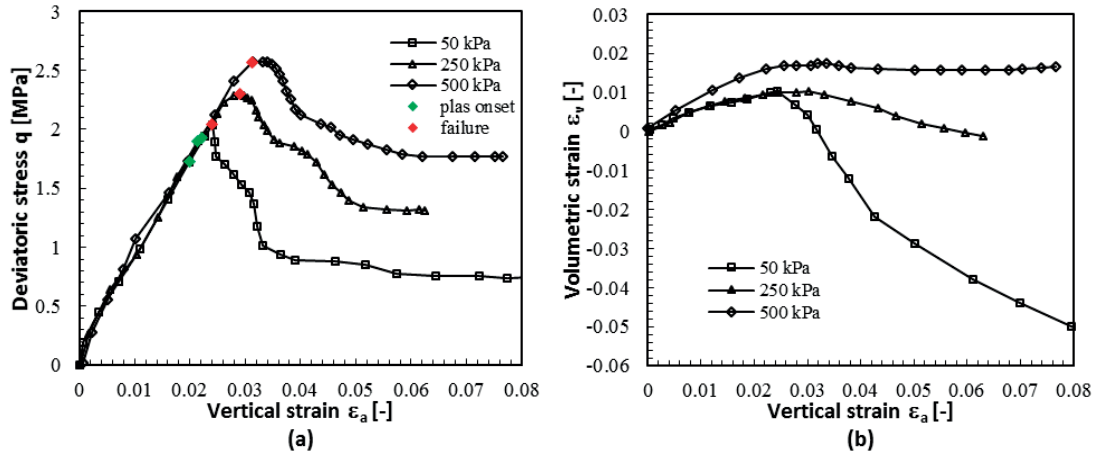


Figure 4-10: Vertical strain as a function of deviatoric stress for LaBiche shale at three different confining pressures (a). In red the final failure points and in green the plastic onset. Data digitalized from the work of Wong (1998); Vertical strain as a function volumetric strain for LaBiche shale at three different confining pressures (b). Data digitalized from the work of Wong (1998).

From the state of stress at the onset of plasticity it is possible to calibrate the initial yield surface with a quadratic interpolation of the data in the (p, q) plane. In Figure 4-11 it is shown such interpolation with the coefficient of the second degree polynomial of the form

$$q = a_{pol} \tilde{p}^2 + b_{pol} \tilde{p} + c_{pol} . \quad (4.64)$$

The same procedure applies for the final yield surface, which is interpolated with a linear function representing cohesive-frictional failure conditions as

$$q = d_{pol} \tilde{p} + e_{pol} . \quad (4.65)$$

From these interpolations it is then possible to retrieve the parameters of the plastic yield surface by simply applying the following conversion formulae

$$\begin{aligned} \beta &= d_{pol} \\ \gamma &= e_{pol} \\ r_{ha0} &= c_{pol} / \gamma \\ \alpha &= a_{pol} / (1 - r_{ha0}) \\ \delta &= (b_{pol} / \beta - r_{ha0}) / (1 - r_{ha0}) \end{aligned} , \quad (4.66)$$

which in the given case yields to

$$\begin{aligned}
 \beta &= d_{pol} = 0.845 \\
 \gamma &= e_{pol} = 1431.0 \text{ kPa} \\
 r_{ha0} &= c_{pol} / \gamma = 0.447 \\
 \alpha &= a_{pol} / (1 - r_{ha0}) = -0.0021 \text{ kPa}^{-1} \\
 \delta &= (b_{pol} / \beta - r_{ha0}) / (1 - r_{ha0}) = 4.480
 \end{aligned}
 \tag{4.67}$$

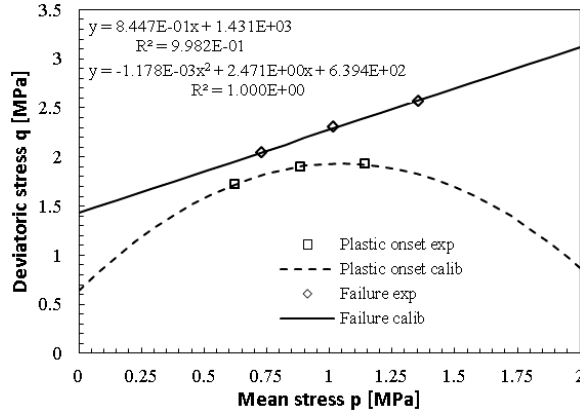


Figure 4-11: Calibration of initial and final yield surface in mean effective stress vs deviatoric effective stress space for LaBiche shale.

The calibration of the plastic compressibility parameter χ_h in equation (4.29) is done by computing the norm of the plastic strain between the onset of plasticity and the peak conditions. In the present case, an approximated solution (not all the components of strain are known for a given point, since the data was retrieved manually from figures, so only vertical strains components were used) yields $\chi_h = 7 \times 10^{-3}$, where χ_h was calibrated separately for each test and then averaged.

The calibration of damage can be achieved by non-linear regression of the damage function given in equation (4.46). As damage represents softening, experimental values of d can be computed as

$$d = 1 - \frac{\sigma_M}{\sigma}, \tag{4.68}$$

where σ_M is the maximum value of stress (i.e., stress at peak), while k_d can be computed, once the plastic strain are known, with equations (4.43), (4.44) and (4.45).

Usually damage evolution depends on the confinement, and while some shale exhibit lower values of the softening rate with increasing mean stress (less brittle behavior), some other examples seem to maintain the same rate of softening (Corkum and Martin, 2007). In the

present formulation no dependency of the brittleness on the mean stress was used, mainly to avoid over-complication, but also due to the fact that not all shales exhibit the same trend of brittleness with confinement. In the present case, for LaBiche shale the calibration of the damage law was based on the values of softening at 50 kPa of confinement. Figure 4-12 shows the result of this process, which yields $\alpha_d = 8.3 \times 10^{-3}$ and $\beta_d = 0.368$.

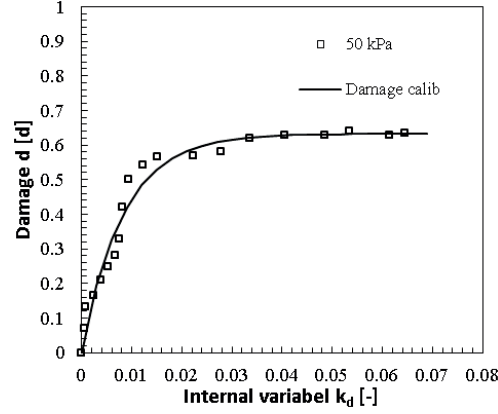


Figure 4-12: Calibration damage parameters for LaBiche shale: calibration is done with non-linear regression on the data relative to test at 50 kPa of confinement pressure.

For the calibration of the non-associated parameter at peak, the non-associated plastic potential reads

$$g_p = \tilde{q} - [(1 - s_h) \beta \tilde{p} + \gamma], \quad (4.69)$$

and in principal frame of reference the volumetric plastic strain increment writes

$$\dot{\epsilon}_v^p = \dot{\epsilon}_{11}^p + \dot{\epsilon}_{22}^p + \dot{\epsilon}_{33}^p, \quad (4.70)$$

and the deviatoric plastic strain increment as

$$\dot{\epsilon}_d^p = \frac{1}{3} \sqrt{(\dot{\epsilon}_{11}^p - \dot{\epsilon}_{22}^p)^2 + (\dot{\epsilon}_{33}^p - \dot{\epsilon}_{22}^p)^2 + (\dot{\epsilon}_{11}^p - \dot{\epsilon}_{33}^p)^2}. \quad (4.71)$$

The equation of the evolution of plastic strain reads

$$\dot{\epsilon}_{ij}^p = \dot{\lambda}^p \frac{\partial g^p}{\partial \tilde{\sigma}_{ij}}, \quad (4.72)$$

and by simple algebra, we can obtain the values for plastic deviatoric and volumetric strain increment during the softening phase (i.e., when damage activates and plastic saturation is reached)

$$\begin{aligned} \dot{\epsilon}_v^p &= \beta (s_h - 1) \\ \dot{\epsilon}_d^p &= \frac{1}{\sqrt{2}} \end{aligned} \quad (4.73)$$

The slope of the curve in the plastic deviatoric as a function of the plastic volumetric strain plot is defined as

$$m_s = \frac{\dot{\epsilon}_v^p}{\dot{\epsilon}_d^p} = \sqrt{2} \beta (s_h - 1). \quad (4.74)$$

so that m_s can be computed as the ratio between volumetric and deviatoric plastic strain increment at each point, β is known and the evolution of s_h can be computed along with k_{ps} . A non-linear regression can then be performed on equation (4.37) to find the value of parameter ψ_h . In the current Chapter, such a procedure was applied for all confinement pressures to find ψ_h , while its final value for analysis was obtained by averaging and yields $\psi_h = 0.19$. Figure 4-13 shows the results of this procedure for the three different confinements.

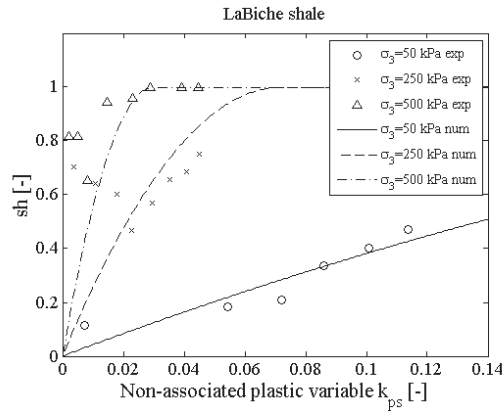


Figure 4-13: Calibration of dilatancy parameter for LaBiche shale: calibration is done with non-linear regression on the data relative to test at 50, 250 and 500 kPa of confinement pressure.

4.7. Validation of the constitutive behavior against experimental findings

4.7.1. Mechanical behavior

Based on the calibration procedure for LaBiche Shale illustrated in section 4.6, the 11 parameters of the proposed model were retrieved and are illustrated in Table 4-1.

4.7 Validation of the constitutive behavior against experimental findings

Table 4-1: Set of parameters used for the simulation of triaxial tests on LaBiche shale.

Parameter	Values	Units
E	95000	kPa
ν	0.25	-
α	$-2.2e^{-3}$	kPa ⁻¹
β	0.845	-
γ	1431	kPa
δ	4.48	-
r_{ha0}	0.44	-
χ_h	$7.0e^{-3}$	-
ψ_h	$1.9e^{-1}$	-
α_d	$8.3e^{-3}$	-
β_d	0.368	-

The numerical simulations performed are purely mechanical conventional triaxial compression tests, and are performed by firstly applying a confining pressure in isotropic conditions on a 3D quadratic single element square model, and then, by imposing the shear phase by applying a vertical displacement in compression until residual post-peak conditions are reached. Experimental tests are conducted in specimens with drained conditions, so that the stresses can be representative of effective stress conditions. Figure 4-14 compares experimental and numerical results for three different initial confining pressures, which are maintained constant during the shearing phase. The experimental results in the stress strain space are in good agreement with the numerical computation using the proposed model. The main features of the deformative behavior are correctly predicted. A slight discrepancy is observed in the post-peak phase at increasing confinement: this is mainly due to the assumption that damage evolution law, which controls the softening, does not depend on mean pressure. This is particularly true for certain shales and in a given range of mean stress, although for LaBiche a slight decrease of brittleness is observed at higher confinements. Concerning the volumetric behavior, since the parameter that controls the evolution of dilatancy was calibrated on an average of the three confining stresses, a higher discrepancy is observed at the confinement of 50 kPa while good agreement between experiments and simulation is observed at 250 and 500 kPa. Once again, a non-linear non-associated plastic potential would yield better results. Given the scarcity of highly reliable volumetric measurements on shale, and the difficulties of finding a unique trend, a linear plastic potential was postulated.

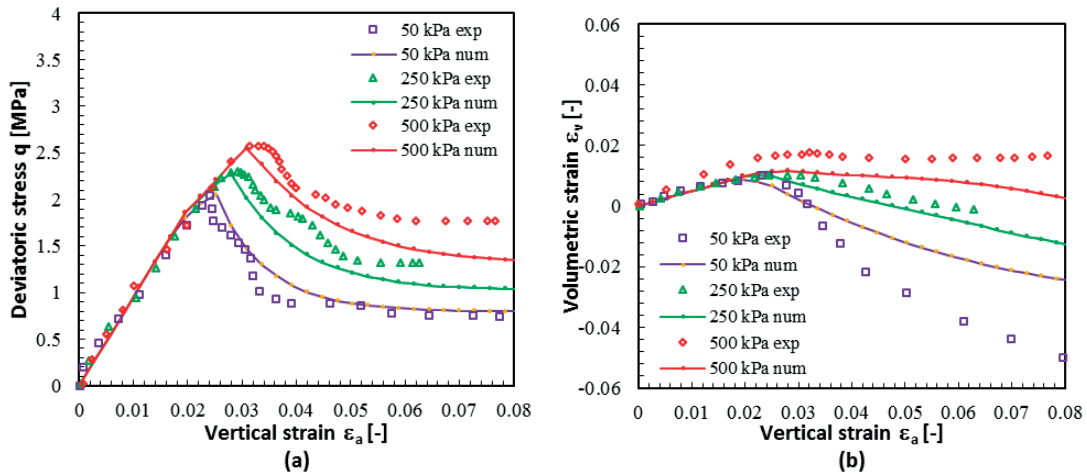


Figure 4-14: Comparison between numerical and experimental triaxial tests LaBiche shale in (a) the deviatoric stress vs axial strain space and (b) in the volumetric strain vs vertical strain space. Data retrieved from (Wong, 1998).

A further set of undrained triaxial compression tests, in water saturated conditions, and with different initial isotropic confining pressure, was used as a further validation example. These tests were performed by (Gräsle and Plischke, 2011) on Opalinus Clay from the Mont Terri site, Switzerland, although no volumetric strain and pore water pressure data are available. Therefore, the validation is once again purely mechanical, while the state of stress can be interpreted as representative of total stress conditions. Table 4-2 shows the values of the parameters calibrated for this set of data. The calibration procedure that was followed is analogous to the one exposed for LaBiche shale and thus, it will not be explained in details. Comparison between results from the numerical analyses and the experimental data are shown in Figure 4-15. Good agreement is observed between numerical predictions and experimental data. The linear elastic phase, followed by plastic hardening, is correctly reproduced until the peak of stress is reached. Assuming a linear yield surface for peak conditions proved to be a correct choice for the material under investigation, and the stress dependency is correctly reproduced. Post-peak softening is accounted with a damage evolution law that yields to final residual conditions where the deviatoric stress remains constant. Unloading in the post-peak phase at confinement of 3 MPa shows how the degradation of elasticity between experimental and numerical results coincide. A slight discrepancy can be observed at 10 MPa confinement. Globally the proposed constitutive model shows its ability to reproduce the experimental behavior of Opalinus Clay.

4.7 Validation of the constitutive behavior against experimental findings

Table 4-2: Set of parameters used for the simulation of undrained triaxial tests on Opalinus Clay from the Mont Terri site.

Parameter	Values	Units
E	14000	MPa
ν	0.3	-
α	$-7.45e^{-2}$	MPa^{-1}
β	1.43	-
γ	10.63	MPa
δ	1.765	-
r_{ha0}	0.416	-
χ_h	$4.0e^{-3}$	-
ψ_h	$4.0e^3$	-
α_d	$2.0e^{-3}$	-
β_d	0.3	-

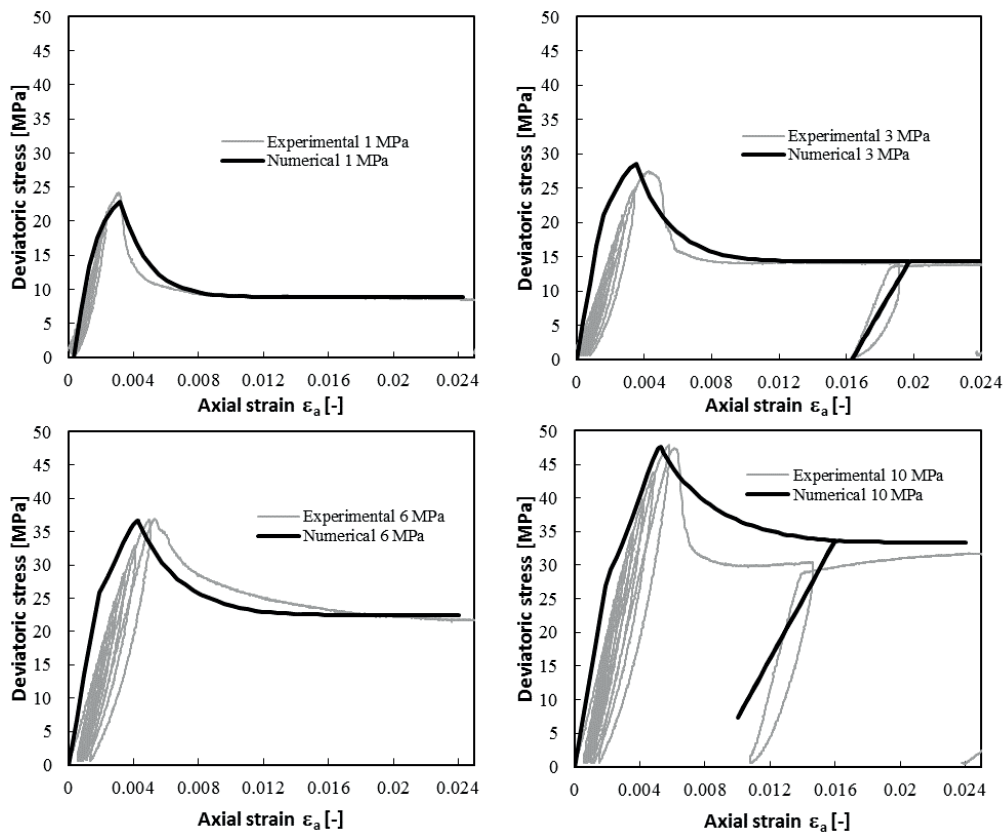


Figure 4-15: Comparison between numerical and experimental undrained triaxial tests on Opalinus clay from Mont Terri site at different confining pressure and for sample with vertical bedding (i.e., bedding parallel to the direction of maximum principal stress). Data from Gräsle and Plischke (2011).

4.7.2. Hydro-mechanical undrained behavior

A third set of experimental tests is used to furtherly validate the model in coupled hydro-mechanical conditions. The formulation and equilibrium equations for the coupled problem were presented in section 4.3. The experimental results consist in a set of undrained triaxial tests on Opalinus Clay from the Schlattingen site, Switzerland, for which the evolution of pore pressure in the specimen is known (Jahns, 2013). The parameters are therefore calibrated on the hydraulic effective stress, while simulations are run with full hydro-mechanical couplings in ideally undrained conditions, i.e., no flow occurs in the specimen. An initial total confining pressure, along with initial pore water pressure, is applied to the material. It follows a shearing phase applied by vertical displacement increment, while confining stress is kept constant. Hydraulic boundaries are set as impermeable, so that the undrained shearing phase is simulated and a pore pressure increase is expected as a result of compression of the material. Ideally the pore pressure increase inside the specimen is homogeneous in space, so that no pore water flow is expected. Table 4-3 shows the values of the parameters used for the numerical simulations in coupled hydro-mechanical undrained conditions. Value of the Biot's coefficient was set to be 0.7, according to the suggestion given by Vilarrasa et al. (2015).

Table 4-3: Set of parameters used for the simulation of undrained triaxial tests on Opalinus Clay from Schlattingen site and calibrated on the known pore water effective stress.

Parameter	Values	Units
E	11000	MPa
ν	0.3	-
α	$-5.55e^{-3}$	MPa ⁻¹
β	1.41	-
γ	12.83	MPa
δ	0.961	-
r_{ha0}	0.853	-
χ_h	$4.87e^{-4}$	-
ψ_h	$1.0e^{-3}$	-
α_d	$6.0e^{-4}$	-
β_d	0.48	-
b	0.7	-

Figure 4-16 shows a good agreement for the three cases of different initial confining pressure and pore water pressure comparison between numerical and experimental results, in the case of hydro-mechanical coupled triaxial tests in undrained conditions. The comparison is made for the total vertical stress (purple), effective vertical stress (red) and evolution of induced pore water pressure in the specimen (green). Experimental results of the pore water pressure show a slight increase due to the compression in the pre-peak phase, followed by quasi-constant values in the post-peak. Numerical results can validate the choice of Biot's

coefficient $b = 0.7$, along with the values of the non-associated plastic parameter. In the post-peak phase, in order to limit excessive increase of the induced pore water pressure, dilatancy must reach null values within a certain range of strain. The global agreement between experimental and numerical results can lead to state that the proposed constitutive model, along with the hydro-mechanical formulation adopted in *Code_Aster*, can be successfully employed in coupled hydro-mechanical conditions.

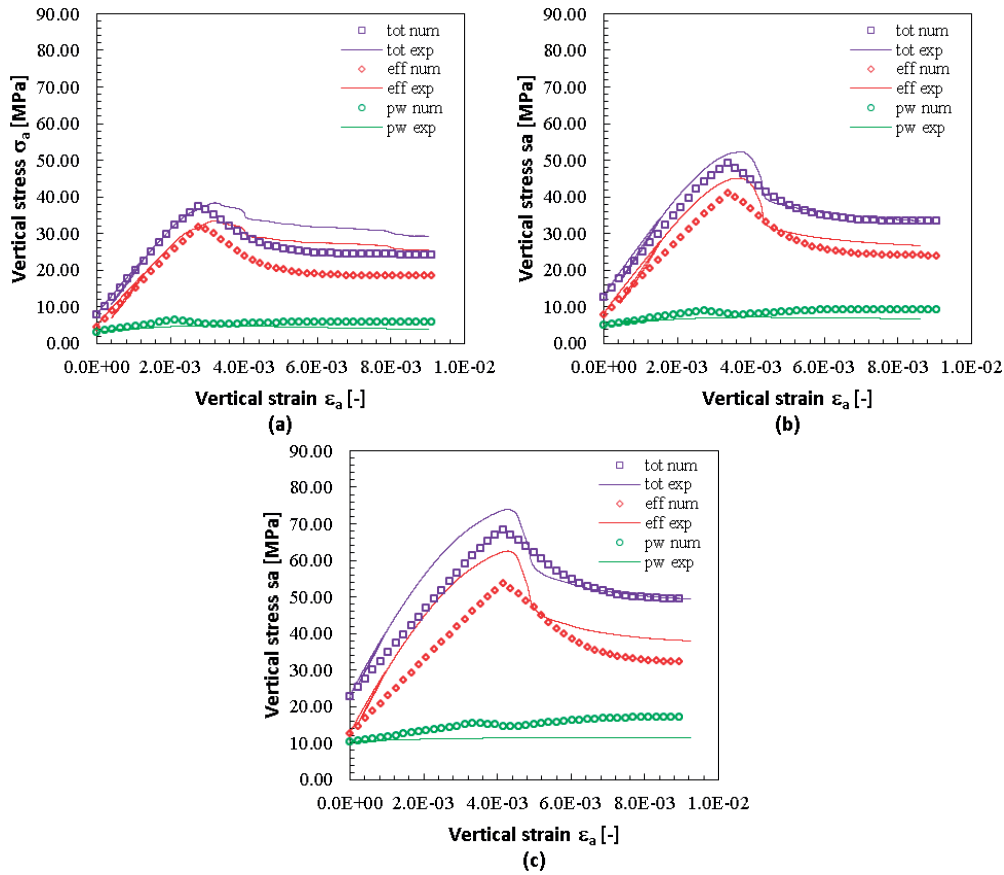


Figure 4-16: Comparison between numerical and experimental undrained triaxial tests on Opalinus clay from Shclattingen site at different confining pressure and for sample with vertical bedding (i.e. bedding parallel to the direction of maximum principal stress). The displayed curves refer to the vertical total stress (purple), the vertical effective stress (red) and pore water pressure evolution. Initial confinement is: (a) $\sigma_3=7.73$ MPa and $p_w=3.16$ MPa, (b) $\sigma_3=12.74$ MPa and $p_w=4.93$ MPa and (c) $\sigma_3=22.78$ MPa and $p_w=10.26$ MPa. Data from Jahns (2013).

4.8. Conclusions

A constitutive model coupling isotropic plasticity and damage theories was developed in the current work. Such a model is a direct extension and improvement of the model previously

developed in the work of Parisio et al. (2015). The initial non-linear second degree yield surface represents the onset of inelastic permanent strain, while during the process of plastic hardening the surface expands toward the cap and degenerates into a linear yield locus of the cohesive-frictional type. The model can account for true triaxial strength, i.e., more specifically on the dependency of the peak strength locus on Lode's angle. This topic will be furtherly expanded and treated in Chapter 5. A non-associated plastic potential formulation was proposed in order to avoid over estimation of dilatancy. The plastic model, formulated in the damage effective stress space, was coupled with an isotropic damage law of the exponential type that is responsible for the post-peak softening behavior along with the degradation of elastic properties. The calibration of the full set of material parameters was carefully illustrated for LaBiche shale, while numerical simulations of conventional triaxial compression tests were run and compared to experimental data. Global agreement in both dry and undrained conditions (total stress interpretation) showed how the formulated model, with all of its features, is suited to represent the mechanical behavior of shale. In order to test and validate the model in coupled hydro-mechanical conditions, a third set of triaxial tests, in undrained conditions for which the pore water pressure was known, was used. Good agreement between experiments and numerical predictions demonstrated how the model can successfully reproduce the hydro-mechanical behavior of shale.

4.9. Acknowledgements

The authors would like to acknowledge Swisstopo, ENSI and the Mont Terri Project for the financial support to this work. The authors would like also to thank Dr. Werner Gräsle from BGR, Germany, for providing the triaxial test data in the framework of the Mont Terri LT experiment and Dr. Silvio Geiger from NAGRA for providing data relative to Opalinus Clay at Schlattingen. Authors wish to thank EDF R&D for the assistance in the numerical implementation of the constitutive model in *Code_Aster*, and in particular Dr. Sylvie Granet, Dr. Roméo Fernandes, Dr. Sam Cuvilliez and Dr. Simon Raude.

4.10. References

- [D5.04.01], Introduire un nouveau comportement. Documentation version 12, Code_Aster, www.code-aster.org.
- Amann, F., Button E.A., Evans K.F., Gischig, V. S., Blümel, M., 2011. Experimental study of the brittle behavior of Clay shale in short-term unconfined compression. *Rock Mech Rock Eng* 44 (4), 415-430.
- Amann, F., Kaiser, P. K., Button E.A., 2012. Experimental study of the brittle behavior of Clay shale in rapid confined compression. *Rock Mech Rock Eng* 44 (1), 21-33.

- Amann, F., Martin, C. D., Wild, K. M., 2015. The role of capillary suction and dilatancy on the interpretation of the confined strength of clay shales. Montreal: ISRM Congress 2015 Proceedings- Int'l Symposium on Rock Mechanics, 8p.
- Abdi, H., Labrie, D., Nguyen, T.S., Barnichon, J.D., Su, G., Evgin, E., Simon, R., Fall, M., 2015. Laboratory investigation on the mechanical behaviour of Tournemire argillite. *Can Geotech J* 52, 268-282.
- Ambrose, J., 2014. Failure of Anisotropic Shales under Triaxial Stress Conditions. Ph.D. Thesis, Imperial College London.
- Baud, P., Schubnel, A., Wong, T.F., 2000. Dilatancy, compaction, and failure mode in Solnhofen limestone. *J Geophys Res-Sol Ea* 105, 19289-19303.
- Chazallon, C., Hicher, P.Y., 1998. A constitutive model coupling elastoplasticity and damage for cohesive-frictional materials. *Mech Cohes-Frict Mat* 3, 41-63.
- Chen, L., Shao, J.F., Huang, H.W., 2010. Coupled elastoplastic damage modeling of anisotropic rocks. *Comput Geotech* 37, 187-194.
- Chen, L., Shao, J.F., Zhu, Q.Z., Duveau, G., 2012. Induced anisotropic damage and plasticity in initially anisotropic sedimentary rocks. *Int J Rock Mech Min* 51, 13-23.
- Chiarelli, A.S., Shao, J.F., Hoteit, N., 2003. Modeling of elastoplastic damage behavior of a claystone. *Int J Plasticity* 19, 23-45.
- Corkum, A.G., Martin, C.D., 2007. The mechanical behaviour of weak mudstone (Opalinus Clay) at low stresses. *Int J Rock Mech Min* 44, 196-209.
- Einav, I., Houlsby, G.T., Nguyen, G.D., 2007. Coupled damage and plasticity models derived from energy and dissipation potentials. *Int J Solids Struct* 44, 2487-2508.
- Gräsle, W., Plischke, I., 2011. LT-A Experiment: Mechanical Behavior of Opalinus Clay, Data report from Phase 15. Mont Terri Technical Note TN 2010-86.
- Grassl, P., Jirásek, M., 2006. Damage-plastic model for concrete failure. *Int J Solids Struct* 43, 7166-7196.
- Haghighat, E., Pietruszczak, S., 2015. On modeling of discrete propagation of localized damage in cohesive-frictional materials. *Int J Num Analyt Meth Geomech* 39, 1774-1790.
- Horsrud, P., Sonstebo, E.F., Boe, R., 1998. Mechanical and petrophysical properties of north sea shales. *Int J Rock Mech Min* 35, 1009-1020.
- Hu, D., Zhou, H., Shao, J., 2013. An anisotropic damage-plasticity model for saturated quasi-brittle materials. *Int J Numer Anal Met* 37, 1691-1710.
- Imran, I., Pantazopoulou, S.J., 2001. Plasticity model for concrete under triaxial compression. *J Eng Mech-Asce* 127, 281-290.
- Jahns, E., 2013. Geomechanical laboratory tests on Opalinus Clay cores from the bore hole Schlattingen SLA-1. Nagra Work Report NAB.

- Jason, L., Huerta, A., Pijaudier-Cabot, G., Ghavamian, S., 2006. An elastic plastic damage formulation for concrete: Application to elementary tests and comparison with an isotropic damage model. *Comput Method Appl M* 195, 7077-7092.
- Jia, Y., Song, X.C., Duveau, G., Su, K., Shao, J.F., 2007. Elastoplastic damage modelling of argillite in partially saturated condition and application. *Phys Chem Earth* 32, 656-666.
- Josh, M., Esteban, L., Delle Piane, C., Sarout, J., Dewhurst, D., Clennell, M., 2012. Laboratory characterisation of shale properties. *J Petrol Sci Eng* 88, 107-124.
- Ju, J.W., 1989. On Energy-Based Coupled Elastoplastic Damage Theories - Constitutive Modeling and Computational Aspects. *Int J Solids Struct* 25, 803-833.
- Lee, J.H., Fenves, G.L., 1998. Plastic-damage model for cyclic loading of concrete structures. *J Eng Mech-Asce* 124, 892-900.
- Lemaitre, J., Chaboche, J., 1990. *Mechanics of solid materials*. Cambridge University Press, Cambridge.
- Lemaître, J., Desmorat, R., 2005. *Engineering damage mechanics : ductile, creep, fatigue and brittle failures*. Springer, Berlin ; New York.
- Maier, G., Hueckel, T., 1979. Nonassociated and Coupled Flow Rules of Elastoplasticity for Rock-Like Materials. *Int J Rock Mech Min* 16, 77-92.
- Makhnenko, R.Y., Labuz, J.F., 2015. Dilatant hardening of fluid-saturated sandstone. *J Geophys Res-Sol Ea* 120, 909-922.
- Marigo, J., 1981. Formulation d'une loi d'endommagement d'un matériau élastique. *CR Acad. Sci. Paris II* 292, 1309-1312.
- McLamore, R., Gray, K., 1967. A strength criterion for anisotropic rocks based upon experimental observations, Annual Meeting of the American Institute of Mining, Metallurgical, and Petroleum Engineers. Society of Petroleum Engineers.
- Nauroy, J.-F., 2011. *Geomechanics applied to the petroleum industry*. Editions Technip.
- Niandou, H., Shao, J.F., Henry, J.P., Fourmaintraux, D., 1997. Laboratory investigation of the behaviour of Tournemire shale. *Int J Rock Mech Min* 34, 3-16.
- Ortiz, M., 1985. A Constitutive Theory for the Inelastic Behavior of Concrete. *Mech Mater* 4, 67-93.
- Pariso, F., Samat, S., Laloui, L., 2015. Constitutive analysis of shale: a coupled damage plasticity approach. *Int J Solids Struct* 75-76, 88-98.
- Plassart, R., Fernandes, R., Giraud, A., Hoxha, D., Laigle, F., 2013. Hydromechanical modelling of an excavation in an underground research laboratory with an elastoviscoplastic behaviour law and regularization by second gradient of dilation. *Int J Rock Mech Min* 58, 23-33.

- Popp, T., Salzer, K., 2007. Anisotropy of seismic and mechanical properties of Opalinus clay during triaxial deformation in a multi-anvil apparatus. *Phys Chem Earth* 32, 879-888.
- Popp, T., Salzer, K., Minkley, W., 2008. Influence of bedding planes to EDZ-evolution and the coupled HM properties of Opalinus Clay. *Phys Chem Earth* 33, S374-S387.
- Puzrin, A., 2012. Constitutive modelling in geomechanics: introduction. Springer Science & Business Media.
- Renner, J., Rummel, F., 1996. The effect of experimental and microstructural parameters on the transition from brittle failure to cataclastic flow of carbonate rocks. *Tectonophysics* 258, 151-169.
- Rousset, G., 1988. Comportement mécanique des argiles profondes.
- Rudnicki, J.W., Rice, J.R., 1975. Conditions for Localization of Deformation in Pressure-Sensitive Dilatant Materials. *J Mech Phys Solids* 23, 371-394.
- Rybacki, E., Reinicke, A., Meier, T., Makasi, M., Dresen, G., 2015. What controls the mechanical properties of shale rocks? - Part I: Strength and Young's modulus. *J Petrol Sci Eng* 135, 702-722.
- Salari, M.R., Saeb, S., Willam, K.J., Patchet, S.J., Carrasco, R.C., 2004. A coupled elastoplastic damage model for geomaterials. *Comput Method Appl M* 193, 2625-2643.
- Sarout, J., Molez, L., Guéguen, Y., Hoteit, N., 2007. Shale dynamic properties and anisotropy under triaxial loading: experimental and theoretical investigations. *Physics and Chemistry of the Earth, Parts A/B/C* 32, 896-906.
- Shao, J.F., Jia, Y., Kondo, D., Chiarelli, A.S., 2006. A coupled elastoplastic damage model for semi-brittle materials and extension to unsaturated conditions. *Mech Mater* 38, 218-232.
- Simo, J., Hughes, T., 1998. *Computational inelasticity*. Springer, New York.
- Van Eekelen, H., 1980. Isotropic yield surfaces in three dimensions for use in soil mechanics. *Int J Numer Anal Met* 4, 89-101.
- Vardoulakis, I., Sulem, J., 1995. *Bifurcation analysis in geomechanics*. Chapman & Hall. Chapman & Hall, Glasgow.
- Vilarrasa, V., Carrera, J., Olivella, S., 2013. Hydromechanical characterization of CO₂ injection sites. *International Journal of Greenhouse Gas Control* 19, 665-677.
- Vilarrasa, V., Makhnenko, R., Laloui, L., 2015. Influence of Poromechanical and Thermal Properties of the Caprock on the Safety of CO₂ Storage, Second EAGE Workshop on Geomechanics and Energy.
- Wong, R., 1998. Swelling and softening behaviour of La Biche shale. *Can Geotech J* 35, 206-221.

Wong, T.F., Baud, P., 2012. The brittle-ductile transition in porous rock: A review. *J Struct Geol* 44, 25-53.

5. A generalized failure surface for the strength of geomaterials accounting for intrinsic anisotropy and true triaxial conditions

Authors: F. Parisio and L. Laloui.

Status: to be submitted to International Journal of Rock Mechanics and Mining Science.

Contributions: The literature review, data collection, model developments, comparative study, result interpretation and the manuscript writing were carried out by F. Parisio. L. Laloui overviewed the contribution, edited the text and is the senior responsible author (SRA) of the publication.

Abstract

The proposed plastic yield surface of model MS2 takes into account the true triaxial nature of the strength of geomaterials, commonly known as Lode's angle dependency of strength, which is here investigated. Additionally, as focus of this work is placed on the constitutive and numerical modeling of shale, it appeared clear the necessity of including a description of intrinsic anisotropy in the failure surface. This second peculiarity is included with a formulation of mixed invariants of the stress and fabric tensors. Both extensions share the same philosophy as they can be applied to simpler failure surfaces, allowing great flexibility in model formulation. The new failure surface is called model MS3 and is tested against experimental data regarding both true triaxial and anisotropic strength separately. Two parallel comparative studies are then carried out, and the performance of MS3 failure surface is compared with the one of classical failure criteria for true triaxial and intrinsic anisotropy of geomaterials. Results demonstrate the consistency of the proposed model MS3, which can be regarded as a generalized failure criterion for geomaterials. Finally, everything is inserted into the deformation description of model MS3, so that the updated failure surface is included in the coupled plastic-damage framework of model MS3.

Keywords: modified Van Eekelen, intrinsic anisotropic geomaterials, fabric tensor anisotropy, true triaxial conditions.

5.1. Introduction

In the isotropic coupled plastic-damage model MS2 presented in Chapter 4, the plastic yield function after the hardening phase represents the strength envelope of the material and will be referred here as the failure surface. Since the goal is to model quasi-brittle geomaterials, failure is here intended as the maximum stress reached during deformation before the brittle-softening phase takes place. The failure surface was formulated in terms of two invariants of the damage effective stress tensor in the $p-q$ plane. Therefore, its shape in the octahedral plane is circular. To have a more realistic mechanical description of the strength envelope that better agrees with experimental findings, the failure surface is extended by introducing a dependency on a third invariants of stress, Lode's angle, and having therefore a non-circular shape in the octahedral plane. This is achieved with a modified Van Eekelen formulation (Van Eekelen, 1980). Furthermore, as the model was specifically developed to describe the

mechanical behavior of shale, an extension to include intrinsic anisotropy is also carried out by introducing a scalar variable that depends on the invariants of stress and fabric tensors following the work of Pietruszczak and Mroz (2000, 2001). The goal is therefore to extend the strength envelope of the constitutive model MS2 to account for true triaxial and anisotropic conditions. Focus will be placed solely on the failure surface, which will be modified to account for the over-mentioned phenomena. Plastic hardening equations and plastic potential surface will not be modified, as well as the isotropic damage model and its coupling with plasticity, which will also be kept in the damage effective stress space.

In order to validate both the true triaxial and anisotropic extension, a comparison with other formulations and with different materials was carried out. To do so, the triaxial extension was tested by using the results from the work of Colmenares and Zoback (2002), and recent results from the work of Ambrose (2014) were used to test the anisotropic extension. More specifically, in the work of Colmenares and Zoback (2002), experimental results of true triaxial strength of 5 different geomaterials from literature are reported. Different failure criteria common in geomechanics are then calibrated with respect to the experimental data, and their failure stress predictions are compared with experiments to assess the performance of the failure criteria. In a similar spirit, in Ambrose (2014) a series of experimental results on the anisotropic strength of several shales and schists are reported, along with original data on two additional sedimentary shales. Once again, the experimental results are used to test the performances of two common anisotropic yield criteria. In the present work the performance of the proposed formulation is tested by adding to the works of Colmenares and Zoback (2002) and Ambrose (2014) the results from proposed failure criterion, so that it can be compared with other formulations against extensive experimental results. In addition, for the anisotropic validation, data on Opalinus Clay was added to the experimental set. The performance of all of the models is measured in terms of normalized errors (Normalized Root Mean Square Error), so that different data set can be compared as well with each other.

5.2. True triaxial behavior of geomaterials

Since the late 60's research on the mechanical behavior of geomaterials has highlighted the dependency of strength on stress paths in the octahedral plane, i.e., for combinations of principal stresses that fall out of the conventional triaxial compression set up. In the octahedral section, the failure envelope of soils and rocks is generally non circular and resembles a smooth triangle, as experimental evidence show for sandy soils (Lade and Duncan, 1975a) and clayey soils (Lade and Musante, 1978), while for rocks this was evidenced, e.g., in the works of Handin et al. (1967) and Mogi (1971a, 1972, 1973) and for concrete by Chinn and Zimmerman (1965), Kupfer et al. (1969) and Mills and Zimmerman

(1970). Figure 5-1 shows from experimental results of Solenhofen Limestone (Handin et al., 1967) that strength is lower in extension than in compression.

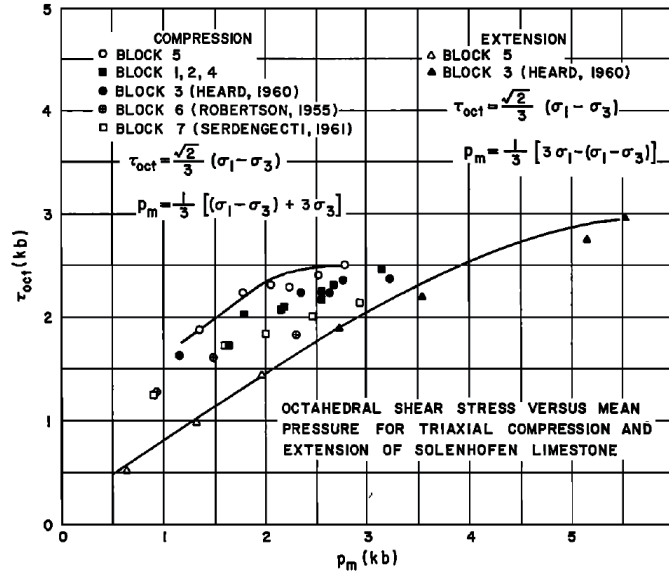


Figure 5-1: Experimental behavior from Solenhofen Limestone (Figure from: Handin et al (1967)). It can be seen how the shear strength in triaxial compression conditions is higher than in triaxial extension conditions.

In rock mechanics literature, this is often referred to as strength dependence on the intermediate principal stress, as some of the most common yield criteria like Mohr-Coulomb and Hoek-Brown, are formulated as functions of maximum and minimum principal stresses. On the other hand, in soil mechanics, but also for concrete, true triaxial conditions are often referred to as strength dependency on Lode's angle. This could originate from the fact that yield criteria like Drucker-Prager and Von Mises were common in both disciplines. Some clarifications on these aspects are necessary.

First, we define the three invariants of stress, starting from the first invariant as

$$I_1 = \sigma_{ii} . \tag{5.1}$$

The second reads

$$J_2 = \frac{1}{2} s_{ij} s_{ij} , \tag{5.2}$$

and the third

$$J_3 = \det s_{ij} , \tag{5.3}$$

where σ_{ij} is stress tensor and s_{ij} is the deviatoric stress tensor defined as

$$s_{ij} = \sigma_{ij} - \frac{I_1}{3} \delta_{kk}. \quad (5.4)$$

A first set of invariants that could be used is therefore (I_1, J_2, J_3) . Alternatively, the following three invariants of stress are more commonly used in geomechanics

$$\begin{aligned} p &= \frac{I_1}{3} \\ q &= \sqrt{3J_2} \\ \theta &= \frac{1}{3} \arcsin \left[\frac{3\sqrt{3}}{2} \left(\frac{J_3}{J_2^{3/2}} \right) \right] \end{aligned}, \quad (5.5)$$

where p is the mean stress, q is the deviatoric stress and θ is Lode's angle. In the current definition of Lode's angle $\theta = 30^\circ$ represents triaxial compression conditions and $\theta = -30^\circ$ indicates triaxial extension conditions. Figure 5-2 shows the graphical representation of stress invariants. Von Mises plasticity (Mises, 1913) is formulated in terms of the second stress invariant J_2 and represents shear failure conditions that are independent of mean pressure (purely cohesive behavior), while Drucker-Prager yield criterion (Drucker and Prager, 1952) extends Von Mises plasticity by introducing dependence on the first invariant of stress I_1 , i.e., mean stress dependency of shear strength (cohesive-frictional behavior). Both criteria, formulated in terms of stress invariants, depend on the three principal stress components. In the octahedral plane projection, they have circular shapes, which implies no dependency of strength on Lode's angle and strength in triaxial compression is equal to the one in triaxial extension conditions.

Mohr-Coulomb failure criterion relates failure conditions of pressure sensitive granular material to the shear stress acting on the failure plane and implicitly does not depend on the intermediate principal stress σ_2 . Hoek-Brown failure function (Hoek and Brown, 1980) is a non-linear criterion for which failure conditions also do not depend on the intermediate principal stress, but only on the maximum and minimum principal stresses.

Both Mohr-Coulomb and Hoek-Brown failure criteria projection in the octahedral plane is non-circular, i.e., the predicted strength in triaxial compression is greater than the one in triaxial extension, which relates more closely to the experimental behavior observed in geomaterials. On the other hand, the shape in the octahedral plane cannot be controlled and results as a direct consequence of the formulation that depends on the maximum and minimum principal stresses. The confusion can arise from the fact that strength in some models formulated in terms of maximum and minimum principal stresses does not depend on the intermediate principal stress, but has a Lode's angle dependency. On the contrary, other

models formulated with first two invariants of stress, in which strength depends on all principal stress components, show no Lode's angle dependency but a dependency on the intermediate principal stress σ_2 . In conventional triaxial compression conditions, two components of the principal stress tensor are equal, tests with Lode's angles in extension can be simulated and part of the true triaxial behavior can still be retrieved. For those values of Lode's angle between pure compression and extension, it is necessary to control all three components of principal stress tensor, which should all be different from each other. This is referred to as strength dependency on the intermediate principal stress.

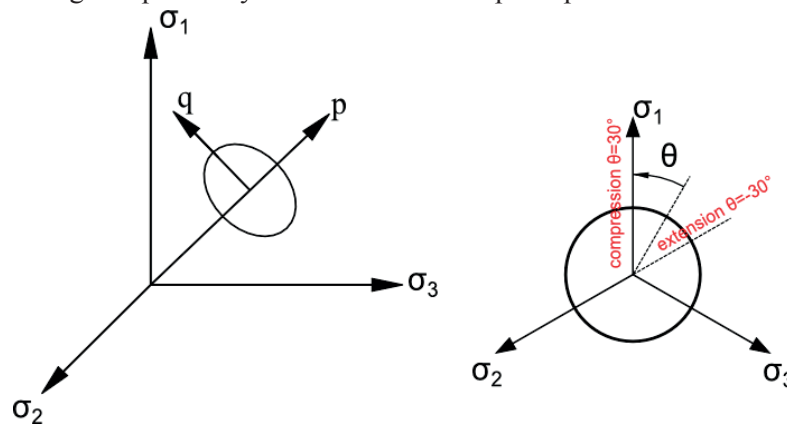


Figure 5-2: Schematic representation of the meaning of the three invariants of stress, in the principal stress space with the hydrostatic axis and deviatoric axis, and in the octahedral plane with the meaning of Lode's angle.

Modeling true triaxiality of strength envelope has been achieved in literature by the formulation of failure criteria that depend on a set of three independent invariants of stress that control the shape of the failure function in the three dimensional stress space. Some of these models have failure surfaces formulated for natural geomaterials (Argyris et al., 1974; Gudehus, 1973; Jiang and Pietruszczak, 1988; Lade and Duncan, 1975b; Matsuoka and Nakai, 1974; Van Eekelen, 1980; Wiebols and Cook, 1968; Zienkiewicz and Pande, 1977). More recently, Lee et al (2012) proposed an extension of the classical Mohr-Coulomb and Hoek-Brown criteria in the tri-dimensional stress space as smooth and convex surfaces. For failure criteria of concrete, one can refer to the work of Menetrey and Willam (1995), Ottosen (1977) and Willam and Warnke (1975).

In the current Chapter, the model MS2 formulated in Chapter 4 is extended to include non-circularity in the octahedral plane by a modified Van Eekelen formulation (Van Eekelen, 1980). The formulation is presented along with the meaning of material parameter controlling it. To validate the proposed formulation, a series of true triaxial tests performed in 5 different rocks is used for calibration, and the error associated is compared with the performance of 3 other failure criteria (Mohr-Coulomb, Hoek-Brown and modified Lade). Results demonstrate

how the proposed formulation can successfully capture the true triaxial behavior of different rocks.

5.3. Intrinsic anisotropic behavior of sedimentary geomaterials

As many shales and schists have a layered structure due to the sedimentation process, many of their physical properties are anisotropic. More specifically, the beddings are symmetry planes and shale can be regarded as a transversely isotropic material. In the present contribution, focus will be placed on the intrinsic transversely isotropic nature of the strength properties. An example of this characteristic is shown in Figure 5-3a, where data on the strength dependency in conventional triaxial compression conditions as a function of the weakness plane orientation is shown for Penrhyn slate (Attewell and Sandford, 1974). Figure 5-3b shows the dependency of deviatoric strength on the bedding inclination angle at different confining pressures for Anger schist (Duveau et al., 1998). It can be seen how the maximum strength is reached with the configuration of horizontal beddings, i.e., the bedding strike perpendicular to the direction of the maximum principal stress (vertical load in this case), while the minimum strength is reached for the configuration in which the beddings are inclined between 30° and 45° . It is worthwhile noticing that, for both materials, when beddings are parallel to the direction of the maximum principal stress, the strength is smaller than for perpendicular beddings. This is a particular feature that in other transversely isotropic shales is less pronounced, while for other shales like Opalinus Clay it can also be inverted (Gräsle and Plischke, 2010). The importance of including intrinsic anisotropy in the mechanical description of shale appears clear particularly for what concerns its strength, as in many applications that involve rock failure (e.g., tunnel excavation or borehole drilling) inelastic strains are usually one order of magnitude bigger than elastic ones.

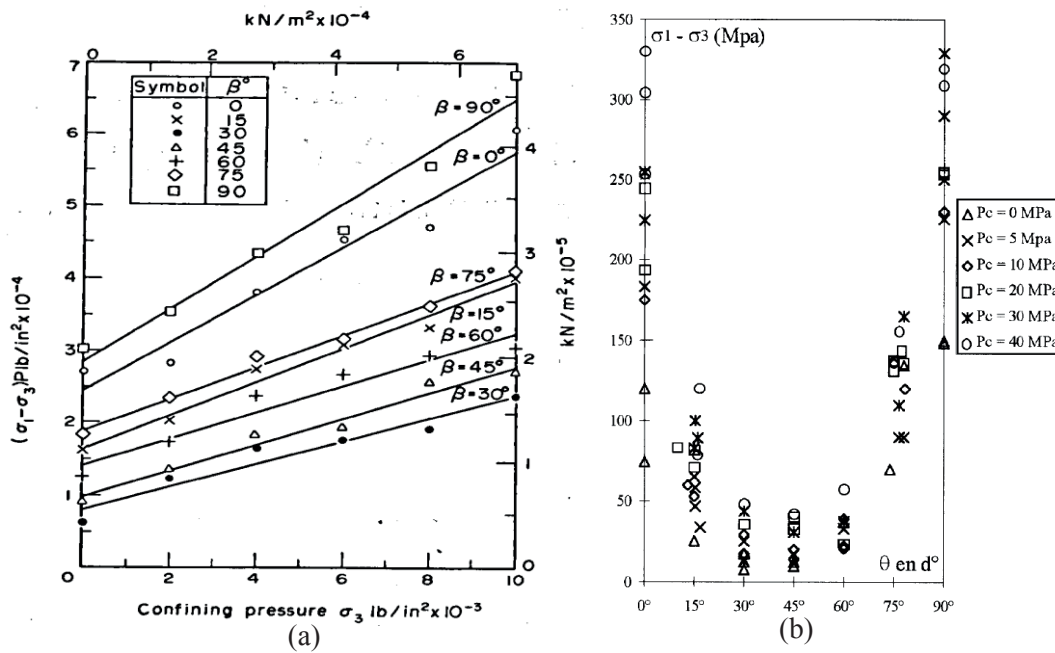


Figure 5-3: It is shown the dependency of the linear strength to confining pressure of Penrhyn slate at different angles of the weakness planes (a), where angles of 0° correspond to vertical beddings and 90° to horizontal ones (picture from Attewell and Sandford (1974)) and the deviatoric stress at failure in function of the bedding inclination (b) (0° vertical and 90° horizontal) and for different confining pressures of Anger schist (picture from Duveau et al. (1998)).

Within the framework of the constitutive model MS2, the plastic yield function at final conditions represents the maximum strength envelope of the material. In order to include anisotropy in the strength envelope, the failure criterion is therefore extended by employing the theory originally developed in Pietruszczak and Mroz (2000, 2001). Several anisotropic failure criteria for geomaterials were proposed in literature, and a good and extensive review can be found in the work of Duveau et al. (1998), where failure envelopes are classified into three main categories: mathematical continuous criteria, weakness plane criteria and empirical criteria.

Mathematical continuous criteria are formulated via a mathematical expression that infers a continuous variation of strength properties with the structural characteristics of anisotropy usually employing a description based on invariants of the stress and fabric tensors. They are sound in terms of frame invariance and particularly adapted to numerical simulations and tri-dimensional conditions, although they suffer shortcomings for those materials where the beddings are particularly weak compared to the matrix, and the degree of strength anisotropy is high. Among those criteria are included the early works of Hill (1950) for frictionless materials and Tsai and Wu (1971) for composites. The ones of Pariseau (1968) and Pietruszczak and Mroz (2000) are more specific for geomaterials.

Discontinuous yield criteria take into account the physical presence of bedding planes and can be seen as a special case of multi-mechanism plasticity, i.e., final failure of the material is the result of the lowest available resistance between intact rock matrix and directional failure along the discontinuity planes. Despite the sound description of the mechanics of failure, this family of criteria usually suffers from difficulties in tri-dimensional implementation and the abrupt transition from matrix to bedding failure does not fit well weakly anisotropic geomaterials. The Jaeger Weakness Plane criterion (Jaeger, 1960) and the Hoek criterion (Hoek, 1964) are two examples of discontinuous failure criteria.

Finally, empirical criteria provide a description of strength anisotropy which is based on empirical laws derived from laboratory results. Despite their simplicity, as reported in the conclusions of the comparative study carried out in Duveau et al. (1998), their physical meaning is not always clear and are often limited to bi-dimensional cases. For these reasons, they will not be furtherly discussed here.

The main goal of the present work is to extend the capabilities of model MS2 so that it can predict the strength of intrinsic anisotropic geomaterials. To model intrinsic anisotropic strength, the failure surface is extended by including a scalar variable that contains information on the material structure by using the framework proposed by Pietruszczak and Mroz (2000, 2001). The choice of such approach resides in the fact that it allows great flexibility in the model formulation, analogously to the modified Van Eekelen formulation for modeling true triaxial strength. This approach allows the formulation of a model in isotropic conditions that can be then extended to cover anisotropy, which is making this formulation to gain popularity among the geomechanics community (Chen et al., 2010; Le and Nguyen, 2014; Pardoen et al., 2015). The proposed formulation will be tested against 10 different sedimentary rocks and its performance compared to other two anisotropic failure criteria, as in the spirit of the comparative study carried out for true triaxial strength predictions. The two selected failure criteria for comparison are such that one belongs to the family of discontinuous model, i.e., the Jaeger weakness plane model (JWP), and the other one to the family of continuous mathematical criteria, i.e., the Pariseau model. Data on the failure of different intrinsic anisotropic shales are taken from the work of Ambrose (2014), along with the calibrated parameters for the two failure criteria used for comparison. Furthermore, Opalinus Clay strength results from Gräsle and Plischke (2010) are analyzed. The calibration of material parameters for the proposed formulation is carried out with a non-linear numerical fitting technique.

5.4. Van-Eekelen type formulation to model strength dependency on Lode's angle

The failure surface of the plastic model MS2, which represents a strength envelope, was formulated in terms of the first two invariants of the stress tensor as

$$f^p = q - f_{q-p}^p(p, r_{ha}). \quad (5.6)$$

Specifically, at peak stress conditions, where the yield surface represents the maximum strength of the material, equation (5.6) reads

$$f_p = q - (\beta p + \gamma), \quad (5.7)$$

which implies that the plastic yield surface is circular in the octahedral plane. In order to improve the formulation and to represent within the plastic failure surface the dependency of strength on true triaxial conditions, the formulation is extended as

$$f^p = q - f_{q-p}^p(p, r_{ha})r(\mathcal{G}), \quad (5.8)$$

where $r(\mathcal{G})$ is a function that describes the shape of the failure envelope in the octahedral plane and depends on Lode's angle \mathcal{G} . The maximum strength envelope is now described by

$$f_p = q - (\beta p + \gamma)r(\mathcal{G}). \quad (5.9)$$

This approach allows the separation between the failure criterion in the (p, q) plane and its shape in the octahedral plane, so that more flexibility can be achieved in the formulation of the failure criterion. Several formulations were proposed in the literature for the shape function $r(\mathcal{G})$, among which, for geomaterials, we highlighted the ones of Argyris et al. (1974), Chiarelli et al. (2003), Ottosen (1977), Van Eekelen (1980) and Willam and Warnke (1975). In the present contribution we propose a formulation directly derived from the original model proposed by Van Eekelen (1980). The original function was written as

$$r_l(\theta) = \alpha_\theta [1 - \beta_\theta \sin(3\theta)]^n, \quad (5.10)$$

where α_θ , β_θ and n as material parameters. In his original work, Van Eekelen suggested that parameter $n = -0.229$ for an optimized shape, while the condition $\alpha_\theta \geq 0$ must be satisfied at all times. The new formulation was obtained by imposing unity to equation (5.10) in triaxial compression conditions, i.e.,

$$r_l(\theta = 30^\circ) = \alpha_\theta (1 - \beta_\theta)^n = 1, \quad (5.11)$$

which leads to the following condition

$$\alpha_\theta = \frac{1}{(1 - \beta_\theta)^n}. \quad (5.12)$$

Thus, the proposed modified expression for Van Eekelen model in terms of second and third stress invariants reads

$$r_1(\theta) = \left(\frac{1 - \beta_\theta \frac{3\sqrt{3}}{2} \frac{J_3}{J_2^{3/2}}}{1 - \beta_\theta} \right)^{-0.229}, \quad (5.13)$$

so that the failure criterion in equation (5.9) becomes

$$f_p = q - (\beta p + \gamma) \left[\frac{1 - \beta_\theta \sin(3\theta)}{1 - \beta_\theta} \right]^{-0.229}. \quad (5.14)$$

This function is continuous and smooth in the octahedral plane, and convexity is ensured if the following condition is respected

$$|\beta_\theta| \leq \frac{1}{2} \left[\frac{4 + 13n}{(1+n)(1-9n^2)} \right]^{1/2} \quad \text{for} \quad -\frac{3}{11} \leq n \leq 0, \quad (5.15)$$

which, for the assumed value $n = -0.229$, leads to $|\beta_\theta| \leq 0.7925$ which satisfies as well $\alpha_\theta \geq 0$ for all possible values of β_θ , belonging to the interval $[0, 0.7925]$. Compared to the original formulation, the proposed one retains only one material parameter, β_θ , which controls the shape of the failure function in the octahedral plane. Figure 5-4 shows how the parameter β_θ controls the shape of the failure function in the octahedral plane. For $\beta_\theta = 0$, a circular shape is recovered, while to ensure convexity, its maximum value is $\beta_\theta = 0.7925$, which originates in the maximum difference between strength in triaxial compression and triaxial extension. Negative values of the shape parameter β_θ are theoretically possible, and will have the effect of rotating the surface and predicting higher values of strength in extension than in compression, always imposing unity of function $r(\mathcal{G})$ in triaxial compression. Despite evidence that some geomaterials exhibit higher friction angles in extension than in compression (Makhnenko and Labuz, 2014; Makhnenko et al., 2015), global deviatoric strength in extension is always smaller or equal to global strength on compression meridian and therefore, parameter β_θ should always be non-negative.

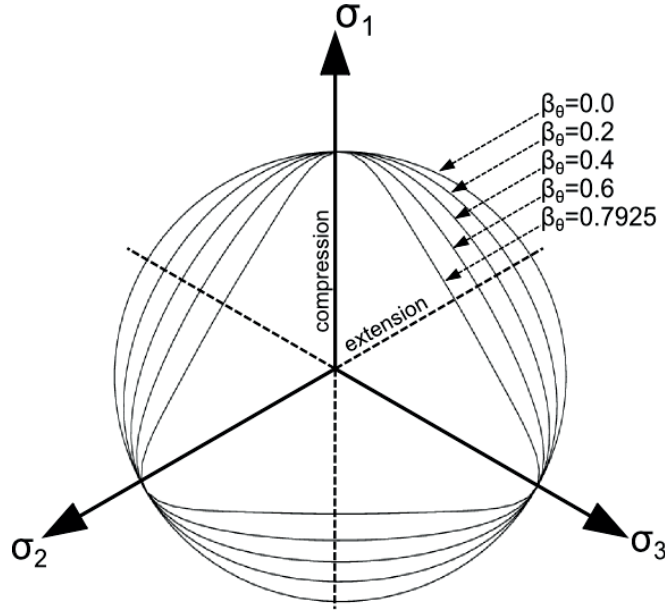


Figure 5-4: Influence of shape parameter β_θ on the shape of the yield function in the octahedral plane.

The proposed formulation of $r(\mathcal{G})$ can be well adapted to strain hardening plastic models, e.g., the one proposed of model MS2, in which the full hardening yield surface reads

$$f_p = q - \left\{ (1 - r_{ha}) \alpha p^2 + [(1 - \delta) r_{ha} + \delta] \beta p + r_{ha} \gamma \right\} \left(\frac{1 - \beta_\theta \frac{3\sqrt{3}}{2} \frac{J_3}{J_2^{3/2}}}{1 - \beta_\theta} \right)^{-0.229}, \quad (5.16)$$

so that the onset of plasticity will not be equal in triaxial extension and compression conditions. Figure 5-5 illustrates the effect that the proposed formulation has on the tri-dimensional space and in combination with the hardening plasticity model MS2 proposed in Chapter 4 and recalled here in equation (5.16). It can be seen that in the tri-dimensional space the proposed formulation is a smooth continuous convex function containing a cap toward the hydrostatic axis that degenerates into a linear criterion at maximum strength conditions (end of the hardening phase).

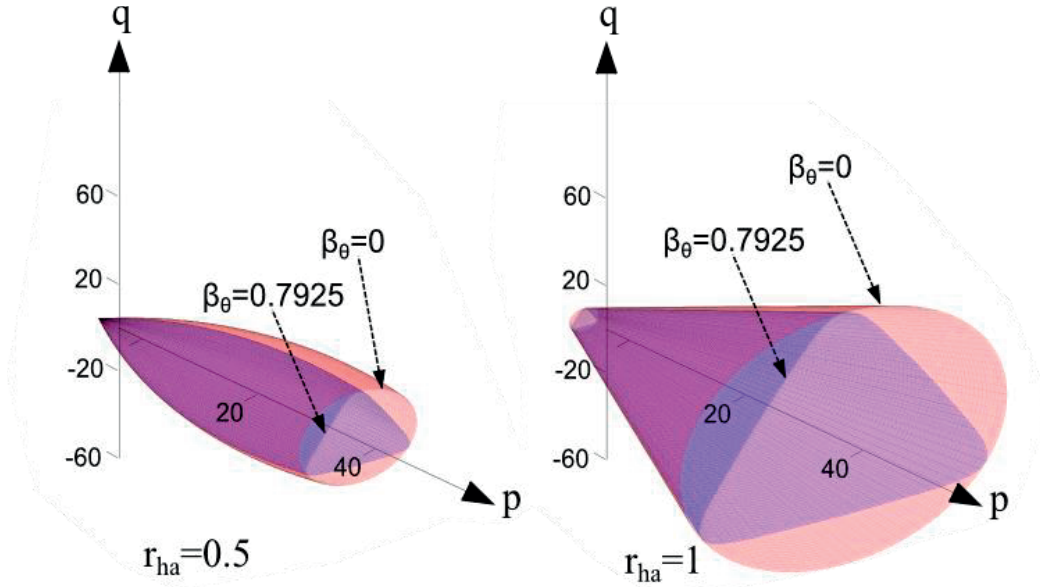


Figure 5-5: Three dimensional plot of the yield surface showing the effect of the proposed formulation in the octahedral plane and for two different values of the hardening function r_{ha} .

5.5. Anisotropic extension of the constitutive model

In this section we present the anisotropic extension of the failure surface of model MS2 presented in Chapter 4 and extended in the previous section to describe failure in true triaxial conditions. The theory employed was developed in the works of Pietruszczak and Mroz (2000, 2001) and its mathematical formulation will be here presented following their original work. The main idea behind this family of models is that the description of the anisotropic behavior can be included in the failure criterion f_p by adding a scalar variable x that is function of the stress σ_{ij} and fabric a_{ij} tensors as

$$f_p = f_p(p, q, \theta, \boldsymbol{\varepsilon}^p, x(\sigma_{ij}, a_{ij})). \quad (5.17)$$

The fabric or structural tensor a_{ij} contains information relative to the material structure, in this case the presence and orientation of bedding planes. The main frame of reference of the problem, along with the definition of principal material frame of reference, is illustrated in Figure 5-6.

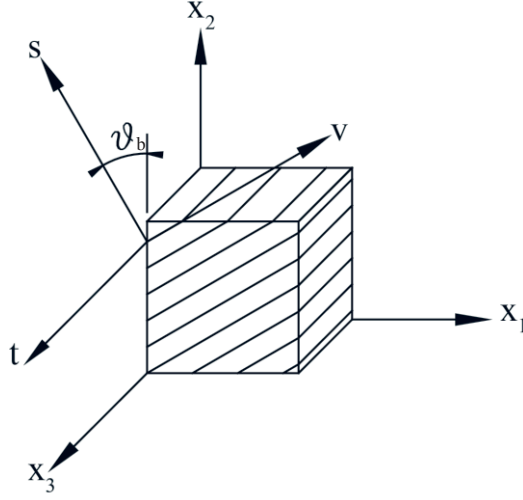


Figure 5-6: Definition of the frame of reference of the problem along with the inclination angle of the bedding and the principal structural frame of reference.

In the formulation, anisotropy will be described by the relative orientation between the principal frame of reference of the stress and fabric tensors. The fabric tensor can be expressed by spectral decomposition in its principal frame of reference (which coincides with the bedding axes) as

$$a_{ij} = a_1 v_i v_j + a_2 s_i s_j + a_3 t_i t_j, \quad (5.18)$$

where v , s and t correspond to the directions of the principal fabric framework. The Cauchy's stress tensor is σ_{ij} and is defined in the material frame of reference x_1, x_2 and x_3 , while the tractions acting on the principal fabric framework can be written as

$$\begin{aligned} L_1 &= \sqrt{\tilde{\sigma}_{11}^2 + \tilde{\sigma}_{12}^2 + \tilde{\sigma}_{13}^2} \\ L_2 &= \sqrt{\tilde{\sigma}_{12}^2 + \tilde{\sigma}_{22}^2 + \tilde{\sigma}_{23}^2} \\ L_3 &= \sqrt{\tilde{\sigma}_{13}^2 + \tilde{\sigma}_{23}^2 + \tilde{\sigma}_{33}^2} \end{aligned}, \quad (5.19)$$

where $\tilde{\sigma}_{ij}$ is the effective stress tensor acting in the principal fabric framework defined as

$$\tilde{\sigma}_{ij} = \Sigma_{ik} \sigma_{kl} \Sigma_{jl}, \quad (5.20)$$

with Σ_{ij} being the rotation tensor between framework x_1, x_2 and x_3 and fabric principal framework v, s and t . The unit vector defining the loading direction in the principal fabric framework is

$$l_i = \frac{L_i}{\sqrt{L_k L_k}} = \frac{L_i}{\sqrt{L_1^2 + L_2^2 + L_3^2}}, \quad (5.21)$$

and the projection of the structure tensor a_{ij} into the loading direction l_i reads

$$x = a_{ij} l_i l_j. \quad (5.22)$$

Fabric tensor a_{ij} can be expressed through its deviatoric and spherical decomposition as

$$a_{ij} = \hat{x} \delta_{ij} + \bar{a}_{ij}, \quad (5.23)$$

where the spherical part is given by

$$\hat{x} = \frac{a_{kk}}{3}, \quad (5.24)$$

and \bar{a}_{ij} is the deviator of the fabric tensor. Equation (5.22) can be rewritten as

$$x = \hat{x} + \bar{a}_{ij} l_i l_j = \hat{x} (1 + \Omega_{ij} l_i l_j), \quad (5.25)$$

with

$$\Omega_{ij} = \frac{\bar{a}_{ij}}{\hat{x}}. \quad (5.26)$$

Higher orders of tensor Ω can be defined via diadic product as

$$\begin{aligned} \Omega_{ijkl} &= d_1 \Omega_{ij} \Omega_{kl} \\ \Omega_{ijklmn} &= d_2 \Omega_{ij} \Omega_{kl} \Omega_{mn}, \end{aligned} \quad (5.27)$$

where d_1 and d_2 are material parameters. A better representation for geomaterials yields higher order expression of the scalar variable in equation (5.24) as,

$$x = \hat{x} \left[1 + \Omega_{ij} l_i l_j + \Omega_{ijkl} l_i l_j l_k l_l + \Omega_{ijklmn} l_i l_j l_k l_l l_m l_n \right], \quad (5.28)$$

so that combining together equations (5.27) and (5.28) the following description of the anisotropic variable can be achieved

$$x = \hat{x} \left[1 + \Omega_{ij} l_i l_j + d_1 (\Omega_{ij} l_i l_j)^2 + d_2 (\Omega_{ij} l_i l_j)^3 \right]. \quad (5.29)$$

In the principal material frame the following holds true

$$\Omega_{ij} l_i l_j = \Omega_{11} l_1^2 + \Omega_{22} l_2^2 + \Omega_{33} l_3^2, \quad (5.30)$$

while for a transversely isotropic material, with fabric reference defined in Figure 5-6, $\Omega_{11} = \Omega_{33} = \bar{\Omega}$. Given that Ω_{ij} is a traceless tensor, the following holds valid

$$\Omega_{11} + \Omega_{22} + \Omega_{33} = 0, \quad (5.31)$$

and by noting that $l_1^2 + l_2^2 + l_3^2 = 1$, equation (5.29) becomes

$$x = \hat{x} \left\{ 1 + \bar{\Omega} (1 - 3l_2^2) + d_1 \left[\bar{\Omega} (1 - 3l_2^2) \right]^2 + d_2 \left[\bar{\Omega} (1 - 3l_2^2) \right]^3 \right\}, \quad (5.32)$$

which represents the spatial perturbation of quantity x around its average value \hat{x} . The perturbation over space is operated by tensor Ω_{ij} . A scalar variable defined as in equation (5.32) carries the anisotropic information as a mixed formulation of invariants of the stress and fabric tensors. In the present extension of the constitutive model MS2 to account for anisotropy, the choice was to extend the description of the material by introducing the above formulation in variable γ , which defines the intercept of the deviatoric axis at null mean stress. The new scalar variable therefore reads

$$\gamma(\tilde{\sigma}_{ij}, \Omega_{ij}) = \hat{\gamma} \left[1 + \bar{\Omega}(1 - 3l_2^2) + d_1 \bar{\Omega}^2 (1 - 3l_2^2)^2 + d_2 \bar{\Omega}^3 (1 - 3l_2^2)^3 \right], \quad (5.33)$$

and the yield function is

$$f_p = q - \left\{ (1 - r_{ha}) \alpha(p)^2 + [(1 - \delta)r_{ha} + \delta] \beta p + r_{ha} \gamma(\sigma_{ij}, \Omega_{ij}) \right\} r(\theta). \quad (5.34)$$

At failure (i.e. at the end of the isotropic hardening)

$$f_p = q - \left[\beta p + \gamma(\sigma_{ij}, \Omega_{ij}) \right] r(\theta), \quad (5.35)$$

which can be seen as a classical Drucker-Prager formulation extended to include anisotropy and true triaxiality. Anisotropy is introduced in the scalar variable γ , which now depends on a combination of invariants of the structure and stress tensors and four material parameters, i.e., $\hat{\gamma}$, $\bar{\Omega}$, d_1 and d_2 . The proposed failure surface extended to cover true triaxial and anisotropic conditions will be referred to as MS3 failure surface.

5.6. Material parameters calibration

In the following, the calibration procedure of the failure surface proposed will be illustrated in detail for both the true triaxial modified Van Eekelen formulation and the anisotropic formulation. The procedure is then applied separately to two different sets of experimental results: one that highlights true triaxial strength and one that highlights intrinsic anisotropic strength.

5.6.1. Calibration of the modified Van Eekelen formulation

A series of experimental data on different rocks was used to calibrate the failure criterion in true triaxial conditions and to test it against other formulations. The materials under studies are KTB amphibolite, Shirahama sandstone, Yuubari shale, Duham dolomite and Solenhofen limestone. The principal stress components at failure were retrieved from the publication of Colmenares and Zoback (2002), while original data can be found for KTB amphibolite in Chang and Haimson (2000), for Dunham dolomite and Solenhofen limestone in Mogi (1971b) and for Shirahama sandstone and Yuubari shale in Takahashi and Koide (1989). The

three parameters β , γ and β_θ of the model from equation (5.14) are calibrated against experimental results with the non-linear least square solver by employing MATLAB[®] function lsqcurvefit (The MathWorks, 2011a), which solves the following

$$\min_{\alpha_j} \|F(\alpha_j, x) - y\|_2^2 = \min_{\alpha_j} \sum_i [F(\alpha_j, x_i) - y_i]^2, \quad (5.36)$$

where α_j is the vector of function parameters, x_i are the input data and y_i are the output data both in matrix or vector form. In the present problem, parameters are

$$\alpha_j = \begin{bmatrix} \beta \\ \gamma \\ \beta_\theta \end{bmatrix}, \quad (5.37)$$

and the input values are defined as the mean stress p_i and Lode's angle at failure θ_i

$$x_i = \begin{bmatrix} p_i \\ \theta_i \end{bmatrix}, \quad (5.38)$$

output is defined as the deviatoric stress at failure q_i

$$y_i = [q_i], \quad (5.39)$$

so that function $F(\alpha_j, x_i)$ can be written as

$$F(\alpha_j, p_i, \theta_i) = (\alpha_1 p_i + \alpha_2) \left[\frac{1 - \alpha_3 \sin(3\theta_i)}{1 - \alpha_3} \right]^{-0.229}, \quad (5.40)$$

and the non-linear least square problem takes the form

$$\min_{\alpha_j} \sum_i [F(\alpha_j, p_i, \theta_i) - q_i]^2. \quad (5.41)$$

By knowing the values of the three principal stresses at failure, the three invariants can be computed and through the solution of Equation (5.41) the three coefficient of the yield surface retrieved. Table 5-1 reports the results of the calibration process in terms of values of the yield function parameters for the 5 rocks under study. Figure 5-7 shows the shape function $r(\mathcal{G})$ in the octahedral plane for different values of the calibrated parameter β_θ , one for each material.

Table 5-1: Parameters values for the proposed model for the 5 different materials under investigation. The parameters were obtained via non-linear regression of the yield function.

MS3 model parameters			
Parameter	β	γ	β_θ
	[-]	[MPa]	[-]
KTB amphibolite	1.78	105	0.765
Shirahama sandstone	1.42	38	0.673
Yuubari shale	1.10	61	0.637
Dunham dolomite	1.17	224	0.590
Solenhofen limestone	1.03	214	0.544

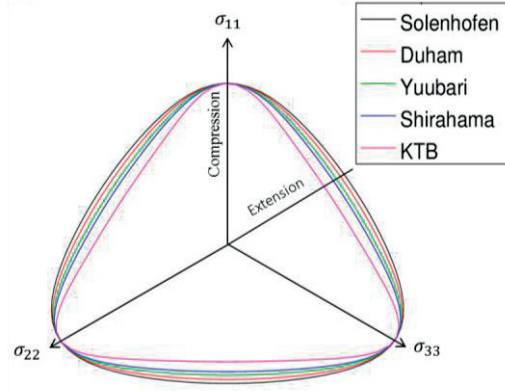


Figure 5-7: Shape function $r(g)$ in the octahedral plane for the 5 rocks under study with β_θ parameter obtained via non-linear least square fitting.

We discuss here an alternative calibration procedure, which could be particularly useful and quick in cases where only triaxial compression and triaxial extension data are available. In such cases the parameters β and γ can be calibrated with a classical linear interpolation of strength data in triaxial compression. Successively, for every failure point in triaxial extension, it is possible to compute the average normalized strength in the octahedral plane \bar{R}_π^{TXE}

$$\bar{R}_\pi^{TXE} = \sum_{i=1}^n \left[\frac{1}{n} \frac{q_i^{TXE}}{(\beta p_i^{TXE} + \gamma)} \right], \quad (5.42)$$

where q_i^{TXE} and p_i^{TXE} are respectively the deviatoric and mean stresses for all the points at triaxial extension failure. By imposing that the yield criterion of equation (5.14) verifies the

average normalized strength in triaxial extension conditions, and by remembering that along the triaxial extension meridian $\sin(-3\theta^{TXE}) = -1$, we can write

$$\bar{R}_\pi^{TXE} = \left[\frac{1 + \beta_\theta}{1 - \beta_\theta} \right]^{-0.229}. \quad (5.43)$$

By solving equation (5.43) parameter β_θ is retrieved. This procedure is simple, relatively fast, and could be useful in certain circumstances (i.e., only triaxial extension and triaxial compression tests available), although a full non-linear fitting procedure yields better results for complex loading conditions where all the three components of the principal stress tensor are simultaneously controlled.

5.6.2. Calibration of the anisotropic extension of the yield criteria

To calibrate the model parameters involved in the anisotropic extension of the failure criterion, we followed the same method employed in the previous section for the true triaxial behavior, i.e., a non-linear least square solver by employing MATLAB[®] function `lsqcurvefit` (The MathWorks, 2011a). In a triaxial compression configuration $r(\tilde{\theta}) = 1$, while generalized loading vector l_2^2 reads

$$l_2^2 = \frac{\sigma_{yy}^2 \cos^2 \theta_b + \sigma_{xx}^2 \sin^2 \theta_b}{\sigma_{xx}^2 + \sigma_{yy}^2 + \sigma_{zz}^2}, \quad (5.44)$$

where the stress tensor is defined in the framework x_1, x_2 and x_3 and θ_b defines the rotation of the principal material framework. For conventional triaxial compression, in which two stress components are controlled simultaneously, $\sigma_{yy} = \sigma_1$ and $\sigma_{xx} = \sigma_{zz} = \sigma_3$ so that l_2^2 becomes

$$l_2^2 = \frac{\sigma_1^2 \cos^2 \theta_b + \sigma_3^2 \sin^2 \theta_b}{\sigma_1^2 + 2\sigma_3^2}. \quad (5.45)$$

At failure, the state of stress σ_1 and σ_3 and the orientation angle θ_b are known, so that l_2^2, p and q can be computed. In this case the vector of material parameters is

$$\alpha_j = \begin{bmatrix} \beta \\ \hat{\gamma} \\ \bar{\Omega} \\ d_1 \\ d_2 \end{bmatrix}, \quad (5.46)$$

while input values are

$$x_i = \begin{bmatrix} p_i \\ l_2^2 \end{bmatrix}, \quad (5.47)$$

and the output

$$y_i = [q_i], \quad (5.48)$$

so that the function $F(\alpha_j, x_i)$ is derived from equation (5.35) in triaxial compression conditions and reads

$$F(\alpha_j, p_i, l_2^2) = \alpha_1 p_i + \alpha_2 \left[1 + \alpha_3 (1 - 3l_2^2) + \alpha_4 \alpha_3^2 (1 - 3l_2^2)^2 + \alpha_5 \alpha_3^3 (1 - 3l_2^2)^3 \right], \quad (5.49)$$

and the minimum problem to solve is

$$\min_{\alpha_j} \|F(\alpha_j, x) - y\|_2^2 = \min_{\alpha_j} \sum_i [F(\alpha_j, x_i) - y_i]^2. \quad (5.50)$$

The above mentioned procedure was applied for the calibration of material parameters of the proposed anisotropic failure criterion to 10 different sedimentary rocks. The data of stress and orientation of the principal fabric framework at failure were retrieved from the work of Ambrose (2014), who performed tests on Bossier Shale and Vaca Muerta Shale and reported the values at failure of Austin Slate, Green River Shale 1 and Green River Shale 2 from McLamore and Gray (1967), Quartz Phyllite and Carbone Phyllite from Ramamurthy et al. (1993), Penrhyn Slate from Attewell and Sandford (1974), Tournemire Shale from Niandou et al. (1997a), while data from Opalinus Clay (shaly facies) data were directly retrieved from Gräsle and Plischke (2010). Table 5-2 shows the values of the parameters after the calibration procedure applied to the specific data set for every material. These parameters will be used to evaluate the theoretical strength predicted by the proposed yield criterion. The strength will then be compared to the experimental data to evaluate the performance of the model.

5.7 Selected failure criteria for the comparative study

Table 5-2: Values of the calibrated parameters for the failure criterion MS3 for the different materials under investigation.

Parameter	β [-]	γ_0 [MPa]	Ω [-]	d_1 [-]	d_1 [-]
Bossier shale	1.26	12.0	1.180	1.850	0.270
Vaca Muerta shale	1.08	41.1	-0.090	80.9	-370
Austin slate	0.91	12.7	2.720	1.620	0.190
Green River shale 1	1.16	105	-0.030	480	-8505
Green River shale 2	0.80	54.3	0.080	102	470
Quartz phyllite	1.34	17.6	0.300	14.1	8.450
Carbona phyllite	1.36	14.6	0.420	8.430	3.770
Penrhyn slate	1.45	13.8	2.230	0.700	0.030
Tournemire shale	0.97	12.4	0.510	3.580	1.120
Opalinus clay	0.97	2.68	1.137	0.530	-0.028

5.7. Selected failure criteria for the comparative study

In order to compare the performance of the failure criterion exposed in the previous sections, a comparison with widely employed failure criteria is proposed. Again, the comparison is divided in two parts, one relative to the true triaxial nature of strength, and another one relative to the intrinsic anisotropy of sedimentary geomaterials.

5.7.1. Failure criteria for the true triaxial extension

To assess the capabilities of the failure surface proposed in equation (5.14) to model the strength of geomaterials in true triaxial conditions, a comparison with 3 other common failure criteria in geomechanics has been carried out. These are the Mohr-Coulomb (MC), Hoek-Brown (HB) and Modified Lade (ML) failure surfaces. The first two do not depend on the intermediate principal stress while the Modified Lade is formulated in terms of two invariants of stress and depends on the intermediate principal stress. All of them have non-circular shapes in the octahedral plane. These models were chosen for two main reasons: the first one is their popularity among geomechanics community; the second one is related to the fact that all of them have non-circular shape in the octahedral plane, and while the first two were formulated in terms of two invariants of stress, the Modified Lade is formulated in terms of three invariants of stress (all three components of the principal stress tensor). In this way the proposed model MS3 can be compared with both families of models (two and three invariants of stress), that all account for non-circular shape of the failure function in the octahedral plane.

The Mohr-Coulomb failure criterion relates failure of a material when the shear stress acting on a specific plane τ_n is greater than the cohesive-frictional forces and writes

$$\tau_n = \sigma_n \tan \phi + c, \quad (5.51)$$

where σ_n is the stress acting on a normal of the failure plane, ϕ is the internal friction angle and c is cohesion. The criterion can be written in principal stress space as

$$f_{MC}^p(\sigma_1, \sigma_3) = \sigma_1 - \frac{1 + \sin \phi}{1 - \sin \phi} \sigma_3 - \frac{2c \cos \phi}{1 - \sin \phi}, \quad (5.52)$$

where σ_1 and σ_3 are respectively the maximum and minimum principal stresses. The criterion does not depend on intermediate principal stress σ_2 and its shape in the octahedral plane is non-circular. For the 5 rocks under studies, values of parameters ϕ and c that will be used in this study were obtained from the calibration performed by Colmenares and Zoback (2002) and are reported in Table 5-3.

Table 5-3: Parameters of the Mohr-Coulomb model taken from Colmenares and Zoback (2002).

Mohr-Coulomb parameters		
Parameter	ϕ [°]	c [MPa]
KTB amphibolite	50.2	54.3
Shirahama sandstone	38.7	22.8
Yuubari shale	26.6	37.1
Dunham dolomite	33.0	122.1
Solenhofen limestone	28.8	110.9

The Hoek-Brown criterion is an empirical model originally derived in Hoek and Brown (1980) in which failure is a non-linear function of the maximum σ_1 and minimum σ_3 principal stresses. The function reads

$$f_{HB}^p(\sigma_1, \sigma_3) = \sigma_1 - \sigma_3 - C_0 \sqrt{\frac{\sigma_3}{C_0} m + s}, \quad (5.53)$$

where C_0 is the unconfined compressive strength of the material, m and s are model parameters. As for the Mohr-Coulomb model the failure does not depend on intermediate principal stress and the shape in the octahedral plane is once again non-circular. Parameter values of the Hoek-Brown model are taken from Colmenares and Zoback (2002) for the five rocks under study and are shown in Table 5-4.

5.7 Selected failure criteria for the comparative study

Table 5-4: Parameters of the Hoek-Brown model taken from Colmenares and Zoback (2002).

Hoek-Brown parameters			
Parameter	C_0 [MPa]	m [-]	s
KTB amphibolite	250.0	30.0	1.0
Shirahama sandstone	65.0	18.2	1.0
Yuubari shale	100.0	6.5	1.0
Dunham dolomite	400.0	8.0	1.0
Solenhofen limestone	370.0	4.6	1.0

The Modified Lade criterion employed here is a three invariants formulation reported in Colmenares and Zoback (2002). The original Lade criterion was proposed for frictional soils in Lade (1977) as a non-linear failure function with non-circular shape in the octahedral plane, while the modified version proposed by Ewy (1999) and reported in Colmenares and Zoback (2002) is a linear formulation updated to include a cohesive component. The failure criterion reads

$$f_{ML}^p(\hat{I}_1, \hat{I}_3) = \frac{\hat{I}_1^3}{\hat{I}_3} - 27 - \frac{4(9 - 27 \sin \phi) \tan^2 \phi}{1 - \sin \phi}, \quad (5.54)$$

where the invariants \hat{I}_1 and \hat{I}_3 are defined as

$$\begin{aligned} \hat{I}_1 &= \sigma_1 + \sigma_2 + \sigma_3 + 3 \frac{c}{\tan \phi} \\ \hat{I}_3 &= \left(\sigma_1 + \frac{c}{\tan \phi} \right) \left(\sigma_2 + \frac{c}{\tan \phi} \right) \left(\sigma_3 + \frac{c}{\tan \phi} \right), \end{aligned} \quad (5.55)$$

where c and ϕ are the equivalent Mohr-Coulomb cohesion and friction and their values, retrieved from Colmenares and Zoback (2002), are reported in Table 5-5.

Table 5-5: Parameters of the Modified Lade criterion taken from Colmenares and Zoback (2002).

Modified Lade parameters		
Parameter	ϕ [°]	c [MPa]
KTB amphibolite	40.4	57.8
Shirahama sandstone	35.0	14.3
Yuubari shale	21.8	37.2
Dunham dolomite	26.6	117.4
Solenhofen limestone	21.8	113.4

5.7.2. Failure criteria for comparison in anisotropic conditions

In order to assess the performance of the proposed anisotropic failure criterion, the predicted values of strength are compared against experimental results on 10 different geomaterials. The comparison will then be made against prediction given by two other failure criteria for anisotropic geomaterials, the Pariseau criterion (PAR) and the Jaeger weakness plane criterion (JWP). In the following the two criteria are presented and a brief explanation of the material parameters is given, while for more details the reader is invited to consult the original works.

As previously mentioned, the Jaeger weakness plane model (Jaeger, 1960) belongs to the discontinuous failure criteria family and predicts that the strength of a transversely isotropic material is governed by the interaction between the intact rock matrix and weakness planes, both described with Mohr-Coulomb failure criterion as

$$\begin{aligned}\tau &= c + \sigma \tan \phi \\ \tau_{wp} &= c_{wp} + \sigma_{wp} \tan \phi_{wp}\end{aligned}\quad (5.56)$$

where τ and σ are the shear and normal stress, respectively, and τ_{wp} and σ_{wp} are the shear and normal stress acting on the bedding planes, respectively, c and ϕ are the cohesion and friction angle of the rock matrix, respectively, and c_{wp} and ϕ_{wp} are the cohesion and friction angle of the bedding planes. The global strength is given by the minimum shear between equations (5.56), and implies an abrupt transition from matrix failure to bedding failure with the change of orientation of the structure inclination. Such a model has proven particularly useful for those materials in which failure is dominated by the beddings, i.e., the strength of weakness planes is much smaller than the one of the rock matrix. One of the main drawbacks is that failure criterion of equation (5.56) predicts the same values of strength for parallel and perpendicular bedding orientations, which is not always the case. For further insights into the failure criterion the reader is referred to the original publication (Jaeger, 1960) or to consult

5.7 Selected failure criteria for the comparative study

the works of Ambrose (2014) and Duveau et al. (1998). The calibrated parameters for the Jaeger weakness plane criterion, along with results of the strength analyses, are taken from the work of Ambrose (2014), with exception of Opalinus Clay. To calibrate the parameters and to evaluate the failure criterion for Opalinus Clay tests, the MATLAB® functions published in Ambrose (2014) were used. Calibration is performed with a linear search in a given grid of parameters. Table 5-6 shows the calibrated parameters of the Jaeger weakness plane criterion (Ambrose, 2014), with the addition of Opalinus Clay.

Table 5-6: Calibrated parameters for the Jaeger weakness plane model Ambrose (2014), while in the present study Opalinus Clay was added.

Jaeger weakness plane				
Parameter	c	ϕ	c_{wp}	ϕ_{wp}
Material	[MPa]	[°]	[MPa]	[°]
Bossier Shale	25.9	29.0	14.1	24.0
Vaca Muerta Shale	33.4	27.0	18.3	26.0
Austin Slate	81.0	22.2	45.2	13.6
Green River Shale 1	67.6	27.8	42.1	30.5
Green River Shale 2	43.8	19.2	27.6	18.7
Quartz Phyllite	21.5	36.6	10.6	27.8
Carbona Phyllite	22.1	32.8	12.4	28.7
Penrhyn Slate	48.3	35.1	34.3	14.7
Tournemire Shale	12.8	24.1	8.8	20.2
Opalinus Clay	3.2	28.3	3.0	20.4

The anisotropic failure criterion of Pariseau (1968) was developed specifically for anisotropic sedimentary geomaterials as a direct extension of the Hill's criterion (Hill, 1950). It is a continuous mathematical formulation containing higher order components of the stress tensor and for transversely isotropic materials writes

$$f_p^{PAR} = \left\{ F(\sigma_{11} - \sigma_{33})^2 + G[(\sigma_{22} - \sigma_{33})^2 + (\sigma_{22} - \sigma_{11})^2] + (2G + 4F)\sigma_{13}^2 + M(\sigma_{23}^2 + \sigma_{12}^2) \right\}^{n/2} - U\sigma_{22} - V(\sigma_{11} + \sigma_{33}) - 1 = 0 \quad (5.57)$$

with the six material parameters F , G , M , U , V and n and the stress tensor defined in the principal material frame s , v and t . The criterion shows a non-linear pressure dependency of the failure envelope governed by parameter n . The whole set of parameters can be calibrated by knowing tensile and compressive strength at different orientation of the bedding planes, although alternative numerical fitting techniques can be used (Duveau et al., 1998). In the present case, the calibration procedure for Opalinus Clay followed is analogous to the one used for the Jaeger weakness plane criterion, i.e., by running published MATLAB scripts in

the work of Ambrose (2014). Table 5-7 shows the set of calibrated parameters for the Pariseau failure criterion. The predicted data of failure of the Pariseau criterion toward the remaining geomaterials were taken as well from Ambrose (2014). Parameter n is equal to one for all the materials.

Table 5-7: Calibrated parameters for the Pariseau failure criterion (Ambrose, 2014), while in the present study Opalinus Clay was added.

Parameter Material	Pariseau				
	F [MPa ⁻²]	G [MPa ⁻²]	U [MPa ⁻¹]	V [MPa ⁻¹]	M [MPa ⁻²]
Bossier Shale	5.01E-05	1.91E-04	9.67E-03	6.05E-03	2.33E-03
Vaca Muerta Shale	1.35E-04	8.75E-05	4.34E-03	5.47E-03	8.41E-04
Austin Slate	4.35E-07	2.42E-05	3.02E-03	1.22E-03	3.74E-04
Green River Shale 1	6.96E-06	3.98E-05	4.34E-03	2.23E-03	2.33E-04
Green River Shale 2	4.35E-07	9.34E-05	5.37E-03	1.71E-03	6.96E-04
Quartz Phyllite	6.14E-05	2.90E-04	1.38E-02	6.90E-03	2.33E-03
Carbona Phyllite	2.90E-04	2.10E-04	9.67E-03	1.00E-02	2.33E-03
Penrhyn Slate	8.22E-05	2.59E-05	2.81E-03	5.28E-03	8.41E-04
Tournemire Shale	5.85E-04	8.41E-04	1.45E-02	1.26E-02	9.34E-03
Opalinus Clay	1.08E-03	7.77E-03	3.87E-02	3.22E-02	6.25E-02

5.8. Analyses and results

In the following we present the results of the analyses carried out in terms of comparison between theoretically predicted vs experimental values of strength for the true triaxial conditions and the anisotropic case. The comparison between the performances of the proposed extended formulation and the failure criteria selected is also presented in details and evaluated. The complete results containing the state of stress at failure from experimental data and the criteria prediction are reported in Appendix C and Appendix D.

5.8.1. True triaxial conditions

The four failure criteria (MC, HB, ML and MS3) were used to calculate, for each geomaterial under study, the theoretical deviatoric stress at failure, for given values of intermediate and minimum principal stress. The main goal is to assess the capabilities of model MS3 to describe the failure conditions of geomaterials in true triaxial conditions. Every experimental data set investigated here was performed for a given value of the minimum principal stress σ_3 , so that a convenient graphical representation is to plot the data in the bi-dimensional space of the intermediate and maximum principal stress (σ_1, σ_2) . For every

material, in Figure 5-8 each set plotted with a different color represents the stress at failure in the (σ_1, σ_2) plane for a given value of σ_3 . The solid lines are theoretical prediction of failure surface in equation (5.14) for given values of σ_3 and are compared in Figure 5-8 against experimental values. It is possible to see how the proposed failure surface can capture well the true triaxial strength of geomaterials. The reader is addressed to consult Colmenares and Zoback (2002) for the visualization of similar plots from the other three failure surfaces of Mohr-Coulomb, Hoek-Brown and Modified Lade.

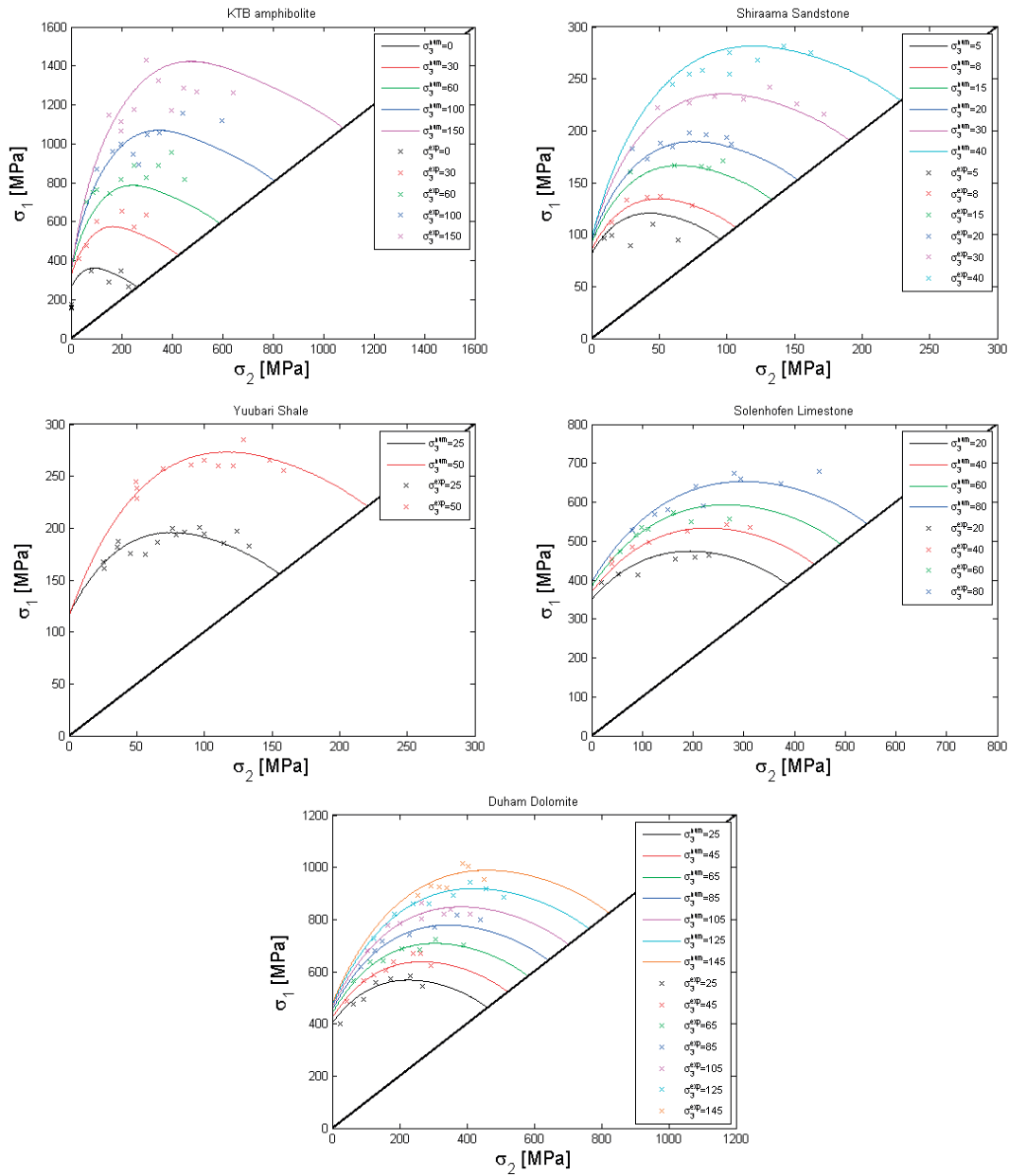


Figure 5-8: Model MS3 predictions (solid lines) against experimental values (dots) for the 5 rocks under studies in the maximum and intermediate principal stress space. Each color represents a constant value of the minimum principal stress.

To quantify the performance of the proposed model, and to compare it with the other three failure surfaces, we compute the scatter between theoretical predictions and experimental values of the deviatoric stress at failure as the Normalized Root Mean Square Error

(NRMSE). NRMSE can be computed from the experimental deviatoric stress at failure q^{ex} and its theoretical prediction q^{th} as

$$NRMSE = \frac{1}{\max_i(q_i^{ex}) - \min_i(q_i^{ex})} \sqrt{\frac{\sum_{i=1}^n (q_i^{ex} - q_i^{th})^2}{n}} . \quad (5.58)$$

NRMSE is a measure of the relative error between experimental data and prediction normalized over the data range. The normalization allows a more direct comparison between the models when compared to experimental data which do not have the same absolute range of values. Table 5-8 reports the results of the analyses in terms of NRMSE of the different models compared against the experimental values of the 5 rocks. An average NRMSE over the five geomaterials is then computed for each model presented. From this result we can state that the proposed formulation with the modified Van Eekelen function globally performs better than the other three models. The worst performing model seems to be the Mohr-Coulomb and this can be explained by the fact that the model does not allow flexibility in the octahedral plane, as the ratio between extension and compression strength is fixed. The Hoek-Brown model shows a smaller global error, and this can be attributed to the non-linear formulation involving three parameters, although the performance is worse than the Modified Lade failure surface. Despite its simplicity, this two parameter criterion is formulated with all three principal stresses and seems more adapted than the previous criteria to describe the true triaxial strength of geomaterials. Finally, the proposed modified Van Eekelen formulation is the one that globally best fits the experimental data under examination. For the single materials, the values of the error for this criterion are always in the range of the other models. The proposed formulation is particularly useful as it can be applied to other criteria formulated in the mean stress-deviatoric stress space along the compressive meridian. In this way much more flexibility is allowed in the choice of a failure surface for a specific material, with proper hardening/softening plasticity laws or damage couplings. Along with its simplicity and adaptability, results demonstrate how well this formulation can describe the strength of geomaterials in true triaxial conditions, making it a simple but powerful mathematical tool for the description of strength in geomaterials.

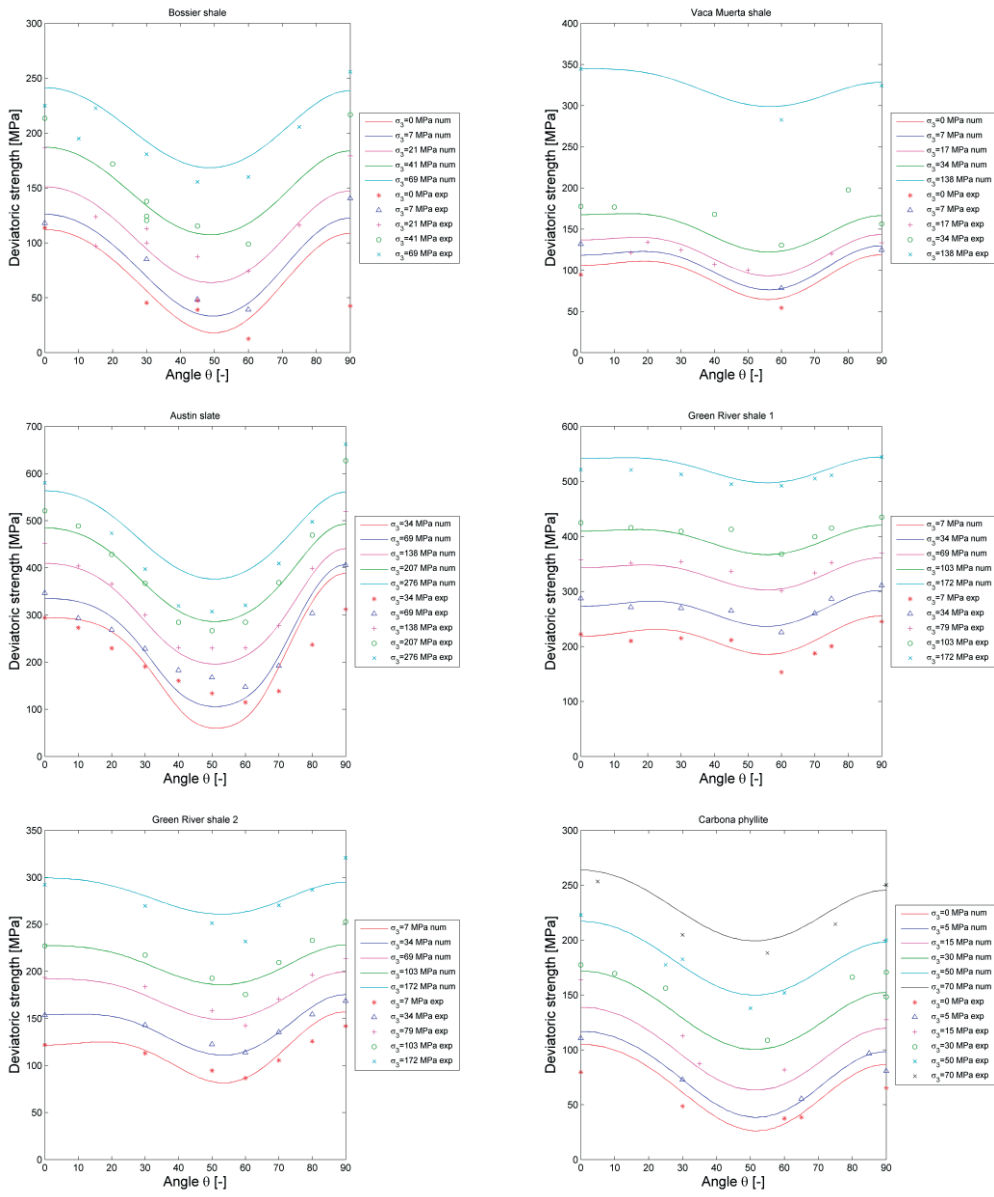
Table 5-8: Results of the analyses in terms of Normalized Root Mean Square Error (NRMSE) between the predicted deviatoric strength of the five models against the experimental deviatoric strength of the five rocks under study (MC=Mohr-Coulomb, HB=Hoek-Brown, ML=Modified Lade, MS3=Proposed modified Van Eekelen).

Performance of different models in terms of NRMSE				
Model	MC	HB	ML	MS3
Rock type	NRMSE [%]			
KTB amphibolite	13.6	8.3	9.5	9.0
Shirahama sandstone	8.1	6.4	10.6	11.4
Yuubari shale	17.7	17.3	24.6	19.9
Dunham dolomite	17.5	17.5	8.4	7.2
Solenhofen limestone	23.1	23.3	14.2	14.0
Mean NRMSE	16.0	14.6	13.4	12.3

5.8.2. Anisotropic conditions

We present here the results of the comparative analyses carried out to assess the performance of the proposed anisotropic formulation compared to the other criteria. The failure criterion proposed in equation (5.35) has been evaluated at different confinements and different bedding plane orientation, with parameters calibrated for each shale under investigation. Figure 5-9 shows the results, where solid lines are theoretical predictions of the failure criterion and dots are relative experimental point. It can be seen the effect of the loading orientation on the strength, whereas the minimum is usually found between 40° and 60° of the orientation angle, while the strength at 0° and 90° differ from each other in almost all of the materials. The anisotropic failure function can correctly reproduce the experimental results and has proven a very good adaptability and flexibility. Special attention should be placed on the case of Opalinus Clay. The scatter of the experimental data seems to be higher compared to the other materials and the reason is that only three inclinations of the weakness planes are available (i.e. 0° , 45° and 90°). This makes the calibration procedure less reliable and therefore, the predictions less accurate than for other materials. Given the third degree of the scalar variable γ that contains the anisotropic information, it can be highly sensitive and shows instabilities. For this reason, its calibration will be more stable and give more reliable data when tests on 4 or more orientations are available. Also, the data seems to be more affected to scatter, as all the failure criteria showed greater values of the error compared to the other materials.

5.8 Analyses and results



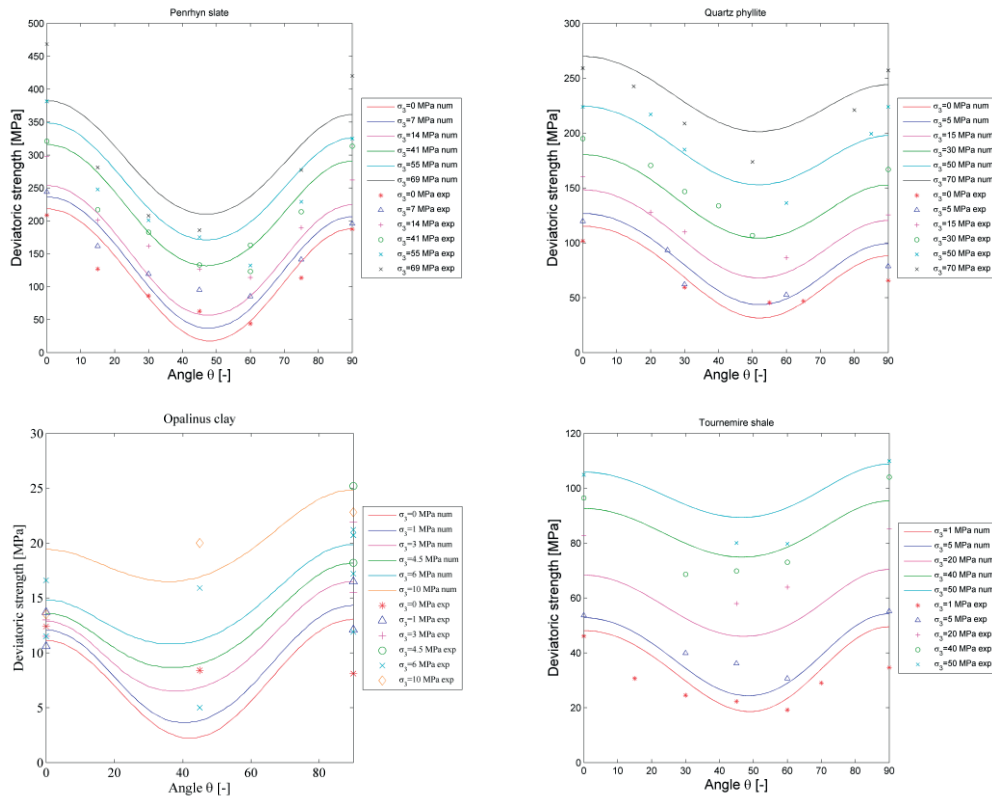


Figure 5-9: Comparison between theoretical predictions (solid lines) and experimental data (dots) in terms of deviatoric stress at failure at different confinement and with different bedding planes orientation for the geomaterials under investigation.

The performance of the proposed anisotropic failure criterion is evaluated in terms of NRMSE as in equation (5.58) and compared to the predictions given by Jaeger weakness plane (JPW) and Pariseau (PAR) failure surfaces. Results of the comparative study are reported in Figure 5-10. The formulation employed shows satisfactory performances compared to the other models, and for certain materials it even gives consistently better results. The global average NRMSE is computed for all the shales for every failure function and is reported in Table 5-9. The highest average error is given by the Jaeger weakness plane criterion, while the lowest error is given by the MS3 proposed model and immediately followed by the Pariseau criterion. It can therefore be stated that such a formulation is equivalent to the most common failure criteria used in geomechanics and globally has a smaller error, while its clear advantages relies in its adaptability to previously formulated isotropic criteria. In order to get more insight into the behavior of the employed formulation for model MS3, the dependence between the NRMSE and the Strength Anisotropy Ratio (SAR) is investigated. SAR is here defined as the ratio between the maximum and the

minimum deviatoric strength for a given confinement. For every experimental data set, the ratio SAR is therefore computed at every confinement, while an averaging procedure allows obtaining an Average Strength Anisotropy Ratio (ASAR) for a given material computed over different confinements. The population correlation coefficient between NRMSE and ASAR, ρ , is computed, for a given model, as

$$\rho = \frac{COV(NRMSE, ASAR)}{\sigma_{NRMSE} \sigma_{ASAR}}, \quad (5.59)$$

where $COV(\cdot)$ is the covariance of data while σ_{NRMSE} and σ_{ASAR} are the standard deviations of the NRMSE and ASAR, respectively. Results show that $\rho = 0.34$ for the JPW criterion, $\rho = 0.18$ for the Pariseau model and $\rho = 0.45$ for the model MS3. This means that there is a stronger correlation between the error of the prediction and the degree of the strength anisotropy for the model MS3. Pariseau criterion is the less affected by the degree of anisotropy. The conclusion that can be drawn is that criterion MS3 is more sensitive to the strength anisotropy ratio and results are more reliable for those materials that exhibit a smooth transition between matrix failure and the weakness plane failure. NRMSE as function of ASAR is graphically reported in Figure 5-11, where it is possible to see the weak correlation between the two parameters. The highest values of the error correspond to data relative to Opalinus Clay and this might be an indicator of the scatter of the experimental data.

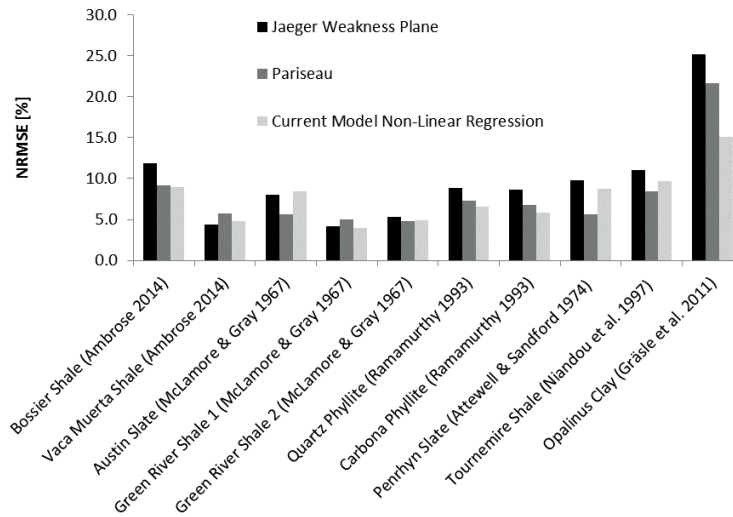


Figure 5-10: Normalized root mean square error for the three yield criteria for the different experimental data sets on geomaterials employed. The performance of the formulation used here is in line with the other yield criteria used for comparison (Jaeger weakness plane and Pariseau).

Table 5-9: Average error for the three failure functions used in the comparative study. The criterion MS2 here proposed shows globally best performances.

Model	Mean total error [%]
Jaeger Weakness Plane	9.7
Pariseau	8.0
MS3 - Non-linear regression	7.7

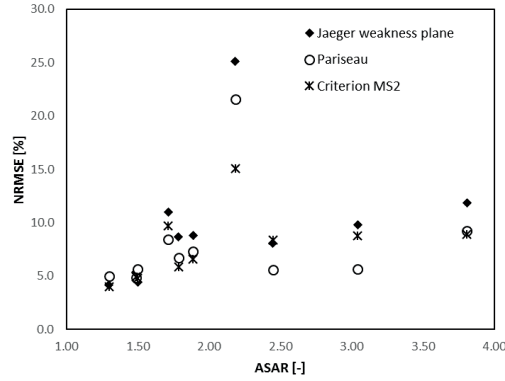


Figure 5-11: Normalized Root Mean Square Error vs Average Strength Anisotropy Ratio for the three failure criteria compared. The highest values of NRMSE are related to Opalinus Clay (shaly facies), evidencing probably the higher scatter in the experimental data.

In conclusion, the proposed yield formulation is coupled with the damage theory within the damage effective stress space as

$$f_p = \tilde{q} - \left\{ (1 - r_{ha}) \alpha (\tilde{p})^2 + [(1 - \delta) r_{ha} + \delta] \beta \tilde{p} + r_{ha} \gamma (\tilde{\sigma}_{ij}, \Omega_{ij}) \right\} r(\tilde{\theta}), \quad (5.60)$$

where the damage effective stress is defined as

$$\tilde{\sigma}_{ij} = (1 - d) \sigma_{ij}, \quad (5.61)$$

with d being the damage internal variable. In the following work, the extended failure surface will be employed to perform numerical analyses of boundary value problems within the finite element method.

5.9. Conclusions

An extension of the failure surface proposed for the isotropic plastic-damage model MS2 presented in detail in Chapter 4 was performed. The motivation relies in the fact that a realistic mechanical description of the strength of geomaterials, and especially sedimentary geomaterials, would require accounting for the true triaxial and anisotropic nature of strength. This has been achieved by extending the isotropic failure surface defined in pure triaxial extension to include true triaxial and intrinsic anisotropic strength. Former extension involved

the definition of a three invariants formulation based on a modified Van Eekelen model, while the latter was achieved by expanding the description of the cohesive components as a function of mixed invariants of stress and fabric tensors. Both formulations share the common feature of being quite flexible, in the sense that can readily be applied to simpler failure criteria to expand their range of predictions. In order to validate the formulation, two sets of experimental tests were used for calibration, and comparison with predicted theoretical values. While true triaxial dependency has generally been observed in a wide variety of geomaterials that include soils, rocks and concrete, intrinsic anisotropy is more peculiar to shales, schists and slates. For this reason, the validation of the true triaxial strength involved a general range of geomaterials including, e.g., sandstones, shales, limestones, dolomites and amphibolites, while the validation of the anisotropic behavior places focus on shales and schists mainly. To get further insight into the performances of the proposed formulation, a comparative study with common failure criteria for geomaterials in true triaxial and anisotropic conditions was carried out. Results showed that the proposed formulation is a valid framework for the expansion of a model, and the performances of the new failure criterion are better in terms of error between theoretical predictions and experimental data than failure criteria most common in geomechanical literature and practice. Such formulation will be retained to perform numerical modeling of boundary value problems including localization of inelastic strains and tunnel excavation analysis that will be presented in the following Chapters.

5.10. Acknowledgements

The authors would like to acknowledge Swisstopo, ENSI and the Mont Terri Project for the financial support to this work. The authors would like also to thank Dr. Werner Gräsle from BGR, Germany, for providing the triaxial test data in the framework of the Mont Terri LT experiment.

5.11. References

- Ambrose, J., 2014. Failure of Anisotropic Shales under Triaxial Stress Conditions. Ph.D. Thesis, Imperial College London.
- Argyris, J.H., Faust, G., Szimmat, J., Warnke, E.P., Willam, K.J., 1974. Recent Developments in Finite-Element Analysis of Prestressed Concrete Reactor Vessels. Nucl Eng Des 28, 42-75.
- Attewell, P.B., Sandford, M.R., 1974. Intrinsic shear strength of a brittle, anisotropic rock—I: experimental and mechanical interpretation, International Journal of Rock Mechanics and Mining Sciences & Geomechanics Abstracts. Elsevier, pp. 423-430.

- Chang, C., Haimson, B., 2000. True triaxial strength and deformability of the German Continental Deep Drilling Program (KTB) deep hole amphibolite. *Journal of Geophysical Research: Solid Earth* 105, 18999-19013.
- Chen, L., Shao, J.F., Huang, H.W., 2010. Coupled elastoplastic damage modeling of anisotropic rocks. *Comput Geotech* 37, 187-194.
- Chiarelli, A.S., Shao, J.F., Hoteit, N., 2003. Modeling of elastoplastic damage behavior of a claystone. *Int J Plasticity* 19, 23-45.
- Chinn, J., Zimmerman, R.M., 1965. Behavior of plain concrete under various high triaxial compression loading conditions. DTIC Document.
- Colmenares, L.B., Zoback, M.D., 2002. A statistical evaluation of intact rock failure criteria constrained by polyaxial test data for five different rocks. *Int J Rock Mech Min* 39, 695-729.
- Drucker, D.C., Prager, W., 1952. Soil Mechanics and Plastic Analysis or Limit Design. *Q Appl Math* 10, 157-165.
- Duveau, G., Shao, J.F., Henry, J.P., 1998. Assessment of some failure criteria for strongly anisotropic geomaterials. *Mech Cohes-Frict Mat* 3, 1-26.
- Ewy, R., 1999. Wellbore-stability predictions by use of a modified Lade criterion. *Spe Drill Completion* 14, 85-91.
- Gräsle, W., Plischke, I., 2010. Laboratory Testing (LT) Experiment: Mechanical Behavior of Opalinus Clay, Final report from Phases 6 – 14. Mont Terri Technical Note TN 2009-07.
- Gudehus, P.D.-I.G., 1973. Elastoplastische stoffgleichungen für trockenen sand. *Ingenieur-Archiv* 42, 151-169.
- Handin, J., Heard, H.C., Magouirk, J.N., 1967. Effects of Intermediate Principal Stress on Failure of Limestone Dolomite and Glass at Different Temperatures and Strain Rates. *J Geophys Res* 72, 611-&.
- Hill, R., 1950. The mathematical theory of plasticity. Clarendon Press, Oxford,.
- Hoek, E., 1964. Fracture of anisotropic rock. *Journal of the South African Institute of Mining and Metallurgy* 64, 501-523.
- Hoek, E., Brown, E.T., 1980. Empirical Strength Criterion for Rock Masses. *Journal of the Geotechnical Engineering Division-Asce* 106, 1013-1035.
- Jaeger, J., 1960. Shear failure of anisotropic rocks. *Geological Magazine* 97, 65-72.
- Jiang, J., Pietruszczak, S., 1988. Convexity of yield loci for pressure sensitive materials. *Comput Geotech* 5, 51-63.
- Kupfer, H., Hilsdorf, H.K., Rusch, H., 1969. Behavior of concrete under biaxial stresses, *Journal Proceedings*, pp. 656-666.

- Lade, P.V., 1977. Elasto-plastic stress-strain theory for cohesionless soil with curved yield surfaces. *Int J Solids Struct* 13, 1019-1035.
- Lade, P.V., Duncan, J.M., 1975a. Cubical triaxial tests on cohesionless soil. *J Geotech Geoenviron* 101.
- Lade, P.V., Duncan, J.M., 1975b. Elastoplastic stress-strain theory for cohesionless soil. *Journal of the Geotechnical Engineering Division* 101, 1037-1053.
- Lade, P.V., Musante, H.M., 1978. Three-dimensional behavior of remolded clay. *Journal of the Geotechnical Engineering Division* 104, 193-209.
- Le, A., Nguyen, T., 2014. Hydromechanical response of a bedded argillaceous rock formation to excavation and water injection 1. *Can Geotech J* 52, 1-17.
- Lee, Y.-K., Pietruszczak, S., Choi B.-H., 2012. Failure criteria for rocks based on smooth approximations to Mohr–Coulomb and Hoek–Brown failure functions. *Int J Rock Mech Min* 56, 146-160.
- Makhnenko, R., Labuz, J., 2014. Plane strain testing with passive restraint. *Rock Mech Rock Eng* 47, 2021-2029.
- Makhnenko, R.Y., Harvieux, J., Labuz, J.F., 2015. Paul-Mohr-Coulomb failure surface of rock in the brittle regime. *Geophys Res Lett* 42, 6975-6981.
- Matsuoka, H., Nakai, T., 1974. Stress-deformation and strength characteristics of soil under three different principal stresses, *Proc. JSCE*, pp. 59-70.
- McLamore, R., Gray, K., 1967. A strength criterion for anisotropic rocks based upon experimental observations, *Annual Meeting of the American Institute of Mining, Metallurgical, and Petroleum Engineers. Society of Petroleum Engineers.*
- Menetrey, P., Willam, K., 1995. Triaxial failure criterion for concrete and its generalization. *Aci Struct J* 92, 311-318.
- Mills, L.L., Zimmerman, R.M., 1970. Compressive strength of plain concrete under multiaxial loading conditions, *Journal Proceedings*, pp. 802-807.
- Mises, R.v., 1913. *Mechanik der festen Körper im plastisch-deformablen Zustand.* *Nachrichten von der Gesellschaft der Wissenschaften zu Göttingen, Mathematisch-Physikalische Klasse* 1913, 582-592.
- Mogi, K., 1971a. Effect of the triaxial stress system on the failure of dolomite and limestone. *Tectonophysics* 11, 111-127.
- Mogi, K., 1971b. Fracture and flow of rocks under high triaxial compression. *J Geophys Res* 76, 1255-1269.
- Mogi, K., 1972. Fracture and flow of rocks. *Tectonophysics* 13, 541-568.
- Mogi, K., 1973. Rock fracture. *Annual Review of Earth and Planetary Sciences* 1, 63.
- Niandou, H., Shao, J., Henry, J., Fourmaintraux, D., 1997. Laboratory investigation of the mechanical behaviour of Tournemire shale. *Int J Rock Mech Min* 34, 3-16.

- Ottosen, N.S., 1977. A failure criterion for concrete. *Journal of the Engineering Mechanics Division* 103, 527-535.
- Pardoen, B., Seyedi, D., Collin, F., 2015. Shear banding modelling in cross-anisotropic rocks. *Int J Solids Struct* 72, 63-87.
- Pariseau, W.G., 1968. Plasticity theory for anisotropic rocks and soil, The 10th US Symposium on Rock Mechanics (USRMS). American Rock Mechanics Association.
- Pietruszczak, S., Mroz, Z., 2000. Formulation of anisotropic failure criteria incorporating a microstructure tensor. *Comput Geotech* 26, 105-112.
- Pietruszczak, S., Mroz, Z., 2001. On failure criteria for anisotropic cohesive-frictional materials. *Int J Numer Anal Met* 25, 509-524.
- Ramamurthy, T., Rao, G.V., Singh, J., 1993. Engineering behaviour of phyllites. *Eng Geol* 33, 209-225.
- Takahashi, M., Koide, H., 1989. Effect of the intermediate principal stress on strength and deformation behavior of sedimentary rocks at the depth shallower than 2000 m, ISRM international symposium. International Society for Rock Mechanics.
- The MathWorks Inc., 2011a, MATLAB and Statistics Toolbox Release, Natick, Massachusetts, United States.
- Tsai, S.W., Wu, E.M., 1971. A general theory of strength for anisotropic materials. *J Compos Mater* 5, 58-80.
- Van Eekelen, H., 1980. Isotropic yield surfaces in three dimensions for use in soil mechanics. *Int J Numer Anal Met* 4, 89-101.
- Wiebols, G.A., Cook, N.G.W., 1968. An Energy Criterion for Strength of Rock in Polyaxial Compression. *Int J Rock Mech Min* 5, 529-&.
- Willam, K., Warnke, E., 1975. Constitutive model for the triaxial behavior of concrete, Proceedings, international association for bridge and structural engineering. ISMES, Bergamo, Italy, pp. 1-30.
- Zienkiewicz, O., Pande, G., 1977. Some useful forms of isotropic yield surfaces for soil and rock mechanics. John Wiley & Sons Ltd, pp. 179-190.

6. Combining micro-dilatant continua framework with plastic-damage constitutive model for the regularization of localized strain

Authors: F. Parisio and L. Laloui.

Status: to be submitted to Geomechanics for the Energy and the Environment.

Contributions: The manuscript was written by F. Parisio, who developed the constitutive model, performed the numerical implementation and analyses. The literature review was carried out by F. Parisio, along with the numerical analyses strategies and results interpretation. L. Laloui overviewed the work, edited the manuscript and is the senior responsible author (SRA) of the publication.

Abstract

Describing the deformation process of sedimentary rocks, and in particular shale, often requires the adoption of material softening constitutive models to account for post-peak brittle deformation. It is known how employing softening constitutive models in Finite Element Analysis leads to pathological mesh dependency of the solution if no regularization techniques are associated. To avoid such shortcomings, which generate unphysical solutions in terms of dissipated inelastic energy, several techniques based on the introduction of a characteristic length in the material description exist. In modeling geomaterials, several authors have applied micro-enriched continua description, in which a characteristic length of the material is introduced via the gradient of elastic strains for an enhanced variational formulation. However, spurious localization band expansion usually appears when non-linear softening laws are postulated, finally leading to stress locking type of phenomena. In the following contribution we investigate the structural response by employing the constitutive model MS3 developed in *Code_Aster* and a second gradient of dilation regularization. Numerical analyses of biaxial compression in plane strain conditions are carried out within the framework of a micro-dilatant enriched continuum for the regularization of localized inelastic strain. The main advantages of combining plastic-damage models for shale with micro-dilatant continua are shown via a series of numerical examples. Results show the most influential parameters that control localization. The pathological mesh dependency is successfully removed and localization band growth properly controlled by employing a non-associated plastic potential.

Keywords: localized inelastic strains, pathological mesh dependency, micro-polar dilatant continua, plastic damage modeling

6.1. Introduction

Among sedimentary rocks, shale holds a major role in modern geo-energy and geo-environmental applications. Due to its low hydraulic conductivity and its ability to self-heal microcracks, is seen as a potential host rock in deep geological repository of high-level nuclear waste storage in countries such as Switzerland (Bossart et al., 2002; Bossart et al., 2004; Salager et al., 2013), Belgium (François et al., 2009; Pardoën et al., 2014) and France (Angelini et al., 2011; De La Vaissière et al., 2014; Plassart et al., 2013). Low pore size of shale offers as well potential isolation of the adjacent subsurface environment from CO₂

stored in higher permeability reservoirs, making it a good candidate as cap-rock formation (Bennion and Bachu, 2008; Song and Zhang, 2012). More recently, shale draw much of the attention of the research community toward its complete characterization, as unconventional reservoir exploitation became a strong reality in North America (Middleton et al., 2015).

From a mechanical point of view, shale can be inserted in the family of quasi-brittle materials. When compressed, quasi-brittle geomaterials exhibits micro-cracks formation prior to the stress peak. These are responsible for permanent inelastic strain accumulation. Micro-cracks growth and coalescence will eventually lead to post-peak softening, where dilatant behavior is observed as localized strains into finite shear bands (Rybacki et al., 2015). Therefore, from a constitutive point of view, coupled-plastic damage models offer the best and most representative solution to describe the experimental behavior of shale (Chen et al., 2012; Chiarelli et al., 1999; Parisio et al., 2015). Plasticity alone will predict permanent inelastic strain while damage alone can account for the reduction of elastic moduli (as observed, e.g., in Opalinus Clay by Gräsle and Plischke (2011)). Plasticity and damage properly combined together and with the adequate formulation can represent both physical phenomena.

Plastic-damage models are formulated such that they can predict the post-peak softening behavior of shale (whether plasticity or damage, or sometimes both, are responsible for the softening behavior). Softening models, under certain conditions, can originate localization of inelastic strains into a finite size band with a weak discontinuity separating it from the homogeneous surroundings. From a mathematical point of view, when such conditions are met, the differential equation of rate equilibrium loses ellipticity and the description of the strain softening continuum becomes non-objective and the problem ill-posed (Jirásek, 2007). When performing FEM analyses, or more generally when a spatial discretization is employed, loss of ellipticity implies that inelastic strains will localize into finite size bands with dimension generally equivalent to the smallest elements size. Energy dissipation is related to the element size, and for an element size that tends to zero also inelastic dissipation will tend to zero (De Borst et al., 1993), which is physically unacceptable.

The goal of the present work is to demonstrate how coupling between plastic-damage model MS3 and second gradient of dilatancy formulated by Fernandes et al. (2008), which is a micromorphic continuum description based on Cosserat's theory (Cosserat and Cosserat, 1909), offers a consistent and objective description of the mechanical behavior in shale without pathological mesh dependency. Models that couple plasticity with second gradient theory of elastic strains, as in, e.g., Chambon et al. (2001), might suffer from a pathological expansion of the localization band when the softening modulus is non-linear and reaches null values (Jirásek and Rolshoven, 2009). The advantage of approaching the problem with a second gradient of dilatancy formulation is that the localization band growth can be stopped

by non-associated plastic flow rule (Fernandes, 2009). Recurring to a relaxation technique of the regularization operator can be avoided. Moreover, this formulation is less time consuming and provides higher computational efficiency.

In the present work, first, a quick outlook at the most common regularization techniques is presented. The constitutive model MS3 developed in Chapters 4 and 5 for the mechanical description of shale is employed. The mathematical formulation of the second gradient of elasticity for dilatant media is exposed and numerical analyses in plane strain conditions are presented. These analyses were performed with the open source FEM software *Code_Aster*, developed by Électricité de France (EDF) (www.code-aster.org), in which the second gradient of dilatancy was already implemented. The analyses are designed so that the proposed combination of damage-plasticity and second gradient of dilation can be thoroughly investigated. Results demonstrate how the proposed framework can be a valid tool to model localized inelastic strains and damage.

6.2. Strain localization and regularization techniques

Classical localization analysis for dilatant geomaterials, which has the goal of finding under which conditions a weak discontinuity will be formed, was founded on the early work of Rudnicki and Rice (1975). A necessary but not sufficient condition for the loss of ellipticity and the formation of a localized solution is that the determinant of the localization tensor is null^c

$$\det M_{ij} = 0. \quad (6.1)$$

The localization tensor M_{ij} is defined as

$$M_{ij} = E_{ijkl}^t s_k s_l, \quad (6.2)$$

where s_i is a unit vector normal to the weak discontinuity surface while E_{ijkl}^t is the tangent stiffness tensor. For a given tangent stiffness tensor, through localization analysis, it is possible to find a given unit vector s_i under which the localization tensor becomes singular and a weak discontinuity develops across the surface of normal s_i . Examples of localization analysis for isotropic scalar damage models was given by Rizzi et al. (1995), and by Lemaitre et al. (2000) for an anisotropic damage model. For coupled plastic-damage models one can refer to the work of de Borst et al. (1999) for gradient plasticity or gradient damage theories, while the contribution of Haddag et al. (2009) focuses its localization analysis on anisotropic

^c The localization tensor can be obtained by multiplying the acoustic tensor by the mass density ρ .

plasticity of the Hill's type with isotropic scalar damage in large strain theory. More specific to geomechanical applications, localization analysis on partially saturated porous media was performed by Borja (2004).

In general, to overcome the non-objectivity of the description of the standard softening continuum, several regularization techniques were proposed in literature. A simple yet effective way to provide appropriate energy dissipation, and therefore a consistent stress-strain relationship during localized deformation, is the application of a mesh adjusted softening modulus (Bažant and Oh, 1983; Grassl, 2009; Pietruszczak and Mroz, 1981), also referred to as crack band approach or fracture energy trick. As the name suggests, the principal idea is to adjust the softening response based on the characteristics of the mesh. Despite its simplicity and consistency, particular care must be put in place as the localized band width is not only controlled by element size, but also by the element type, shape, direction of the band and numerical integration scheme (Jirásek and Bauer, 2012).

Viscoplasticity has proven efficient in controlling localization by introducing rate dependence in the constitutive equations (Das and Buscarnera, 2014; Das et al., 2013; Lorent and Prevost, 1990; Needleman, 1988). When, for example, deformation localizes into a finite band of one element, the rate of deformation inside that element increases and according to the viscous law the element increases its rigidity transferring strain increment to the neighboring elements and preventing excessive localization (Niazi et al., 2013). The mathematical explanation given by Forest and Lorentz (2004) states that for rate-dependent constitutive behavior the tangent operator is positive definite and, therefore, ill-posedness of the problem (so called loss of ellipticity) can be avoided.

Despite its effectiveness in both static and dynamic problems (Needleman, 1988) and its relative simplicity for numerical implementation, viscoplasticity introduces a physical time dependence even in quasi-static problems, making it difficult to calibrate viscosity coefficient for such problems (often considered a numerical technique for regularization). Additionally, Forest and Lorentz (2004) have shown that, after a critical time, damage gradient dramatically increases, resulting in an additional one-element size band with dissipated energy tending to zero (pathological mesh dependency). For these reasons, viscoplastic regularization techniques should be carefully employed when dealing with quasi-static problems and non-local approaches are to be preferred.

The idea behind more non-local approaches is that at the constitutive level the formulation is enriched, so that the state at one point does not only depend on the current and previous history, but also contains information on the structure, i.e., neighboring points, introducing, therefore, a characteristic length controlling the localization band size in the material. Regularization techniques provide localization limiters, so that pathological mesh-dependency is removed and the dissipated energy can be properly modeled.

Non-local continua of the integral type were widely employed to the scope and a consistent and extended review can be found in the work of Bažant and Jirásek (2002). The main concept behind these models is that a given variable (which could be representative of the inelastic process in case of plasticity or damage) is computed as a spatial average over a finite given length of influence. Pioneering work in non-local plasticity was proposed by Bažant and Lin (1988), while a comparison between different non-local softening plasticity models in a mono-dimensional problem can be found in Jirásek and Rolshoven (2003). Analogously, non-local integral type damage models were proposed in, e.g., Pijaudier-Cabot and Bazant (1987), where the average is taken over the damage energy release rate, and in Bazant and Pijaudier-Cabot (1988), in which the average operator acts on the damage variable. For combined plasticity-damage model one can refer to the work of Charlebois et al. (2010).

Alternatively, instead of the integral operator of internal variables, its differential formulation can be applied, originating therefore in gradient type models, where the constitutive equations can contain higher order terms. Gradient of internal variables models offers regularization only when inelastic processes start to develop. Models can be divided into models that account for gradient of damage or damage related variables as in Alessi et al. (2015), Comi (1999), Lorentz et al. (2011) and Peerlings et al. (1996, 1998), and models that account for gradient of plastic strain or plastic internal variables as in Aifantis (1984), De Borst and Mühlhaus (1992), De Borst and Pamin (1996), Mühlhaus and Alfantis (1991) and Zhang and Schrefler (2000).

On the contrary, gradient of elastic strain models, also known as micropolar continua or enriched continua, offers regularized solutions even in the elastic phase where no dissipation takes place. Such models can be considered to be weakly non-local according to Jirásek and Rolshoven (2009) and are in a certain way extensions to the classical work on elastic-strain gradient theory of Toupin (1962) and Mindlin (1964). The work of Chambon et al. (1998) and Chambon et al. (2001) contain an extension of such theories of local second gradient elasticity to elasto-plastic framework for dry cohesive-frictional materials, successively extended to porous fluid saturated materials in Collin et al. (2006).

According to the results of the analyses carried out by Jirásek and Rolshoven (2009), a more realistic approach is formulated in the work of Fleck and Hutchinson (1993) and Fleck and Hutchinson (1997), where the yield limit does not depend only on the stress (Cauchy's stress) but also on the double stress. In this family of second gradient models, since the constitutive equations contain plastic strain gradient, the localized zone is bounded and does not increase upon plastic deformation, avoiding stress-locking (on the contrary, further materials instability is reported in Jirásek and Rolshoven (2009)). To improve computational efficiency

and to avoid pathological enlargement of the localized band upon inelastic strains^d, a second gradient model based on dilation volumetric strains was proposed in the works of Fernandes (2009) and Fernandes et al. (2008).

In the present work this latter theory is efficiently employed in combination of the previously developed plastic-damage model MS3 for quasi-brittle geomaterials (shale in particular). Mesh independency analysis is carried out and the expansion of the dissipation band is limited thanks to the non-associated formulation proposed. The plastic model is a non-linear yield surface that degenerates into a final linear cohesive-frictional surface at the end of the hardening phase. Pressure dependence of the localization band is investigated with the proposed formulation and results seem to be in accordance with previous analyses with Cosserat type of continua presented in Alshibli et al. (2006). The influence of the anisotropic formulation on the localized behavior is investigated along with the influence of the size of the specimen. With localization control, governing equations remain hyperbolic during the softening phase, the solution is physically meaningful and pathological mesh dependency is removed. The combination of damage-plasticity and second gradient of dilation continua provide a consistent and sound framework for modeling objectively dilatant quasi-brittle geomaterials like shale or other sedimentary rocks, where dissipation phenomena are accompanied by accumulation of microvoids (damage), particle rearrangement and dilatancy (plasticity) leading to post-peak localization phenomena.

6.3. Micropolar continua and the second gradient of dilatancy

We present in what follows the constitutive equations of the mechanical formulation of the second gradient of dilation model as implemented in *Code_Aster* ([R5.04.03], 2013) and reported in Fernandes (2009), Fernandes et al. (2008) and Plassart et al. (2013). The main goal of this formulation is to improve computational efficiency by reducing the number of degrees of freedom per node compared to classical second gradient of elastic strain theories. We briefly recall the salient passages from the general formulation of micromorphic continua to the second gradient of dilatancy (Fernandes, 2009). The general micromorphic continua variational formulation reads

$$\int_{\Omega} \left(\sigma_{ij} \frac{\partial \bar{u}_i}{\partial x_j} + \tau_{ij} \left(\bar{f}_{ij} - \frac{\partial \bar{u}_i}{\partial x_j} \right) + \Sigma_{ijk} \frac{\partial \bar{f}_{ij}}{\partial x_k} \right) dv = \int_{\partial\Omega} (t_i \bar{u}_i + T_{ij} \bar{f}_{ij}) ds, \quad (6.3)$$

^d This latter feature is valid only in the case of non-associated plastic models in which the rate of plastic volumetric strain becomes gradually null upon plastic strain increase.

for any mathematically admissible fields of displacement \bar{u}_i and micro-deformation gradient \bar{f}_{ij} (to be intended as a given quantity and not the gradient of any specific fields). t_i are traction forces and T_{ij} are the double tractions acting on boundary $\partial\Omega$, both kinematical conjugate of \bar{u}_i and \bar{f}_{ij} . Either tractions or their kinematical conjugate are known. Imposing equality between the micro gradient and the macro gradients simplifies the formulation, i.e.,

$$\bar{f}_{ij} = \frac{\partial \bar{u}_i}{\partial x_j}, \quad (6.4)$$

which in turn yields the following variational formulation

$$\int_{\Omega} \left(\sigma_{ij} \frac{\partial \bar{u}_i}{\partial x_j} + \Sigma_{ijk} \frac{\partial^2 \bar{u}_i}{\partial x_j \partial x_k} \right) dv = \int_{\partial\Omega} (p_i \bar{u}_i + P_i D\bar{u}_i) ds, \quad (6.5)$$

valid again for any kinematically admissible field \bar{u}_i . p_i is the external force per unit area and P_i is the double external force per unit area and they are expressed as

$$p_i = \sigma_{ij} n_j - n_k n_j D\Sigma_{ijk} - \frac{D\Sigma_{ijk}}{Dx_k} n_j - \frac{D\Sigma_{ijk}}{Dx_j} n_k + \frac{Dn_l}{Dx_l} \Sigma_{ijk} n_j n_k - \frac{Dn_j}{Dx_k} \Sigma_{ijk}, \quad (6.6)$$

$$P_i = \Sigma_{ijk} n_j n_k$$

where n_i is the outgoing normal vector to the boundary $\partial\Omega$. In this general case, the micromorphic deformation gradient model has proven to successfully prevent excessive localization, since it introduces a spatial gradient in the general formulation. Considering then a continuum formulation with microdilation, the kinematic can be described by the displacement field u_i , the microvolume variation χ and its gradient. The conjugated variables in this case can be defined as: the Cauchy stress field σ_{ij} conjugated to the displacement gradient; the micro dilation stress κ (as in the terminology introduced by Fernandes (2009)) conjugated to the microdilatancy relative to the macrodilatancy $\varepsilon_{kk} - \chi$; the double dilation stress S_i conjugated to the gradient of microvolume variation $\partial\chi/\partial x_i$. Once again the variational formulation writes

$$\int_{\Omega} \left(\sigma_{ij} \frac{\partial \bar{u}_i}{\partial x_j} + \kappa (\bar{\varepsilon}_{kk} - \bar{\chi}) + S_j \frac{\partial \bar{\chi}}{\partial x_j} \right) dv = \int_{\partial\Omega} (t_i \bar{u}_i + m \bar{\chi}) ds, \quad (6.7)$$

valid for any admissible kinematic field $(\bar{u}_i, \bar{\chi})$ with boundary conditions expressed as

$$\begin{aligned} t_i &= \sigma_{ij} n_j + \kappa \delta_{ij} n_j \\ m &= S_j n_j \end{aligned} \quad (6.8)$$

Analogously to the choice that was made with the micro-deformation gradient being equal to the macro-deformation gradient, once again the choice of the micro-dilatation variation can be equalized to the macroscopic dilation so that $\chi = \varepsilon_{kk}$ and the variational formulation will become

$$\int_{\Omega} \left(\sigma_{ij} \frac{\partial \bar{u}_i}{\partial x_j} + S_j \frac{\partial^2 \bar{u}_i}{\partial x_j \partial x_i} \right) dv = \int_{\partial\Omega} (p_i \bar{u}_i + P_i D\bar{u}_i) ds, \quad (6.9)$$

with boundary conditions

$$\begin{aligned} p_i &= \sigma_{ij} n_j - n_i n_j DS_j - \frac{DS_j}{Dx_j} n_i - \frac{DS_j n_j}{Dx_i} + \frac{Dn_k}{Dx_k} S_j n_j n_i \\ P_i &= S_j n_i n_j \end{aligned} \quad (6.10)$$

If $P_i = 0$ then the first boundary condition can be rewritten as (see for details Fernandes et al. (2008))

$$p_i = \sigma_{ij} n_j - \frac{\partial S_j}{\partial x_j} n_i. \quad (6.11)$$

The equilibrium equation takes the form

$$\frac{\partial \sigma_{ij}}{\partial x_j} - \frac{\partial^2 S_j}{\partial x_j \partial x_i} = 0. \quad (6.12)$$

With the use of C0 finite elements with Lagrangian multipliers (Fernandes, 2009) the final equation of virtual work implemented in *Code_Aster* becomes

$$\int_{\Omega} \left(\sigma_{ij} \frac{\partial \bar{u}_i}{\partial x_j} + S_j \frac{\partial \bar{\chi}}{\partial x_j} - \Lambda (\bar{\varepsilon}_{kk} - \bar{\chi}) + \bar{\Lambda} (\varepsilon_{kk} - \chi) \right) dv = \int_{\partial\Omega} (p_i \bar{u}_i + P_i D\bar{u}_i) ds, \quad (6.13)$$

where the additional field χ was introduced and forced to be $\varepsilon_{kk} = \chi$ with a Lagrangian multiplier field Λ . The above equation is valid for any kinematically admissible fields \bar{u}_i , $\bar{\chi}$ and $\bar{\Lambda}$. The constitutive equation of the second gradient part is a linear elastic one, and for the case of micro-dilatant media writes

$$S_i = K \frac{\partial \varepsilon_{kk}}{\partial x_i}, \quad (6.14)$$

where

$$K = (n+1)a, \quad (6.15)$$

where n is the dimension of the considered space and a is an elasticity coefficient which can be related to the internal length (Plassart et al., 2013). However, its determination is not straight forward and implies the analytical knowledge of the consistent tangent operator for the softening branch. Given the complexity of the constitutive law proposed in the present study, its analytical determination was not investigated and an empirical procedure is used instead.

6.4. Numerical model in plane strain conditions

In order to illustrate the principal features of the mechanical behavior of the plastic damage constitutive model MS3 with the illustrated regularization technique based on micro-dilatant continua, a series of numerical examples is presented. These examples are based on a single model in 2D plane strain conditions. The sample is 1 m high and 0.5 m large, subjected to vertical loading in the form of imposed displacement Δy , with constraint vertical displacement on the bottom and constraint horizontal displacement at the bottom central node (to avoid rigid body movements). The model geometry, mesh, boundary and loading conditions, are illustrated in Figure 6-1. In order to facilitate the appearance of a localized band, a small defect was inserted in the model where cohesion is 99% of the original one (the blue square in the bottom left of the model shown in Figure 6-1).

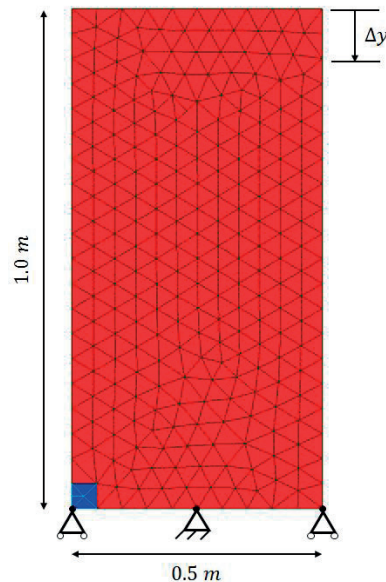


Figure 6-1: Schematic representation of the numerical model, with mesh and boundary conditions applied. In blue it is shown the small part of the model where cohesion is reduced to 99% of the original one in order to facilitate the appearance of a shear band.

As snap-back type phenomena are in this case possible and will finally depend on the thickness of the localization band, no vertical displacement can be assumed as driving variable, as it might not be a monotonically growing function. Therefore, a load control technique based on the deformation increment was employed (Fernandes, 2009; Lorentz and Badel, 2004). Such technique is based on the concept that the deformation increment at a given time step will remain close to the deformation increment at the beginning of the time step for at least a Gauss' point in the structure ([R5.03.80], 2013). This implies that at least one point in the structure will preserve its deformation mode. For load control method, a new scalar unknown $\bar{\xi}(t^n)$ controlling the load in the system at time step t^n and an additional equation are introduced. The system is rewritten as

$$\begin{cases} F^{\text{int}}(\bar{u}_i, t^n) = F^{\text{ext}}(\bar{\xi}(t^n)) \\ P(\varepsilon_{ij}^n) = C \end{cases}, \quad (6.16)$$

where C is dimensionless and strictly positive data and ε_{ij}^n is the strain tensor at time step t^n . For the load control method based on the deformation increment, and hereby used in the following analyses, P is the control function and writes (Fernandes et al., 2008)

$$P(\varepsilon_{ij}^n) = \max_G \left[\frac{\varepsilon_{ij}^{n-1}}{\hat{\varepsilon}^{n-1}} (\varepsilon_{ij}^n - \varepsilon_{ij}^{n-1}) \right], \quad (6.17)$$

where $\hat{\varepsilon}$ designs a norm of the strain tensor, which is defined as

$$\hat{\varepsilon} = \sqrt{\varepsilon_{ij} \varepsilon_{ij}}, \quad (6.18)$$

and subscript G denotes Gauss' points of the structure. Employing this load control technique will facilitate in obtaining a solution in case of snap-back, although there is no a priori guarantee that a solution will be found. For further information, the reader is invited to consult the work of Crisfield (1981), Fernandes (2009) and Lorentz and Badel (2004).

6.5. Numerical analyses

In the following, the results of the different analyses that were performed on the presented numerical model are reported. The goal is to highlight the principal features of the plastic-damage model in combination with the regularizing effect of the second gradient of dilatancy theory. The general behavior is firstly investigated, while subsequently focus is placed in investigating how the results depend on mesh size, non-associated potential and confining stress.

6.5.1. Comparison between homogeneous, non-regularized and regularized solution

Table 6-1 shows the basic parameters of the constitutive model for numerical analyses. Some parameters will be changed in the upcoming sections to illustrate their effect in combination with the micro-dilatant continuum formulation.

Table 6-1: basic set of parameters used for numerical simulations in plane strain conditions.

Parameter	Values	Units
E	10000	MPa
ν	0.3	-
α	$-7.45e^{-2}$	MPa ⁻¹
β	1.43	-
γ	10.63	MPa
δ	1.765	-
r_{ha0}	0.416	-
χ_h	$4.0e^{-3}$	-
ψ_h	$4.0e^{-2}$	-
α_d	$1.5e^{-2}$	-
β_d	0.3	-
β_θ	0.73	-
a	0.1	MPa m ²

A first set of three analyses is performed. Firstly, the model is analyzed in homogeneous conditions. In order to achieve this condition and avoid the formation of a localized solution, the trigger of the defect is de-activated and strength is homogeneous in all the sample. Then, an analysis in presence of the defect is performed without employing any regularization technique. Finally, a third analysis in presence of a defect and with the second gradient of dilation formulation is performed.

Figure 6-2a shows the vertical force as a function of the vertical displacement for three cases: the homogeneous case, where no localization takes place; the non-regularized solution with localized inelastic strains and the regularized solution. The second gradient of dilation formulation works properly in combination with the damage-plasticity model proposed, as the regularized solution represents an intermediate case between the homogeneous solution (maximum energy dissipation) and the localized non-regularized solution (minimum energy dissipation). Snap-back phenomena are observed in the localized non-regularized case and in the localized case with regularization, while, as expected, the homogeneous solution does not show this type of phenomena. The load control technique employed showed its ability to follow the snap-back branch for the proposed case. Figure 6-2b shows a zoom of Figure 6-2a, so that the effect of the regularization in terms of inelastic softening behavior can be better appreciated. The bifurcation point is close to the maximum of stress and represents the onset of localization.

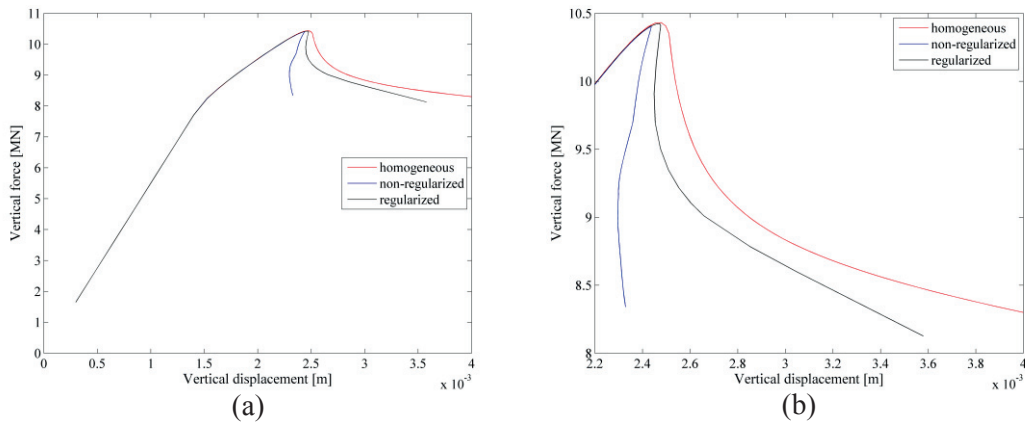


Figure 6-2: vertical displacement vs vertical total force acting on the top boundary of the three tests: homogeneous solution, non-regularized solution and second gradient of dilatancy regularization (a). Zoom in the displacement-force curve to highlight how the regularized solution is placed between the two extreme solutions in terms of dissipation (b): the non-regularized solution represents the lower limit of dissipation (with snap-back phenomenon) while the homogeneous solution represents the upper limit in terms of energy dissipation.

Figure 6-3a displays the distribution of damage in the deformed specimens at the end of the analyses for the localized non-regularized solution and Figure 6-3b for the localized solution obtained with micro-dilatant continua formulation. When no regularization is employed, localization takes place and concentrates on a band which is the size of the smallest element. This can be well seen in Figure 6-3a. Damage concentrates on a band which is roughly the size of the smallest elements, dissipation is the minimum possible and a strong and pronounced snap-back is observed (Figure 6-2). In the case of micro-dilatant continua, Figure 6-3b shows that the localization of damage is controlled and the band has a given size, which, for the assumed parameters, is of roughly, 8 elements wide.

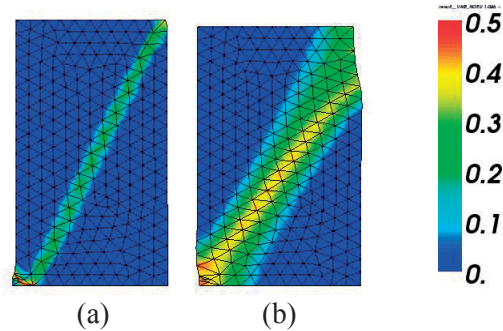


Figure 6-3: Distribution of damage for the non-regularized case (a) and the regularized one (b), deformation factor of 20.

6.5.2. Effects of the second gradient of dilatancy regularization

In the following, only the analysis carried out with the localization control technique of the second gradient of dilatancy is retained. Figure 6-4a reports the evolution of damage and Figure 6-4b the evolution of the plastic multiplier along a vertical cut line in the middle of the sample. Figure 6-7a shows the evolution of the active plastic zone distribution inside the sample at the onset of localization and Figure 6-7b at the end of the analysis. From both figures, the effect of the non-associated potential can be appreciated. The degree of regularization that is offered by the micro-dilatant continua finally depends on the evolution of the macro-dilation, as micro and macro-dilation are set to be equal, i.e., $\chi = \varepsilon_{kk}$.

Figure 6-4a shows the evolution of damage. The effect of the regularization is observed by the creation of a band of a given size. During the loading process damage increases but the band does not expand indefinitely. This is confirmed by the evolution of the plastic multiplier, i.e., the active plastic zone in the model (Figure 6-4b), which increases in magnitude but shows a decrease in the band size. The phenomenon is attributed to the non-associated potential: volumetric plastic strain is stopped at a certain value of the plastic strain norm and the regularization effect decreases, avoiding therefore spurious expansion of the localization band upon deformation. This effect is somehow similar to what is observed in the model of Fleck and Hutchinson (1993, 1997) as reported in Jirásek and Rolshoven (2009). It differs from the classical behavior of micro polar continua with non-linear softening branches (Jirásek and Rolshoven 2009), where the regularization acts on the purely elastic strains. Before reaching bifurcation, the plastic zone is still homogeneous and it localizes in a band in the softening phase. The band remains with a more or less constant thickness while it changes inclination when the behavior becomes non-associated.

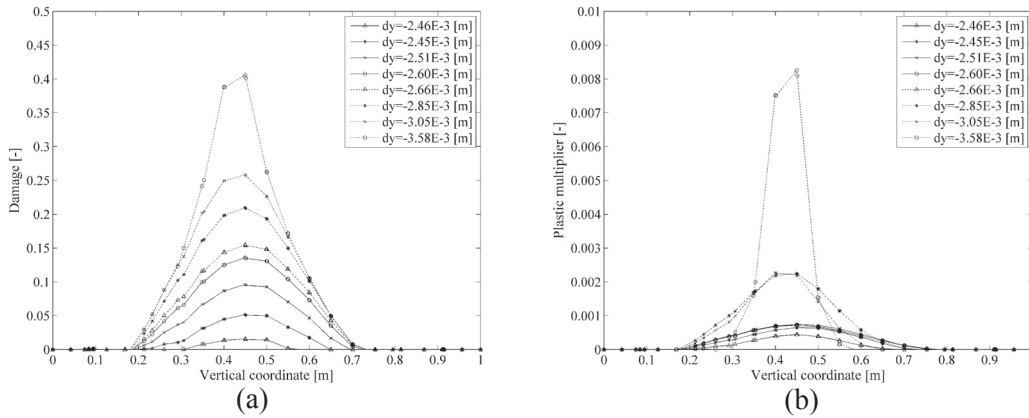


Figure 6-4: Evolution of damage distribution along a vertical cut in the middle of the specimen (a). The non-associated constitutive law does not allow the localized band to indefinitely expand upon plastic deformation. Evolution of the plastic multiplier distribution along a vertical cut in the middle of the specimen (b). It can be better appreciated how the plastic increment is narrowed during the deformation process in the softening regime so that no further expansion of the localized is possible.

Figure 6-5 shows the evolution of the damage field in the specimen. The sequence of images corresponds to an increase in the loading curve from top left to bottom right. The instances shown in Figure 6-5 are represented by the curve plotted in Figure 6-6. Localization is triggered first by the imperfection placed in the bottom left of the specimen, the band then starts to develop and expand in the specimen during the softening response while damage keeps increasing. Excessive expansion is then stopped by the non-associated plastic behavior and the thickness of the damage band remains quite constant without unphysical expansions.

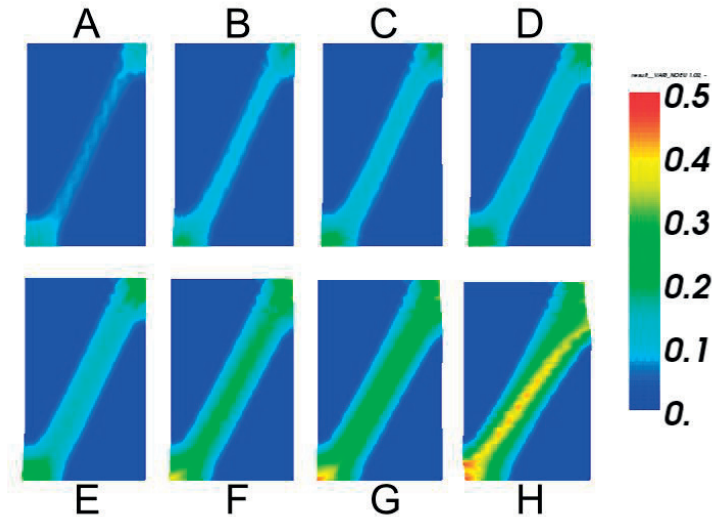


Figure 6-5: evolution of damage in the specimen for the regularized case with given parameters (deformation factor of 20).

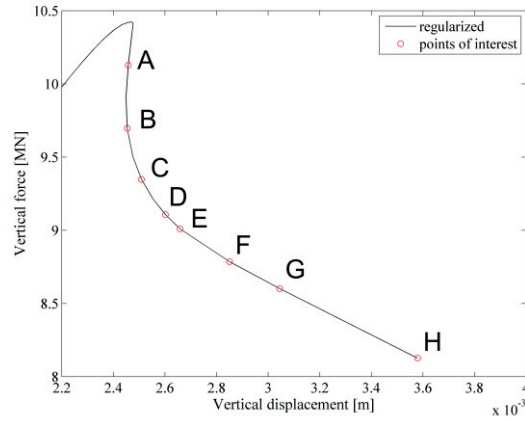


Figure 6-6: plot of the points of interests in the force vs displacement curve. At these points is shown, in Figure 6-5, the distribution of damage inside the model.

Figure 6-7a illustrates the evolution of the plastic active zone (in red) inside the specimen with the deformation process at the onset of localization and Figure 6-7b at residual conditions. The inclination of the band depends on the dilatancy coefficient. It is a known result and, e.g., for a granular material in biaxial compression conditions, the following expression of the inclination angle of the localization zone ω was proposed by (Vardoulakis, 1980)

$$\omega = 45^\circ + \frac{1}{4}(\phi + \psi), \quad (6.19)$$

where ϕ is the friction angle and ψ is the dilatancy angle. In the present case, as $\beta = 1.43$, theoretical predictions yield $\omega = 62.6^\circ$ at bifurcation and $\omega = 53.8^\circ$ when dilatancy equals zero. A rough estimate from the results of the numerical analyses gives values of $\omega = 63.4^\circ$ at bifurcation point (i.e., $dy = 2.45 \times 10^{-3} m$) and $\omega = 60.9^\circ$ at final residual conditions (i.e., $dy = 3.60 \times 10^{-3} m$), which shows the effect of the non-associated potential also in terms of inclination of the localized band.

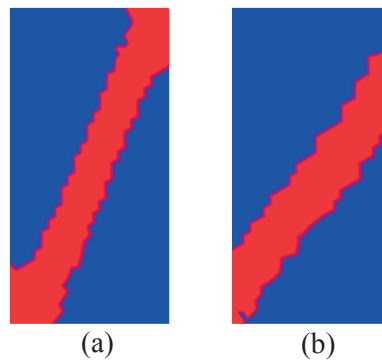


Figure 6-7: evolution of plastic active zone for the regularized case with given parameters at the onset of localization (immediate post-peak) (a) and at the end of the deformation process ($dy=3.6e-3$ m) (b).

Figure 6-8a shows the distribution inside the specimen of vertical strain and Figure 6-8b displays the vertical displacement distribution, both at the end of the softening phase ($dy = 3.60 \times 10^{-3} m$). Vertical displacement field shows that the sample is deforming almost rigidly with an upper triangle sliding with rigid body motion above a lower triangle. The two are separated by the localized band, as shown in Figure 6-8b in the vertical strain field, where it can be seen that all the deformation of the specimen is there concentrated. The deformed mesh at the final step compared to the initial configuration is shown in Figure 6-9a, while the field of global displacement vectors is shown in Figure 6-9b. This deformation modality was detected in most of the experimental tests in triaxial conditions in, e.g., Opalinus Clay (Gräsle and Plischke, 2011). Although this test is a biaxial compression in plane strain conditions, the pattern is similar.

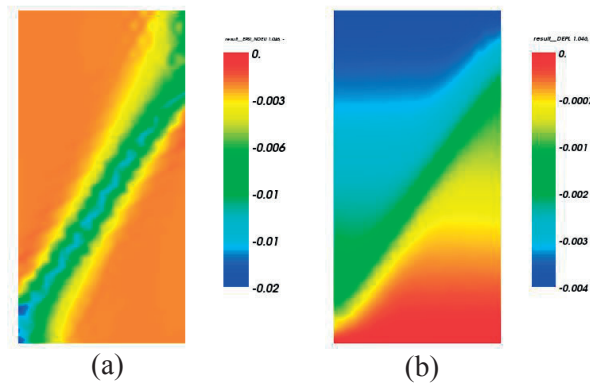


Figure 6-8: final fields of vertical strain (a) and vertical displacement (b) for the regularized case with given parameters.

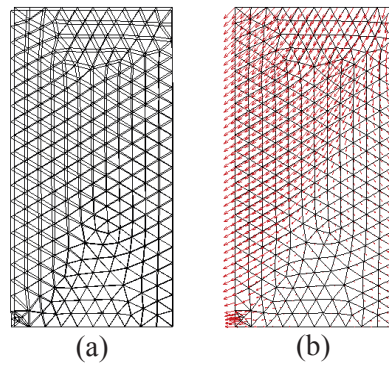


Figure 6-9: deformed mesh at the end of the loading process (a) and displacement vector field (b) with amplification factor of 3.

6.5.3. Element size influence

In this section the dependency of the results with the micro dilatant continuum formulation on the mesh size are investigated. A second finer mesh is built within the same specimen and is subjected to the same loading and boundary conditions, as well as material parameters. The first is a medium mesh employed in the previous sections and containing 483 elements, while the second is refined and contains 1839 elements.

Figure 6-10a shows the comparison between the two meshes in terms of vertical force as a function of vertical displacement and Figure 6-10b for damage evolution at the mid-point of the specimen. Results show that with the micro dilatant continuum formulation, the proposed plastic-damage model with softening does not show pathological mesh dependency. The curves for the two models almost coincide, so that we can state that the proposed solution offers proper regularization and overcomes the ill-posedness of the problem even when coupled with plastic-damage models. Upon mesh refinement the solution remains stable and the predicted energy dissipation does not decrease as will happen when no regularization technique is employed. Figure 6-11 shows the comparison of the damage field distribution for the two meshes under study at $dy = 2.52 \times 10^{-3} m$. The thickness of the localized band remains constant for the two models and no mesh dependency appears.

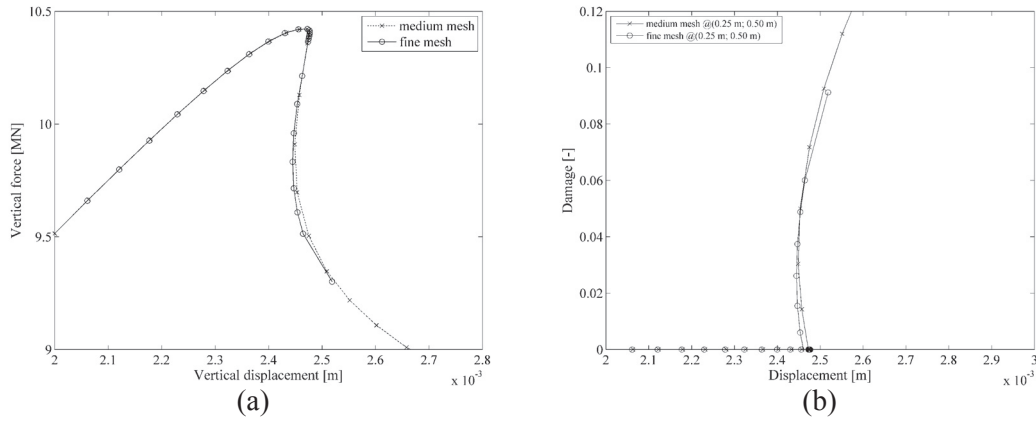


Figure 6-10: zoom of vertical force vs vertical reaction comparison for the medium and fine mesh (a) and evolution of damage at the center point (b).

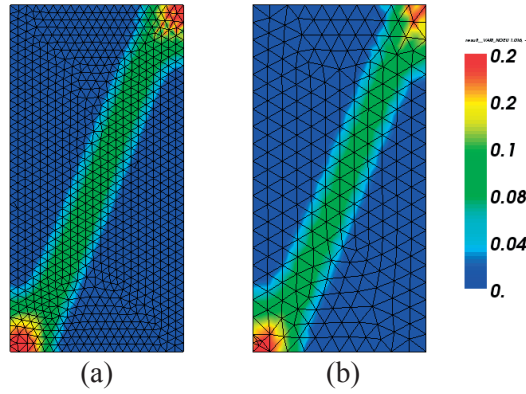


Figure 6-11: damage for finer mesh (a) and for coarser mesh (b).

6.5.4. Non-associativity effect

In order to get more insights into the mechanical behavior of the proposed constitutive model with the micro dilatant regularization technique, the effect of the non-associativity parameter is studied. Since the regularization effect is based on the volumetric dilatant strain, a non-associated plastic potential will have a direct influence in the localization control. The non-associativity has the effect of avoiding unphysical expansion of the localized band, which in turn will lead to homogeneous conditions with inelastic loading. With the non-associated formulation, the volumetric strain is not allowed to grow indefinitely. The regularization effect is at a certain point stopped, so that the localized band thickness remains constant. To highlight this effect, a case with reduced values of ψ_h was analyzed. The new value of ψ_h is 1×10^{-2} , which will, in turn, have the effect of anticipating, in the stress-strain

behavior, the limiting of the regularization effects. In other words, regularization will be stopped earlier in the loading process. Numerical model and loading conditions are the same as for the previous analysis.

A first analysis at material point level is performed to understand the effects of the parameter ψ_h in the stress-strain curve. Figure 6-12 shows the comparison at material point level between the values of the two parameters. In the deviatoric stress as function of the axial strain the curve with less deviatoric strain ($\psi_h = 1 \times 10^{-2}$) appears with a less brittle behavior (Figure 6-12a), showing higher values of residual stress compared to the case of $\psi_h = 4 \times 10^{-2}$. This is due to the fact that the curves are plotted as a function of the axial strain ε_a . Since damage softening depends on a measure of plastic deviatoric strain increment, the behavior coincides when both curves are plotted as a function of the deviatoric strain ε_q . For a given vertical strain, the volumetric strain is smaller for the case of $\psi_h = 4 \times 10^{-2}$, which implies that the deviatoric strain ε_q is greater for $\psi_h = 4 \times 10^{-2}$ compared to $\psi_h = 1 \times 10^{-2}$. This in turn implies that the deviatoric stress q will be higher for $\psi_h = 1 \times 10^{-2}$. The apparent less brittleness in the $q - \varepsilon_a$ plot is therefore explained by the fact that for a given ε_a it corresponds a greater value of q for $\psi_h = 1 \times 10^{-2}$.

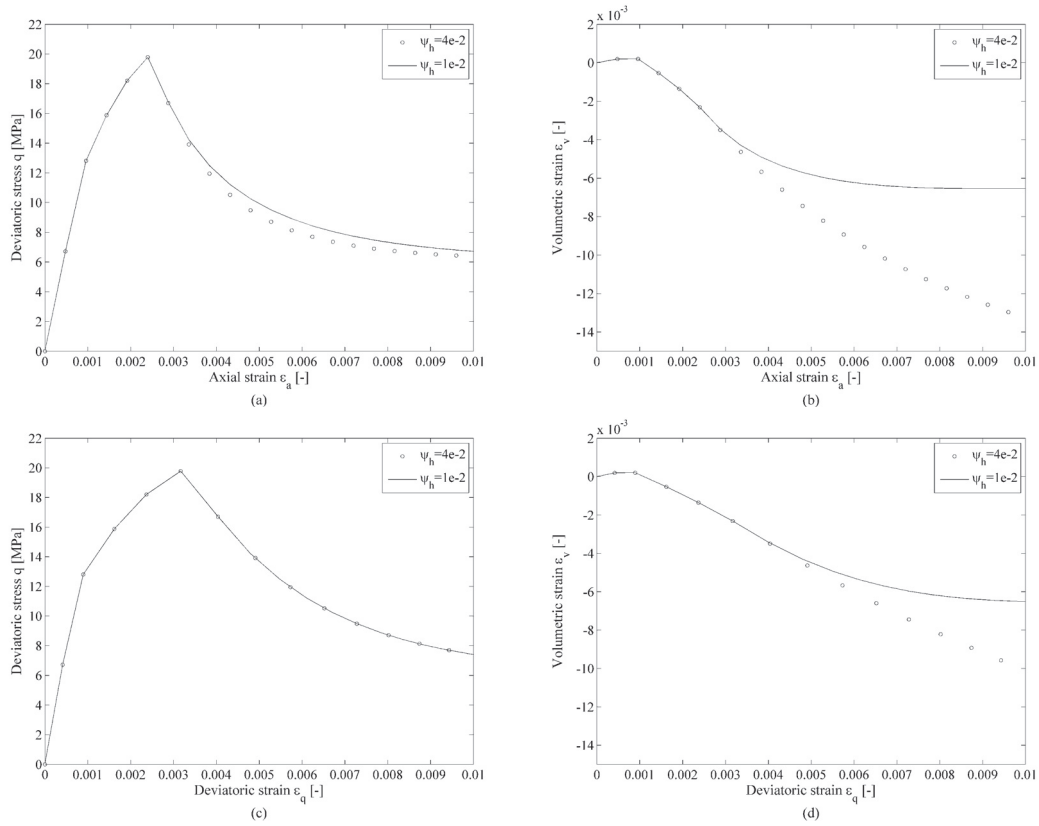


Figure 6-12: effect of the dilation parameter at material point level in the deviatoric stress vs vertical strain (a), volumetric strain vs vertical strain (b), deviatoric stress vs deviatoric strain (c) and deviatoric stress vs volumetric strain (d).

The two cases of biaxial compression are then performed. The first one was already illustrated in section 6.5.2, while the second one has all the same characteristic except the value of ψ_h which now is 1×10^{-2} .

Figure 6-13 shows the comparison between results of the plane strain compression model in terms of vertical force as a function of vertical displacement. For the case where less dilatancy is allowed, the apparent less brittleness is also observed as well as a second instability appearing in the softening phase. The latter phenomenon is due to the fact that when dilatancy does not take place anymore due to non-associativity, the effects of regularization are stopped. As previously mentioned, this type of secondary instability is similar to the one observed in the Fleck and Hutchinson model by (Jirásek and Rolshoven, 2009).

Figure 6-14 illustrates damage (a) and plastic multiplier (b) distribution along a vertical line cutting the specimen at its center. The plastic multiplier distribution localizes into a narrower band when dilatancy tends to zero, resulting in a damage increase within more or less the

same thickness of the localized plastic multiplier distribution. Although this prevent the phenomenon of non-physical localized band expansion, particular care must be placed when selecting the parameter ψ_h for numerical analyses in combination with second gradient of dilation regularization technique. Values that are too small might lead to instabilities in the behavior, where the inelastic strains and damage localize once again into a narrow band.

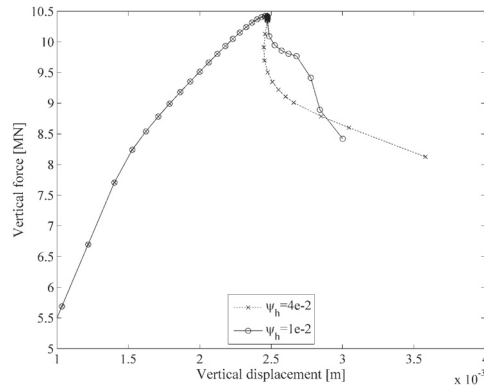


Figure 6-13: vertical force vs vertical displacement with influence of the non-associated parameter.

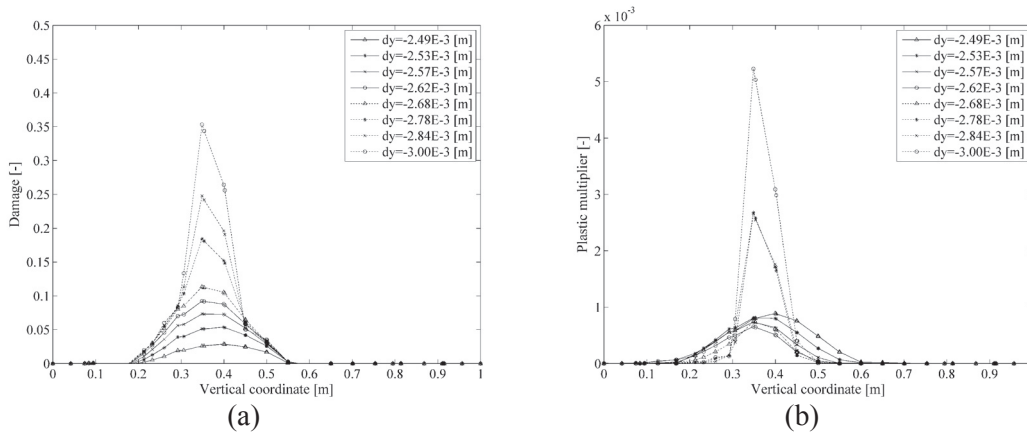


Figure 6-14: damage distribution (a) and plastic multiplier evolution along vertical central line (b) for the case with less dilatancy.

Figure 6-15 shows the evolution of damage distribution in the model for the two cases. At the top, the case of $\psi_h = 4 \times 10^{-2}$ is shown and the one for $\psi_h = 1 \times 10^{-2}$ is shown at the bottom. The effect of the non-associated parameter can be well appreciated in terms not only of the band thickness, as was previously stated, but also on the band inclination. The inclination of the localized band depends on the dilatancy angle for a Drucker-Prager non-associated plasticity.

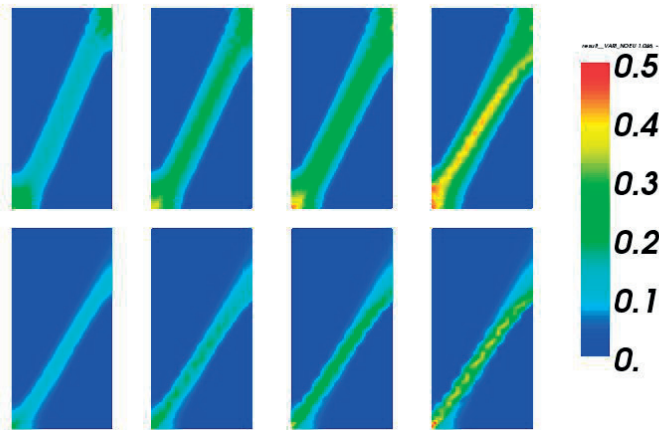


Figure 6-15: damage evolution for the case of $\psi_h = 4 \times 10^{-2}$ (top) and for the case of $\psi_h = 1 \times 10^{-2}$ (bottom).

6.5.5. Confinement effect

The following set of numerical analyses is dedicated to investigate the effect that confinement has on the structural behavior of the numerical model in plane strain compression conditions. Four additional cases for numerical analyses were prepared, with material parameters given in Table 6-1. The first phase now consists in applying a confining pressure at the top and sides of the specimen, then vertical strain increment is applied at the top and lateral confining pressure is kept constant. The applied confining pressures in the first phase for the four cases are 1 MPa, 3 MPa, 6 MPa and 10 MPa, respectively.

Figure 6-16 shows the results in terms of damage distribution inside the sample for the four different confinements, which are increasing from top left to bottom right. With an increase in confining pressure, the thickness of the shear band decreases. This is once again due to the fact that regularization depends on volumetric dilatant strains. With higher confinements, the global dilation becomes smaller and therefore the regularizing effect of the micro dilation continuum as well. Analogous results were found in numerical analysis with micropolar continua in the work of Alshibli et al. (2006). The state of stress has also an influence in the orientation of the localization band. The shear band thickness should therefore be investigated for a given range of confinements of a specific application when employing micro dilatant continuum regularization.

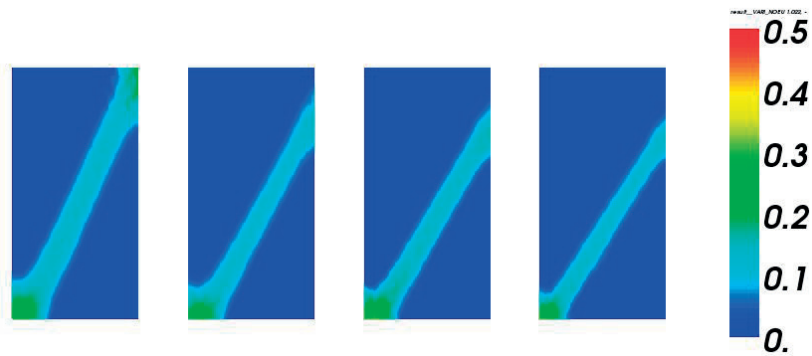


Figure 6-16: damage distribution with increasing confinement from left to right of 1 MPa, 3 MPa, 6 MPa and 10 MPa.

6.5.6. Anisotropy effect

The effects that accounting for the anisotropic behavior has on the results on biaxial compression are studied with a set of three additional numerical examples. In this case the material parameters used for the simulations are reported in Table 6-2, with the addition of the anisotropic parameters characterizing Equation (5.33). The anisotropic parameters were obtained from a calibration procedure on selected results on triaxial tests on OPA from (Gräsle and Plischke, 2010). As the numerical study is a demonstrative example, the material parameters set is not pretended to be fully representative of the behavior of OPA. The numerical analyses are conducted on three different numerical models, all based on the one illustrated in Figure 6-1. The difference between the three models consists in the inclination of the weakness planes (bedding planes) with respect to the horizontal axis. Three directions are considered in the study, 0° (horizontal beddings), 45° and 90° (vertical beddings).

A first set of numerical analyses is performed to illustrate the constitutive behavior in presence of transversal anisotropic strength. The analyses are performed on a single element tri-dimensional cubic model with no confinement, so that maximum stress represents the unconfined compression strength (UCS) for the given set of material parameters. The tests are performed with different inclinations of the bedding planes. Figure 6-17a shows the results in terms of vertical stress as a function of vertical strain for three different inclinations of the bedding planes. It can be appreciated the effect of anisotropic plasticity in terms of UCS dependence on the bedding inclination. The maximum strength is reached with vertical planes configuration and the minimum in this case is when beddings strike with a dip of 45° . The configuration with horizontal beddings has a smaller strength compared to the one where beddings are vertical. A secondary effect of considering anisotropic strength, is that brittleness is direction dependent. It results from the specific form of the constitutive equations adopted. Damage acts as a softening control mechanism by reducing peak strength

at a rate given by parameter α_d . As maximum strength decreases, the post-peak stress drop (softening) is smaller on the same strain evolution. This implies a decreased brittleness, as evidenced in Figure 6-17a.

Table 6-2: set of parameters used for numerical simulations in plane strain conditions with anisotropic plastic behavior.

Parameter	Values	Units
E	2000	MPa
ν	0.35	-
α	$-7.45e^{-2}$	MPa ⁻¹
β	1.03	-
γ	3.22	MPa
δ	1.0	-
r_{ha0}	0.7	-
χ_h	$4.0e^{-3}$	-
ψ_h	$4.0e^{-1}$	-
α_d	$1.5e^{-2}$	-
β_d	0.3	-
β_θ	0.674	-
Ω	1.1	-
d_1	2.2	-
d_2	0.64	-
a	0.1	MPa m ²

Figure 6-17b illustrates the load displacement curves obtained from the FEM results in biaxial compression configuration. The numerical model (mesh and boundary conditions) is illustrated in Figure 6-1, while every curve in Figure 6-17b corresponds on a different inclination of the bedding planes. A first phase is carried out where a confinement of 6 MPa is applied, then shearing is performed by applying a vertical displacement with the load-control method illustrated in Section 6.4. The effects of anisotropy can be observed also in presence of localized behavior. In particular, the effects on the maximum strength are equivalent to what was observed at the constitutive level, where maximum strength is reached at 90° inclination of the beddings, minimum at 45° and the configuration with horizontal beddings (0°) shows intermediate values of strength. Of particular interest, in this case, is the reduced brittleness at lower values of strength. As can be observed from the load displacement curve in Figure 6-17b, while the sample at 90° shows an abrupt stress drop in the post-peak phase (highly brittle), the sample at 45° shows a more ductile behavior (quasi-brittle) and a less pronounced stress drop. The sample at 0° has intermediate values of brittleness.

We believe that localization has an additional effect in reducing/increasing brittleness compared to results at material point level. More specifically, when the constitutive response

shows more brittleness in the post-peak phase (e.g., beddings at 90°), the localized band is narrower, resulting in smaller dissipated energy that turns in an even more brittle structural response. Localization, in this case, acts as brittleness amplifier of what is observed in terms of the constitutive response. The confirmation of this behavior can be observed in Figure 6-18, where the damage distribution at the end of the analyses is shown for samples at 90° (Figure 6-18a), 45° (Figure 6-18b) and 0° (Figure 6-18c). The size of the damage localization band is inversely proportional to the maximum strength, i.e., higher strength will show more brittleness in the post peak-phase.

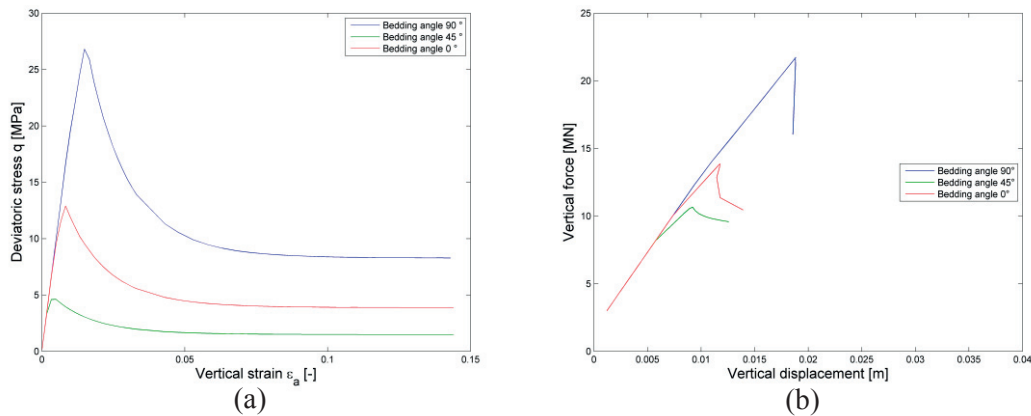


Figure 6-17: constitutive response at the material point level for different inclinations of the bedding planes (a) and load displacement curve for different inclinations of the bedding planes in biaxial compression conditions with localized behavior (b).

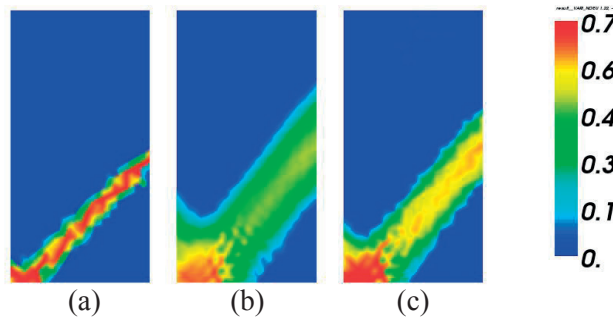


Figure 6-18: damage distribution for different inclinations of the bedding planes, 90° (a), 45° (b) and 0° (c).

6.5.7. Upscaling size

Finally, we illustrate the upscaling of the second gradient of dilatancy elastic parameter. To do so, results of analyses based on a model of 0.5×1 m size are compared to results obtained based on a model of 5×10 m. For simplicity, the first model will be called the “small” one and the second the “big” one. Both models boundary and loading conditions are the same one

illustrated for the previous analyses in Figure 6-1. The material parameters are the same as the ones illustrated in Table 6-2. The only difference between the big and small model resides in the value of the second gradient of dilatancy parameter a . As the area of the big model is 100 greater than the small one, the second gradient of dilatancy parameter a is increased equivalently. For the small model, such value is 0.1 MPa m^2 , while for the big model is 10 MPa m^2 . The analyses of both models are performed in plane strain conditions, with an applied confinement of 6 MPa . The anisotropic configuration is with beddings inclined at 45° .

Figure 6-19 illustrates the comparison between results from the big and the small model in terms of normalized load displacement curves. The force is normalized by dividing it by the length of the horizontal side and the displacement is normalized by dividing its values by the length of the vertical side. The normalization is performed to obtain a measure of global stresses and strains, so that different sizes can be directly compared. The comparison in Figure 6-19 shows that the proposed way of upscaling the parameter controlling the second gradient of dilatancy response produces the same normalized load displacement curve between small and big model. In other words, although the dissipated energy is greater in the big model compared to the small one, the response is equivalent in terms of global measures of stresses and strain.

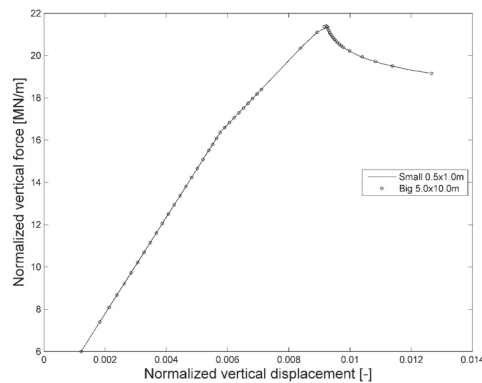


Figure 6-19: load displacement curve comparison of the two sizes models in terms of normalized variables.

Figure 6-20 shows the distribution of damage at the last point of the analyses for the small model (Figure 6-20a) and the big model (Figure 6-20b). In this visualization, both model have been scaled to result having the same size. While this is useful for a direct visual comparison, the damage distribution in both model at their real size is illustrated in Figure 6-21. From Figure 6-20 we can appreciate the fact that the localized damage has an equivalent nature in

both samples, although the absolute size of the localized are differs in the two models as illustrated in Figure 6-21.

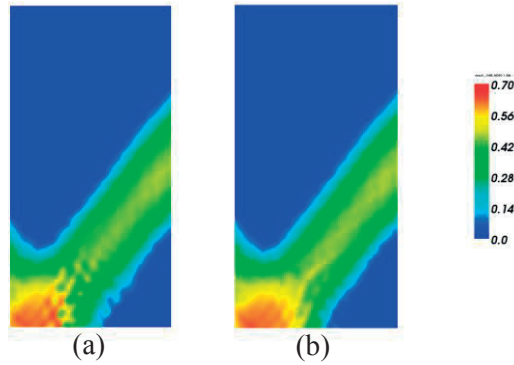


Figure 6-20: damage distribution for two different sizes of the specimen, 0.5x1.0m (a) and 5x10m (b).

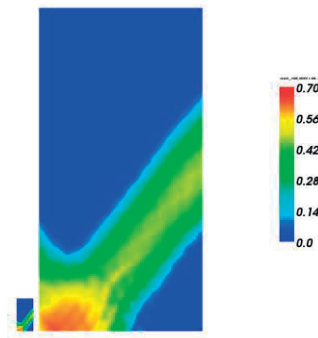


Figure 6-21: damage distribution comparison for the two sizes of the specimen at real scale.

It has to be kept in mind that in doing upscaling (or, alternatively, downscaling), the size of the localized damage band can be controlled to deliver the same response in terms of stresses and strains. On the contrary, if the parameter controlling the second gradient of dilatancy remains unchanged, dissipation becomes smaller upon increasing size and the global response becomes more brittle. Size dependency of the mechanical response can be accounted for in the proposed anisotropic plastic-damage model coupled with the second gradient of dilatancy. There is, at present, still some uncertainties on what is the localized damage representative of and what should be the size of the localized band. As an example, while at small laboratory scale size, the localized damage band could be representative of a condensed zone of microcracks that are responsible for the failure of the specimen, at large geological scale, the localized damage band could be representative of large faults of several meter depth with many interconnected fractures. As in continuum damage mechanics the damage variable

represents the density of defects in a certain volume (surface), the localized size depends strongly on the scale at which the problem is analyzed.

6.6. Conclusions

The proposed coupled plastic-damage model MS3 was implemented in the FEM solver *Code_Aster*, which offers the possibility of performing regularized computations with a second gradient of dilation formulation (Fernandes, 2009; Fernandes et al., 2008). This enhanced description of the continuum introduces a spatial dependency on the equilibrium equation, which is equivalent to introduce an internal length, and has regularizing effects in boundary value problems.

The motivation of such a choice is related to the fact that the plastic damage model MS3 exhibits softening in the post-peak phase of the mechanical response, and suffers therefore from pathological mesh dependency given the ill-posedness of the problem (so called loss of ellipticity). In the present contribution, the combined effect of the plastic-damage model and the second gradient of dilatancy continuum was investigated with a series of numerical examples in biaxial plane strain conditions.

The regularization technique proved to be effective in delivering physically meaningful solutions. The dissipated energy and the size of the localized inelastic band are function of the softening modulus, second gradient elastic parameter and the non-associated potential. An internal length is introduced in the continuum description and the ill-posedness of the problem can be overcome. The effects of a non-associated plastic potential on the localization of strains are investigated. As regularization depends on dilatancy, the non-associated variable (i.e., the evolution of the dilatancy angle) has a direct effect on the size of the localized inelastic band. On the one hand, this allows to control the size of the localization and avoiding spurious band expansion. On the other hand, particular care in the choice of model parameters must be put in order to avoid secondary instabilities in the post-peak phase. Upon mesh refinement the solution remains stable, with a structural response that does not depend on the element size. The non-associativity shows to have an effect in the orientation of the shear band. This is in agreement with previous theoretical and experimental findings. Numerical analyses where lateral confinement was applied, shows as well a direct dependence of the size of the localization band on the state of stress. A higher mean stress implies a global lower dilatancy, which in turn will result in a smaller localized zone. The anisotropic plasticity plays a major role not only by influencing the maximum strength, but also by influencing the post-peak response, which becomes more brittle in configuration when higher strength is available (in this case, vertical beddings). An upscaling example was proposed, showing the importance that size effects have in the global structural response. The

value of the parameter controlling the second gradient of dilatancy should depend on the size of the investigated problem.

Finally, the proposed framework can be used to deliver physically meaningful numerical predictions for quasi-brittle dilatant geomaterials in the presence of mechanical instabilities related to the softening behavior. The coupled plastic-damage model MS3 with the second gradient of dilatancy framework will be furtherly employed for numerical predictions of tunnel excavation in Opalinus Clay at the Mont Terri site, Switzerland.

6.7. Acknowledgements

The authors would like to acknowledge Swisstopo, ENSI and the Mont Terri Project for the financial support to this work. Authors wish to thank Dr. Sylvie Granet, Dr. Roméo Fernandes and Dr. Simon Raude of EDF R&D for the precious insight of the second gradient of dilatancy modeling in *Code_Aster*.

6.8. References

- [R5.03.80], 2013. Méthodes de pilotage du chargement. Documentation version 12, Code_Aster, www.code-aster.org.
- [R5.04.03], 2013. Modélisation second gradient. Documentation version 12, Code_Aster, www.code-aster.org.
- Aifantis, E., 1984. On the microstructural origin of certain inelastic models. *Journal of Engineering Materials and technology* 106, 326-330.
- Alessi, R., Marigo, J.-J., Vidoli, S., 2015. Gradient damage models coupled with plasticity: Variational formulation and main properties. *Mech Mater* 80, Part B, 351-367.
- Alshibli, K.A., Alsaleh, M.I., Voyiadjis, G.Z., 2006. Modelling strain localization in granular materials using micropolar theory: numerical implementation and verification. *Int J Numer Anal Met* 30, 1525-1544.
- Angelini, O., Chavant, C., Chénier, E., Eymard, R., Granet, S., 2011. Finite volume approximation of a diffusion-dissolution model and application to nuclear waste storage. *Mathematics and Computers in Simulation* 81, 2001-2017.
- Bažant, Z., Lin, F.B., 1988. Non-local yield limit degradation. *Int J Numer Meth Eng* 26, 1805-1823.
- Bažant, Z.P., Jirásek, M., 2002. Nonlocal integral formulations of plasticity and damage: survey of progress. *Journal of Engineering Mechanics*.
- Bažant, Z.P., Oh, B.H., 1983. Crack band theory for fracture of concrete. *Matériaux et construction* 16, 155-177.

- Bazant, Z.P., Pijaudier-Cabot, G., 1988. Nonlocal continuum damage, localization instability and convergence. *Journal of applied mechanics* 55, 287-293.
- Bennion, B., Bachu, S., 2008. Drainage and imbibition relative permeability relationships for supercritical CO₂/brine and H₂S/brine systems in intergranular sandstone, carbonate, shale, and anhydrite rocks. *SPE Reservoir Evaluation & Engineering* 11, 487-496.
- Borja, R.I., 2004. Cam-Clay plasticity. Part V: A mathematical framework for three-phase deformation and strain localization analyses of partially saturated porous media. *Comput Method Appl M* 193, 5301-5338.
- Bossart, P., Meier, P.M., Moeri, A., Trick, T., Mayor, J.-C., 2002. Geological and hydraulic characterisation of the excavation disturbed zone in the Opalinus Clay of the Mont Terri Rock Laboratory. *Eng Geol* 66, 19-38.
- Bossart, P., Trick, T., Meier, P.M., Mayor, J.C., 2004. Structural and hydrogeological characterisation of the excavation-disturbed zone in the Opalinus Clay (Mont Terri Project, Switzerland). *Appl Clay Sci* 26, 429-448.
- Chambon, R., Caillerie, D., El Hassan, N., 1998. One-dimensional localisation studied with a second grade model. *European Journal of Mechanics-A/Solids* 17, 637-656.
- Chambon, R., Caillerie, D., Matsushima, T., 2001. Plastic continuum with microstructure, local second gradient theories for geomaterials: localization studies. *Int J Solids Struct* 38, 8503-8527.
- Charlebois, M., Jirásek, M., Zysset, P.K., 2010. A nonlocal constitutive model for trabecular bone softening in compression. *Biomechanics and modeling in mechanobiology* 9, 597-611.
- Chen, L., Shao, J.F., Zhu, Q.Z., Duvieu, G., 2012. Induced anisotropic damage and plasticity in initially anisotropic sedimentary rocks. *Int J Rock Mech Min* 51, 13-23.
- Chiarelli, A.S., Sibai, M., Shao, J.F., Hoteit, N., 1999. Modeling of anisotropic elastoplastic damage in shale rocks. *Numerical Models in Geomechanics - Numog Vii*, 21-26.
- Collin, F., Chambon, R., Charlier, R., 2006. A finite element method for poro mechanical modelling of geotechnical problems using local second gradient models. *Int J Numer Meth Eng* 65, 1749-1772.
- Comi, C., 1999. Computational modelling of gradient-enhanced damage in quasi-brittle materials. *Mechanics of Cohesive-frictional Materials* 4, 17-36.
- Cosserat, E., Cosserat, F., 1909. *Théorie des corps déformables*. Paris.
- Crisfield, M.A., 1981. A Fast Incremental-Iterative Solution Procedure That Handles Snap-Through. *Comput Struct* 13, 55-62.
- Das, A., Buscarnera, G., 2014. Simulation of localized compaction in high-porosity calcarenite subjected to boundary constraints. *Int J Rock Mech Min* 71, 91-104.

- Das, A., Nguyen, G.D., Einav, I., 2013. The propagation of compaction bands in porous rocks based on breakage mechanics. *Journal of Geophysical Research: Solid Earth* 118, 2049-2066.
- De Borst, R., Mühlhaus, H.-B., 1992. Gradient-dependent plasticity: formulation and algorithmic aspects. *International Journal for Numerical Methods in Engineering* 35, 521-539.(1992).
- De Borst, R., Pamin, J., 1996. Some novel developments in finite element procedures for gradient-dependent plasticity. *Int J Numer Meth Eng* 39, 2477-2505.
- De Borst, R., Pamin, J., Geers, M.G., 1999. On coupled gradient-dependent plasticity and damage theories with a view to localization analysis. *European Journal of Mechanics-A/Solids* 18, 939-962.
- De Borst, R., Sluys, L., Mühlhaus, H.-B., Pamin, J., 1993. Fundamental issues in finite element analyses of localization of deformation. *Eng Computation* 10, 99-121.
- De La Vaissière, R., Gerard, P., Radu, J.P., Charlier, R., Collin, F., Granet, S., Talandier, J., Piedevache, M., Helmlinger, B., 2014. Gas injection test in the Callovo-Oxfordian claystone: Data analysis and numerical modelling, *Geological Society Special Publication*, pp. 427-441.
- Fernandes, R., 2009. Modélisation numérique objective des problèmes hydromécaniques couplés dans le cas des géomatériaux. Thèse de doctorat à l'école doctorale Université jean Fourier (Grenoble1), 107-136.
- Fernandes, R., Chavant, C., Chambon, R., 2008. A simplified second gradient model for dilatant materials: theory and numerical implementation. *Int J Solids Struct* 45, 5289-5307.
- Fleck, N., Hutchinson, J., 1993. A phenomenological theory for strain gradient effects in plasticity. *J Mech Phys Solids* 41, 1825-1857.
- Fleck, N., Hutchinson, J., 1997. Strain gradient plasticity. *Advances in applied mechanics* 33, 296-361.
- Forest, S., Lorentz, E., 2004. Localization phenomena and regularization methods. *Local Approach to Fracture*. Paris, Les Presses de l'Ecole des Mines, 311-371.
- François, B., Laloui, L., Laurent, C., 2009. Thermo-hydro-mechanical simulation of ATLAS in situ large scale test in Boom Clay. *Comput Geotech* 36, 626-640.
- Gräsle, W., Plischke, I., 2010. Laboratory Testing (LT) Experiment: Mechanical Behavior of Opalinus Clay, Final report from Phases 6 – 14. Mont Terri Technical Note TN 2009-07.
- Gräsle W., Plischke I., 2011. LT-A Experiment: Mechanical Behavior of Opalinus Clay, Data Report from Phase 15.

- Grassl, P., 2009. On a damage-plasticity approach to model concrete failure. Proceedings of the Institution of Civil Engineers: Engineering and Computational Mechanics 162, 221-231.
- Grassl, P., Jirásek, M., 2006. Damage-plastic model for concrete failure. *Int J Solids Struct* 43, 7166-7196.
- Haddag, B., Abed-Meraim, F., Balan, T., 2009. Strain localization analysis using a large deformation anisotropic elastic-plastic model coupled with damage. *Int J Plasticity* 25, 1970-1996.
- Jirásek, M., 2007. Mathematical analysis of strain localization. *Revue Européenne de Génie Civil* 11, 977-991.
- Jirásek, M., Bauer, M., 2012. Numerical aspects of the crack band approach. *Comp & Struct* 110, 60-78.
- Jirásek, M., Rolshoven, S., 2003. Comparison of integral-type nonlocal plasticity models for strain-softening materials. *Int J Eng Sci* 41, 1553-1602.
- Jirásek, M., Rolshoven, S., 2009. Localization properties of strain-softening gradient plasticity models. Part I: Strain-gradient theories. *Int J Solids Struct* 46, 2225-2238.
- Lemaitre, J., Desmorat, R., Sauzay, M., 2000. Anisotropic damage law of evolution. *European Journal of Mechanics-A/Solids* 19, 187-208.
- Lorentz, E., Badel, P., 2004. A new path-following constraint for strain-softening finite element simulations. *Int J Numer Meth Eng* 60, 499-526.
- Lorentz, E., Cuvilliez, S., Kazymyrenko, K., 2011. Convergence of a gradient damage model toward a cohesive zone model. *Cr Mecanique* 339, 20-26.
- Loret, B., Prevost, J.H., 1990. Dynamic strain localization in elasto-(visco-) plastic solids, Part 1. General formulation and one-dimensional examples. *Comput Method Appl M* 83, 247-273.
- Middleton, R.S., Carey, J.W., Currier, R.P., Hyman, J.D., Kang, Q., Karra, S., Jiménez-Martínez, J., Porter, M.L., Viswanathan, H.S., 2015. Shale gas and non-aqueous fracturing fluids: Opportunities and challenges for supercritical CO₂. *Applied Energy* 147, 500-509.
- Mindlin, R.D., 1964. Micro-structure in linear elasticity. *Arch Ration Mech An* 16, 51-78.
- Mühlhaus, H.-B., Alfantis, E., 1991. A variational principle for gradient plasticity. *Int J Solids Struct* 28, 845-857.
- Needleman, A., 1988. Material rate dependence and mesh sensitivity in localization problems. *Comput Method Appl M* 67, 69-85.
- Niazi, M., Wisselink, H., Meinders, T., 2013. Viscoplastic regularization of local damage models: revisited. *Computational Mechanics* 51, 203-216.

- Pardoen, B., Levasseur, S., Collin, F., 2014. Using Local Second Gradient Model and Shear Strain Localisation to Model the Excavation Damaged Zone in Unsaturated Claystone. *Rock Mech Rock Eng* 48, 691-714.
- Parisio, F., Samat, S., Laloui, L., 2015. Constitutive analysis of shale: a coupled damage plasticity approach. *Int J Solids Struct* 75-76, 88-98.
- Peerlings, R., De Borst, R., Brekelmans, W., Geers, M., 1998. Gradient-enhanced damage modelling of concrete fracture. *Mechanics of Cohesive-frictional Materials* 3, 323-342.
- Peerlings, R.H.J., De Borst, R., Brekelmans, W.A.M., De Vree, J.H.P., 1996. Gradient enhanced damage for quasi-brittle materials. *Int J Numer Meth Eng* 39, 3391-3403.
- Pietruszczak, S., Mroz, Z., 1981. Finite element analysis of deformation of strain-softening materials. *Int J Numer Meth Eng* 17, 327-334.
- Pijaudier-Cabot, G., Bazant, Z.P., 1987. Nonlocal damage theory. *Journal of Engineering Mechanics* 113, 1512-1533.
- Plassart, R., Fernandes, R., Giraud, A., Hoxha, D., Laigle, F., 2013. Hydromechanical modelling of an excavation in an underground research laboratory with an elastoviscoplastic behavior law and regularization by second gradient of dilation. *Int J Rock Mech Min* 58, 23-33.
- Rizzi, E., Carol, I., Willam, K., 1995. Localization analysis of elastic degradation with application to scalar damage. *Journal of Engineering Mechanics* 121, 541-554.
- Rudnicki, J.W., Rice, J., 1975. Conditions for the localization of deformation in pressure-sensitive dilatant materials. *J Mech Phys Solids* 23, 371-394.
- Rybacki, E., Reinicke, A., Meier, T., Makasi, M., Dresen, G., 2015. What controls the mechanical properties of shale rocks? - Part I: Strength and Young's modulus. *J Petrol Sci Eng* 135, 702-722.
- Salager, S., François, B., Nuth, M., Laloui, L., 2013. Constitutive analysis of the mechanical anisotropy of Opalinus Clay. *Acta Geotech* 8, 137-154.
- Simo, J., Hughes, T., 1998. *Computational inelasticity*. Springer, New York.
- Song, J., Zhang, D., 2012. Comprehensive review of caprock-sealing mechanisms for geologic carbon sequestration. *Environ Sci Technol* 47, 9-22.
- Toupin, R.A., 1962. Elastic materials with couple-stresses. *Arch Ration Mech An* 11, 385-414.
- Van Eekelen, H., 1980. Isotropic yield surfaces in three dimensions for use in soil mechanics. *Int J Numer Anal Met* 4, 89-101.
- Vardoulakis, I., 1980. Shear Band Inclination and Shear Modulus of Sand in Biaxial Tests. *Int J Numer Anal Met* 4, 103-119.

- Zhang, H.W., Schrefler, B.A., 2000. Gradient-dependent plasticity model and dynamic strain localisation analysis of saturated and partially saturated porous media: one dimensional model. *European Journal of Mechanics-A/Solids* 19, 503-524.

7. Hydro-mechanical modeling of tunnel excavation in anisotropic shale with coupled damage-plasticity and micro-dilatant regularization

Authors: F. Parisio, V. Vilarrasa and L. Laloui.

Status: to be submitted to Engineering Geology.

Contributions: F. Parisio developed preliminary research on the FE-tunnel excavation, designed the features of the numerical analysis, calibrated the material parameters, ran the numerical analyses and performed the results interpretation. V. Vilarrasa contributed with suggestions and insight concerning the material parameters calibration of Opalinus Clay, the design of the numerical model and the interpretation of the results. The manuscript was written by F. Parisio and edited by V. Vilarrasa and L. Laloui, who is the senior responsible author (SRA) of the publication.

Abstract

Geological nuclear waste disposal will imply the excavation of a large number of galleries in low-permeable rocks. To integrate the effects of excavation on the rock, a consistent numerical model for the simulation of the excavation process in low-permeable anisotropic sedimentary shale is proposed here. To validate the approach, recorded data from the FE-tunnel excavated in Opalinus Clay at the Mont Terri Underground Research Laboratory are used. A 2D coupled hydro-mechanical FEM model of the FE-tunnel is built in the software *Code_Aster*. A second gradient of dilatancy formulation is employed to avoid spurious mesh dependent behavior originating from the softening behavior of the MS3 coupled damage-plasticity model developed in the previous chapters. The approach is validated by comparing numerical predictions and in-situ observations during and after tunnel excavation in terms of displacements, pore water pressure and degradation of elasticity (damage). The mechanical parameters are calibrated partly based on laboratory experiments and partly based on values available in the literature. Despite no adjustments are made to fit in-situ results, a good agreement between numerical predictions and experimental in-situ monitored data is obtained, giving a correct prediction of the evolution of the Excavation Damaged Zone is correctly predicted. This modeling approach is considered to be suited for the purpose of simulating tunnel excavation in low-permeable anisotropic quasi-brittle shales.

Keywords: tunnel excavation in shale, anisotropic damage-plasticity of shales, nuclear waste storage, Mont Terri URL, Excavation Damaged Zone, Code_Aster, Opalinus Clay.

7.1. Introduction

Deep geological disposal is commonly accepted by the international community as the safest solution for long-term storage of high level spent nuclear fuel (Feiveson et al., 2011). The concept makes use of a multiple barrier system consisting in placing the fuel in metal canisters surrounded by swelling bentonite material and placing this multibarrier system inside deep underground tunnels excavated in low-permeable rocks. The key for the success of the projects depends on proper design of all of the above mentioned components (Sanchez

et al., 2012). Thus, the properties of the host geomaterial should be such that radionuclides do not reach the environment in case that they could escape from the engineered barrier system. While some countries have adopted solutions in which the host geology consists in granite (e.g., Canada, Sweden and Finland), others have chosen as host material sedimentary indurated clays or shales (e.g., France, Belgium and Switzerland). Shales and hard clays have demonstrated to be successful candidates due to their low-permeability and self-healing capacity, which should guarantee proper isolation and avoid radio-nuclide dispersion into the surrounding environment (Gens et al., 2007).

Opalinus Clay (OPA), a low-permeable anisotropic shale, is currently considered in Switzerland as a potential host rock for nuclear waste disposal purposes (Thury and Bossart, 1999). To study in detail the hydrogeological, geochemical and geomechanical properties of OPA the Mont Terri Project, located in northern Switzerland, was created in 1995 (Thury and Bossart, 1999). There are 15 international partners taking part in the project and the management is carried out by the Swiss Federal Office of Topography (swisstopo). Though more than 100 small, medium and large scale experiments took place since its foundation and other are still ongoing or planned for the future, no radioactive material will ever be stored in this facility (Bossart and Thury, 2007).

OPA from the Mont Terri site is a Mesozoic indurated clay/shale formed in marine sedimentation conditions. OPA mineralogy is composed by 40 to 80% of clay particles and the rest consists in silicates, carbonates and quartz (Bossart et al., 2002; Thury and Bossart, 1999). OPA has a Young's modulus that ranges from 2 to 10 GPa. Based on its failure mechanism, OPA can be considered as a quasi-brittle geomaterial because it exhibits small values of plastic strain in the pre-peak response and the post-peak is accompanied by strain softening, dilation and degradation of elasticity (Parisio et al., 2015). Due to the layered structure of OPA, almost all of the mechanical, hydraulic and thermal properties are anisotropic (Bock, 2009). Hydraulic conductivity varies between 10^{-14} m/s to 10^{-12} m/s in the intact material (Bock, 2009) and increases by several orders of magnitude close to excavated galleries, where a fracture network, the so-called Excavation Damaged Zone (EDZ), is generated by the excavation process and deteriorates the mechanical and hydraulic properties (Bossart et al., 2002).

The increased hydraulic conductivity and lowered mechanical strength and stiffness in the EDZ can create concerns related to the safety of deep repositories. Therefore, the EDZ has been widely studied and analyzed in order to get fundamental insights regarding its formation and the evolution of its mechanical and hydraulic characteristics (e.g., Rutqvist (2015) and Tsang et al. (2005)). According to Bossart et al. (2002), the EDZ in OPA at Mont Terri site extends to roughly a tunnel radius from the tunnel walls and can be divided in two zones: an inner zone extending to up half a tunnel diameter and consisting of an interconnected fracture

network with a hydraulic conductivity several orders of magnitude greater than the undisturbed rock; an outer zone, extending from half to a tunnel diameter, and consisting in non-connected fractures partially filled with pore water. In the outer zone the hydraulic conductivity is lower than in the inner zone, but higher than the undisturbed material. Furthermore, this increase in transmissivity is highly anisotropic because shear slip occurring in the fractures inside the EDZ causes a large transmissivity increase in the direction perpendicular to shear due to dilation, but the increase is minimum in the direction parallel to shear (Rutqvist and Stephansson, 2003; Vilarrasa et al., 2011). A more detailed review of the many experiments and studies related to the characterization of the EDZ at the Mont Terri Underground Rock Laboratory (URL) can be found in the work of Lisjak et al. (2015).

Among these experiments, the FE-Experiment is very valuable to better understand the processes involved in the formation and evolution of the EDZ due to the wide range of data collected during its initial phase. The FE Full-scale Emplacement experiment is a real 1:1 scale experiment in which three canisters, surrounded by bentonite will simulate the heating released by nuclear waste for 15 to 20 years (Vogt et al., 2013). For this purpose, a 50 m long tunnel with a 3 m diameter was excavated at full face in OPA and is referred to as FE-tunnel. The excavation procedure was monitored in terms of tunnel radial convergence measurements, pore pressure evolution and inclinometers data with sensors installed in pre-drilled boreholes (Daneluzzi et al., 2013). Additionally, geophysical measurements were performed around the tunnel after excavation was completed (Jaeggi et al., 2014). Further assessment of the fracture network was conducted by borehole logs and geophysical measurements from the surroundings of the EDZ in the FE-tunnel (Jaeggi et al., 2014).

The complex mechanisms involved in the formation of the EDZ include inelastic processes such as dilatancy and damage accumulation, pore pressure decrease and desiccation of the material caused by ventilation. The complexity of the involved processes has made the numerical modeling of the formation of the EDZ a difficult and challenging task to achieve (Lisjak et al., 2015; Tsang et al., 2012). A short review of the modeling studies of the early stage^e of the excavation process in OPA at the Mont Terri site can be found as well in the work of Lisjak et al. (2015). In the same work, a combined continuous/discrete purely mechanical approach is used to predict the fracture pattern around the FE-tunnel in the early stages of excavation. Accounting for the pore water pressure in coupled hydro-mechanical conditions allows to extend the analyses to long-term conditions, where time dependent consolidation plays an important role. The evolution of the EDZ in the longer term has been

^e Early stages intended at the undrained deformation process extending in time up to a few days after lining installation.

studied for OPA at the Mont Terri URL, Switzerland (Boidy et al., 2002; Haghghat and Pietruszczak, 2015; Levasseur et al., 2010; Rutqvist et al., 2013), and for Callovo-Oxfordian argillite at the Underground Research Laboratory Meuse/Haute Marne, France (Pardoen et al., 2015; Plassart et al., 2013; Shao et al., 2008).

Compared to previous studies, which often consist in hardening/softening plasticity (Levasseur et al., 2010; Pardoen et al., 2015; Plassart et al., 2013), one of the main novelties in this contribution is the introduction of an isotropic continuum damage model coupled with anisotropic plasticity. As OPA can be considered a quasi-brittle material, continuum damage coupled with inelastic strains distribution is more consistent in representing the EDZ around tunnels compared to purely plastic strain distribution. Furthermore, hydro-mechanical couplings allow to carry out analysis in the medium/long term, when pore pressure changes due to pressure diffusion becomes significant.

The goal of the present contribution is to demonstrate how the combination of all the concepts developed from Chapter 4 to Chapter 6 can be successfully applied to model the excavation process of the FE-tunnel in coupled hydro-mechanical conditions. This will constitute a validation in two senses: firstly, the developed constitutive model MS3 and the calibration of its material parameters can be validated as a consistent set for OPA; secondly, the proposed approach can be followed as a consistent tool to model the combined hydro-mechanical behavior of OPA at the Mont Terri site.

To achieve this goal, a numerical model representative of the FE-tunnel is build. The anisotropic failure surface of model MS3 are taken from the anisotropic calibration illustrated in Chapter 5. We present the hydro-mechanical formulation of the second gradient of dilatancy that we use in our model. Then, the simulation results of the FE-tunnel are compared to in-situ measurements of radial tunnel convergences, pore water pressure evolution from sensors and geophysical measurements of elastic p-wave velocity around the tunnel. We finally assess the validity of this model based on the comparison with the field measurements.

7.2. The Mont Terri Project and the FE-Experiment

The Mont Terri anticline in northern Switzerland was formed in the folding process of the Jura mountains (Thury and Bossart, 1999) and the Mont Terri URL is located inside the formation of OPA, next to a motorway tunnel at an approximate depth of 300 m. The formation of OPA has a dip of approximately 45° degrees. The direct implication is that the layered structure of OPA, composed by the bedding planes that were formed during the deposition process in marine environment is also striking at approximately 45° dip. OPA at Mont Terri URL is furtherly subdivided into several facies according to mineralogical composition and physical properties. The most important ones, which constitute the majority

of the URL, are shaly facies and sandy facies. In situ pore water pressure is around 2 MPa in the far field. The maximum principal in-situ stress is subvertical and while the measures of the magnitude of the principal stresses are considered to be reliable, uncertainties still remain on the inclination (Martin and Lanyon, 2003). The magnitude of the three principal total stress components is 6.5 MPa for the vertical stress, 4.5 MPa for the maximum horizontal stress and 2.5 MPa for the minimum principal stress acting on a plane perpendicular to the FE-tunnel advancing direction (Lisjak et al., 2015; Martin and Lanyon, 2003). Figure 7-1 shows the position of the Mont Terri URL in the Swiss map along with the local geological map and fault systems and a transversal section of the URL with the Mont Terri anticline (Bossart et al., 2017).

Inside the Mont Terri URL, a system of several tunnels was excavated during the expansion of the laboratory to host new experiments. Figure 7-2a displays the three dimensional layout of the gallery system in the URL (Bossart et al., 2017). The FE-tunnel construction took place from March to October 2012 (Daneluzzi et al., 2013) (see the gallery in color purple in Figure 7-2a). The tunnel was excavated in full face with an advancement rate of roughly 1 to 1.5 m per strike, or alternatively 1 to 1.5 m per day. It has a total length of 50 m and the diameter of the excavation is approximately 3 m. The tunnel is located in the shaly facies of Opalinus Clay. While bedding planes strike at approximately 45° from the horizontal in most of the URL, they strike at a dip of approximately 33° in the FE-tunnel (Lisjak et al., 2015). From the 50 m long tunnel, we consider in this study for comparison between numerical and experimental results the section that goes from tunnel meter (TM) 9 to tunnel meter 38, i.e., the 29 m indicated as plug section and test section in Figure 7-2b. The support consists of sprayed shotcrete lining with steel wire mesh and anchors of which layout depends on the local conditions (Daneluzzi et al., 2013).

7.2 The Mont Terri Project and the FE-Experiment

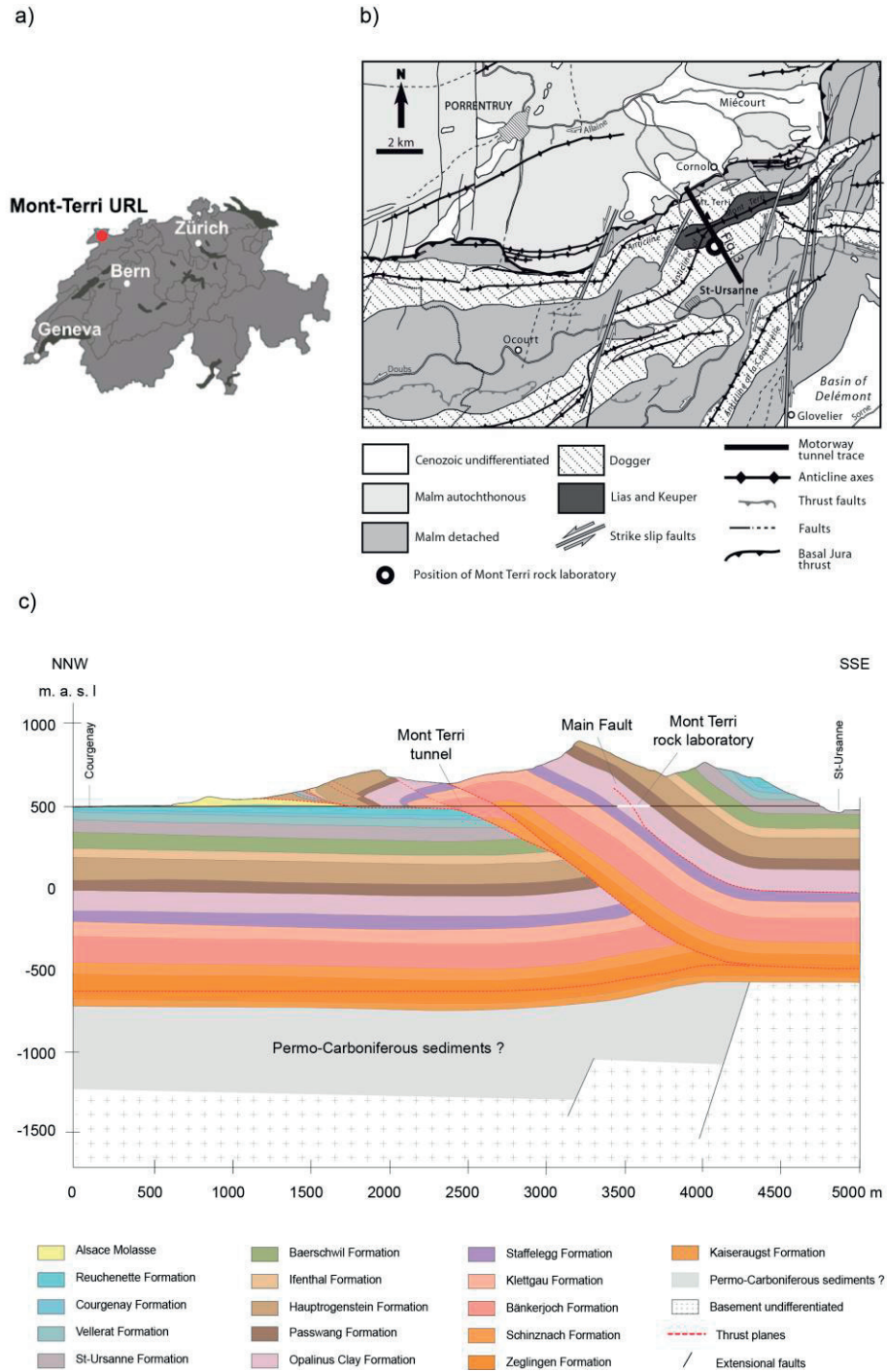


Figure 7-1: Location of the Mont Terri URL in the Swiss map (a), local geology with fault systems (b) and transversal geological section of the URL with the Mont Terri anticline and the Opalinus Clay formation (c). Image taken from (Bossart et al., 2017).

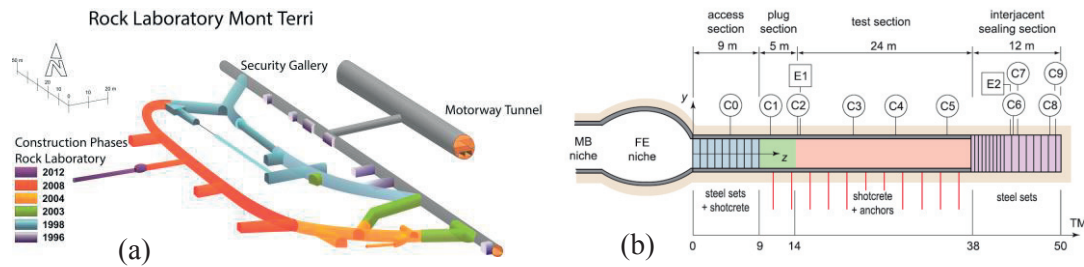


Figure 7-2: (a) Three dimensional layout of the Mont Terri URL tunnel system and (b) schematic longitudinal section of the FE-tunnel with emplaced support and measurements sections. In purple it is shown the construction of the FE-tunnel, dating of 2012 (a). Images taken from (Bossart et al., 2017) (a) and from (Lisjak et al., 2015) (b).

The goal of the FE Full-scale Emplacement experiment is to simulate a real case of excavation, canister and bentonite back-filling emplacement and subsequent heating in a 1:1 scale. In order to get the needed information, a complex and extended monitoring system was designed and put in place. Amongst the mentioned data, the measures of the surface tunnel displacements with radial convergence targets, pore pressure measurements with sensors installed in pre-drilled boreholes and post-excitation geophysical measurements of elastic wave velocities are of particular interest for the present study (Jaeggi et al., 2014).

Tunnel walls deformation was measured with the aid of automatic geodesic convergence measurements. Three dimensional reflectors were installed in different sections of the tunnel after excavation and lining installation. Measurements were carried out continuously with two theodolites type Leica TCRA 1102 and Leica TDA 5005, which operated on a network of known points inside the URL galleries system (Daneluzzi et al., 2013). The position in the longitudinal profile of the FE-tunnel of the radial convergence sections considered in the present study are indicated in Figure 7-2b with labels C1, C2, C3, C4 and C5, which are positioned at TM 10.6, TM 14.3, TM 21.8, TM 27.6 and TM 34.3, respectively. Figure 7-3a indicates the position of the reflectors in the tunnel cross section and Figure 7-3b shows their actual position in the FE-tunnel. The position of the optical targets in terms of inclination angle from the vertical direction in a clockwise sense is indicated in Table 7-1.

Table 7-1: Inclination angles from the vertical direction in clockwise sense of the optical targets for the radial tunnel walls convergence measurement.

Target	Angle
<i>P1</i>	-120°
<i>P2</i>	-60°
<i>P3</i>	0°
<i>P4</i>	60°
<i>P5</i>	120°

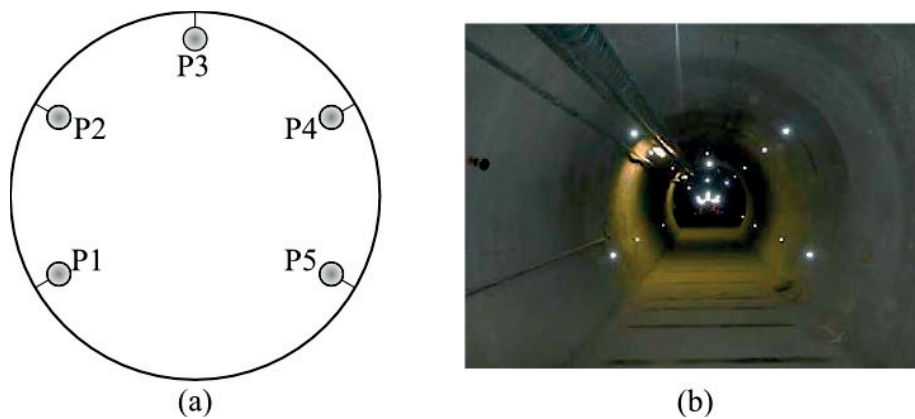


Figure 7-3: Schematic position of convergence targets reflectors (a) and installed targets in the FE-tunnel (b) (Daneluzzi et al., 2013).

Six boreholes BFE-A002, BFE-A003, BFE-A004, BFE-A005, BFE-A006 and BFE-A007 were drilled sub-parallel to the FE-tunnel prior excavation. Each borehole was equipped with six multi-packer systems to record pore pressure evolution in OPA during and after tunnel excavation. The full layout and geometry of the boreholes can be found in Lisjak et al. (2015) and Trick et al. (2013). In the present study, 6 measuring points are considered for comparison between in-situ measured data and numerical outcomes. Figure 7-4 illustrates the position of the measuring points and the distance from tunnel walls of the pore water pressure sensors in a cross section of the FE-tunnel. The measuring points are located at different TM sections. Since the numerical model is bi-dimensional, their projection is considered in the present study. The time evolution will be considered here, so that for each section day 0 corresponds to the tunnel front position at a given point in the longitudinal section of the tunnel.

Ultrasonic measurements of p-wave velocities were performed inside two boreholes drilled at TM 40.75 m and other two at TM 42.25 m (Jaeggi et al., 2014). In the present study only measurements at TM 40.75 m are considered. In this section, measurements were performed from 0 to 5.5 m from tunnel walls at a borehole drilled horizontally and from 6 to 14 m in a

borehole drilled at a dip of -55° from the horizontal, both in the right side of the tunnel. Since the decreasing of elastic p-wave velocity in the borehole drilled at a dip of -55° are negligible, only measurements from the horizontal borehole at TM 40.75 m will be taken into consideration. The elastic p-wave velocity can be used as an indirect measure of damage (Lemaitre et al., 2009). More specifically, Young's modulus is smaller in a damaged material than in the intact one, implying therefore smaller velocity of the elastic p-wave. The correlation between damaged \tilde{E} and undamaged E Young's moduli directly relates to damage as

$$\tilde{E} = (1 - d)E, \quad (7.1)$$

where d is the damage internal variable. The elastic wave velocity in a damaged material \tilde{v}_L writes

$$\tilde{v}_L = \sqrt{\frac{\tilde{E}}{\rho} \frac{1 - \nu}{(1 + \nu)(1 - 2\nu)}}, \quad (7.2)$$

and the elastic wave velocity in an undamaged medium v_L is

$$v_L = \sqrt{\frac{E}{\rho} \frac{1 - \nu}{(1 + \nu)(1 - 2\nu)}}, \quad (7.3)$$

where ρ is the density of the material and ν the Poisson's ratio. Finally, the elastic wave velocity measurements can be directly related to damage as

$$d = 1 - \frac{\tilde{v}_L^2}{v_L^2}. \quad (7.4)$$

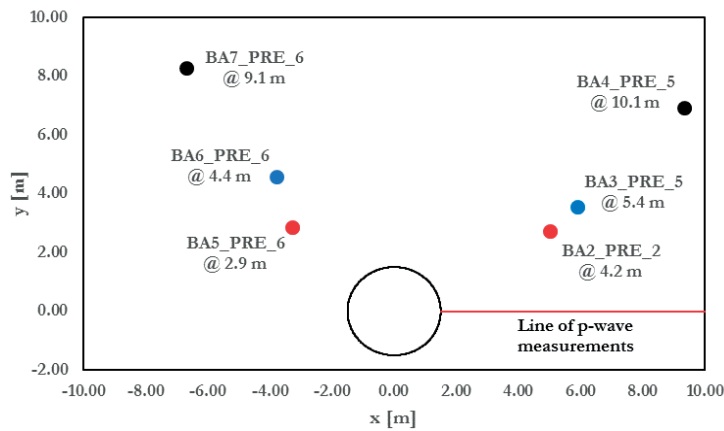


Figure 7-4: Position in the tunnel cross section of pore pressure sensors considered in the present study. In the red line is shown the borehole position in which p-wave velocities were measured. The distance from the tunnel walls is indicated for every sensor.

7.3. Numerical model of the FE-Tunnel

The FE-tunnel control section between TM 9 and TM 38 is far enough from the initial MB-niche (Figure 7-2b) and the end of the tunnel so that bi-dimensional conditions can be considered as representative.

The numerical model for FEM analysis is therefore built in bi-dimensional plane strain conditions. The model is built in the open source FEM solver *Code_Aster* (www.code-aster.org), where we previously implemented the constitutive model MS3.

To simulate the excavation process, the convergence-confinement method is applied (Carranza-Torres and Fairhurst, 1999). Analyses are carried out in coupled hydro-mechanical conditions. All experimental quantities evolving with time (pore pressure and displacements) will be properly translated to the zero time, i.e., the time at which the tunnel front is at a given section.

No tunnel lining is applied in the numerical model. Ovalization and out-of-roundness of the tunnel lining are reasonably believed to originate stress concentrations and local beak-ups. In this case, the structure loses continuity and global stiffness. Furthermore, no details about the mechanical behavior of the contact zone between shotcrete and OPA are known. Shear stresses can be triggered by differential strains between OPA and shotcrete and breakouts in the contact are as well plausible. For these reasons, despite the shotcrete having a Young's modulus of 8 GPa after one day, recent numerical studies suggested that if the lining is modeled as linear elastic with no inelastic behavior, then a Young's modulus of 10 MPa should be adopted to reproduce the field observations (Lisjak et al., 2015). The reduced value

of lining stiffness, almost three orders of magnitude lower than intact shotcrete, has negligible influence in the final results, as preliminary numerical analyses that we performed in pure mechanical conditions have shown. Furthermore, the highest convergences were observed in the test zone, where shotcrete lining and wire mesh were applied (Jaeggi et al., 2014). Given these limitations, the lining is not emplaced in the numerical study.

The numerical model is built in 2D plane strain conditions and is representative of the FE-tunnel cross section. The tunnel is 3 m in diameter and is inserted in an outer square box of 60 m sides. The dimensions of the outer box, which is representative of the rock mass, were chosen to avoid boundary effects at the tunnel, i.e., stress state remains homogeneous and undisturbed at a far enough distance. Figure 7-5 indicates the tunnel geometry, along with the dip direction of the bedding planes (33°) and the initial state of stress and pore water pressure.

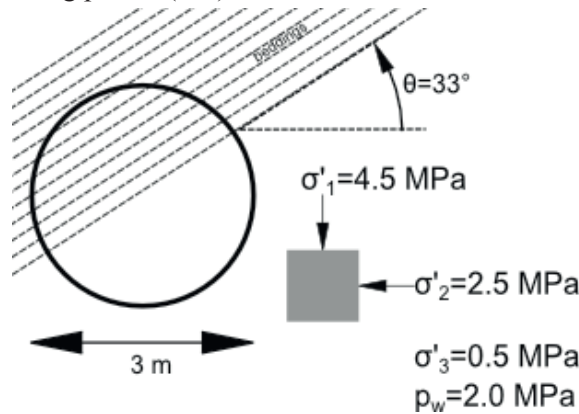


Figure 7-5: Schematic model representation with tunnel geometry, bedding inclination and initial in-situ stress tensor and pore water pressure.

Figure 7-6 shows the global mesh of the model and the refined zone around the tunnel. The refined zone around the tunnel walls has the objective of better capturing the stronger gradients of the stress and pore pressure fields which will develop. The mesh consists in triangular six nodes quadratic plane strain elements and with gradually increasing size toward the outer boundaries of the model. Horizontal displacements are blocked on the outer left and right sides of the model and vertical displacements are blocked on the bottom boundary of the whole model shown in Figure 7-6a. The effective stress is initialized with a maximum vertical principal effective stress of 4.5 MPa, an intermediate horizontal effective stress of 2.5 MPa and a minimum out of plane effective stress of 0.5 MPa. The pore water pressure field is initialized at 2 MPa. For consistency, a vertical total stress of 6.5 MPa is applied on the top boundary of the model.

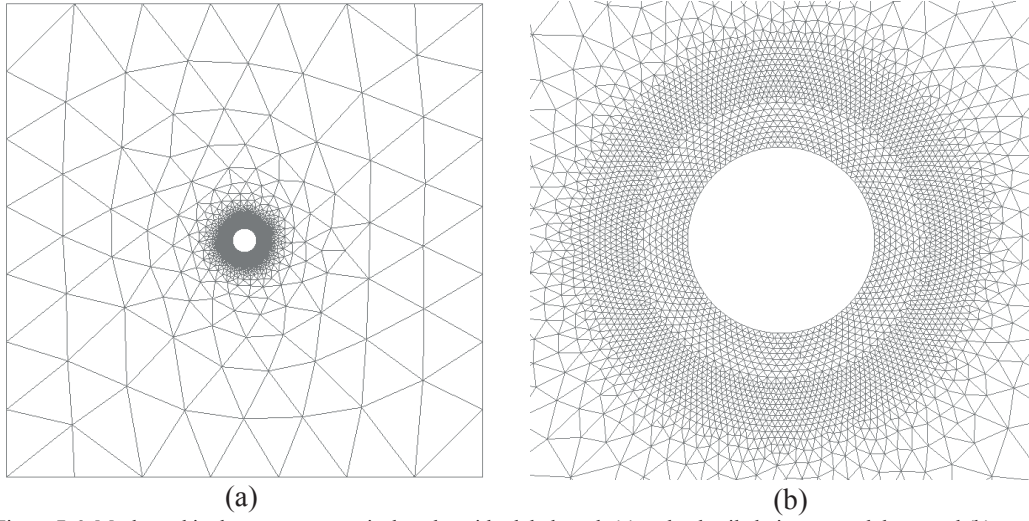


Figure 7-6: Mesh used in the present numerical study, with global mesh (a) and a detailed view around the tunnel (b).

The convergence-confinement method used to simulate the excavation process implies a first calculation step with blocked displacements of the tunnel walls. The nodal reactions at the tunnel walls are computed and to simulate the tunnel excavation process, released over time until they equal zero. The curve that is used for the deconfinement rate at tunnel walls is the one proposed by (Carranza-Torres and Fairhurst, 1999). The deconfinement is a function of the tunnel front position as

$$\lambda_D = \left[1 + \exp\left(\frac{-x}{0.55D}\right) \right]^{-1.7}, \quad (7.5)$$

where x is the tunnel front position, D the tunnel diameter and λ_D is the deconfining function applied to the nodal reactions as

$$R = (1 - \lambda_D) R^0, \quad (7.6)$$

where R^0 is the initial nodal reaction. The tunnel front position varies with time, so the deconfinement function λ_D can be rewritten as a function of time taking into account the advancement of 1 m per day. Thus, at every time instant, a given reaction can be computed using the evolution of the deconfinement λ_D as function of time given in Figure 7-7. Negative times are in this case fictitious, i.e., they correspond to the fact that the tunnel excavation front has not crossed the given section yet. Time equal to zero corresponds to the instant in which the tunnel front is at the given section.

Analogously, a new coefficient λ_{DW} is introduced for the reduction of the pore water pressure at the tunnel walls with time. This has the scope of simulating the drainage process of the

tunnel excavation, i.e., after the front has passed a given section, the pore water pressure at the tunnel walls is assumed in equilibrium with the atmospheric value. From the measurements of the pore water pressure evolution during the FE-tunnel excavation (Trick et al., 2013), it appears that the pressure drop happens when the tunnel excavation front is still quite far (more than two diameters) and is relatively sudden. The pore water pressure evolution in the tri-dimensional reality is a complex process and depends on several factors, including stress redistribution, fracture opening and consolidation. Based on the observed experimental behavior, in the current numerical model we assumed that the pore water pressure at the tunnel walls drops quickly to null values when the tunnel front is roughly at 2 diameters distance from the considered section. We assume that the pressure drop at the tunnel walls nodes takes place during one day starting seven days before the excavation front reached the given section, given the advancement rate of 1 m per day and a diameter of 3 m. The decreasing function of λ_{DW} is also illustrated in Figure 7-7.

Displacements were recorded with optical measures installed after the excavation front passed a given section. Generally, they were installed and started recording data approximately one day after the excavation. The interpretation of the numerical results will account for this fact.

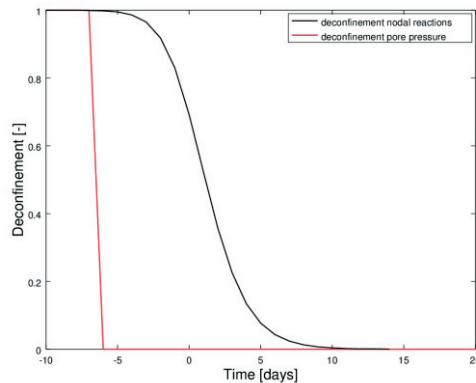


Figure 7-7: Deconfinement functions for the nodal reactions (black) and pore pressure (red) at the tunnel walls. Negative times indicate the excavation front has not passed the given section yet.

7.4. Hydro-mechanical formulation of the second gradient of dilatancy model

We propose here the extension to porous media of the micro-dilatation model presented in Chapter 6. The principle of virtual power reads ([R5.04.03], 2013; Fernandes, 2009; Fernandes et al., 2008; Plassart et al., 2013)

$$\int_{\Omega} \left(\sigma_{ij} \frac{\partial \bar{u}_i}{\partial x_j} + S_j \frac{\partial^2 \bar{u}_i}{\partial x_i \partial x_j} \right) dv = \int_{\partial\Omega} (p_i \bar{u}_i + P_i D \bar{u}_i) ds$$

$$- \int_{\Omega} \dot{m}_w \bar{p}_w dv + \int_{\Omega} M_j^w \frac{\partial \bar{p}_w}{\partial x_j} dv = \int_{\partial\Omega} M_w^{ext} \bar{p}_w ds$$
(7.7)

and is valid for any admissible kinematic field of displacement \bar{u}_i and pore water pressure \bar{p}_w .

The meaning of the symbols entering in the first of Equations set (7.7) is explained in detail in Section 6.3. The symbols related to the second of Equations set (7.7) are explained in details in Section 4.3, where the poroelastic formulation is given.

7.5. Calibration of material parameters

The constitutive model employed for the analyses of tunnel excavation is MS3, which was presented in Chapter 4 and extended in Chapter 5 to cover anisotropic and true triaxial strength. The process of calibrating the material parameters of the constitutive model was illustrated in detail in the previous Chapters. Such process is here followed for determining some parameters and it is complemented for the rest of the parameters using data available in the literature.

Table 7-2 shows the full set of material parameters subsequently used for the tunnel excavation analysis. The elasticity parameters are taken from literature values (Bock, 2009) and adjusted to better represent the behavior of the rock mass. For the proposed application, elastic strains are estimated to be responsible for around 10 % of the final tunnel convergence. Therefore, adopting a linear elastic isotropic law will not lead to major differences in the global behavior compared to linear elastic anisotropic behavior. In Bock (2009), the recommended value of the isotropic tangent Young's modulus is 3 GPa and the Poisson's ratio 0.29. In the present study a value of 2 GPa for the Young's modulus and 0.35 for the Poisson's ratio is adopted. The parameters involved in the anisotropic failure surface, i.e., $\beta, \hat{\gamma}, \Omega, d_1$ and d_2 are taken from the calibration of Chapter 5 against the set of experimental data on shaly facies of OPA from Gräsle and Plischke (2010). Damage evolution parameters and plastic compressibility are kept with the same values of the sandy facies, which are the ones calibrated in Chapter 4. It is worth remembering that the parameters that have the most direct influence on the shear band size in boundary value problems are the ones controlling damage and dilatancy evolution, as was evidence by the results reported in Chapter 6. The calibration of dilatant and damage parameters is therefore done in parallel with the parameters involved in the second gradient of dilatancy model and will be illustrated in the following. In order to have pre-peak plastic strains, the final yield surface is scaled with the parameter r_{hal} set to 0.7. δ is equal to one, which implies constant

friction during the strain hardening process. Finally, the Biot's coefficient, 0.7, is taken from the suggestions of Vilarrasa et al. (2015) and validated for OPA at Schlattigen site. The hydraulic conductivity is set to 2×10^{-13} m/s for intact OPA as suggested by Bock (2009). However, preliminary numerical analyses we performed show that a more representative value of the hydraulic conductivity would be 4×10^{-12} m/s, when the EDZ is included. This value yields good results in comparison with in situ recorded data.

Table 7-2: Material parameters used for the numerical simulation of FE-tunnel excavation.

Name	Parameter	Value	Unit
<i>Youngs' modulus</i>	E	2000	MPa
<i>Poisson's ratio</i>	ν	0.35	-
<i>Yield par.</i>	α	-0.0745	MPa ⁻¹
<i>Friction coefficient</i>	β	0.967	-
<i>Cohesive coefficient</i>	γ	2.683	MPa
<i>Scaling friction</i>	δ	1	-
<i>Initial bounding surface</i>	r_{ha0}	0.7	-
<i>Plastic compressibility</i>	χ_h	4×10^{-3}	-
<i>Dilatancy parameter</i>	ψ_h	4×10^{-1}	-
<i>Fabric tensor eigenvalue</i>	Ω_1	1.137	-
<i>Anisotropic parameter 1</i>	$d1$	0.53	-
<i>Anisotropic parameter 2</i>	$d2$	-0.0277	-
<i>True triaxial parameter</i>	β_θ	0.674	-
<i>Damage steepness</i>	α_d	0.015	-
<i>Residual damage</i>	β_d	0.3	-
<i>Hydraulic conductivity</i>	k	4×10^{-12}	m/s
<i>Biot's coefficient</i>	b	0.7	-

Figure 7-8a shows the stress strain behavior from numerical analyses at material point level of OPA with the parameters calibrated for OPA that are reported in Table 7-2. The results are relative to purely mechanical unconfined compression tests at several orientations of the bedding angles, with 0° being horizontal and 90° vertical bedding planes. The data of unconfined compressive strength (UCS) are compared with a recent work from Haghghat and Pietruszczak (2015), in which the authors based their calibration on the results of UCS from the work of Lisjak et al. (2014). Compared to those previous studies, the present calibration, which is based on the tests on shaly facies reported in Gräsle and Plischke (2010), yields smaller values of the UCS.

According to Plassart et al. (2013), the analytical procedure to calibrate the second gradient of dilatancy parameter depends on the adopted constitutive model. So far, this procedure was extended for the model of Drucker-Prager in Fernandes et al. (2008) and for the model of Hujieux in Foucault et al. (2011). At present time, such a procedure was not developed for the model MS3. Plassart et al. (2013) suggested that in this case a numerical semi-empirical approach to calibrate parameter a can be adopted. In the semi-empirical approach, the goal is to relate parameter a to the length of localization, so that a good estimate can be obtained. To achieve this, a biaxial compression test is performed. The model of the biaxial compression is similar to the one presented in Section 6.4, although dimensions are increased by a factor of ten, so that the increased model is 5 m wide and 10 m high and its size is closer to the tunnel scale. A defect in the lower right corner like the one illustrated in Figure 6-1 is included to facilitate the triggering of a localized solution. This test has the goal of obtaining the value of parameter a related to the size of the localization. For the FE-tunnel application, the continuous damage distribution is representative of the micro-cracks density in a given volume or surface. As the thickness of the EDZ extends up to 1.5 m from the tunnel walls, the goal is to obtain a similar thickness of the localized damaged area. Figure 7-9 illustrates the active damaged area in the sample, where the blue zone is the undamaged material and the red zone is the damaged part. The thickness of the damaged area is around 1 m and the value of parameter a to obtain this result was set to 10 MPa·m². This value of a is used in the numerical analysis of the excavation of the FE-tunnel. Further detail on the calibration process can be found in Appendix G.

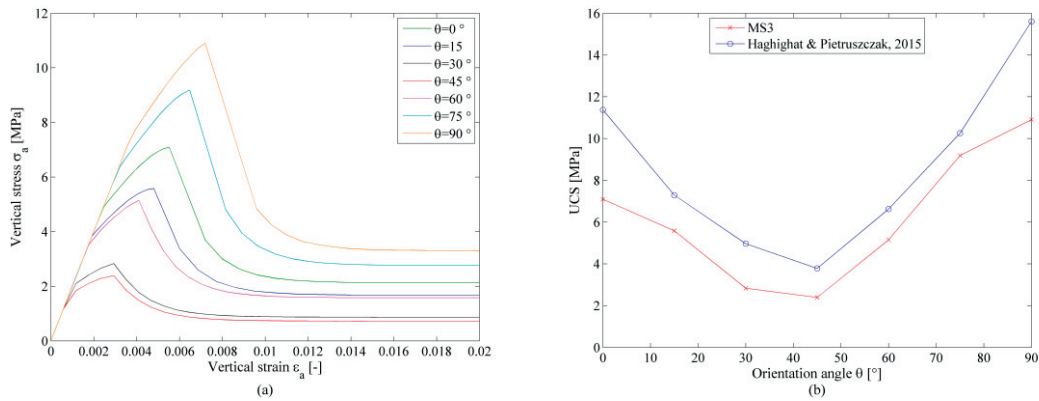


Figure 7-8: Stress strain curves at unconfined conditions for different bedding angle orientation (a) and comparison between predicted UCS in the present model and in the one proposed by Haghghat and Pietruszczak (2015) (b).



Figure 7-9: Localized damaged zone inside the sample. Blue color represents undamaged part and red damage above 5%. The thickness of the damaged area represents an internal characteristic length for the FE-tunnel application.

7.6. Simulation results of the FE-Tunnel

Simulation results of the FE-tunnel are analyzed in terms of the evolution of the pore water pressure, displacement and damage fields over time. As previously mentioned, time 0 days corresponds to the excavation front being at the given section. At the front, roughly 30% of the unloading already happened, as can be seen in Figure 7-7.

7.6.1. Analysis of the pore pressure field

Figure 7-10 shows the distribution of the pore pressure around the tunnel at different times after the excavation front has passed a given section. Units are indicated in Pa. After one day, mechanical stress redistribution and consolidation are the responsible phenomena for the pressure drop. At roughly one radius from the tunnel walls, the pressure field after one day was not yet influenced by the consolidation process and the mechanical unloading. After ten days, the blue zone, which has null pore pressure (i.e., atmospheric pressure), increases in size anisotropically. Actually, pressure drops more rapidly in the direction of the bedding planes than perpendicular to them. This phenomenon can be related to inelastic loading of the material. Plasticity develops around the tunnel walls where stresses are higher than the available strength (which is anisotropic). Dilatant plastic strain takes place and an increase of volumetric strain is observed. Through the continuity equation of the hydro-mechanical coupled formulation, a dilatant volumetric strain will have the effect of reducing the pore water pressure. The shape of the pressure drop is therefore mainly influenced by this coupled hydro-mechanical phenomenon. In the longer time span, the consolidation of the rock mass takes over as a result of the dissipation of pore water pressure. For this reason, after 200 days, the shape of the pressure drop is roughly circular. A pore pressure increase can be observed after ten days at roughly two tunnel diameters. This is caused mainly by mechanical phenomena of stress redistribution and re-equilibration of the pore pressure field. Based on the authors experience, the magnitude of this pressure increase depends on the rate of mechanical unloading and the hydraulic conductivity. Faster processes or lower conductivity will lead to higher pressure increase.

Figure 7-11 illustrates the comparison between numerical predictions and experimental measurements of the pore pressure evolution at different points of the model. The geometrical position of the points that are used in this comparison is illustrated in Figure 7-4. The boreholes in which the pore pressure sensors are installed are drilled almost parallel to the tunnel advancing direction. Therefore, in order to compare the results at different location, the sensor positions are projected onto the plane of the tunnel section, while the timing is normalized so that day 0 corresponds to the tunnel front passing a given section in which the sensor is located. Figure 7-11a shows points located in the left side and Figure 7-11b shows points located in the right side of the model. Because at day 0 the tunnel front is at the given section the pore pressure decrease has already started. After roughly 60 days, the tunnel invert was renovated and this generated a disturbance in the pore pressure signal that can be observed in all the experimental curves of Figure 7-11.

Numerical predictions are in good agreement with in-situ measurements for what concerns the late stages, i.e., when steady state conditions are met and consolidation phenomena are dominating. Higher discrepancy is observed in the early stages, which can be attributed to the

fact that the numerical model is bi-dimensional. Thus, it is therefore not straight forward to define an adequate pore pressure reduction function. In this case, it was postulated based on the observations. Qualitatively, the pore pressure increase at the tunnel front can be captured at short distances from the tunnel walls, as can be seen in Figure 7-11b for the solid red curve. Quantitatively, this pressure increase is late compared to in-situ measurements. Once again, the possible explanation is related to the fact that the present analysis is bi-dimensional, and uncertainties related on the definition of the pore pressure and nodal reaction unloading functions could be at the origin of this discrepancy. From the in-situ observations, the pore pressure drop is anticipated. A possible improvement could be made with a simple back-analysis with 3D HM model in elastic conditions. An analysis of the pore pressure evolution at specific location as a function of the tunnel excavation rate and the tunnel front advancement, performed iteratively until numerical results match the behavior observed in-situ, could lead to a better understanding of the pore pressure unloading function and thus improve the prediction capabilities of the bi-dimensional model. The definition of the pore water pressure unloading function in the analysis input file is given in Appendix B.

Furthermore, the pore pressure drop in the in-situ measurements starts when the tunnel is at more than two diameters from a given section. The early pressure drop suggests that local fractures or faults coinciding with the longitudinal direction of the tunnel might be responsible of this accelerated response, which can hardly be captured by continuous model. The predictions are in much better agreement in the longer term, when pore pressure stabilizes. Globally, the numerical model gives satisfactory results in terms of pore pressure predictions.

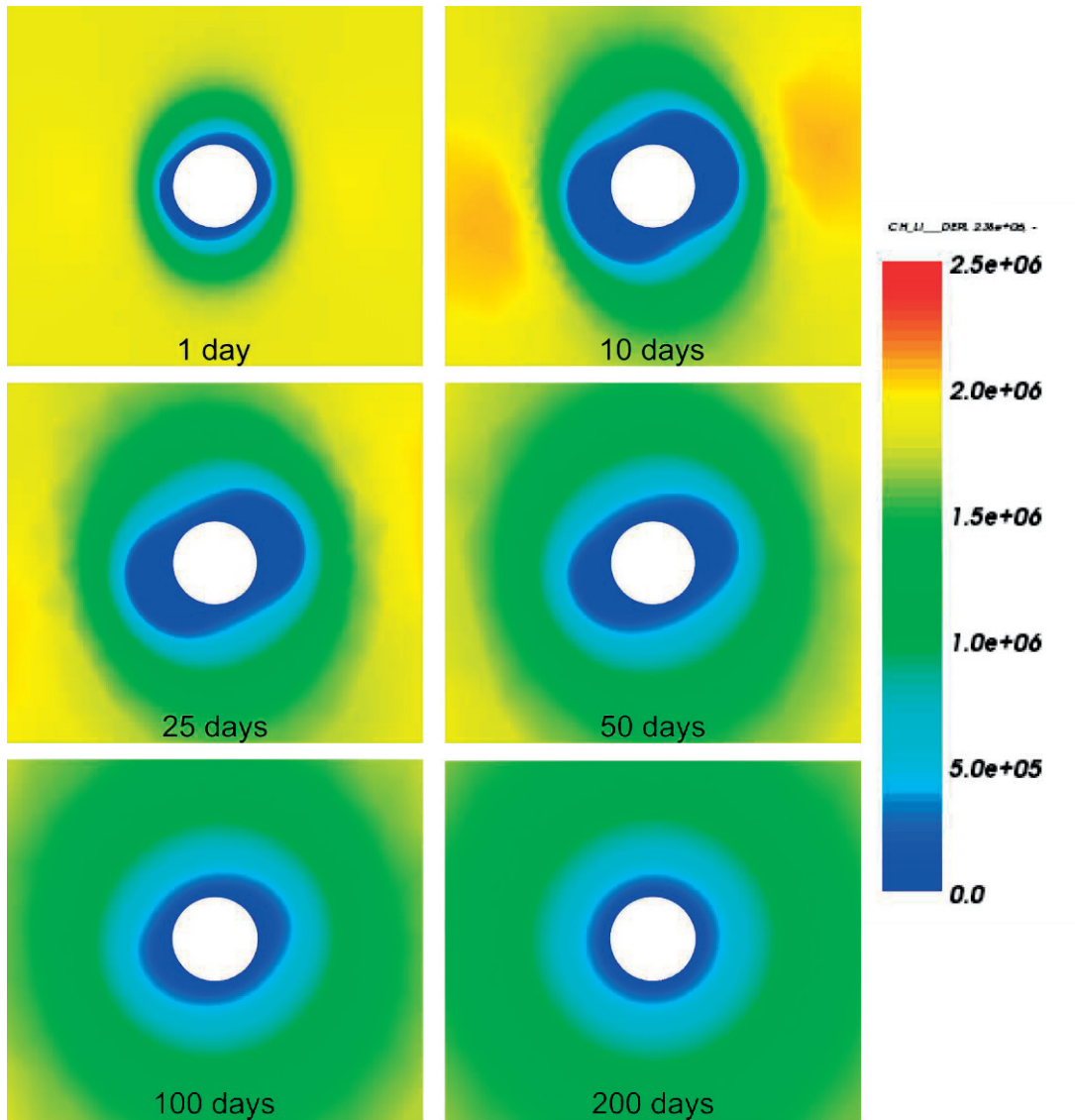


Figure 7-10: Pore pressure evolution in the model at different times (0 day is the tunnel front position). Pressure scale is indicated in Pa.

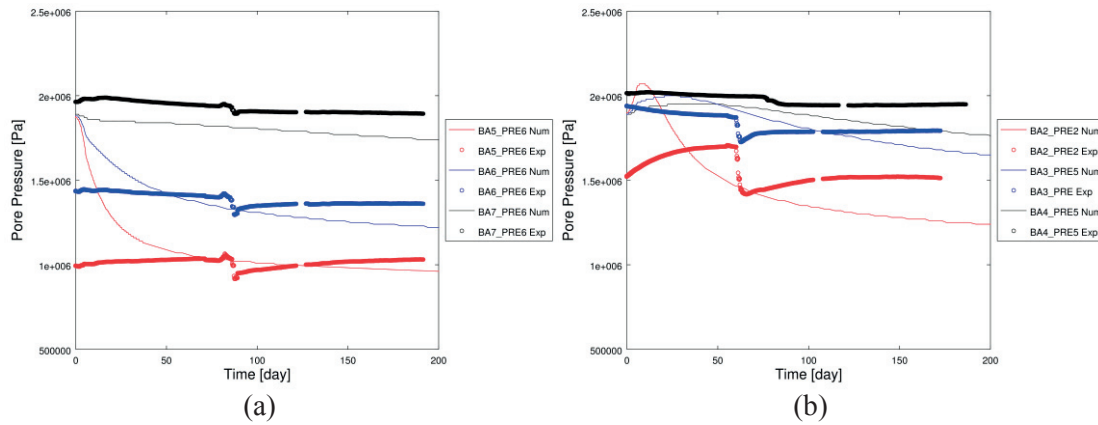


Figure 7-11: Comparison between numerical predictions and in situ measured data for different points (for the geometry refer to Figure 7-4). Points in (a) are located at the left side of the model and points in (b) at the right side.

7.6.2. Damage distribution

Figure 7-12 illustrates the damage distribution around the tunnel at different times after the excavation process. After one day, no damage has yet developed around the tunnel. The mechanical stress concentration did not reach plastic saturation and, therefore, damage has not started yet. After ten days from the excavation, damage starts to develop in the locations where stresses are higher than the available anisotropic strength. The process is time dependent due to the evolution of pore pressure. At the end of the simulated process, after 200 days, a value of roughly 0.6 of damage is observed close to the tunnel walls. The extension of the damaged zone is approximately one tunnel radius. The orientation of the damaged zone can be directly related to the pore pressure drop observed between 10 and 100 days in Figure 7-10.

Figure 7-13 shows the comparison between computed damage and experimental values along a horizontal line on the right side of the tunnel (see Figure 7-4 for the exact position). The experimental values of damage are computed from elastic wave velocity measurements in borehole BFE-E4 as detailed in Section 7.2. The reason for negative values of damage is related to the adopted method of calculation. The elastic wave velocity of the intact material is computed as the average wave velocity between 2 and 5.5 m from tunnel walls. The scatter in the measurement can therefore originate negative values of damage. A good agreement of damage between numerical predictions and back calculated values from elastic wave velocity is observed. Damage has a value of approximately 0.6 close to the tunnel walls both from the numerical results and the measurements. An agreement between measurements and numerical results also exists in the extension of the damaged zone, which extends to a distance of approximately 1 to 1.5 m from the tunnel walls, as shown by null values of damage at

distances greater than 1.5 m. Damage, at the metric scale, is seen as fracture and micro-fracture density in the material and can be taken as an indicator of the presence of the EDZ.

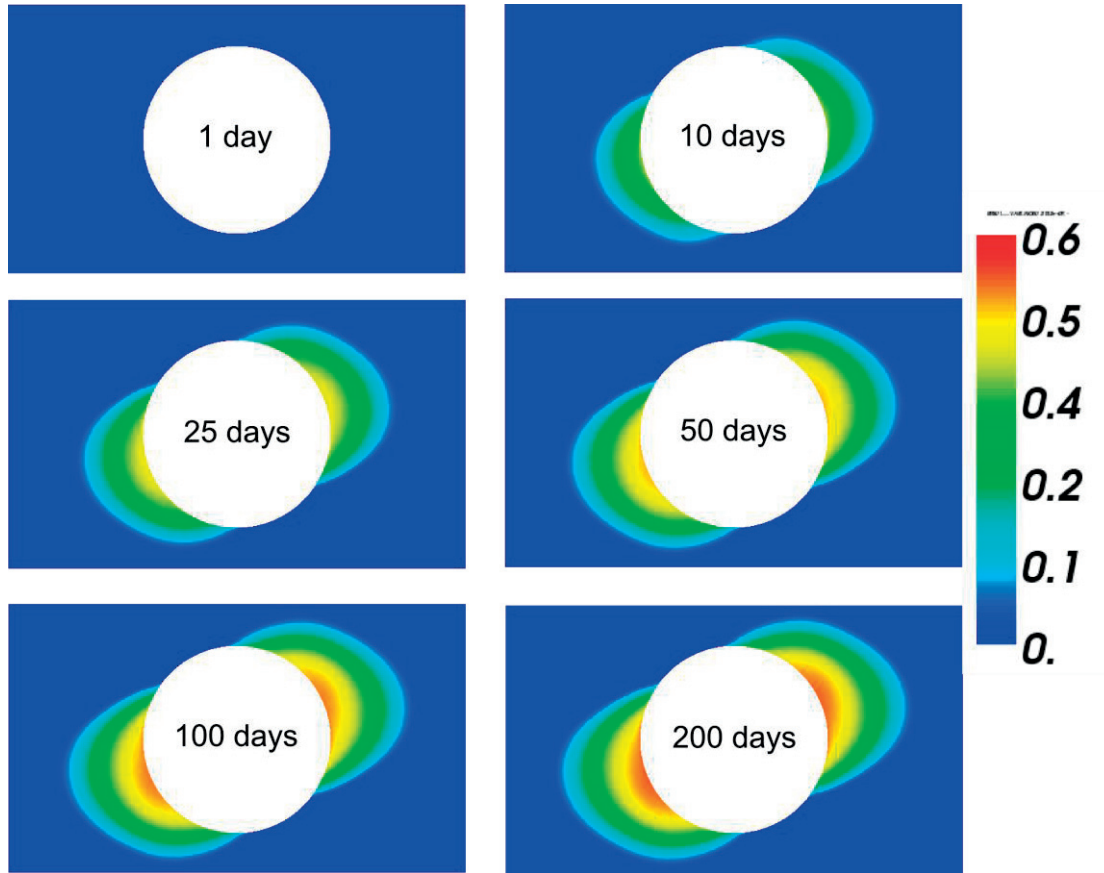


Figure 7-12: Damage distribution evolution in the model at different times (0 day is the tunnel front position).

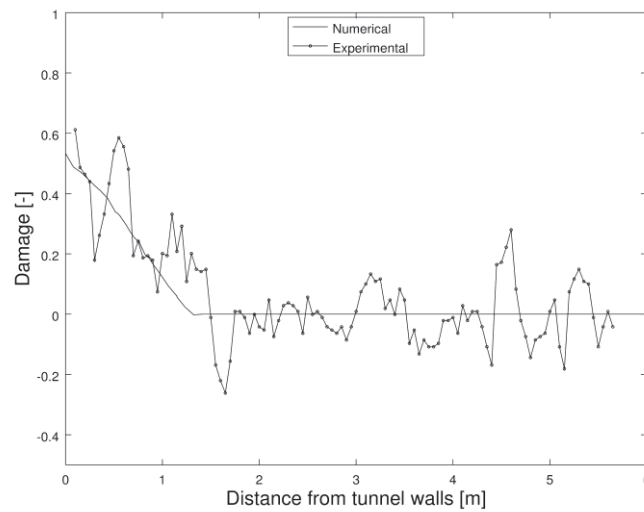


Figure 7-13: Comparison between damage distribution in the numerical model and damage computed from measurement of elastic p-wave velocity inside in-situ borehole (for position refer to Figure 7-4).

The orientation of the damaged zone can be better understood with the aid of the scheme in Figure 7-14. The red line shows the UCS around the tunnel and the black line the elastic circumferential stress when the tunnel is fully excavated (purely based on the effective stress tensor and not taking into account consolidation). At the tunnel walls, the circumferential stress components is the only one acting, so that conditions are equivalent to unconfined compression. Failure is expected in those areas where the circumferential stress exceeds the available strength (UCS). Five characteristic points are shown and the equivalent unconfined compression configuration is shown in the lower part of Figure 7-14. Points A and C are located at the crown and the right side, respectively. Points B, D and E are such that the configuration of the bedding planes in unconfined compression is of 0° (S-Sample), 60° (X-Sample) and 90° (P-Sample), respectively. From this Figure it can be clearly understood how the shape of the damaged zone around the tunnel depends on the combination between the state of stress and the available anisotropic strength.

Figure 7-12 compares the shape of the damaged zone (solid red area) with results from the work of Lisjak et al. (2015) (blue and red lines), in which a short-term purely mechanical analyses of tunnel excavation with an hybrid FEM-DEM technique was performed. With this technique, fractures are simulated as strength degradation of interface elements in the mesh in a cohesive-crack approach. There is a global good agreement between the shape of the EDZ from the two modeling approaches. The slight differences may arise from the fact that

parameters in our study are obtained with another set of material parameters and UCS is smaller in the S-Samples configuration.

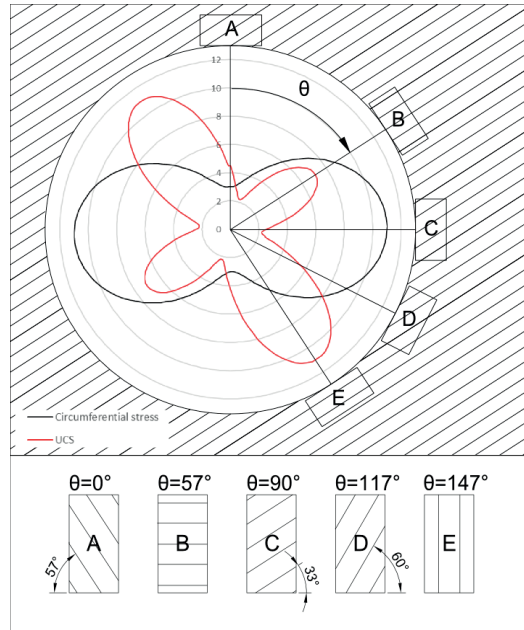


Figure 7-14: Illustration of the variation of UCS and circumferential stress around the tunnel walls along with characteristic point and the respective configuration of bedding planes in an unconfined compression conditions.

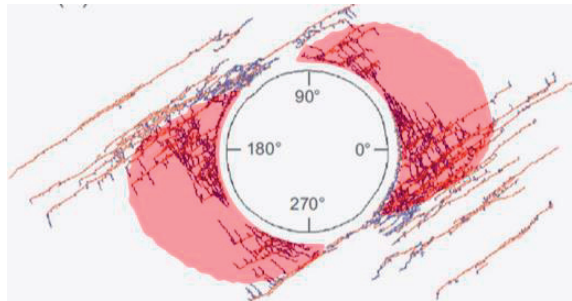


Figure 7-15: Comparison obtained by superposition of damage in the present model at 200 days (in red) and the fracture distribution from Lisjak et al. (2015) at full de-confinement (red and blue lines).

7.6.3. Comparison of tunnel wall radial convergence with in-situ measurements

Figure 7-16 illustrates the comparison between numerical predictions and measurements of the evolution of displacements with time for the 5 different targets (see Figure 7-3 for their position) and for the 5 sections considered in the present study. The displacements at sections TM 10.6, TM 14.3, TM 21.8, TM 27.6 and TM 34.3 are reported against a single curve obtained from the numerical model for each target. The numerical model is representative of

a generalized section, while in-situ measurements might experience scatter between each section due to local heterogeneities^f (i.e., faults or pre-existing fractures, different excavation profiles, etc.). The numerical predictions are consistent with the measured data, both in terms of absolute values as well as displacement increase with time. Within the considered time span, consolidation seems to be the only responsible phenomenon for the delayed deformation process and no mechanical creep phenomena are believed to play a major role. The highest discrepancy between numerical predictions and measurements is observed at convergence target P5. In their work, Martin and Lanyon (2003) used elastic numerical predictions to draw a conceptual model of the breakouts and failure distribution around tunnels and boreholes in OPA at the Mont Terri URL. It is a powerful and yet simple representation, although for anisotropic materials like OPA, breakouts distribution is not only a function of stress concentration (a fairly valid assumption for isotropic material) but depends also on the anisotropic strength distribution. This phenomenon can be well explained by recurring to the simple scheme of Figure 7-14. We recall that the solid black line indicates the circumferential stress acting around the tunnel and the red line the available anisotropic unconfined compressive strength given by model MS3 and with parameters given in Table 7-2. Breakouts are expected in those areas where the acting stress exceeds the available strength (as, e.g., shown for damage distribution in Figure 7-12). In the current model, the smallest strength available in unconfined compression conditions is found when the bedding planes are inclined between 33° and 45° counterclockwise from the horizontal axis. These conditions are met, e.g., at the right wall. This is a direct consequence of the strength parameters calibration inherited from Chapter 5, which is based on the set of experimental triaxial compression tests performed on shaly facies of OPA by Gräsle and Plischke (2010). In these tests, only directions of bedding planes at 0°, 45° and 90° are investigated and the calibration procedure results in a strength minimum available between 30° and 45° (see, e.g., Figure 5-9). On the contrary, from the data collected during the FE-tunnel excavation, major breakouts are experienced at target P5 location, i.e., roughly where sample D from Figure 7-14 is found. Sample D has a bedding inclination of roughly 60°. This suggests that the minimum strength available in triaxial compression tests should be found at this orientation. Such hypothesis gains even more strength if the results from triaxial compression tests on other shales under study are considered (see Figure 5-9), where usually minimum strength is found around 60° of beddings inclination. Furthermore, results from triaxial compression tests in OPA at the Schalttingen site showed that the minimum strength is found at 60°

^f In this case, local is referred to the tunnel circumference and not to the whole rock laboratory.

inclination of the beddings (Jahns, 2013). This is the reason for the discrepancy between numerical predictions and experimental results. It appears clear that a better representation of the breakouts and failures distribution around FE-tunnel necessitates and improvement in the characterization of the anisotropic behavior of OPA at the laboratory scale.

Furthermore, at point E in Figure 7-14, buckling instabilities are possible, as the circumferential stress acts parallel to the bedding planes. Better predictions could be achieved if the capabilities to simulate buckling in the constitutive model are added. Finally, even though this is not the case, when the state of stress reaches higher values of anisotropy (i.e., on principal stress component is much greater than the other two), tensile failure could also play a dominant role in the failure mechanisms. This would be of particular importance, e.g., at other locations of the laboratory (or other sites), where measures suggest that the state of stress could exhibit a higher degree of anisotropy leading to an increase of the likelihood of tensile failures.

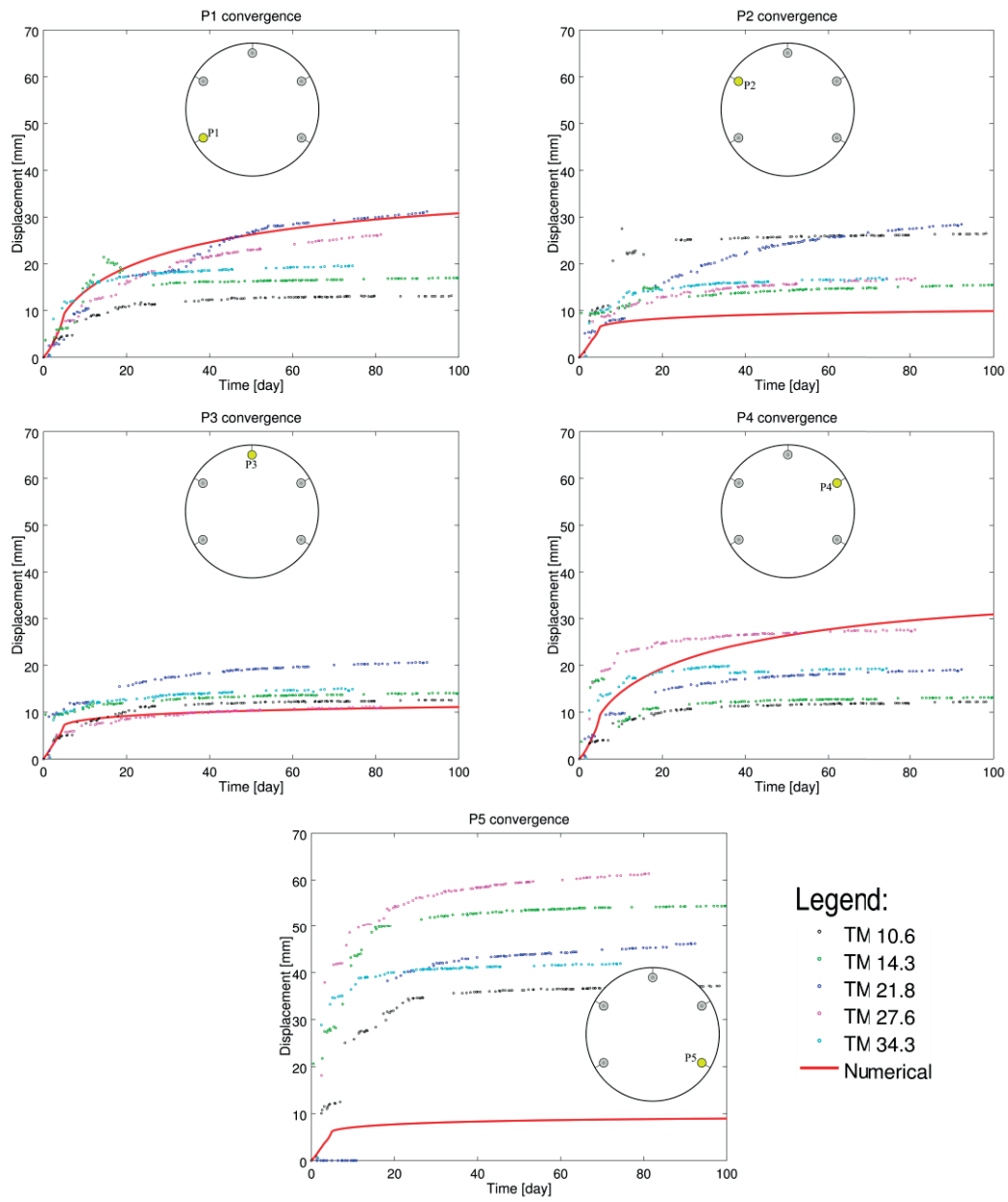


Figure 7-16: Displacement evolution with time at different optical targets (see Figure 7-3) in the numerical model (red) and for the different sections considered in the present study (TM refers to tunnel meter).

7.7. Conclusions

We have proposed a consistent modeling approach to simulate the excavation procedure in an anisotropic sedimentary shale. The constitutive model MS3 is specifically developed for plasticity, and was carefully calibrated to reproduce the behavior of OPA. The numerical simulation of the excavation of the FE-tunnel was performed in hydro-mechanical coupled conditions, and a second gradient of dilatancy formulation was employed. The parameters were calibrated based on laboratory tests and literature values, so that numerical predictions of tunnel excavation were not adjusted to fit experimental data. The validation of the model consisted in a detailed comparison between numerical predictions and observed in-situ measurements of pore water pressure evolution, displacement evolution and degradation of elasticity. Good agreement between numerical predictions and in-situ measured values was found, so that the model can successfully reproduce the majority of the complex phenomena governing excavations in OPA.

Several advantages can be highlighted in the proposed approach. Combining damage and plasticity carries the advantage of better describing the inelastic processes of the mechanical behavior of shale. The approach that was followed to include anisotropy can correctly reproduce the strength of the rock mass and the deformation pattern around a tunnel. The second gradient of dilatancy formulation has proven to be a consistent and powerful tool to avoid spurious mesh dependency. The extension of the damage zone is correctly predicted, as well as the degradation of elasticity around the tunnel. The hydro-mechanical coupling carries additional information compared to purely mechanical approaches, and the evolution of the displacements with time can be correctly predicted without recurring to mechanical creep law.

This work fulfills two purposes: on the one hand, the followed approach can be considered as a valid tool to model the excavation process in low-permeable, anisotropic quasi-brittle geomaterials; on the other hand, the numerical results of the analysis constitute an additional validation of the material parameters of OPA and give important insights on the complex coupled phenomena that govern its mechanical behavior. The results can be successfully used to design future experimental activities at the Mont Terri URL, e.g., excavation of new galleries, but also can give precious insights in the experimental characterization of OPA at the laboratory scale. Understanding correctly the behavior of OPA at both the laboratory and the field scale, constitutes a fundamental step for the safety improvement of deep geological repositories of high level nuclear waste.

7.8. Acknowledgements

The authors wish to thank the Swiss Federal office of Topography (swisstopo), the Eidgenössisches Nuklearsicherheitsinspektorat ENSI and the Mont Terri Project for financing this work. The authors wish to thank Dr. Paul Bossart and Dr. David Jäggi of swisstopo and Dr. Werner Gräsle of BGR, Germany, for providing data concerning the excavation of the FE-tunnel as well as precious insights into the behavior of Opalinus Clay at the field and laboratory scale. The authors would also like to thank Dr. Sylvie Granet, Dr. Roméo Fernandes and Dr. Simon Raude of EDF (Électricité de France) R&D for their important suggestions and clarifications related to the tunnel excavation procedure in *Code_Aster*.

7.9. References

- [R5.04.03], 2013. Modélisation second gradient. Documentation version 12, Code_Aster, www.code-aster.org.
- Bock, H., 2009. RA Experiment: Updated Review of the Rock Mechanics Properties of the Opalinus Clay of the Mont Terri URL based on Laboratory and Field Testing. Mont Terri Project, Technical Report 2008-04.
- Boidy, E., Bouvard, A., Pellet, F., 2002. Back analysis of time-dependent behaviour of a test gallery in claystone. *Tunn Undergr Sp Tech* 17, 415-424.
- Bossart, P., Bernier, F., Birkholzer, J., Bruggeman, C., Connoll, P., Dewonck, S., Fukaya, M., Herfor, M., Jensen, M., Matray, J.-M., Mayor, J.C., Moeri, A., Oyama, T., Schuster, K., Shigeta, N., Vietor, T., Wiczorek, K., 2017. Geologic setting and overview of key experiments in the Mont Terri rock laboratory. *Swiss J Geosci* (in preparation).
- Bossart, P., Meier, P.M., Moeri, A., Trick, T., Mayor, J.-C., 2002. Geological and hydraulic characterisation of the excavation disturbed zone in the Opalinus Clay of the Mont Terri Rock Laboratory. *Eng Geol* 66, 19-38.
- Bossart, P., Thury, M., 2007. Research in the Mont Terri Rock laboratory: quo vadis? *Physics and Chemistry of the Earth, Parts A/B/C* 32, 19-31.
- Carranza-Torres, C., Fairhurst, C., 1999. The elasto-plastic response of underground excavations in rock masses that satisfy the Hoek–Brown failure criterion. *Int J Rock Mech Min* 36, 777-809.
- Daneluzzi, R., Burrus, F., Küttel, T., 2013. Pilot Project FE Gallery: Execution of the FE Gallery. Mont Terri Technical Note TN 2013-103.
- Feiveson, H., Mian, Z., Ramana, M., von Hippel, F., 2011. Managing nuclear spent fuel: Policy lessons from a 10-country study. *Bulletin of the Atomic Scientists* 27.

- Fernandes, R., 2009. Modélisation numérique objective des problèmes hydromécaniques couplés dans le cas des géomatériaux. Thèse de doctorat à l'école doctorale Université Jean Fourier (Grenoble1), 107-136.
- Fernandes, R., Chavant, C., Chambon, R., 2008. A simplified second gradient model for dilatant materials: theory and numerical implementation. *Int J Solids Struct* 45, 5289-5307.
- Foucault, A., Voldoire, F., Modaresi, A., 2011. On the numerical implementation of a multi-mechanism cyclic plasticity model associated to a dilation second gradient model aiming strain localization mitigation. 9th International work-shop on bifurcation and degradation in geomaterials, May23–26; 2011. Porquerolles, France.
- Gens, A., Vaunat, J., Garitte, B., Wileveau, Y., 2007. In situ behaviour of a stiff layered clay subject to thermal loading: observations and interpretation. *Géotechnique* 57 (2), 207-228.
- Gräsle, W., Plischke, I., 2010. Laboratory Testing (LT) Experiment: Mechanical Behavior of Opalinus Clay, Final report from Phases 6 – 14. Mont Terri Technical Note TN 2009-07.
- Haghighat, E., Pietruszczak, S., 2015. On the mechanical and hydraulic response of sedimentary rocks in the presence of discontinuities. *Geomechanics for Energy and the Environment* 4, 61-72.
- Jahns, E., 2013. Geomechanical laboratory tests on Opalinus Clay cores from the bore hole Schlattingen SLA-1. Nagra Work Report NAB.
- Jaeggi, D., Wymann, L., Burrus, F., Becker, J., P, B., 2014. FE-E (EDZ-characterization in the vicinity of the FE-gallery) Experiment Synthesis of the excavation damaged zone (EDZ) (Draftversion). Mont Terri Technical Note TN 2014-33.
- Lemaitre, J., Chaboche, J.-L., Benallal, A., Desmorat, R., 2009. *Mécanique des matériaux solides-3eme édition*. Dunod.
- Levasseur, S., Charlier, R., Frieg, B., Collin, F., 2010. Hydro-mechanical modelling of the excavation damaged zone around an underground excavation at Mont Terri Rock Laboratory. *Int J Rock Mech Min* 47, 414-425.
- Lisjak, A., Garitte, B., Grasselli, G., Müller, H., Vietor, T., 2015. The excavation of a circular tunnel in a bedded argillaceous rock (Opalinus Clay): short-term rock mass response and FDEM numerical analysis. *Tunn Undergr Sp Tech* 45, 227-248.
- Lisjak, A., Grasselli, G., Vietor, T., 2014. Continuum–discontinuum analysis of failure mechanisms around unsupported circular excavations in anisotropic clay shales. *Int J Rock Mech Min* 65, 96-115.
- Martin, C., Lanyon, G., 2003. Measurement of in-situ stress in weak rocks at Mont Terri Rock Laboratory, Switzerland. *Int J Rock Mech Min* 40, 1077-1088.

- Pardoen, B., Seyedi, D., Collin, F., 2015. Shear banding modelling in cross-anisotropic rocks. *Int J Solids Struct* 72, 63-87.
- Pariso, F., Samat, S., Laloui, L., 2015. Constitutive analysis of shale: a coupled damage plasticity approach. *Int J Solids Struct* 75-76, 88-98.
- Plassart, R., Fernandes, R., Giraud, A., Hoxha, D., Laigle, F., 2013. Hydromechanical modelling of an excavation in an underground research laboratory with an elastoviscoplastic behaviour law and regularization by second gradient of dilation. *Int J Rock Mech Min* 58, 23-33.
- Rutqvist, J., 2015. Fractured rock stress-permeability relationships from in situ data and effects of temperature and chemical-mechanical couplings. *Geofluids* 15, 48-66.
- Rutqvist, J., Chen, F., Birkholzer, J., Liu, H.-H., Müller, H., Garitte, B., Vietor, T., 2013. Modeling of coupled thermo-hydro-mechanical processes at Mont Terri heater experiment in Opalinus Clay, using TOUGH-FLAC, Proceedings of the 2013 International High-Level Radioactive Conference (IHLRWM).
- Rutqvist, J., Stephansson, O., 2003. The role of hydromechanical coupling in fractured rock engineering. *Hydrogeol J* 11, 7-40.
- Sánchez, M., Gens, A., Olivella, S., 2012. THM analysis of a large-scale heating test incorporating material fabric changes. *Int J Num Analyt Meth Geomech*, 36(4), 391-421.
- Shao, H., Schuster, K., Sönnke, J., Bräuer, V., 2008. EDZ development in indurated clay formations—In situ borehole measurements and coupled HM modelling. *Physics and Chemistry of the Earth, Parts A/B/C* 33, S388-S395.
- Thury, M., Bossart, P., 1999. The Mont Terri rock laboratory, a new international research project in a Mesozoic shale formation, in Switzerland. *Eng Geol* 52, 347-359.
- Trick, T., Gräfe, K., Rösli, U., 2013. FE-A experiment: WP3: Multi-Packer-System (MPS) installed in BFE-A002, BFE-A003, BFE-A004, BFE-A005, BFE-A006 and BFE-A007; Data trend report after one year. Mont Terri Technical Note TN 2012-19.
- Tsang, C.-F., Barnichon, J., Birkholzer, J., Li, X.L., Liu, H., Sillen, X., 2012. Coupled thermo-hydro-mechanical processes in the near field of a high-level radioactive waste repository in clay formations. *Int J Rock Mech Min* 49, 31-44.
- Tsang, C.-F., Bernier, F., Davies, C., 2005. Geohydromechanical processes in the Excavation Damaged Zone in crystalline rock, rock salt, and indurated and plastic clays—in the context of radioactive waste disposal. *Int J Rock Mech Min* 42, 109-125.
- Vilarrasa, V., Koyama, T., Neretnieks, I., Jing, L., 2011. Shear-induced flow channels in a single rock fracture and their effect on solute transport. *Transport Porous Med* 87, 503-523.

7.9 References

- Vilarrasa, V., Makhnenko, R., Laloui, L., 2015. Influence of Poromechanical and Thermal Properties of the Caprock on the Safety of CO₂ Storage, Second EAGE Workshop on Geomechanics and Energy.
- Vogt, T., Müller, H., Garitte, B., Sakaki, T., Vietor, T., 2013. Excavation Induced Hydraulic Response of Opalinus Clay-Investigations of the FE-Experiment at the Mont Terri URL in Switzerland, AGU Fall Meeting Abstracts, p. 1276.

8. Conclusions and perspectives

This thesis is aimed at developing a consistent modeling strategy for the hydro-mechanical behavior of shale, with a particular focus toward Opalinus Clay. To achieve this goal, proper constitutive models were developed and tested. The resulting final damage-plastic constitutive model has been implemented into the FEM solver *Code_Aster*, so that analyses of coupled hydro-mechanical boundary value problems can be performed. In the following, the general conclusions are drawn based on the results presented in this thesis. Furtherly, insights and perspectives for the development of future research works are addressed.

8.1. General conclusions

Advanced constitutive models are necessary in many applications that involve temperature, suction and stress changes, such as nuclear waste storage, CO₂ storage and unconventional hydrocarbon production. Several experimental evidences have shown separately that strength in geomaterials depends on these three variables. In the current work we have proposed a constitutive model in which strength predictions account for all of the above mentioned effects. More specifically, the goal was to investigate the role of stress paths different than purely triaxial compression in case of non-isothermal and unsaturated conditions. Results on two case studies relative to geological nuclear waste storage and CO₂ sequestration applications evidenced the importance that the three effects have when combined. Even in multiphysics conditions, stress paths in which Lode's angle is different than the one in pure triaxial compression are most common. In such cases, simulation results illustrated that not considering a reduced strength in extension can lead to dangerous overestimation of the available strength.

Shale formations gained importance in recent years as are often encountered in advanced geo-energetic and geo-environmental applications, including nuclear waste storage, CO₂ storage and unconventional hydrocarbon production. Although the main focus of the thesis is directed toward the modeling of shales for nuclear waste storage applications, the results obtained are applicable as well to other fields of research and practice involving the modeling of shale. The mechanical description of the constitutive behavior of quasi-brittle geomaterials, and shale in particular, is a complex task that can be best undertaken with a plastic-damage coupled approach. Currently, several kind of constitutive models coupling damage and plasticity are available in the literature. Despite this richness, we felt the necessity of exploring new different combinations of damage and plasticity and formulate a new constitutive model specifically tailored for shale. The employed criteria for formulating a new model largely depend on the results that are to be obtained. While the constitutive description

must represent the most important characteristics of the physical behavior with the highest possible fidelity, simplicity and easiness of parameter calibration remain an asset for practical complex applications such as hydro-mechanical tunnel excavation analysis. With this in mind, two different combinations of damage and plasticity theories were developed in the first part of the thesis.

In the first approach, which has resulted in a constitutive model called MS1, damage is coupled with the elastic energy associated with a measure of the elastic tensile strains. It is physically sound, thermodynamically consistent and has proven to deliver reliable predictions of the mechanical behavior of shale. Shortcomings were found in the way in which the predicted strength increases with confinement and on the difficulties related to material parameters calibration with the most widespread experimental characterization tests, such as conventional triaxial compression tests.

To overcome these shortcomings, a new combination of damage and plasticity lead to the formulation of model MS2. While it shares some features with the previous model, MS2 has a different philosophy as it relates damage increase to a measure of plastic strain increment at the peak of stress. Inelastic onset is a non-linear function of the mean stress and, at plastic saturation, the failure envelope degenerates into a linear function of the mean stress. Failure can be better controlled as the interaction of damage and plasticity is limited. The model philosophy is more oriented toward a phenomenological mechanical approach and the characterization of model parameters can be done straight forward from the most common laboratory tests in geomechanics. The model was implemented in the FEM solver *Code_Aster* with an implicit scheme, which guarantees robustness and stability of the numerical solution. The validation examples showed good agreement between the numerical predictions and the experimental results. Good agreement between numerical predictions and experimental results were observed even in case of hydro-mechanical couplings in triaxial undrained conditions. The hypothesis made in the model formulation proves to be correct.

In order to account for complexities related to the true triaxial and anisotropic nature of strength, a further extension of model MS2 lead to the formulation of model MS3. In this last model, the plastic envelope, which represents the failure envelope of the material, is extended to account true triaxial and anisotropic strength. While the first characteristic is common to all kind of geomaterials, including soils, rocks and concrete, the second characteristic is peculiar to many shales having a bedded structure with schistosity planes. Both expansions, i.e., the true triaxial and the anisotropic formulation, share the same idea: the constitutive model can be formulated in isotropic conditions in conventional triaxial compression space and later extended to account for both features. The advantage, compared to the most common failure surfaces for geomaterials available in literature, consists in the higher flexibility of the model, as few parameters allow deep control of the shape of the yield

surface. The comparative study demonstrated that the new failure surface MS3 produces a smaller error against several sets of experimental data if compared to some of the most common failure surfaces in geomechanics. Therefore, another advantage of the model is its capability of producing better results in terms of strength predictions.

Several regularization techniques were proposed in literature to control excessive localization during FEM analyses employing strain softening models. Among them, micromorphic continuum formulation was widely employed for analyzing geomaterials. We made use of a particular case of micromorphic continuum formulation called second gradient of dilatancy. Compared to second gradient of elasticity model, this formulation, which is available in *Code_Aster*, retains less additional degrees of freedom and has therefore a much higher computational efficiency. We proposed a numerical study in which the structural response of the model MS3 in combination with second gradient of dilatancy is investigated. Results have demonstrated how this combination leads to consistent description of localized inelastic strains in presence of plastic-damage behavior. Pathological mesh dependency is successfully removed and the unphysical expansion of the localized zone is avoided thanks to the non-associated plastic potential employed. Anisotropy showed to have an important influence in terms of global structural response in case of localized behavior. The size of the problem must also be taken into account, as the global dissipation is controlled by the localized damage band.

The hydro-mechanical FEM tunnel analysis was designed as a powerful validation example of all of the developed concepts. Results of the numerical analysis were extensively compared to in-situ measurements collected during the excavation of the FE-tunnel at the Mont Terri site. The constitutive model, along with the employed regularization technique and hydro-mechanical description, have proven to be a highly efficient tool to solve hydro-mechanical excavation problems in anisotropic shale that involve failure. Consistent agreement between numerical predictions and experimental measurements was found. Compared to purely plastic approaches, adding damage to the formulation is more representative of the quasi-brittle nature of the material (as it is a measure of defects density). Unlike to purely mechanical studies, the hydro-mechanical coupled conditions allowed to perform long-term analyses in which pore water pressure decrease is responsible for changes in the effective stress state and delayed deformation.

8.2. Future perspectives

Results of the analyses carried out in this thesis can be particularly useful not only to draw possible future development margins in terms of constitutive and numerical approach, but also in the experimental characterization of OPA.

8.2.1. Experimental perspectives and recommendations

The correct representation of the pore water pressure role in OPA is a fundamental issue. At the repository site, OPA is water saturated and throughout the whole process of waste storage (from excavation to long-term disposal conditions) the role of the hydro-mechanical couplings must be correctly predicted. It is therefore necessary to have a complete characterization at the laboratory scale in which the role of the pore water pressure is known, so that the constitutive response in terms of effective stress is well understood. Given the very low permeability of OPA, its laboratory characterization is a difficult task to achieve and technical improvements should be sought in this sense.

The effect of anisotropic behavior should also be better understood. At present, only limited data is available in terms of triaxial tests results. Usually, for OPA, a few directions of the bedding planes are investigated. As shown in Chapter 5, other shales had much wider ranges of investigated directions. As a result of this shortcoming, the error given by all the failure surfaces compared to experimental tests on OPA was much higher than when compared to data regarding other shales that are available in the literature. A better understanding of the anisotropic strength behavior of OPA is crucial for delivering highly reliable numerical predictions. The same concept applies to the true triaxial strength of OPA. Currently, no data is available. We showed in the thesis the importance of true triaxial strength of geomaterials. Once again, this has a direct implication in numerical analyses, as the knowledge of the Lode's angle dependency of strength can improve numerical predictions.

Additional measurements during laboratory testing could also be helpful to the modeling community in order to better understand the mechanical behavior of OPA. As an example, for the developed damage model, acoustic emissions during laboratory testing would have proven an extremely powerful tool in determining the damage accumulation in the sample. These recommendations can be helpful in the future in order to deliver complete and reliable experimental protocols in the laboratory testing of OPA.

8.2.2. Constitutive and numerical perspectives and recommendations

The premise to this section is that any possible improvement in the constitutive behavior must be justified by additional experimental findings that are available. The proposed constitutive model MS3 was based, to the fullest extent possible, on the actual experimental knowledge that was available.

An important improvement of the developed model MS3 is related to the effects that temperature and suction have on the strength of shales. In OPA at Mont Terri, during the ventilation phase that follows tunnel excavation, the material desaturates and additional superficial cracking can appear as a consequence. Extending the concept of damage to include desiccation cracking could improve the performances of the model and widen its

applicability. The same consideration is valid for temperature effects. While drastic cooling can lead as well to induced cracking in a non-free to deform configuration, temperature increase can deteriorate the properties of the material and reduce its strength. This will be particularly important in the early years of repository conditions, where temperature in the rock mass will increase due to the heat generated by the nuclear material inside the canisters. In the longer term, and especially in combination with temperature effects, mechanical creep is believed to play as well an important role in the definition of the mechanical response of OPA. Thermo-visco-plastic or thermo-visco-elastic constitutive behavior will have the effect of a stress relaxation induced both by the rate of loading and the temperature. In the proposed model, these effects should be included for a proper description of the repository conditions in the long term (several years).

Another important aspect to be considered is the upscaling of material parameters from the laboratory to the field scale. The behavior at the field scale is influenced by the pre-existing fracture network and it is believed that the deformation and strength characteristics of the material are lower than the one measured at the laboratory scale. Understanding this upscaling is an important step in order to be able to switch from laboratory to field scale results. Numerical analyses in plane strain conditions have shown how important is the choice of the scale of the problem in terms of structural response. Further investigations in this direction could lead to proper values of up-scaled (or down-scaled) parameters.

In the present study of the FE-tunnel analysis, the concrete lining with wire mesh was not modeled as, according to the suggestions of previous studies, local breakage lead to a global reduced stiffness of the lining of several orders of magnitude. This is an interesting aspect that should deserve a further investigation. Lining behavior is influenced, on one side, by the mechanical behavior of the concrete forming it, and on the other by the rock-structure interaction forces that develop at the interface between lining and rock mass. A proper understanding of these forces from an experimental point of view can lead to the formulation of specific laws of damageable-like interface elements.

Finally, we focused on the possible future perspectives of research on OPA related to the nuclear waste repository conditions. Taking a broader look, all of these concepts could be easily applied to other shales and the evolutions in terms of constitutive modeling capabilities could be related to other geomechanical problems, like CO₂ storage or unconventional oil and gas exploitation.

Appendix A. Plastic multipliers of the thermo-mechanical model

We detail in this Appendix how to obtain the plastic multipliers from the thermo-mechanical part of the model from the Prager's consistency condition

$$\begin{cases} \mathbf{dF} = \frac{\partial \mathbf{F}}{\partial \boldsymbol{\sigma}'} : \mathbf{d}\boldsymbol{\sigma}' + \frac{\partial \mathbf{F}}{\partial \pi} \cdot \frac{\partial \pi}{\partial \lambda^p} \cdot \lambda^p \leq \mathbf{0} \\ \mathbf{dF}' \cdot \lambda^p \geq 0, \quad \lambda^p \geq 0 \end{cases} \quad (\text{A.1})$$

Taking into account that the effective stress increment in response to a prescribed strain increment can be expressed as

$$\mathbf{d}\boldsymbol{\sigma}' = \mathbf{E} : (\mathbf{d}\boldsymbol{\varepsilon} + \boldsymbol{\beta}_T dT - \mathbf{G} \cdot \lambda^p), \quad (\text{A.2})$$

where $\mathbf{G} = \partial \mathbf{g} / \partial \boldsymbol{\sigma}'$ is the flow direction matrix and \mathbf{g} is the plastic potential vector, the consistency condition can be rewritten as

$$\begin{cases} \mathbf{dF} = \mathbf{J} : \mathbf{E} : \mathbf{d}\boldsymbol{\varepsilon} + \mathbf{J} : \mathbf{E} : \boldsymbol{\beta}_T dT - (\mathbf{H} + \mathbf{J} : \mathbf{E} : \mathbf{G}) \cdot \lambda^p \leq \mathbf{0} \\ \mathbf{dF}' \cdot \lambda^p \geq 0, \quad \lambda^p \geq 0 \end{cases}, \quad (\text{A.3})$$

where $\mathbf{J} = \partial \mathbf{F} / \partial \boldsymbol{\sigma}'$ and $\mathbf{H} = -\partial \mathbf{F} / \partial \pi \cdot \partial \pi / \partial \lambda^p$ is the hardening moduli matrix. The elastic stiffness matrix has the form

$$\mathbf{E} = \begin{bmatrix} K + \frac{4}{3}G & K - \frac{2}{3}G & K - \frac{2}{3}G & 0 & 0 & 0 \\ & K + \frac{4}{3}G & K - \frac{2}{3}G & 0 & 0 & 0 \\ & & K + \frac{4}{3}G & 0 & 0 & 0 \\ & \text{Symmetric} & & 2G & 0 & 0 \\ & & & & 2G & 0 \\ & & & & & 2G \end{bmatrix}, \quad (\text{A.4})$$

and the derivative of the yield surfaces vector with respect to the effective stress tensor is

$$\mathbf{J} = \begin{bmatrix} \frac{\partial f_{iso}}{\partial \sigma'_{11}} & \frac{\partial f_{iso}}{\partial \sigma'_{22}} & \frac{\partial f_{iso}}{\partial \sigma'_{33}} & \frac{\partial f_{iso}}{\partial \sigma'_{12}} & \frac{\partial f_{iso}}{\partial \sigma'_{13}} & \frac{\partial f_{iso}}{\partial \sigma'_{23}} \\ \frac{\partial f_{dev}}{\partial \sigma'_{11}} & \frac{\partial f_{dev}}{\partial \sigma'_{22}} & \frac{\partial f_{dev}}{\partial \sigma'_{33}} & \frac{\partial f_{dev}}{\partial \sigma'_{12}} & \frac{\partial f_{dev}}{\partial \sigma'_{13}} & \frac{\partial f_{dev}}{\partial \sigma'_{23}} \end{bmatrix}, \quad (\text{A.5})$$

where the derivatives of the isotropic yield surface are

$$\begin{aligned} \frac{\partial f_{iso}}{\partial \sigma'_{11}} &= \frac{\partial f_{iso}}{\partial \sigma'_{22}} = \frac{\partial f_{iso}}{\partial \sigma'_{33}} = \frac{1}{3}, \\ \frac{\partial f_{iso}}{\partial \sigma'_{12}} &= \frac{\partial f_{iso}}{\partial \sigma'_{13}} = \frac{\partial f_{iso}}{\partial \sigma'_{23}} = 0, \end{aligned} \quad (\text{A.6})$$

and the derivatives of the deviatoric yield surface are obtained using the chain rule

$$\frac{\partial f_{dev}}{\partial \boldsymbol{\sigma}'} = \frac{\partial f_{dev}}{\partial q} \frac{\partial q}{\partial \boldsymbol{\sigma}'} + \frac{\partial f_{dev}}{\partial p'} \frac{\partial p'}{\partial \boldsymbol{\sigma}'} + \frac{\partial f_{dev}}{\partial \sin(3\vartheta)} \frac{\partial \sin(3\vartheta)}{\partial \boldsymbol{\sigma}'} \quad (\text{A.7})$$

where

$$\begin{aligned} \frac{\partial f_{dev}}{\partial q} &= 1, \\ \frac{\partial f_{dev}}{\partial p'} &= M \left[b - 1 + b \ln \left(\frac{p'd}{p'_c} \right) \right] r_{dev}, \\ \frac{\partial f_{dev}}{\partial \sin(3\vartheta)} &= -3\sqrt{3}a_L b_L n_L (1 + b_L \sin(3\vartheta))^{n_L-1} p' \left(1 - b \ln \left(\frac{p'd}{p'_c} \right) \right) r_{dev}, \end{aligned} \quad (\text{A.8})$$

and

$$\frac{\partial q}{\partial \sigma'_{ij}} = \begin{cases} \frac{3}{2q} (\sigma'_{ij} - p'), & \text{if } i = j \\ \frac{3\sigma'_{ij}}{q}, & \text{if } i \neq j \end{cases}, \quad (\text{A.9})$$

$$\frac{\partial p'}{\partial \sigma'_{ij}} = \frac{\delta_{ij}}{3}, \quad (\text{A.10})$$

$$\frac{\partial \sin(3\vartheta)}{\partial \boldsymbol{\sigma}'} = -\frac{3\sqrt{3}}{2J_{2D}^{3/2}} \left((\mathbf{s}^2)' - \frac{2}{3} J_{2D} \mathbf{I} - \frac{3J_{3D} \mathbf{s}}{2J_{2D}} \right),$$

or

$$\frac{\partial \sin(3\vartheta)}{\partial \sigma'_{ii}} = -\frac{3\sqrt{3}}{2J_{2D}^{3/2}} \times \quad , \quad (\text{A.11})$$

$$\times \left[\frac{1}{3} \left(2(\sigma'_{ii} - p')^2 - 2(\sigma'_{kk} - p')^2 + \sigma'_{ij}{}^2 + \sigma'_{ik}{}^2 - 2\sigma'_{jk}{}^2 \right) - \frac{3J_{3D}}{2J_{2D}} (\sigma'_{ii} - p') \right],$$

$$\frac{\partial \sin(3\vartheta)}{\partial \sigma'_{ij}} = -\frac{3\sqrt{3}}{2J_{2D}^{3/2}} \left[-2\sigma'_{ij} (\sigma'_{kk} - p') + 2\sigma'_{jk} \sigma'_{ki} - \frac{3J_{3D}}{2J_{2D}} 2\sigma'_{ij} \right], \text{ if } i \neq j$$

where δ_{ij} is the delta Kronecker.

The hardening moduli matrix has the form

$$\mathbf{H} = \begin{bmatrix} -\frac{\partial f_{iso}}{\partial \lambda_{iso}^p} & -\frac{\partial f_{iso}}{\partial \lambda_{dev}^p} \\ -\frac{\partial f_{dev}}{\partial \lambda_{iso}^p} & -\frac{\partial f_{dev}}{\partial \lambda_{dev}^p} \end{bmatrix}, \quad (\text{A.12})$$

where

$$\begin{aligned} -\frac{\partial f_{iso}}{\partial \lambda_{iso}^p} &= -\frac{\partial f_{iso}}{\partial r_{iso}} \frac{\partial r_{iso}}{\partial \varepsilon_v^p} \frac{\partial \varepsilon_v^p}{\partial \lambda_{iso}^p} - \frac{\partial f_{iso}}{\partial p'_c} \frac{\partial p'_c}{\partial \varepsilon_v^p} \frac{\partial \varepsilon_v^p}{\partial \lambda_{iso}^p} = p'_c \frac{(1 - (r_{iso} - r_{iso}^e))^2}{c} + p'_c \beta r_{iso}, \\ -\frac{\partial f_{iso}}{\partial \lambda_{dev}^p} &= -\frac{\partial f_{iso}}{\partial r_{dev}} \frac{\partial r_{dev}}{\partial \varepsilon_d^p} \frac{\partial \varepsilon_d^p}{\partial \lambda_{dev}^p} - \frac{\partial f_{iso}}{\partial p'_c} \frac{\partial p'_c}{\partial \varepsilon_v^p} \frac{\partial \varepsilon_v^p}{\partial \lambda_{dev}^p} = p'_c \beta r_{iso} \alpha \left(M - \frac{q}{p'} \right), \\ -\frac{\partial f_{dev}}{\partial \lambda_{iso}^p} &= -\frac{\partial f_{dev}}{\partial r_{iso}} \frac{\partial r_{iso}}{\partial \varepsilon_v^p} \frac{\partial \varepsilon_v^p}{\partial \lambda_{iso}^p} - \frac{\partial f_{dev}}{\partial p'_c} \frac{\partial p'_c}{\partial \varepsilon_v^p} \frac{\partial \varepsilon_v^p}{\partial \lambda_{iso}^p} = Mp'b\beta r_{dev}, \\ -\frac{\partial f_{dev}}{\partial \lambda_{dev}^p} &= -\frac{\partial f_{dev}}{\partial r_{dev}} \frac{\partial r_{dev}}{\partial \varepsilon_d^p} \frac{\partial \varepsilon_d^p}{\partial \lambda_{dev}^p} - \frac{\partial f_{dev}}{\partial p'_c} \frac{\partial p'_c}{\partial \varepsilon_v^p} \frac{\partial \varepsilon_v^p}{\partial \lambda_{dev}^p} = \\ &= Mp' \left(1 - b \ln \left(\frac{p'd}{p'_c} \right) \right) \frac{(1 - (r_{dev} - r_{dev}^e))^2}{a} + Mp'b\beta \alpha \left(M - \frac{q}{p'} \right) r_{dev}, \end{aligned} \quad , (\text{A.13})$$

where the derivatives of the degrees of plastification of the isotropic and deviatoric mechanisms are $\partial r_{iso}/\partial \varepsilon_v^p = (1 - (r_{iso} - r_{iso}^e))^2 / c$ and $\partial r_{dev}/\partial \varepsilon_d^p = (1 - (r_{dev} - r_{dev}^e))^2 / a$, respectively. The flow direction matrix is

$$\mathbf{G} = \begin{bmatrix} \frac{\partial g_{iso}}{\partial \sigma'_{11}} & \frac{\partial g_{iso}}{\partial \sigma'_{22}} & \frac{\partial g_{iso}}{\partial \sigma'_{33}} & \frac{\partial g_{iso}}{\partial \sigma'_{12}} & \frac{\partial g_{iso}}{\partial \sigma'_{13}} & \frac{\partial g_{iso}}{\partial \sigma'_{23}} \\ \frac{\partial g_{dev}}{\partial \sigma'_{11}} & \frac{\partial g_{dev}}{\partial \sigma'_{22}} & \frac{\partial g_{dev}}{\partial \sigma'_{33}} & \frac{\partial g_{dev}}{\partial \sigma'_{12}} & \frac{\partial g_{dev}}{\partial \sigma'_{13}} & \frac{\partial g_{dev}}{\partial \sigma'_{23}} \end{bmatrix}^t, \quad (\text{A.14})$$

where the derivatives of the isotropic plastic potential are

$$\begin{aligned} \frac{\partial g_{iso}}{\partial \sigma'_{11}} &= \frac{\partial g_{iso}}{\partial \sigma'_{22}} = \frac{\partial g_{iso}}{\partial \sigma'_{33}} = \frac{1}{3}, \\ \frac{\partial g_{iso}}{\partial \sigma'_{12}} &= \frac{\partial g_{iso}}{\partial \sigma'_{13}} = \frac{\partial g_{iso}}{\partial \sigma'_{23}} = 0, \end{aligned} \quad (\text{A.15})$$

and the derivatives of the deviatoric plastic potential are obtained using the chain rule

$$\frac{\partial g_{dev}}{\partial \sigma'} = \frac{\partial g_{dev}}{\partial q} \frac{\partial q}{\partial \sigma'} + \frac{\partial g_{dev}}{\partial p'} \frac{\partial p'}{\partial \sigma'} + \frac{\partial g_{dev}}{\partial \sin(3\vartheta)} \frac{\partial \sin(3\vartheta)}{\partial \sigma'}, \quad (\text{A.16})$$

where

$$\begin{aligned} \frac{\partial g_{dev}}{\partial q} &= 1, \\ \frac{\partial g_{dev}}{\partial p'} &= \alpha \left(M - \frac{q}{p'} \right), \\ \frac{\partial g_{dev}}{\partial \sin(3\vartheta)} &= -3\sqrt{3}a_L b_L n_L (1 + b_L \sin(3\vartheta))^{n_L - 1} \frac{\alpha}{\alpha - 1} p' \left(1 - \frac{1}{\alpha} \left(\frac{p'd}{p'_c} \right)^{\alpha - 1} \right), \end{aligned} \quad (\text{A.17})$$

and the derivatives of the stress variables with respect to the effective stress tensor are given by Eqs. (A9) – (A11).

The products of these matrices become

$$\mathbf{A} = \mathbf{J} : \mathbf{E} : \mathbf{d}\boldsymbol{\varepsilon} = \left(\begin{array}{c} K \varepsilon_v \\ \frac{3G}{q} \sum_{i=1,2,3} \varepsilon_{ii} (\sigma'_{ii} - p') + \frac{6G}{q} (\varepsilon_{12} \sigma'_{12} + \varepsilon_{13} \sigma'_{13} + \varepsilon_{23} \sigma'_{23}) + jK \varepsilon_v + L_f \end{array} \right), \quad (\text{A.18})$$

where $j = M \left[b - 1 + b \ln(p'd / p'_c) \right] r_{dev}$ and L_f is the contribution due to the Lode's angle, which reads

$$\begin{aligned}
 L_f &= -\frac{3\sqrt{3}G}{J_{2D}^{3/2}} \frac{\partial f_{dev}}{\partial \sin(3\vartheta)} (L_{f1} + L_{f2} + L_{f3} + L_{f4} + L_{f5} + L_{f6}), \\
 L_{f1} &= \varepsilon_{11} \left[\frac{1}{3} \left(2(\sigma'_{11} - p')^2 - (\sigma'_{22} - p')^2 - (\sigma'_{33} - p')^2 + \sigma'_{12}{}^2 + \sigma'_{13}{}^2 - 2\sigma'_{23}{}^2 \right) - \frac{3J_{3D}}{2J_{2D}} (\sigma'_{11} - p') \right], \\
 L_{f2} &= \varepsilon_{22} \left[\frac{1}{3} \left(2(\sigma'_{22} - p')^2 - (\sigma'_{33} - p')^2 - (\sigma'_{11} - p')^2 + \sigma'_{12}{}^2 + \sigma'_{23}{}^2 - 2\sigma'_{13}{}^2 \right) - \frac{3J_{3D}}{2J_{2D}} (\sigma'_{22} - p') \right], \\
 L_{f3} &= \varepsilon_{33} \left[\frac{1}{3} \left(2(\sigma'_{33} - p')^2 - (\sigma'_{11} - p')^2 - (\sigma'_{22} - p')^2 + \sigma'_{13}{}^2 + \sigma'_{23}{}^2 - 2\sigma'_{12}{}^2 \right) - \frac{3J_{3D}}{2J_{2D}} (\sigma'_{33} - p') \right], \\
 L_{f4} &= \varepsilon_{12} \left[-2\sigma'_{12} (\sigma'_{33} - p') + 2\sigma'_{13}\sigma'_{23} - \frac{3J_{3D}}{J_{2D}} \sigma'_{12} \right], \\
 L_{f5} &= \varepsilon_{13} \left[-2\sigma'_{13} (\sigma'_{22} - p') + 2\sigma'_{12}\sigma'_{23} - \frac{3J_{3D}}{J_{2D}} \sigma'_{13} \right], \\
 L_{f6} &= \varepsilon_{23} \left[-2\sigma'_{23} (\sigma'_{11} - p') + 2\sigma'_{12}\sigma'_{13} - \frac{3J_{3D}}{J_{2D}} \sigma'_{23} \right],
 \end{aligned} \tag{A.19}$$

$$\mathbf{B} = \mathbf{J} : \mathbf{E} : \boldsymbol{\beta}_T dT = \begin{pmatrix} K\beta'_s dT \\ jK\beta'_s dT \end{pmatrix} \tag{A.20}$$

$$\mathbf{J} : \mathbf{E} : \mathbf{G} = \begin{pmatrix} K & K\alpha \left(M - \frac{q}{p'} \right) \\ jK & \bar{H} + L_{\bar{H}} \end{pmatrix} \tag{A.21}$$

where $\bar{H} = \frac{9G}{2q^2} \sum_{i=1,2,3} (\sigma'_{ii} - p')^2 + \frac{18G}{q^2} (\sigma'_{12}{}^2 + \sigma'_{13}{}^2 + \sigma'_{23}{}^2) + jK\alpha \left(M - \frac{q}{p'} \right)$ and

$$L_{\bar{H}} = L_{\bar{H}_1} + L_{\bar{H}_2} + L_{\bar{H}_3},$$

$$L_{\bar{H}_1} = -\frac{3\sqrt{3}}{2J_{2D}^{3/2}} \frac{3G^2}{q} \frac{\partial g_{dev}}{\partial \sin(3\vartheta)} \left[\begin{array}{l} (\sigma'_{11} - p')^3 + (\sigma'_{22} - p')^3 + (\sigma'_{33} - p')^3 - \\ -\sigma'^2_{12}(\sigma'_{33} - p') - \sigma'^2_{13}(\sigma'_{22} - p') - \sigma'^2_{23}(\sigma'_{11} - p') - \\ -\frac{3J_{3D}}{2J_{2D}} [(\sigma'_{11} - p')^2 + (\sigma'_{22} - p')^2 + (\sigma'_{33} - p')^2] \end{array} \right],$$

$$L_{\bar{H}_2} = L \left\{ \begin{array}{l} \left[\frac{1}{3} (2(\sigma'_{11} - p')^2 - (\sigma'_{22} - p')^2 - (\sigma'_{33} - p')^2 + \sigma'^2_{12} + \sigma'^2_{13} - 2\sigma'^2_{23}) - \frac{3J_{3D}}{2J_{2D}} (\sigma'_{11} - p') \right]^2 + \\ + \left[\frac{1}{3} (2(\sigma'_{22} - p')^2 - (\sigma'_{33} - p')^2 - (\sigma'_{11} - p')^2 + \sigma'^2_{12} + \sigma'^2_{23} - 2\sigma'^2_{13}) - \frac{3J_{3D}}{2J_{2D}} (\sigma'_{22} - p') \right]^2 + \\ + \left[\frac{1}{3} (2(\sigma'_{33} - p')^2 - (\sigma'_{11} - p')^2 - (\sigma'_{22} - p')^2 + \sigma'^2_{13} + \sigma'^2_{23} - 2\sigma'^2_{12}) - \frac{3J_{3D}}{2J_{2D}} (\sigma'_{33} - p') \right]^2 \end{array} \right\},$$

$$L_{\bar{H}_3} = L \left\{ \begin{array}{l} \left[-2\sigma'_{12}(\sigma'_{33} - p') + 2\sigma'_{13}\sigma'_{23} - \frac{3J_{3D}}{J_{2D}} \sigma'_{12} \right]^2 + \\ + \left[-2\sigma'_{13}(\sigma'_{22} - p') + 2\sigma'_{12}\sigma'_{23} - \frac{3J_{3D}}{J_{2D}} \sigma'_{13} \right]^2 + \\ + \left[-2\sigma'_{23}(\sigma'_{11} - p') + 2\sigma'_{12}\sigma'_{13} - \frac{3J_{3D}}{J_{2D}} \sigma'_{23} \right]^2 \end{array} \right\},$$

(A.22)

$$\text{where } L = \frac{27G}{2J_{2D}^3} \frac{\partial f_{dev}}{\partial \sin(3\vartheta)} \frac{\partial g_{dev}}{\partial \sin(3\vartheta)}.$$

$$\mathbf{C} = \mathbf{H} + \mathbf{J} : \mathbf{E} : \mathbf{G} = \begin{pmatrix} C_{11} & C_{12} \\ C_{21} & C_{22} \end{pmatrix}. \quad (\text{A.23})$$

To obtain the values of the plastic multipliers, we have to solve the consistency equations

$$\begin{cases} dF_{iso} = A_1 + B_1 - C_{11}\lambda_{iso}^p - C_{12}\lambda_{dev}^p = 0 \\ dF_{dev} = A_2 + B_2 - C_{21}\lambda_{iso}^p - C_{22}\lambda_{dev}^p = 0 \end{cases}. \quad (\text{A.24})$$

If only one yield surface is active at a time, when the isotropic plastic mechanism is active, the plastic multipliers are

$$\lambda_{iso}^p = \frac{A_1 + B_1}{C_{11}} = \frac{K \varepsilon_v + K \beta'_s dT}{p'_c \left(1 - (r_{iso} - r_{iso}^e)\right)^2 / c + p'_c \beta r_{iso} + K}, \lambda_{dev}^p = 0, \quad (A.25)$$

and when the deviatoric plastic mechanism is active, the plastic multipliers are

$$\lambda_{iso}^p = 0, \lambda_{dev}^p = \frac{A_2 + B_2}{C_{22}} = \frac{\frac{3G}{q} \sum_{i=1,2,3} \varepsilon_{ii} (\sigma'_{ii} - p') + \frac{6G}{q} (\varepsilon_{12} \sigma'_{12} + \varepsilon_{13} \sigma'_{13} + \varepsilon_{23} \sigma'_{23}) + jK (\varepsilon_v + \beta'_s dT) + L_f}{C_{22}}, \quad (A.26)$$

where

$$C_{22} = Mp' (1 - b \ln(p'd/p'_c)) \left(1 - (r_{dev} - r_{dev}^e)\right)^2 / a + Mp'b\beta\alpha (M - q/p') r_{dev} + \bar{H} + L_{\bar{H}}, \quad (A.27)$$

If the two plastic mechanisms were active at the same time, the stress state would be on the intersection between the two yield surfaces.

Appendix B. Plastic multiplier of the water retention model

We detail in this Appendix how to obtain the plastic multiplier of the water retention model from the consistency equation

$$\begin{cases} \mathrm{d} f_H = \frac{\partial f_H}{\partial s} \mathrm{d} s + \frac{\partial f_H}{\partial \pi_H} \cdot \frac{\partial \pi_H}{\partial \lambda_H^p} \cdot \lambda_H^p \leq 0 \\ \mathrm{d} f_H \cdot \lambda_H^p \geq 0, \quad \lambda_H^p \leq 0 \end{cases} \quad (\text{B.1})$$

Since the internal variable of the water retention model is the plastic increment of the degree of saturation, the derivatives that appear in the consistency equation read

$$\begin{aligned} \frac{\partial f_H}{\partial s} &= \text{sign} \left(\ln \left(\frac{s}{s_D} \right) + \frac{1}{2} \ln \left(\frac{s_{D_0}}{s_{e_H}} \right) \right) \frac{1}{s} \\ \frac{\partial f_H}{\partial \mathrm{d} S_l^p} &= \text{sign} \left(\ln \left(\frac{s}{s_D} \right) + \frac{1}{2} \ln \left(\frac{s_{D_0}}{s_{e_H}} \right) \right) \left(-\frac{1}{s_D} \right) s_D \beta_H \cdot \\ \frac{\partial \mathrm{d} S_l^p}{\partial \lambda_H^p} &= \frac{\partial f_H}{\partial s} \end{aligned} \quad (\text{B.2})$$

Thus, the consistency equation results in

$$\mathrm{d} f_H = \text{sign} \left(\ln \left(\frac{s}{s_D} \right) + \frac{1}{2} \ln \left(\frac{s_{D_0}}{s_{e_H}} \right) \right) \frac{\mathrm{d} s}{s} - \beta_H \frac{1}{s} \lambda_H^p = 0, \quad (\text{B.3})$$

and therefore, the plastic multiplier is

$$\lambda_H^p = \text{sign} \left(\ln \left(\frac{s}{s_D} \right) + \frac{1}{2} \ln \left(\frac{s_{D_0}}{s_{e_H}} \right) \right) \frac{\mathrm{d} s}{\beta_H}. \quad (\text{B.4})$$

Appendix C. Data tables of true triaxial failure of rocks

In this appendix are reported the values of the stress tensor at failure from experimental data of KTB amphibolite, Duham dolomite, Solenhofen limestone, Shirahama sandstone and Yuubari shale along with the deviatoric stress at failure from the numerical predictions of the Mohr-Coulomb, Hoek-Brown, modified Lade and MS3 models.

KTB Amphibolite							
Experimental data				Mohr-Coulomb	Hoek-Brown	Modified Lade	MS3
σ_1	σ_2	σ_3	q_{exp}	q_{num}	q_{num}	q_{num}	q_{num}
[MPa]	[MPa]	[MPa]	[MPa]	[MPa]	[MPa]	[MPa]	[MPa]
158	0	0	158	300	250	263	263
160	0	0	160	300	250	263	263
176	0	0	176	300	250	263	263
346	79	0	314	269	221	338	332
291	149	0	252	260	218	378	299
347	197	0	301	264	228	377	283
267	229	0	250	272	240	385	274
410	30	30	380	499	536	379	399
479	60	30	435	485	522	409	444
599	100	30	537	468	505	462	487
652	200	30	557	439	475	525	476
571	249	30	471	433	467	534	450
637	298	30	527	432	464	547	432
702	60	60	642	698	716	471	530
750	88	60	676	684	702	517	575
766	103	60	686	677	695	541	607
745	155	60	643	655	673	613	644
816	199	60	697	640	658	645	667
888	249	60	752	625	643	664	652
828	299	60	681	614	631	685	641
887	347	60	727	607	624	691	615
954	399	60	782	604	620	703	578
815	449	60	654	606	621	704	564
868	100	100	768	963	901	634	711
959	164	100	829	933	871	721	815
1001	199	100	856	917	856	764	857
945	248	100	782	898	837	810	876
892	269	100	722	891	830	832	888
1048	300	100	866	880	820	840	877
1058	349	100	861	866	806	869	882
1155	442	100	932	845	788	898	843
1118	597	100	882	834	782	923	767
1147	150	150	997	1294	1090	804	916
1065	198	150	892	1271	1067	881	1005
1112	199	150	938	1271	1066	899	1023
1176	249	150	980	1248	1044	956	1076
1431	298	150	1214	1227	1024	1011	1130
1326	348	150	1091	1208	1005	1048	1148
1169	399	150	920	1190	989	1085	1167
1284	448	150	1018	1174	975	1120	1151
1265	498	150	988	1160	964	1140	1138
1262	642	150	965	1132	945	1177	1076

Appendix C. Data tables of true triaxial failure of rocks

Dunham Dolomite							
Experimental data				Mohr-Coulomb	Hoek-Brown	Modified Lade	MS3
σ_1	σ_2	σ_3	q_{exp}	q_{num}	q_{num}	q_{num}	q_{num}
[MPa]	[MPa]	[MPa]	[MPa]	[MPa]	[MPa]	[MPa]	[MPa]
400	24	25	376	511	491	419	419
475	62	25	433	493	473	451	462
496	94	25	440	479	459	482	469
560	130	25	491	466	447	496	476
573	173	25	491	454	435	498	483
585	233	25	490	444	426	512	490
544	269	25	450	442	424	517	468
486	43	45	442	559	552	454	454
566	94	45	498	535	529	489	511
586	124	45	506	523	516	519	519
607	159	45	514	510	504	532	526
639	183	45	538	503	497	542	538
671	241	45	554	490	484	552	523
670	263	45	549	487	481	547	520
622	293	45	501	484	478	548	516
567	63	65	503	607	608	489	508
636	113	65	549	583	584	522	545
642	152	65	539	567	568	554	568
687	208	65	564	548	549	574	568
684	259	65	548	536	537	580	574
725	306	65	579	528	529	588	565
701	390	65	551	525	526	592	559
620	84	85	536	654	658	523	542
682	126	85	578	634	638	552	581
718	150	85	603	624	627	578	590
743	230	85	599	595	598	605	618
771	304	85	607	576	580	619	617
818	371	85	639	568	571	638	607
798	440	85	618	567	570	636	604
680	103	105	576	702	705	555	575
776	165	105	643	673	676	608	624
784	202	105	636	658	661	618	647
804	265	105	635	637	639	639	663
822	331	105	635	620	623	666	664
839	351	105	647	617	619	659	660
820	411	105	622	609	612	674	651
863	266	105	691	636	639	640	662
726	123	125	602	751	749	587	625
823	186	125	669	721	720	638	673
859	241	125	683	699	698	670	689
862	288	125	670	683	682	685	710
893	359	125	682	664	663	695	709
942	411	125	718	655	654	702	699
918	458	125	690	650	649	711	692
887	510	125	660	649	648	713	690
892	254	145	699	749	741	697	739
929	292	145	721	735	728	707	744
924	319	145	708	726	719	715	753
922	342	145	700	719	712	722	746
1016	387	145	779	708	701	738	753
1003	404	145	762	704	697	745	749
953	451	145	706	697	690	750	740

Appendix C. Data tables of true triaxial failure of rocks

Solenhofen Limestone							
Experimental data				Mohr-Coulomb	Hoek-Brown	Modified Lade	MS3
σ_1	σ_2	σ_3	q_{exp}	q_{num}	q_{num}	q_{num}	q_{num}
[MPa]	[MPa]	[MPa]	[MPa]	[MPa]	[MPa]	[MPa]	[MPa]
395	19	20	375	413	414	361	361
414	52	20	379	397	398	392	386
413	91	20	363	382	383	407	410
455	165	20	383	362	363	426	408
459	203	20	382	358	359	415	402
464	231	20	384	357	358	417	400
442	40	40	402	449	453	397	397
455	40	40	415	449	453	397	397
486	80	40	427	431	434	410	418
496	113	40	424	418	421	423	444
526	190	40	431	396	400	442	440
542	267	40	436	389	392	457	430
534	312	40	429	392	395	444	430
472	57	60	413	488	490	411	431
516	87	60	443	474	476	421	439
535	100	60	457	468	470	444	453
529	111	60	446	463	465	448	467
573	162	60	470	444	447	450	468
551	196	60	439	435	437	467	477
556	271	60	431	423	425	475	480
529	81	80	449	524	522	447	466
569	125	80	468	503	502	460	484
580	150	80	469	493	491	469	493
641	205	80	510	474	473	493	512
592	221	80	458	470	468	500	508
674	280	80	524	458	457	497	513
659	294	80	507	456	455	505	510
648	373	80	492	455	454	511	488
678	448	80	523	466	465	503	481

Appendix C. Data tables of true triaxial failure of rocks

Shirahama Sandstone							
Experimental data				Mohr-Coulomb	Hoek-Brown	Modified Lade	MS3
σ_1	σ_2	σ_3	q_{exp}	q_{num}	q_{num}	q_{num}	q_{num}
[MPa]	[MPa]	[MPa]	[MPa]	[MPa]	[MPa]	[MPa]	[MPa]
97	9	5	90	110	99	83	100
99	15	5	89	107	96	87	97
89	29	5	75	102	91	95	112
110	45	5	92	98	88	106	108
95	64	5	79	97	88	103	106
112	15	8	101	118	114	85	118
133	26	8	117	114	109	111	114
136	41	8	115	109	104	101	128
137	51	8	114	107	103	108	126
128	74	8	104	105	102	109	105
160	29	15	139	138	142	128	135
167	61	15	135	128	131	128	144
166	81	15	131	126	129	143	140
164	87	15	129	126	128	130	140
171	97	15	135	126	129	138	140
183	30	20	158	157	162	126	156
173	41	20	144	152	158	131	152
188	51	20	155	149	154	137	168
185	60	20	149	146	151	143	165
198	72	20	159	143	148	151	161
196	85	20	154	141	146	160	159
194	100	20	151	140	145	153	157
187	103	20	145	140	145	156	157
222	49	30	183	186	190	169	191
227	72	30	180	178	182	181	183
233	91	30	180	173	177	193	197
230	112	30	174	169	173	189	192
242	132	30	184	169	173	187	173
226	152	30	171	171	174	188	175
216	172	30	168	175	178	191	164
245	60	40	196	219	218	188	209
255	72	40	201	214	213	213	224
258	82	40	200	210	209	219	220
255	102	40	192	204	203	211	234
275	102	40	211	204	203	211	234
268	123	40	200	200	199	225	228
282	142	40	210	198	197	221	207
275	162	40	204	198	197	235	207

Appendix C. Data tables of true triaxial failure of rocks

Yuubari Shale							
Experimental data				Mohr-Coulomb	Hoek-Brown	Modified Lade	MS3
σ_1	σ_2	σ_3	q_{exp}	q_{num}	q_{num}	q_{num}	q_{num}
[MPa]	[MPa]	[MPa]	[MPa]	[MPa]	[MPa]	[MPa]	[MPa]
161	26	25	136	160	162	141	160
168	26	25	142	160	162	141	160
182	36	25	152	155	157	145	156
187	36	25	157	155	157	146	155
175	45	25	141	151	153	150	151
175	56	25	137	147	149	156	167
186	65	25	145	145	146	162	164
200	76	25	155	142	143	169	161
194	79	25	149	141	143	170	160
196	85	25	151	140	142	174	159
201	96	25	153	139	141	164	157
194	100	25	147	139	140	167	157
186	114	25	139	139	141	178	139
197	124	25	150	140	141	169	140
183	133	25	140	142	143	176	142
228	50	50	178	201	206	178	198
239	50	50	189	201	206	178	198
245	50	50	195	201	206	178	198
257	69	50	198	192	197	187	209
261	90	50	194	184	189	198	201
266	100	50	195	181	186	203	217
260	110	50	187	179	184	209	214
260	122	50	185	176	181	198	211
285	129	50	207	175	180	204	209
266	148	50	187	174	179	200	189
256	159	50	178	174	179	208	188

Appendix D. Data tables of anisotropic failure of rocks

In this appendix are reported the values of the inclination of bedding planes and the stress tensor at failure from experimental data of Bossier Shale, Vaca Muerta Shale, Austin Slate, Green River Shale-1, Green River Shale-2, Quartz Phyllite, Carbone Phyllite, Penrhyn Slate, Tournemire Shale and Opalinus Clay along with the deviatoric stress at failure from the numerical predictions of the Jaeger Weakness Plane (JPW), Pariseau and MS3 models.

Bossier Shale						
Experimental data				JPW	Pariseau	MS3
β	σ_1	σ_3	q_{exp}	q_{num}	q_{num}	q_{num}
[-]	[MPa]	[MPa]	[MPa]	[MPa]	[MPa]	[MPa]
90	42	0	42	88	106	109
60	12	0	12	44	63	31
45	47	0	47	51	57	21
45	39	0	39	51	57	21
30	45	0	45	88	64	56
0	114	0	114	88	101	112
90	147	7	140	101	121	129
60	46	7	39	53	72	52
45	55	7	48	62	66	42
30	92	7	85	101	73	76
0	125	7	118	101	117	133
90	200	21	179	127	153	168
75	137	21	116	106	121	140
60	95	21	74	73	91	95
45	108	21	87	84	83	86
30	134	21	113	127	93	115
30	121	21	100	127	93	115
15	118	21	97	127	122	156
15	144	21	124	127	122	156
0	207	21	187	127	147	172
90	258	41	217	166	201	225
60	140	41	99	101	119	159
45	157	41	115	117	108	150
30	179	41	138	166	121	175
30	166	41	124	166	121	175
30	162	41	120	166	121	175
20	213	41	172	166	144	201
0	255	41	213	166	193	228
90	325	69	256	218	264	308
75	274	69	206	204	209	284
60	229	69	160	139	156	247
45	224	69	156	162	143	238
30	250	69	181	218	160	261
15	291	69	223	218	210	295
10	264	69	195	218	231	303
0	294	69	225	218	253	310

Appendix D. Data tables of anisotropic failure of rocks

Vaca Muerta Shale						
Experimental data				JPW	Pariseau	MS3
β	σ_1	σ_3	q_{exp}	q_{num}	q_{num}	q_{num}
[-]	[MPa]	[MPa]	[MPa]	[MPa]	[MPa]	[MPa]
60	54	0	54	59	91	66
0	95	0	95	109	112	106
90	132	7	125	121	117	130
60	85	7	78	70	101	78
0	139	7	132	121	124	118
90	151	17	133	138	134	143
75	137	17	120	123	127	122
50	117	17	100	92	111	97
40	124	17	107	129	112	113
30	142	17	124	138	117	131
20	151	17	134	138	127	140
15	139	17	121	138	132	140
90	191	34	156	166	162	166
80	232	34	197	166	158	157
60	165	34	130	113	139	123
40	202	34	168	170	135	140
10	211	34	177	166	166	168
0	212	34	178	166	171	167
90	462	138	324	338	329	328
60	421	138	283	275	283	300
0	482	138	344	338	349	345

Appendix D. Data tables of anisotropic failure of rocks

Austin Slate						
Experimental data				JPW	Pariseau	MS3
β	σ_1	σ_3	q_{exp}	q_{num}	q_{num}	q_{num}
[-]	[MPa]	[MPa]	[MPa]	[MPa]	[MPa]	[MPa]
90	346	34	312	283	318	389
80	271	34	237	283	267	328
70	173	34	138	183	202	189
60	149	34	115	144	166	82
50	168	34	134	136	152	61
40	195	34	160	153	154	103
30	225	34	190	213	172	197
20	264	34	229	283	210	264
10	307	34	273	283	267	290
0	329	34	294	283	302	294
90	475	69	406	325	368	407
80	373	69	304	325	310	345
70	261	69	192	211	234	212
60	216	69	147	166	192	125
50	236	69	167	158	176	106
40	252	69	183	176	178	136
30	297	69	228	246	199	222
20	338	69	269	325	243	296
10	362	69	293	325	309	328
0	416	69	347	325	350	335
90	657	138	519	409	468	441
80	537	138	399	409	394	386
70	415	138	277	268	298	279
60	368	138	230	211	245	213
50	368	138	230	200	224	196
40	369	138	231	224	227	220
30	438	138	300	312	254	287
20	504	138	366	409	310	359
10	542	138	404	409	394	399
0	590	138	452	409	446	410
90	834	207	627	492	569	492
80	676	207	469	492	479	447
70	576	207	369	325	362	360
60	492	207	285	256	297	303
50	474	207	267	243	272	286
40	491	207	284	272	276	309
30	574	207	367	378	308	366
20	635	207	428	492	377	431
10	696	207	489	492	478	473
0	728	207	521	492	542	485
90	938	276	662	576	670	560
80	773	276	497	576	564	522
70	685	276	409	382	426	447
60	596	276	321	300	350	392
50	583	276	307	285	320	376
40	595	276	319	319	325	398
30	673	276	397	445	363	450
20	749	276	473	576	443	511
0	856	276	580	576	637	564

Appendix D. Data tables of anisotropic failure of rocks

Green River Shale - 1						
Experimental data				JPW	Pariseau	MS3
β	σ_1	σ_3	q_{exp}	q_{num}	q_{num}	q_{num}
[-]	[MPa]	[MPa]	[MPa]	[MPa]	[MPa]	[MPa]
90	252	7	245	236	318	255
75	207	7	200	219	267	227
70	194	7	187	183	202	211
60	160	7	153	161	166	188
45	218	7	211	224	152	198
30	222	7	215	236	154	227
15	217	7	210	236	172	228
0	229	7	222	236	210	218
90	345	34	311	264	267	302
75	321	34	287	284	302	274
70	294	34	260	247	368	260
60	260	34	226	218	310	239
45	299	34	265	284	234	248
30	304	34	270	284	192	277
15	306	34	271	284	176	280
0	322	34	287	284	178	273
90	439	69	370	345	199	361
75	421	69	352	345	243	336
70	403	69	334	327	309	323
60	370	69	301	289	350	304
45	406	69	337	345	468	313
30	423	69	354	345	394	341
15	420	69	351	345	298	347
0	427	69	358	345	245	343
90	538	103	435	405	224	421
75	518	103	415	405	227	398
70	503	103	399	405	254	385
60	471	103	368	360	310	368
45	516	103	413	405	394	377
30	513	103	409	405	446	404
15	519	103	416	405	569	412
0	528	103	425	405	479	409
90	717	172	544	525	362	544
75	684	172	511	525	297	524
70	677	172	505	525	272	514
60	664	172	492	503	276	499
45	667	172	495	525	308	507
30	685	172	513	525	377	532
15	693	172	521	525	478	543
0	694	172	521	525	542	542

Appendix D. Data tables of anisotropic failure of rocks

Green River Shale - 2						
Experimental data				JPW	Pariseau	MS3
β	σ_1	σ_3	q_{exp}	q_{num}	q_{num}	q_{num}
[-]	[MPa]	[MPa]	[MPa]	[MPa]	[MPa]	[MPa]
90	149	7	142	130	133	157
80	133	7	126	130	127	143
70	112	7	105	106	116	112
60	93	7	87	86	106	87
50	101	7	95	85	101	83
30	120	7	113	130	107	116
0	129	7	122	130	128	121
90	203	34	169	157	159	175
80	189	34	154	157	156	162
70	170	34	135	139	142	135
60	148	34	114	113	130	115
50	157	34	122	111	125	112
30	177	34	143	157	132	141
0	188	34	154	157	157	154
90	282	69	213	191	202	199
80	265	69	196	191	193	189
70	239	69	171	181	175	168
60	211	69	142	146	161	152
50	227	69	158	144	154	149
30	253	69	184	191	162	175
0	263	69	194	191	194	192
90	356	103	253	225	240	228
80	336	103	233	225	229	219
70	313	103	210	222	208	202
60	279	103	175	180	191	189
50	296	103	193	178	183	186
30	321	103	217	225	193	209
0	330	103	227	225	230	227
90	493	172	321	292	316	294
80	459	172	287	292	302	288
70	443	172	270	292	274	274
60	404	172	232	247	251	263
50	424	172	251	244	241	261
30	442	172	270	292	254	280
0	465	172	292	292	303	299

Appendix D. Data tables of anisotropic failure of rocks

Quartz Phyllite						
Experimental data				JPW	Pariseau	MS3
β	σ_1	σ_3	q_{exp}	q_{num}	q_{num}	q_{num}
[-]	[MPa]	[MPa]	[MPa]	[MPa]	[MPa]	[MPa]
90	66	0	66	87	84	88
65	47	0	47	52	69	46
55	45	0	45	50	65	32
30	59	0	59	87	72	69
0	102	0	102	87	97	115
90	84	5	79	98	96	99
60	58	5	53	58	75	49
30	67	5	62	98	81	80
25	98	5	93	98	87	92
0	125	5	120	98	110	127
90	140	15	125	121	119	120
60	101	15	86	73	94	73
30	125	15	110	121	101	102
20	143	15	128	121	115	125
0	175	15	160	121	137	149
90	197	30	167	156	154	152
50	137	30	107	103	117	104
40	164	30	134	145	120	114
30	177	30	147	156	131	135
20	200	30	170	156	149	158
0	225	30	195	156	177	180
90	274	50	224	202	201	198
85	249	50	199	202	198	195
60	186	50	136	128	158	157
30	235	50	185	202	171	181
20	267	50	217	202	194	203
0	274	50	224	202	231	224
90	327	70	257	248	247	244
80	291	70	221	248	235	237
50	244	70	174	170	187	202
30	279	70	209	248	210	228
15	313	70	243	248	255	257
0	329	70	259	248	284	270

Appendix D. Data tables of anisotropic failure of rocks

Carbana Phyllite						
Experimental data				JPW	Pariseau	MS3
β	σ_1	σ_3	q_{exp}	q_{num}	q_{num}	q_{num}
[-]	[MPa]	[MPa]	[MPa]	[MPa]	[MPa]	[MPa]
90	65	0	65	81	81	87
65	39	0	39	44	66	42
60	37	0	37	42	63	33
30	49	0	49	81	65	61
0	80	0	80	81	92	105
90	86	5	81	93	93	98
85	102	5	97	93	92	96
65	60	5	55	53	75	53
30	78	5	73	93	75	73
0	115	5	110	93	106	117
90	142	15	127	116	117	120
60	97	15	82	70	91	69
35	102	15	87	116	90	83
30	128	15	113	116	94	95
0	179	15	164	116	133	139
90	178	30	148	152	153	152
90	201	30	171	152	153	152
80	196	30	166	152	146	143
55	139	30	109	100	115	101
25	186	30	156	152	131	140
10	199	30	169	152	163	166
0	207	30	177	152	174	172
90	250	50	200	199	200	198
60	202	50	152	134	156	155
50	188	50	138	149	148	150
30	232	50	182	199	162	176
25	227	50	177	199	173	187
0	273	50	223	199	229	217
90	320	70	250	246	248	246
75	284	70	214	238	225	229
55	258	70	188	175	187	200
30	275	70	205	246	201	225
5	323	70	253	246	279	262

Appendix D. Data tables of anisotropic failure of rocks

Penrhyn Slate						
Experimental data				JPW	Pariseau	MS3
β	σ_1	σ_3	q_{exp}	q_{num}	q_{num}	q_{num}
[-]	[MPa]	[MPa]	[MPa]	[MPa]	[MPa]	[MPa]
90	187	0	187	186	195	188
75	113	0	113	147	145	139
60	44	0	44	93	101	48
45	63	0	63	93	88	20
30	86	0	86	145	99	83
15	127	0	127	186	148	176
0	208	0	208	186	228	218
90	203	7	196	205	213	206
75	148	7	141	155	159	157
60	92	7	85	98	110	66
45	102	7	95	98	96	38
30	126	7	119	153	108	100
15	169	7	162	205	162	195
0	251	7	244	205	249	236
90	276	14	262	223	231	224
75	203	14	190	163	172	174
60	128	14	114	103	120	86
45	141	14	127	103	104	58
30	175	14	162	160	117	116
15	215	14	201	223	175	212
0	312	14	298	223	270	253
90	355	41	313	298	303	291
75	255	41	214	194	226	242
60	205	41	163	123	157	159
60	164	41	123	123	157	159
45	174	41	133	122	137	133
30	224	41	183	191	153	182
15	258	41	217	298	230	273
0	362	41	321	298	354	316
90	380	55	325	335	339	326
75	284	55	229	210	253	279
60	187	55	132	133	175	199
45	230	55	175	132	153	172
30	256	55	201	206	171	219
15	303	55	248	335	257	307
0	437	55	381	335	397	349
90	489	69	420	373	375	362
75	346	69	277	225	279	316
45	255	69	186	142	169	211
30	277	69	208	222	190	256
15	350	69	281	373	284	341
0	537	69	468	373	439	382

Appendix D. Data tables of anisotropic failure of rocks

Tournemire Shale						
Experimental data				JPW	Pariseau	MS3
β	σ_1	σ_3	q_{exp}	q_{num}	q_{num}	q_{num}
[-]	[MPa]	[MPa]	[MPa]	[MPa]	[MPa]	[MPa]
90	36	1	35	41	41	49
70	30	1	29	33	33	34
60	20	1	19	27	29	23
45	23	1	22	29	27	19
30	26	1	25	41	29	30
15	32	1	31	41	35	43
0	47	1	46	41	35	48
90	60	5	55	46	48	54
60	36	5	31	31	34	29
45	41	5	36	34	31	25
30	45	5	40	46	34	34
0	59	5	54	46	45	53
90	105	20	85	67	71	70
60	84	20	64	47	51	50
45	78	20	58	51	47	46
0	103	20	83	67	68	68
90	144	40	104	95	103	95
60	113	40	73	69	73	78
45	110	40	70	74	68	75
30	109	40	69	95	73	80
0	136	40	96	95	98	93
90	160	50	110	108	119	109
60	130	50	80	80	85	93
45	130	50	80	86	78	89
0	155	50	105	108	113	106

Appendix D. Data tables of anisotropic failure of rocks

Opalinus Clay						
Experimental data				JPW	Pariseau	MS3
β	σ_1	σ_3	q_{exp}	q_{num}	q_{num}	q_{num}
[-]	[MPa]	[MPa]	[MPa]	[MPa]	[MPa]	[MPa]
90	8	0	8	11	16	13
0	12	0	12	11	12	11
45	8	0	8	10	10	2
90	18	1	17	12	17	14
90	13	1	12	12	17	14
0	15	1	14	12	12	12
0	12	1	11	12	12	12
90	25	3	22	16	18	16
90	19	3	16	16	18	16
0	15	3	12	16	12	13
0	16	3	13	16	12	13
90	30	5	25	19	19	18
90	23	5	18	19	19	18
90	27	6	21	21	20	20
90	23	6	17	21	20	20
90	18	6	12	21	20	20
90	27	6	21	21	20	20
0	23	6	17	21	13	15
0	18	6	12	21	13	15
45	11	6	5	17	10	11
45	22	6	16	17	10	11
90	30	8	23	24	21	22
90	33	10	23	29	23	25
0	24	10	14	29	14	19
45	30	10	20	21	11	17
45	50	20	30	33	11	31

Appendix E. *Code_Aster* scripts of the constitutive model

In the following appendix we report the 4 mandatory routines that were written for the implementation of the constitutive model MS3 in *Code_Aster* according to the reference manual D5.04.01 available at www.code-aster.org. Such Fortran 90 routines are:

- apdmat.F90, where the specification of the material parameters is given;
- apdcvx.F90, where the computation of the plastic yield surface is performed;
- apdres.F90, where the residual vector for the Newton-Raphson scheme is computed;
- apdlmf.F90, where the damage and other variables are post-processed.

The reader is referred to the above mentioned manual for all the specific details on the implementation of a new constitutive model in *Code_Aster*.

```

subroutine apdmat(mod, imat, nbmat, tempd, materd,&
                 materf, matcst, ndt, ndi, nr,&
                 nvi)
! =====
! COPYRIGHT (C) 1991 - 2011 EDF R&D                               WWW.CODE-ASTER.ORG
! THIS PROGRAM IS FREE SOFTWARE; YOU CAN REDISTRIBUTE IT AND/OR MODIFY
! IT UNDER THE TERMS OF THE GNU GENERAL PUBLIC LICENSE AS PUBLISHED BY
! THE FREE SOFTWARE FOUNDATION; EITHER VERSION 2 OF THE LICENSE, OR
! (AT YOUR OPTION) ANY LATER VERSION.
!
! THIS PROGRAM IS DISTRIBUTED IN THE HOPE THAT IT WILL BE USEFUL, BUT
! WITHOUT ANY WARRANTY; WITHOUT EVEN THE IMPLIED WARRANTY OF
! MERCHANTABILITY OR FITNESS FOR A PARTICULAR PURPOSE. SEE THE GNU
! GENERAL PUBLIC LICENSE FOR MORE DETAILS.
!
! YOU SHOULD HAVE RECEIVED A COPY OF THE GNU GENERAL PUBLIC LICENSE
! ALONG WITH THIS PROGRAM; IF NOT, WRITE TO EDF R&D CODE_ASTER,
!   1 AVENUE DU GENERAL DE GAULLE, 92141 CLAMART CEDEX, FRANCE.
! =====
! =====
      implicit none
#include "asterf_types.h"
#include "asterfort/rcvala.h"
#include "asterfort/utmess.h"
      integer :: nbmat,imat,icodre(26),ndt,ndi,nvi,nr,ii
      real(kind=8) :: materf(nbmat, 2), materd(nbmat, 2), tempd
      real(kind=8) :: tabtmp(26)
      character(len=16) :: nomc(26)
      character(len=3) :: matcst
      character(len=8) :: mod
! =====
! --- RECUPERATION DES DONNEES MATERIAU POUR LA LOI DE APD_LMSEPFL-----
! =====
! IN  IMAT  :  ADRESSE DU MATERIAU CODE -----
!     NBMAT :  NOMBRE DE PARAMETRES MATERIAU -----
!     TEMPD :  TEMPERATURE BIDON -----
!     MOD   :  TYPE DE MODELISATION -----
! OUT MATERD : COEFFICIENTS MATERIAU A T -----
!     MATERF : COEFFICIENTS MATERIAU A T+DT -----
!           MATER(*,1) = CARACTERISTIQUES ELASTIQUES -----
!           MATER(*,2) = CARACTERISTIQUES PLASTIQUES -----
!     MATCST : 'OUI' -----
!     NDT   :  NB TOTAL DE COMPOSANTES TENSEURS -----
!     NDI   :  NB DE COMPOSANTES DIRECTES TENSEURS -----
!     NR    :  NOMBRE D'EQUATION DU SYSTEME NL -----
!     NVI   :  NB DE VARIABLES INTERNES -----
! =====

```

```

! =====
! --- INITIALISATION DE PARAMETRES -----
! =====
      do ii = 1, nbmat
          materd(ii,1) = 0.d0
          materd(ii,2) = 0.d0
          materf(ii,1) = 0.d0
          materf(ii,2) = 0.d0
      end do

! =====
! --- DEFINITION DES CHAMPS -----
! =====
      nomc(1)='YOUNG'
      nomc(2)='POISSON'
          nomc(3)='ALFA_D'
      nomc(4)='BETA_D'
      nomc(5)='A_PL'
      nomc(6)='B_PL'
      nomc(7)='C_PL'
      nomc(8)='D_PL'
      nomc(9)='RHA_0'
      nomc(10)='X_H'
      nomc(11)='S_H'
      nomc(12)='A_VE'
      nomc(13)='B_VE'
          nomc(14)='N_VE'
          nomc(15)='TETA_R'
          nomc(16)='OMEGA'
          nomc(17)='D1'
          nomc(18)='D2'
          nomc(19)='D3'
          nomc(20)='GAM'
          nomc(21)='K1'
      nomc(22)='FNTOL'
          nomc(23)='AXH'
          nomc(24)='BXH'
          nomc(25)='PN0_C'
          nomc(26)='TYPTAN'

! =====
! --- RECUPERATION DES PARAMETRES MATERIAU -----
! =====

      call rcvala(imat, ' ', 'APD_LMSEPFL', 0, ' ', &
          [0.d0], 26, nomc, tabtmp, icodre, &
          1)
    
```

```
! =====
! --- STOCKAGE DES PARAMETRES -----
! =====

materf(1,1)=tabtmp(1)
materf(2,1)=tabtmp(2)
materf(1,2)=tabtmp(3)
materf(2,2)=tabtmp(4)
materf(3,2)=tabtmp(5)
materf(4,2)=tabtmp(6)
materf(5,2)=tabtmp(7)
materf(6,2)=tabtmp(8)
materf(7,2)=tabtmp(9)
materf(8,2)=tabtmp(10)
materf(9,2)=tabtmp(11)
materf(10,2)=tabtmp(12)
materf(11,2)=tabtmp(13)
materf(12,2)=tabtmp(14)
materf(13,2)=tabtmp(15)
materf(14,2)=tabtmp(16)
materf(15,2)=tabtmp(17)
materf(16,2)=tabtmp(18)
materf(17,2)=tabtmp(19)
materf(18,2)=tabtmp(20)
materf(19,2)=tabtmp(21)
materf(20,2)=tabtmp(22)
materf(21,2)=tabtmp(23)
materf(22,2)=tabtmp(24)
materf(23,2)=tabtmp(25)
materf(24,2)=tabtmp(26)

materd=materf

! =====
! --- NOMBRE DE COMPOSANTES -----
! =====

if (mod .eq. '3D') then
  ndt = 6
  ndi = 3
else if ((mod.eq.'D_PLAN') .or. (mod.eq.'AXIS')) then
  ndt = 4
  ndi = 3
else if ((mod.eq.'C_PLAN') .or. (mod.eq.'1D')) then
  call utmess('F', 'ALGORITHM3_92')
else
  call utmess('F', 'ALGORITHM2_20')
```

```
endif
! =====
! --- NOMBRE DE VARIABLES INTERNES -----
! =====
!     nvi = 2
!     write(6,*),'inside apdmat '
! =====
! - NOMBRE DE CONDITIONS NON-LINEAIRES -----
! =====
!     nr = ndt + 2
! =====

    matcst = 'OUI'
end subroutine
```

```

subroutine apdcvx(nr,sigp, vin, nbmat, mater, seuil)
! =====
! COPYRIGHT (C) 1991 - 2011 EDF R&D WWW.CODE-ASTER.ORG
! THIS PROGRAM IS FREE SOFTWARE; YOU CAN REDISTRIBUTE IT AND/OR MODIFY
! IT UNDER THE TERMS OF THE GNU GENERAL PUBLIC LICENSE AS PUBLISHED BY
! THE FREE SOFTWARE FOUNDATION; EITHER VERSION 2 OF THE LICENSE, OR
! (AT YOUR OPTION) ANY LATER VERSION.
!
! THIS PROGRAM IS DISTRIBUTED IN THE HOPE THAT IT WILL BE USEFUL, BUT
! WITHOUT ANY WARRANTY; WITHOUT EVEN THE IMPLIED WARRANTY OF
! MERCHANTABILITY OR FITNESS FOR A PARTICULAR PURPOSE. SEE THE GNU
! GENERAL PUBLIC LICENSE FOR MORE DETAILS.
!
! YOU SHOULD HAVE RECEIVED A COPY OF THE GNU GENERAL PUBLIC LICENSE
! ALONG WITH THIS PROGRAM; IF NOT, WRITE TO EDF R&D CODE ASTER,
! 1 AVENUE DU GENERAL DE GAULLE, 92141 CLAMART CEDEX, FRANCE.
! =====
!
! --- BUT : VALEUR SEUIL POUR ELASTO-PLASTIQUE -----
! =====
! IN : SIG : TENSEUR DES CONTRAINTES (ELASTIQUE) A T+DT -----
! --- : VIN : VARIABLES INTERNES -----
! --- : NBMAT : NOMBRE DE PARAMETRES MATERIAU -----
! --- : MATER : COEFFICIENTS MATERIAU A T+DT -----
! ----- : MATER(*,1) = CARACTERISTIQUES ELASTIQUES -----
! ----- : MATER(*,2) = CARACTERISTIQUES PLASTIQUES -----
! OUT : SEUIL : VALEUR DE seuil -----
! =====
! =====
implicit none
#include "asterc/r8miem.h"
integer :: nbmat,nr
real(kind=8) :: sig(6), mater(nbmat, 2), vin(*), seuil
real(kind=8) :: a_pl,b_pl,c_pl,d_pl,rha_0,xh,a_ve,b_ve,n_ve,teta_r
real(kind=8) :: omega,d1,d2,d3,axh,bxh,pn0_c,teta,eeq
real(kind=8) :: pi=3.141592653589793
real(kind=8) :: rstn(6),r11,r12,r13,elle2,cpl,pn1,qn1,ri1,rj2,rj3
real(kind=8) :: cip,rhb,help,tn1,rteta,rha,sigp(6)
! =====
! --- PARAMETRES DU MODELE -----
! =====
a_pl=mater(3,2)
b_pl=mater(4,2)
c_pl=mater(5,2)
d_pl=mater(6,2)
rha_0=mater(7,2)

```

```

xh=mater(8,2)
a_ve=mater(10,2)
b_ve=mater(11,2)
n_ve=mater(12,2)
teta_r=mater(13,2)
omega=mater(14,2)
d1=mater(15,2)
d2=mater(16,2)
d3=mater(17,2)
axh=mater(21,2)
bxh=mater(22,2)
pn0_c=mater(23,2)

sig(1:3)=sigp(1:3)
sig(4:6)=sigp(4:6)/sqrt(2.0)
! =====
! --- ANGLE DU PLAN ANISOTROPIQUE -----
! =====
teta=teta_r*pi/180.0
! =====
! --- VARIABLE INTERNE PLASTIQUE KP -----
! =====
eeq=vin(1)
! =====
! --- CALCUL PARAMETRE ANISOTROPE -----
! =====
rstn(1)=sin(teta)*(sig(4)*cos(teta)+sig(2)*sin(teta))+cos(teta)*&
(sig(1)*cos(teta)+sig(4)*sin(teta))
rstn(2)=- (sin(teta)*(sig(4)*cos(teta)-sig(1)*sin(teta)))+cos(teta)*&
(sig(2)*cos(teta)-sig(4)*sin(teta))
rstn(3)=sig(3)
rstn(4)=cos(teta)*(sig(4)*cos(teta)+sig(2)*sin(teta))-sin(teta)*&
(sig(1)*cos(teta)+sig(4)*sin(teta))
rstn(5)=sig(5)*cos(teta)+sig(6)*sin(teta)
rstn(6)=sig(6)*cos(teta)-sig(5)*sin(teta)

r11=sqrt(rstn(1)**2.0+rstn(4)**2.0+rstn(5)**2.0)
r12=sqrt(rstn(4)**2.0+rstn(2)**2.0+rstn(6)**2.0)
r13=sqrt(rstn(5)**2.0+rstn(6)**2.0+rstn(3)**2.0)

if(r11.gt.0.0 .and. r12.gt.0.0 .and. r13.gt.0.0)then
if((r11**2+r12**2+r13**2).lt.r8miem())then
elle2=r12/sqrt(r8miem())
else
elle2=r12/sqrt((r11**2+r12**2+r13**2))
end if
cpl=c_pl*(1.+(omega-3.*omega*elle2**2.0)+d1*&

```

```

(omega-3.*omega*elle2**2.0)**2.0+d2*&
(omega-3.*omega*elle2**2.0)**3.0+d3*&
(omega-3.*omega*elle2**2.0)**4.0)
else
cpl=c_pl
end if

! =====
! --- INVARIANTS DE CONTRAINTE -----
! =====

pn1=(sig(1)+sig(2)+sig(3))/3.0
qn1=(1.0/(2.0**0.5))*((sig(1)-sig(2))**2.0+(sig(2)-sig(3))**2.0+&
(sig(3)-
sig(1))**2.0+6.0*(sig(4)**2.0+sig(5)**2.0+sig(6)**2.0))**0.5
ril=sig(1)+sig(2)+sig(3)
rj2=1.0/6.0*((sig(1)-sig(2))**2.0+(sig(1)-sig(3))**2.0+&
(sig(2)-sig(3))**2.0)+(sig(4)**2.0)+(sig(5)**2.0)+(sig(6)**2.0)
qn1=sqrt(3.0*rj2)
rj3=(sig(1)-ril/3.0)*(sig(2)-ril/3.0)*(sig(3)-ril/3.0)

! =====
! --- PARAMETRES ECROUISSAGE PLASTIQUE -----
! =====

if (abs(pn1).lt.pn0_c) then
else
xh=axh*pn1+bxh
end if

if(rha_0.gt.1.0)then
rha=1.0
else
rha=(rha_0-1.0)*(eeq/xh)**2-2.0*(rha_0-1.0)*(eeq/xh)+rha_0
end if

if (eeq.le.xh) then
else
rha=1.
end if

! =====
! --- FONCTION DE L ANGLE DE LODE -----
! =====

if (rj2 .gt. r8miem()) then
help=- (3.0*sqrt(3.0)/2.0*(rj3/(rj2**1.5)))
rteta=((1.-b_ve*help)/(1.0-b_ve))**(n_ve)
else
rj2=r8miem()

```



```
help=- (3.0*sqrt(3.0)/2.0*(rj3/(rj2**1.5)))
rteta=((1.-b_ve*help)/(1.0-b_ve)**(n_ve)
end if

! =====
! --- CALCUL DU SEUIL -----
! =====

seuil=qn1-(a_pl*(1.0-rha)*pn1**2.0-((1.0-d_pl)*rha+d_pl)*&
  b_pl*pn1+cpl*rha)*rteta
end subroutine
```

```

subroutine apdres(typpmod, nmat, materf, timed, timef, &
                nvi, vind, vinf, yd, yf, &
                deps, nr, r)
! =====
! COPYRIGHT (C) 1991 - 2013 EDF R&D WWW.CODE-ASTER.ORG
! THIS PROGRAM IS FREE SOFTWARE; YOU CAN REDISTRIBUTE IT AND/OR MODIFY
! IT UNDER THE TERMS OF THE GNU GENERAL PUBLIC LICENSE AS PUBLISHED BY
! THE FREE SOFTWARE FOUNDATION; EITHER VERSION 2 OF THE LICENSE, OR
! (AT YOUR OPTION) ANY LATER VERSION.
!
! THIS PROGRAM IS DISTRIBUTED IN THE HOPE THAT IT WILL BE USEFUL, BUT
! WITHOUT ANY WARRANTY; WITHOUT EVEN THE IMPLIED WARRANTY OF
! MERCHANTABILITY OR FITNESS FOR A PARTICULAR PURPOSE. SEE THE GNU
! GENERAL PUBLIC LICENSE FOR MORE DETAILS.
!
! YOU SHOULD HAVE RECEIVED A COPY OF THE GNU GENERAL PUBLIC LICENSE
! ALONG WITH THIS PROGRAM; IF NOT, WRITE TO EDF R&D CODE_ASTER,
! 1 AVENUE DU GENERAL DE GAULLE, 92141 CLAMART CEDEX, FRANCE.
! =====
    implicit none
#include "asterf_types.h"
#include "asterfort/apdcvx.h"
#include "asterc/r8miem.h"

! -----
!   CALCUL DES TERMES DU SYSTEME NL A RESOUDRE = -R(DY) POUR LETK
!   IN TYPPMOD      : TYPE DE MODELISATION
!   NMAT           : DIMENSION MATER
!   MATERF        : COEFFICIENTS MATERIAU A T+DT
!   TIMED         : INSTANT T
!   TIMEF         : INSTANT T+DT
!   NVI           : NOMBRE DE VARIABLES INTERNES
!   DEPS          : INCREMENT DE DEFORMATION
!   VIND          : VARIABLES INTERNES A T
!   VINP         : VARIABLES INTERNES A T+DT
!   YD            : VARIABLES A T = ( SIGD 0 XIPD XIVPD (EPSD3))
!   YF            : VARIABLES A T+DT = ( SIGF DLAM XIPF XIVPF (EPS3F))
!   DEPS         : INCREMENT DE DEFORMATIONS
!   DY           : SOLUTION = ( DSIG DLAM DXIP DXIVP (DEPS3))
!   NR           : DIMENSION DU VECTEUR INCONNUES
!   OUT R        : SYSTEME NL A T+DT
! -----
    integer :: nmat, nr, nvi, ndi, ndt
    real(kind=8) :: deps(6), vind(*), vinf(*)
    real(kind=8) :: r(nr), yd(nr), yf(nr), materf(nmat, 2)
    real(kind=8) :: timed, timef
    character(len=8) :: typpmod

```

```

integer :: ii,jj,i
real(kind=8) :: YOUNG,POISSON,ALFA_D,BETA_D,A_PL,B_PL
real(kind=8) :: C_PL,D_PL,RHA_0,XH,YH,A_VE,B_VE,N_VE,TETA_R
real(kind=8) :: OMEGA,D1,D2,D3,GAM,K1,FNTOL,AXH,BXH,PNO_C,TYPTAN
real(kind=8) :: rj2,dqdj2,dj2ds(6),el(6,6),dgds(6),sig(6),dpds(6)
real(kind=8) :: naux,naux2,naux3,normplv,vin(2),dfdq,dfdp,pn1,rha
real(kind=8) :: seuil,rlambp,rkp,rkd,cip,rhb,sigf(6),sigd(6)
real(kind=8) :: depse(6),dsige(6),eplas(6),dv,deq,dev,sha
real(kind=8) :: kapc,gpl,mcoef,apol,bpol,cpol,pmax,depsg(6)
real(kind=8) :: teta,rstn(6),rl1,rl2,rl3,ds11ds(6),ds22ds(6)
real(kind=8) :: ds12ds(6),ds13ds(6),ds23ds(6),drl1ds(6),drl2ds(6)
real(kind=8) :: drl1ds11,drl1ds12,drl1ds13,drl2ds22,drl2ds12
real(kind=8) :: dl22drl1,dl22drl2,dl22drl3,dl22ds(6),l22,cpl,elle2
    real(kind=8) :: ds33ds(6),drl3ds(6),drl2ds23,drl3ds33,drl3ds13
    real(kind=8) :: drl3ds23,dgamdl22,dgamds(6)

```

```

! =====
! --- PARAMETRES MATERIAUX -----
! =====

```

```

YOUNG=materf(1,1)
POISSON= materf(2,1)
ALFA_D=materf(1,2)
BETA_D=materf(2,2)
A_PL=materf(3,2)
B_PL=materf(4,2)
C_PL=materf(5,2)
D_PL=materf(6,2)
RHA_0=materf(7,2)
XH=materf(8,2)
YH=materf(9,2)
A_VE=materf(10,2)
B_VE=materf(11,2)
N_VE=materf(12,2)
TETA_R=materf(13,2)
OMEGA=materf(14,2)
D1=materf(15,2)
D2=materf(16,2)
D3=materf(17,2)
GAM=materf(18,2)
K1=materf(19,2)
FNTOL=materf(20,2)
AXH=materf(21,2)
BXH=materf(22,2)
PNO_C=materf(23,2)
TYPTAN=materf(24,2)

```

```
! =====  
! --- CALCUL DE LA MATRICE ELASTIQUE -----  
! =====  
  
do ii=1,3  
do jj=1,3  
if (ii.eq.jj)then  
el(ii,jj)=(young*(1.0-poisson))/((1.0+poisson)*(1.0-2.0*poisson))  
else  
el(ii,jj)=(young*(poisson))/((1.0+poisson)*(1.0-2.0*poisson))  
end if  
el(ii+3,jj)=0.0  
el(ii,jj+3)=0.0  
end do  
end do  
  
do ii=4,6  
do jj=4,6  
if (ii.eq.jj)then  
el(ii,jj)=2.0*(young)/(2.0*(1.0+poisson))  
else  
el(ii,jj)=0.0  
end if  
end do  
end do  
  
if(nr.eq.8)then  
sigd(1:3)=yd(1:3)  
sigd(4:6)=yd(4:6)  
sigf(1:3)=yf(1:3)  
sigf(4:6)=yf(4:6)  
depsg(1:3)=deps(1:3)  
depsg(4:6)=deps(4:6)  
  
else if(nr.eq.6)then  
sigd(1:3)=yd(1:3)  
sigd(4)=yd(4)  
sigd(5:6)=0.0  
sigf(1:3)=yf(1:3)  
sigf(4)=yf(4)  
sigf(5:6)=0.0  
depsg(1:3)=deps(1:3)  
depsg(4:6)=deps(4:6)  
end if
```

```
! =====
! --- CALCUL VARIABLES INTERNES -----
! =====

vind(1)=yd(nr-1)
vinf(1)=yf(nr-1)
vind(2)=abs(yd(nr))
vinf(2)=abs(yf(nr))

pn1=(sigf(1)+sigf(2)+sigf(3))/3.
if (abs(pn1).lt.pn0_c) then
else
  xh=axh*pn1+bxh
end if

rkp=vinf(1)
rkd=rkp-xh
if (rkd.lt.0.0) then
  rkd=0.0
else
end if

!if(yf(nr).lt.0.0) then
!yf(nr)=0.0
!else
!end if

rlampb=abs(yf(nr))

if (rha_0.gt.1.0) then
  rha=1.0
else
  rha=(rha_0-1.0)*(rkp/xh)**2-2.0*(rha_0-1.0)*(rkp/xh)+rha_0
end if

if (rkp.le.xh) then
else
  rha=1.
end if

sha=(-1.0)*(rkd/yh)**2-2.0*(-1.0)*(rkd/yh)
if (rkd.le.yh) then
else
  sha=1.
end if
```

```

! =====
! --- CALCUL DES DERIVES DU POTENTIEL -----
! =====

  if (nr.eq.8) then
    rj2=1.0/6.0*((sigf(1)-sigf(2))**2.0+(sigf(1)-sigf(3))**2.0+&
      (sigf(2)-sigf(3))**2.0)+(1.0/sqrt(2.0)*sigf(4))**2.0+&
      (1.0/sqrt(2.0)*sigf(5))**2.0+(1.0/sqrt(2.0)*sigf(6))**2.0
  else if (nr.eq.6) then
    rj2=1.0/6.0*((sigf(1)-sigf(2))**2.0+(sigf(1)-sigf(3))**2.0+&
      (sigf(2)-sigf(3))**2.0)+(1.0/sqrt(2.0)*sigf(4))**2.0
  else
    end if

  if (rj2.gt.r8miem()) then
    dqdj2=Sqrt(3.0)/(2.*Sqrt(rj2))
  else
    dqdj2=Sqrt(3.0)/(2.*Sqrt(r8miem()))
  end if

  kapc=0.01
  gpl=Sqrt(3.0*rj2)-kapc*pn1

  dfdp=- (2.*a_pl*pn1*(1.-rha)-(1.-sha)*b_pl*(d_pl+(1.-d_pl)*rha))
  dfdq=1.0

  do ii=1,3
    dpds(ii)=0.3333333333333333
  end do
  do ii=4,6
    dpds(ii)=0.0
  end do

  dj2ds(1)=(2.*(sigf(1)-sigf(2))+2.*(sigf(1)-sigf(3)))/6.
  dj2ds(2)=(-2.*(sigf(1)-sigf(2))+2.*(sigf(2)-sigf(3)))/6.
  dj2ds(3)=(-2.*(sigf(1)-sigf(3))-2.*(sigf(2)-sigf(3)))/6.
  if(nr.eq.8) then
    dj2ds(4)=sigf(4)
    dj2ds(5)=sigf(5)
    dj2ds(6)=sigf(6)
  else if(nr.eq.6) then
    dj2ds(4)=sigf(4)
    dj2ds(5)=0.0
    dj2ds(6)=0.0
  end if

```

```

! =====
! --- CALCUL DU POTENTIEL -----
! =====

do ii=1,6
  dgds(ii)=(dfdp*dpds(ii)+dfdq*dqdj2*dj2ds(ii))
end do

! =====
! --- CALCUL DU SEUIL PLASTIQUE -----
! =====

if(nr.eq.8)then
  depse(1:6)=deps(1:6)-rlambp*dgds(1:6)
  do ii=1,(nr-2)
    dsige(ii)=el(ii,1)*depse(1)+el(ii,2)*depse(2)+el(ii,3)*depse(3)+&
      el(ii,4)*depse(4)+el(ii,5)*depse(5)+el(ii,6)*depse(6)
  end do
  sig(1:6)=yf(1:6)
else if(nr.eq.6)then
  depse(1:4)=deps(1:4)-rlambp*dgds(1:4)
  depse(5:6)=0.0
  do ii=1,(nr-2)
    dsige(ii)=el(ii,1)*depse(1)+el(ii,2)*depse(2)+el(ii,3)*depse(3)+&
      el(ii,4)*depse(4)+el(ii,5)*depse(5)+el(ii,6)*depse(6)
  end do
  sig(1:4)=yf(1:4)
  sig(5:6)=0.0
end if

call apdcvx(nr,sig, vinf, nmat, materf, seuil)

! =====
! --- STOCKAGE DES RESIDUS -----
! =====

naux=0.0
do ii=1,(nr-2)
  naux2=0.0
  naux3=0.0

  do jj=1,6
    if(jj.gt.3)then
      naux2=el(ii,jj)*deps(jj)/sqrt(2.0)+naux2
      naux3=el(ii,jj)*dgds(jj)+naux3
    else
      naux2=el(ii,jj)*deps(jj)+naux2
    end if
  end do
end do

```

```
naux3=el(ii,jj)*dgds(jj)+naux3
end if
end do

if(ii.gt.3)then
r(ii)=(yf(ii)/sqrt(2.0)-yd(ii)/sqrt(2.0)-&
      (naux2)+yf(nr)*naux3)/el(1,1)
else
r(ii)=(yf(ii)-yd(ii)-(naux2)+yf(nr)*naux3)/el(1,1)
end if

end do
naux=(dgds(1)**2.0+(dgds(2)**2.0+(dgds(3)**2.0+&
      (dgds(4)**2.0+(dgds(5)**2.0+(dgds(6)**2.0

normplv=yf(nr)*sqrt(naux)
r(nr-1)=(yf(nr-1)-yd(nr-1)-normplv)

r(nr)=seuil/el(1,1)
end subroutine
```



```
subroutine apdlmf(nvi, vind, nmat, materf, dt,&
                sigd, nr, yd, yf, deps,&
                vinf)
! =====
! COPYRIGHT (C) 1991 - 2013 EDF R&D WWW.CODE-ASTER.ORG
! THIS PROGRAM IS FREE SOFTWARE; YOU CAN REDISTRIBUTE IT AND/OR MODIFY
! IT UNDER THE TERMS OF THE GNU GENERAL PUBLIC LICENSE AS PUBLISHED BY
! THE FREE SOFTWARE FOUNDATION; EITHER VERSION 2 OF THE LICENSE, OR
! (AT YOUR OPTION) ANY LATER VERSION.
!
! THIS PROGRAM IS DISTRIBUTED IN THE HOPE THAT IT WILL BE USEFUL, BUT
! WITHOUT ANY WARRANTY; WITHOUT EVEN THE IMPLIED WARRANTY OF
! MERCHANTABILITY OR FITNESS FOR A PARTICULAR PURPOSE. SEE THE GNU
! GENERAL PUBLIC LICENSE FOR MORE DETAILS.
!
! YOU SHOULD HAVE RECEIVED A COPY OF THE GNU GENERAL PUBLIC LICENSE
! ALONG WITH THIS PROGRAM; IF NOT, WRITE TO EDF R&D CODE_ASTER,
! 1 AVENUE DU GENERAL DE GAULLE, 92141 CLAMART CEDEX, FRANCE.
! =====

implicit none
#include "asterc/r8miem.h"

integer :: val, ndt, nvi, nmat, ndi, nr, ii
real(kind=8) :: materf(nmat, 2)
real(kind=8) :: yd(*), vind(*), dt, deps(6)
real(kind=8) :: yf(*), vinf(*), sigd(6), dam, alfa_d, beta_d
real(kind=8) :: xh, rkp, rkd, sigf(6), axh, bxh, pn0_c, pn1
real(kind=8) :: dpds(6), dj2ds(6), dgds(6), eplas(6), dfdp, deq, dv
real(kind=8) :: a_pl, b_pl, c_pl, d_pl, yh, dfdq, dqdj2
real(kind=8) :: rha, rha_0, rj2, sha

alfa_d=materf(1,2)
beta_d=materf(2,2)
xh=materf(8,2)
axh=materf(21,2)
bxh=materf(22,2)
pn0_c=materf(23,2)
A_PL=materf(3,2)
B_PL=materf(4,2)
C_PL=materf(5,2)
D_PL=materf(6,2)
RHA_0=materf(7,2)
XH=materf(8,2)
YH=materf(9,2)
```

```

if(nr.eq.8) then
sigf(1:3)=yf(1:3)
sigf(4:6)=yf(4:6)

else if(nr.eq.6) then
sigf(1:3)=yf(1:3)
sigf(4)=yf(4)
sigf(5:6)=0.0
end if

pn1=(sigf(1)+sigf(2)+sigf(3))/3.
if (pn1.lt.pn0_c) then
else
xh=axh*pn1+bxh
end if

! =====
! --- CALCUL VARIABLES INTERNES -----
! =====

if (rha_0.gt.1.0) then
rha=1.0
else
rha=(rha_0-1.0)*(vinf(1)/xh)**2-2.0*(rha_0-1.0)*(vinf(1)/xh)+rha_0
end if

if (vinf(1).le.xh) then
else
rha=1.
end if

if((vinf(1)-xh).lt.0.0) then
sha=0.0
else
sha=(-1.0)*((vinf(1)-xh)/yh)**2-2.0*(-1.0)*((vinf(1)-xh)/yh)
end if

if ((vinf(1)-xh).le.yh) then
else
sha=1.
end if

! =====
! --- CALCUL DES DERIVES DU POTENTIEL -----
! =====

if (nr.eq.8) then
rj2=1.0/6.0*((sigf(1)-sigf(2))**2.0+(sigf(1)-sigf(3))**2.0+&
(sigf(2)-sigf(3))**2.0)+(sigf(4)/sqrt(2.0))**2.0+&

```

```

    (sigf(5)/sqrt(2.0))**2.0+(sigf(6)/sqrt(2.0))**2.0
else if (nr.eq.6)then
rj2=1.0/6.0*((sigf(1)-sigf(2))**2.0+(sigf(1)-sigf(3))**2.0+&
    (sigf(2)-sigf(3))**2.0)+(sigf(4)/sqrt(2.0))**2.0
else
end if

if (rj2.gt.r8miem())then
dqdj2=Sqrt(3.0)/(2.*Sqrt(rj2))
else
dqdj2=Sqrt(3.0)/(2.*Sqrt(r8miem()))
end if

dfdp=- (2.*a_pl*pn1*(1.-rha)-(1.-sha)*b_pl*(d_pl+(1.-d_pl)*rha))
dfdq=1.0

do ii=1,3
dpds(ii)=0.3333333333333333
end do
do ii=4,6
dpds(ii)=0.0
end do

dj2ds(1)=(2.*(sigf(1)-sigf(2))+2.*(sigf(1)-sigf(3)))/6.
dj2ds(2)=(-2.*(sigf(1)-sigf(2))+2.*(sigf(2)-sigf(3)))/6.
dj2ds(3)=(-2.*(sigf(1)-sigf(3))-2.*(sigf(2)-sigf(3)))/6.
if(nr.eq.8)then
dj2ds(4)=sigf(4)
dj2ds(5)=sigf(5)
dj2ds(6)=sigf(6)
else if(nr.eq.6)then
dj2ds(4)=sigf(4)
dj2ds(5)=0.0
dj2ds(6)=0.0
end if

do ii=1,6
dgds(ii)=(dfdp*dpds(ii)+dfdq*dqdj2*dj2ds(ii))
end do

dv=0.0
do ii=1,(nr-2)
eplas(ii)=yf(nr)*dgds(ii)
end do
if(vinf(1).gt.xh)then
if(nr.eq.8)then
deq=sqrt(2.0/3.0*(1.0/6.0*((eplas(1)-eplas(2))**2.0+&

```

```
(eplas(1)-eplas(3))**2.0+(eplas(3)-eplas(2))**2.0)+&
eplas(4)**2.0+eplas(5)**2.0+eplas(6)**2.0))
else if(nr.eq.6)then
deq=sqrt(2.0/3.0*(1.0/6.0*((eplas(1)-eplas(2))**2.0+&
(eplas(1)-eplas(3))**2.0+(eplas(3)-eplas(2))**2.0)+eplas(4)**2.0))
end if
dv=sqrt(deq**2.0)
else
end if
vinf(4)=vind(4)+dv

dam=(1.0-beta_d)*(1.0-exp(-(vinf(4)/alfa_d)))
vinf(3)=dam

end subroutine
```

Appendix F. Command file of the 2D tunnel analysis

It is reported in the following the Python script of the *.comm file for the bi-dimensional tunnel analysis performed in Chapter 7. The additional constitutive model parameters are commented in the Python script of Figure A.1. The reader is referred to specific equations numbers for their meaning, which can be found in the manuscript.

The calibration of the different constitutive parameters employed was detailed in the manuscript. For the interpretation of the *.comm file, along with the different commands involved, the reader is invited to consult the manual of *Code_Aster*, freely available at www.code-aster.com, where all the specific details are given.

In the following, a brief description of the relevant aspects of the modeling strategy, with the adopted values, is reported:

1. Time steps: the command `DEFI_LIST_REEL` at line 306 defines the time steps of the analysis. From the beginning of the numerical analysis up to 5.33×10^6 seconds the time steps are of 20000 seconds length, in order to capture the rapid variation of the different fields (stresses, pore pressure, inelastic variables etc.), while in the interval between 5.33×10^6 seconds up to 2.13×10^7 seconds the steps are defined such as the interval is divided into 60 steps. This allows to produce a smaller output file and is justified by the fact that the variation of the different fields is smaller in this interval;
2. Deconfining functions: the two deconfining functions for the nodal reactions and the pore pressure at the tunnel walls are defined with the function `DEFI_FONCTION`, at line 341 and 373, respectively. The two functions are discretized in time and represented by linear segments, while their definition is given in Section 7.3, from which numerical values can be computed;
3. Initial conditions: the initial state of stress and the initial pore water pressure is defined with the command `CREA_CHAMP` at line 383 and 391, respectively. The initial state of stress is defined in terms of effective stress components, which values are given, after literature, in Section 7.3. The pore pressure is defined with uniform value of 2 MPa, as specified also in Section 7.3;
4. Boundary conditions at the tunnel walls: at the beginning of the analysis, a first run is performed in which the vertical and horizontal components of the displacement vector at the tunnel walls node are blocked. This is done with function `AFFE_CHAR_MECA` at line 402. This step is necessary to compute the nodal reactions at the tunnel walls, which will be subsequently released with the deconfining function in order to simulate the excavation process in 2D conditions;
5. Mechanical outer boundary conditions: the mechanical boundary conditions at the outer box of the model are specified with the command `AFFE_CHAR_MECA` at line

410. The conditions are blocked vertical displacement at the bottom of the model and blocked horizontal displacements at the sides. At the vertical boundary, a total stress is applied to equilibrate the total vertical stress, i.e. 6.5 MPa.
6. Hydraulic boundary conditions: the hydraulic conditions at the outer boundary are not specified, which implies that impermeable boundaries are assigned. This conditions is representative of the far field, in which no changes are expected during the tunnel excavation. At the tunnel walls, the pore pressure is assigned to the initial value of 2 MPa, in equilibrium with the whole model, while its evolution with time is controlled by the pore pressure deconfining function as specified at point 2.

In this file are explained the material parameters of the model.
The reference is PhD of Parisio 2016

```
APD_LMSEPFLL = _F(  
YOUNG      =2000e6,      # Young's modulus  
POISSON    =0.35,      # Poisson's ratio  
ALFA_D     =1.5e-2,     # Damage parameter, cf. Ch. 4, Eq. 4.47  
BETA_D     =0.3,       # Damage parameter, cf. Ch. 4, Eq. 4.47  
A_PL       =-0.07449e-6, # Plastic parameter, cf. Ch. 4, Eq. 4.22  
B_PL       =0.967,     # Plastic parameter, cf. Ch. 4, Eq. 4.22  
C_PL       =2.683e6,   # Plastic parameter, cf. Ch. 4, Eq. 4.22  
D_PL       =1.0,      # Plastic parameter, cf. Ch. 4, Eq. 4.22  
RHA_0      =0.7,      # Plastic parameter, cf. Ch. 4, Eq. 4.29  
X_H        =4.0e-3,   # Plastic compressibility, cf. Ch. 4, Eq. 4.29  
S_H        =4.0e-1,   # Non-associated parameter, cf. Ch. 4, Eq. 4.37  
A_VE       =0.7401,   # Van Eekelen parameter, not included here  
B_VE       =0.674,   # Van Eekelen parameter, cf. Ch. 5, Eq. 5.13  
N_VE       =-0.229,   # Van Eekelen parameter, not included here  
TETA_R     =33.0,    # Anisotropic angle (°), cf. Ch. 5, figure 5.6  
OMEGA      =1.1367,  # Anisotropic parameter, cf. Ch. 5, Eq. 5.33  
D1         =0.5299,  # Anisotropic parameter, cf. Ch. 5, Eq. 5.33  
D2         =-0.0277, # Anisotropic parameter, cf. Ch. 5, Eq. 5.33  
D3         =0.0,     # Anisotropic parameter, cf. Ch. 5, Eq. 5.33  
GAM        =0.0,     # Anisotropic parameter, not included here  
K1         =1.0,     # Anisotropic parameter, not included here  
FNTOL      =1.0e-5,  # Numerical tolerance, not included here  
XH         =0.0,     # Brittle-ductile transition, not included here  
BXH        =4.0e-3,  # Brittle-ductile transition, not included here  
PNO_C      =20e30,   # Brittle-ductile transition, not included here  
            # set to high values to de-activate  
TYPTAN     =1        # Numerical parameter, not included here  
) ,
```

Figure A.1: Python command to specify the material parameters of the constitutive model. The parameters that are included in the current version of MS3 are specified along with the reference chapters and equations in the manuscript that the reader is invited to consult for their meaning.

Appendix F. Command file of the 2D tunnel analysis

```
# TITLE : HM EXCAVATION ANALYSIS OF CIRCULAR TUNNEL IN 2D PLANE STRAIN
# CONDITIONS
# =====
# COPYRIGHT (C) 1991 - 2012 EDF R&D WWW.CODE-ASTER.ORG
# THIS PROGRAM IS FREE SOFTWARE; YOU CAN REDISTRIBUTE IT AND/OR MODIFY
# IT UNDER THE TERMS OF THE GNU GENERAL PUBLIC LICENSE AS PUBLISHED BY
# THE FREE SOFTWARE FOUNDATION; EITHER VERSION 2 OF THE LICENSE, OR
# (AT YOUR OPTION) ANY LATER VERSION.
#
# THIS PROGRAM IS DISTRIBUTED IN THE HOPE THAT IT WILL BE USEFUL, BUT
# WITHOUT ANY WARRANTY; WITHOUT EVEN THE IMPLIED WARRANTY OF
# MERCHANTABILITY OR FITNESS FOR A PARTICULAR PURPOSE. SEE THE GNU
# GENERAL PUBLIC LICENSE FOR MORE DETAILS.
#
# YOU SHOULD HAVE RECEIVED A COPY OF THE GNU GENERAL PUBLIC LICENSE
# ALONG WITH THIS PROGRAM; IF NOT, WRITE TO EDF R&D CODE_ASTER,
# 1 AVENUE DU GENERAL DE GAULLE, 92141 CLAMART CEDEX, FRANCE.
# =====
#
# =====
# ANALYSIS: HM-MODELING OF THE FE-EXPERIMENT, TUNNEL EXCAVATION
# AUTHOR: FRANCESCO PARISIO
# E-MAIL: francesco.parisio@epfl.ch
# INSTITUTE: LMS (LABORATOIRE DE MeCANIQUE DES SOLS)
# UNIVERSITY: EPFL
#
# =====
# DESCRIPTION OF THE ANALYSIS
# =====
#
# =====
# GEOMETRY AND NUMERICAL MODEL
# =====
# TUNNEL DIAMETER 3.0m
# CONDITIONS PLANE STRAIN
# REGULARIZATION SECOND GRADIENT OF DILATANCY
# CONSTITUTIVE LAW PLASTIC-DAMAGE MODEL OF PARISIO (2016)
# BEDDING ORIENTATION 33°
#
# =====
# MODELING SEQUENCE
# =====
# STAGE 0:
# INITIAL AND BOUNDARY CONDITIONS, EQUILIBRIUM RUN AND COMPUTATION OF
# NODAL REACTIONS AT TUNNEL WALLS TO APPLY THE CONVERGENCE-CONFINEMENT
```


Appendix F. Command file of the 2D tunnel analysis

```
# METHOD

# STAGE 1:
# EXCAVATION OF THE TUNNEL WITH REALED NODAL REACTIONS AND PORE WATER
# PRESSURE AT THE TUNNEL WALLS

# =====
# START OF THE ANALYSIS, VARIABLES DEFINITION
# =====

DEBUT()
VISCOLIQ = DEFI_CONSTANTE( VALE=1.E-3)
DVISCOL  = DEFI_CONSTANTE( VALE=0.)

ROBIOT=0.7
pw=2.0e6
CONF=5.0e6
cohe=5.0e6
seconv=86400
KINT      = DEFI_CONSTANTE( VALE=4.E-19)

# =====
# READING THE MESH
# =====

mail1 = LIRE_MAILLAGE(FORMAT='MED',);

# =====
# DEFINING THE GROUPS OF NODES
# =====

mail0=CREA_MAILLAGE(MAILLAGE=mail1,
                   QUAD_LINE=_F(TOUT='OUI'))

mail2=CREA_MAILLAGE (MAILLAGE=mail1,
                   CREA_MAILLE=( _F(NOM='outer_reg',GROUP_MA='outer',
                                     PREF_MAILLE='du'),
                                 _F(NOM='inner_reg',GROUP_MA='inner',PREF_MAILLE='ou'),
                                 _F(NOM='exca_reg',GROUP_MA='exca',PREF_MAILLE='cu')))

MAIL=CREA_MAILLAGE(MAILLAGE=mail2,

                  MODI_MAILLE=( _F(GROUP_MA='outer_reg',OPTION='TRIA6_7'),
                                _F(GROUP_MA='inner_reg',OPTION='TRIA6_7'),
                                _F(GROUP_MA='exca_reg',OPTION='TRIA6_7')))
```

Appendix F. Command file of the 2D tunnel analysis

```
MAIL = DEFI_GROUP(reuse=MAIL,
                  MAILLAGE=MAIL,
                  CREA_GROUP_NO=( _F(NOM='tunno1',
                                     GROUP_MA='tunw'),),),)

MAIL = MODI_MAILLAGE( reuse      = MAIL,
                     MAILLAGE   = MAIL,
                     ORIE_PEAU_2D = _F( GROUP_MA = ('top',
                                                    'bottom',
                                                    'left',
                                                    'right'),), )

# =====
# MODEL BEFORE EXCAVATION TO COMPUTE I.C.
# =====

MO=AFFE_MODELE(MAILLAGE=MAIL,
               AFFE=( _F(GROUP_MA='inner',
                        PHENOMENE='MECANIQUE',
                        MODELISATION='D_PLAN_HM',),
                    _F(GROUP_MA='outer',
                        PHENOMENE='MECANIQUE',
                        MODELISATION='D_PLAN_HM',),
                    _F(GROUP_MA='exca',
                        PHENOMENE='MECANIQUE',
                        MODELISATION='D_PLAN_HM',),
                    _F(GROUP_MA='inner_reg',
                        PHENOMENE='MECANIQUE',
                        MODELISATION='D_PLAN_DIL',),
                    _F(GROUP_MA='outer_reg',
                        PHENOMENE='MECANIQUE',
                        MODELISATION='D_PLAN_DIL',),
                ))

# =====
# MODEL BEFORE EXCAVATION TO COMPUTE TUNNEL WALL REACTIONS
# =====

MO1=AFFE_MODELE(MAILLAGE=MAIL,
                AFFE=( _F(GROUP_MA=('outer','inner','top'),
                          PHENOMENE='MECANIQUE',
                          MODELISATION='D_PLAN_HM',),
                    _F(GROUP_MA='inner_reg',
                          PHENOMENE='MECANIQUE',
                          MODELISATION='D_PLAN_DIL',),
                    _F(GROUP_MA='outer_reg',
                          PHENOMENE='MECANIQUE',
```

Appendix F. Command file of the 2D tunnel analysis

```

MODELISATION='D_PLAN_DIL',),),);

# =====
# MODEL AFTER EXCAVATION
# =====

MO2=AFFE_MODELE (MAILLAGE=MAIL,
                 AFFE=( _F(GROUP_MA=('outer','inner','top'),
                           PHENOMENE='MECANIQUE',
                           MODELISATION='D_PLAN_HM',),
                 _F(GROUP_MA='inner_reg',
                     PHENOMENE='MECANIQUE',
                     MODELISATION='D_PLAN_DIL',),
                 _F(GROUP_MA='outer_reg',
                     PHENOMENE='MECANIQUE',
                     MODELISATION='D_PLAN_DIL',),),),);

E_SOL = 2000e6
NU_FICTIF = 0.49999
NU_SOL = 0.35
E_BETON = 2.0E10
NU_BETON = 0.2
RHO_BIDON = 2700.
ALPHA_BIDON = 0.
cohe=10.627e26
edil=10.0e6
bd=0.3
lresu = DEFI_LIST_REEL( VALE=( [sqrt(i*i)/50+1 for i in range(50)]))
ccoef=1.0

# =====
# INITIAL SOIL MODEL FOR NODAL REACTIONS
# =====

SOLO=DEFI_MATERIAU (ELAS=_F (E=E_SOL,
                             NU=NU_SOL,
                             RHO=RHO_BIDON,
                             ALPHA = ALPHA_BIDON,)),
APD LMSEPFL = F (YOUNG
                 =E SOL,
                 POISSON           =NU_SOL,
                 ALFA_D             =1.5e-2,
                 BETA_D             =bd,
                 A_PL               =-0.07449e-6,
                 B_PL               =0.967,
                 C_PL               =2.683e6*ccoef,
                 D_PL               =1.0,
                 RHA_0              =0.7,

```

Appendix F. Command file of the 2D tunnel analysis

```

X_H           =4.0e-3,
S_H           =4.0e-1,
A_VE         =0.7401,
B_VE         =0.674,
N_VE         =-0.229,
TETA_R       =33.0,
OMEGA        =1.1367,
D1           =0.5299,
D2           =-0.0277,
D3           =0.0,
GAM          =0.0,
K1           =1.0,
FNTOL        =1.0e-5,
AXH          =0.0,
BXH          =4.0e-3,
PN0_C        =-20e30,
TYPTAN       =1),
COMP_THM     = 'LIQU_SATU',

THM_INIT     = _F( PRE1           = 1.0,
                  PORO           = 0.14, ),

THM_DIFFU    = _F( RHO           = 2400.,
                  BIOT_COEF      = ROBIOT,
                  PERM_IN        = KINT,
                  PESA_X         = 0.,
                  PESA_Y         = 0.,
                  PESA_Z         = 0., ),

THM_LIQU     = _F( RHO           = 1000.,
                  UN_SUR_K       = 1.0/(2200.e6),
                  VISC           = VISCOLIQ,
                  D_VISC_TEMP    = DVISCOL,
                  ), ),

# =====
# REAL SOIL MODEL
# =====

SOL=DEFI_MATERIAU (ELAS=_F(E=E_SOL,
                          NU=NU_SOL,
                          RHO=RHO_BIDON,
                          ALPHA=ALPHA_BIDON, ),
                  APD_LMSEPFL = _F(YOUNG           =E_SOL,
                                    POISSON         =NU_SOL,
                                    ALFA_D          =1.5e-2,
                                    BETA_D          =bd,

```

Appendix F. Command file of the 2D tunnel analysis

```

A_PL          =-0.07449e-6,
B_PL          =0.967,
C_PL          =2.683e6*ccoef,
D_PL          =1.0,
RHA_0        =0.7,
X_H          =4.0e-3,
S_H          =4.0e-1,
A_VE         =0.7401,
B_VE         =0.674,
N_VE         =-0.229,
TETA_R       =33.0,
OMEGA        =1.1367,
D1           =0.5299,
D2           =-0.0277,
D3           =0.0,
GAM          =0.0,
K1           =1.0,
FNTOL        =1.0e-5,
AXH          =0.0,
BXH          =4.0e-3,
PN0_C        =20e30,
TYPTAN       =1),
COMP_THM     = 'LIQU_SATU',

THM_INIT     = _F( PRE1      = 1.0,
                  PORO      = 0.14, ),

THM_DIFFU    = _F( RHO      = 2400.,
                  BIOT_COEF = ROBIOT,
                  PERM_IN   = KINT,
                  PESA_X    = 0.,
                  PESA_Y    = 0.,
                  PESA_Z    = 0., ),

THM_LIQU     = _F( RHO      = 1000.,
                  UN_SUR_K  = 1.0/(2200.e6),
                  VISC      = VISCOLIQ,
                  D_VISC_TEMP = DVISCOL,
                  ), );

soilreg=DEFI_MATERIAU(ELAS_2NDG=_F(A1=edil,A2=0,A3=0,A4=0,A5=0),,
                    NU=NU_BETON,
                    RHO=RHO_BIDON,
                    ALPHA=ALPHA_BIDON,,);

```

Appendix F. Command file of the 2D tunnel analysis

```
CHMAT1=AFFE_MATERIAU (MAILLAGE=MAIL,
                      AFPE=( _F (GROUP_MA=('outer','inner'),MATER=SOL0),
                              _F (GROUP_MA=('inner_reg','outer_reg'),MATER=soilreg),),)

CHMAT2=AFFE_MATERIAU (MAILLAGE=MAIL,
                      AFPE=( _F (GROUP_MA=('outer','inner'),MATER=SOL),
                              _F (GROUP_MA=('inner_reg','outer_reg'),MATER=soilreg),),)

CHMAT3=AFFE_MATERIAU (MAILLAGE=MAIL,
                      AFPE=( _F (GROUP_MA=('outer','inner'),MATER=SOL),
                              _F (GROUP_MA=('inner_reg','outer_reg'),MATER=soilreg),),)

# =====
# DEFINITION OF TIME STEPS OF THE ANALYSIS
# =====

tfin=4*5.33e6
#tfin=30*seconv
LIX=DEFI_LIST_REEL (DEBUT=0,
                   INTERVALLE=( _F (JUSQU_A=1.0,
                                     NOMBRE=1,),
                                _F (JUSQU_A=10.0,
                                     NOMBRE=1,),
                                _F (JUSQU_A=16*seconv,
                                     NOMBRE=1,),
                                _F (JUSQU_A=25*seconv,
                                     PAS=20000,),
                                _F (JUSQU_A=30*seconv,
                                     PAS=20000,),
                                _F (JUSQU_A=5.33e6,
                                     PAS=20000,),
                                _F (JUSQU_A=tfin,
                                     NOMBRE=60,),
                                ),);

LI=DEFI_LIST_INST (INFO=1,
                  DEFI_LIST=_F (LIST_INST=LIX),
                  ECHEC=_F (SUBD_NIVEAU=20, SUBD_PAS=2),);

# =====
# DECONFINING FUNCTION FOR NODAL REACTIONS
# =====

FO=DEFI_FONCTION (NOM_PARA='INST',
                 VALE=( 10.0,1.0,
                       10.0*seconv,1.0,
```

```

11.0*seconv,1.0,
12.0*seconv,1.0,
13.0*seconv,1.0,
14.0*seconv,1.0,
15.0*seconv,1.0,
16.0*seconv,1.0,
17.0*seconv,1.0,
18.0*seconv,0.999,
19.0*seconv,0.998,
20.0*seconv,0.995,
21.0*seconv,0.986,
22.0*seconv,0.965,
23.0*seconv,0.918,
24.0*seconv,0.830,
25.0*seconv,0.692,
26.0*seconv,0.523,
27.0*seconv,0.358,
28.0*seconv,0.226,
29.0*seconv,0.134,
30.0*seconv,0.0,
31.0*seconv,0.0,
1.0e6*seconv,0.0,
# 1.0e6*seconv,0.134,
),);

# =====
# DECONFINING FUNCTION FOR PORE WATER PRESSURE AT TUNNEL WALLS
# =====

F1=DEFI_FONCTION(NOM_PARA='INST',
                 VALE=( 10.0,1.0,
                       18.0*seconv,1.0,
                       19.0*seconv,0.0,
                       1.0e6*seconv,0.0),);

# =====
# INITIAL FIELD STRESSES AND PORE WATER PRESSURE
# =====

RES1=CREA_CHAMP(TYPE_CHAM='ELGA_SIEF_R',
                OPERATION='AFFE',
                PROL_ZERO='OUI',
                MODELE=MO,
                AFFE=(_F(GROUP_MA=('inner','outer','exca'),

NOM_CMP=('SIXX','SIYY','SIZZ','SIXY','SIPXX','SIPYY','SIPZZ','SIPXY'),
        VALE=(-2.5e6,-4.5e6,-0.5e6,0.0,-pw,-pw,

```

Appendix F. Command file of the 2D tunnel analysis

```

-pw,0.0),),),),
PRE0=CREA_CHAMP (TYPE_CHAM='NOEU_DEPL_R',
                 OPERATION='AFFE',
                 MODELE=MO,
                 AFFE=(_F(TOUT='OUI',
                          NOM_CMP=('PRE1'),
                          VALE=(pw),),),),
# =====
# NULL DISPLACEMENTS AT TUNNEL WALLS (TO COMPUTE NODAL REACTIONS)
# =====
CH210=AFFE_CHAR_MECA (MODELE=MO1,
                     DDL_IMPO=(_F(GROUP_NO='tunno1',DX=0.0,DY=0.0),),
                     ),);
# =====
# MECHANICAL AND HYDRAULIC BOUNDARY CONDITIONS
# =====
CH220=AFFE_CHAR_MECA (MODELE=MO1,
                     FACE_IMPO=(
                         _F( GROUP_MA = 'bottom', DY = 0., ),
                         _F( GROUP_MA = 'right',  DX = 0., ),
                         _F( GROUP_MA = 'left',   DX = 0., ),),),
                     PRES_REP=_F(GROUP_MA='top',
                                   PRES=4.5e6+pw,)),
PREAU      = AFFE_CHAR_MECA( MODELE      = MO1,
                             DDL_IMPO = _F( GROUP_NO='tunno1', PRE1 = pw,
                             )
                             )
# =====
# COMPUTATION WITH BLOCKED NODES AT TUNNEL WALLS
# =====
RESU1=STAT NON LINE (MODELE=MO1,
                    CHAM_MATER=CHMAT1,
                    EXCIT=( _F(CHARGE=CH210,
                                TYPE_CHARGE='DIDI'),
                            _F(CHARGE=CH220, ),
                            _F(CHARGE=PREAU, ), ),
                    SOLVEUR=( _F( METHODE='MUMPS', ), ),
                    COMPORTEMENT=( _F( RELATION      = 'KIT_HM',
                                        RELATION_KIT =

```


Appendix F. Command file of the 2D tunnel analysis

```

('APD_LMSEPFL','LIQU_SATU','HYDR_UTIL'),
      ALGO_INTE='NEWTON_PERT',
      GROUP_MA=('outer','inner')),),
      _F(GROUP_MA=('inner_reg','outer_reg'),
        RELATION='ELAS')),),
      ETAT_INIT=_F(SIGM=RES1,DEPL=PRE0),
      INCREMENT=_F(LIST_INST=LI,
                  INST_INIT=1,
                  INST_FIN=10,),
      NEWTON=_F(MATRICE='TANGENTE',
               REAC_ITER=1,),
      CONVERGENCE=_F(RESI_GLOB_RELA=5.E-6,
                    ITER_GLOB_MAXI=200,
                    ),
      );

# =====
# MECHANICAL BOUNDARY CONDITIONS
# =====

CH51=AFFE_CHAR_MECA(MODELE=MO2,
                   FACE_IMPO=(
                     _F( GROUP_MA = 'bottom', DY = 0., ),
                     _F( GROUP_MA = 'right',  DX = 0., ),
                     _F( GROUP_MA = 'left',   DX = 0., ),),),
                   PRES_REP=_F(GROUP_MA='top',
                                PRES=4.5e6+pw,),);

# =====
# COMPUTATION OF NODAL REACTIONS
# =====

RESU1=CALC_CHAMP(reuse =RESU1,
                RESULTAT=RESU1,
                INST=10.,
                FORCE='REAC_NODA',
                );

# =====
# EXTRACTION OF NODAL REACTIONS
# =====

REANODA=CREA_CHAMP(TYPE_CHAM='NOEU_DEPL_R',
                  OPERATION='EXTR',
                  RESULTAT=RESU1,

```

Appendix F. Command file of the 2D tunnel analysis

```

        NOM_CHAM='REAC_NODA',
        INST=10.,);

CH3=AFFE_CHAR_MECA(MODELE=MO1,
        VECT_ASSE=REANODA,);

# =====
# TUNNEL EXCAVATION ANALYSIS WITH NODAL REACTIONS DECONFINEMENT
# =====

RESU1=STAT_NON_LINE(reuse=RESU1,
        MODELE=MO1,
        CHAM_MATER=CHMAT2,
        EXCIT=( _F(CHARGE=CH3,
                FONC_MULT=F0,),
        _F(CHARGE=PREAU,
                FONC_MULT=F1,),
        _F(CHARGE=CH220,)),),
        SOLVEUR=( _F(METHODE='MUMPS',)),
        COMPORTEMENT=( _F(RELATION = 'KIT_HM',
                RELATION_KIT =
('APD_LMSEPFL','LIQU_SATU','HYDR_UTIL',)),
ALGO_INTE='NEWTON_PERT',ITER_INTE_MAXI=10000,ITER_INTE_PAS=-60,
        GROUP_MA=('outer','inner')),),
        _F(GROUP_MA=('inner_reg','outer_reg'),
        RELATION='ELAS')),),
        ETAT_INIT=_F(EVOL_NOLI=RESU1),
        INCREMENT=_F(LIST_INST=LI,
                INST_INIT=1,
                INST_FIN=tfin),),
        NEWTON=_F(MATRICE='TANGENTE',
                REAC_ITER=1500,
                PAS_MINI_ELAS=10000,),
        #RECH_LINEAIRE=( _F(METHODE='MIXTE',ITER_LINE_MAXI=50,)),),
        CONVERGENCE=_F(RESI_GLOB_RELA=1.E-4,
        #
                RESI_GLOB_MAXI=1.E-1,
                ITER_GLOB_MAXI=5000,
                ),
                );

# =====
# POST PROCESSING - EXTRACTION OF RESULTS
# =====
RESU1=CALC_CHAMP(reuse=RESU1,GROUP_MA=('outer','inner'),CONTRAINTE=('SIG
M_ELNO'),VARI_INTERNE=('VARI_ELNO'),DEFORMATION=('EPSI_ELNO'),

```

Appendix F. Command file of the 2D tunnel analysis

```
RESULTAT=RESU1)

RESU1=CALC_CHAMP(reuse=RESU1,
                 CONTRAINTE='SIGM_NOEU',
                 VARI_INTERNE='VARI_NOEU',
                 DEFORMATION='EPSI_NOEU',
                 RESULTAT=RESU1);

RESU1 = CALC_CHAMP( reuse = RESU1,RESULTAT=RESU1,
                   CONTRAINTE=('SIEF_ELNO'),)

# =====
# POST PROCESSING - PROJECTION OF THE DEPL FIELD TO LINEAR MODEL
# =====

CH_LI=PROJ_CHAMP(RESULTAT=RESU1,MAILLAGE_1=MAIL,MAILLAGE_2=mail0,NOM_CHA
M='DEPL')

# =====
# POST PROCESSING - PRINTING RESULTS .med FORMAT
# =====

IMPR_RESU(FORMAT='MED',RESU=( _F(RESULTAT=RESU1,) , _F(RESULTAT=CH_LI,) ),)

# =====
# POST PROCESSING - CUTLINES
# =====

COUPE1 = INTE_MAIL_2D ( MAILLAGE = MAIL ,
                       INFO = 1 ,
                       DEFI_SEGMENT = _F( ORIGINE   = (1.5 , -50.),
                                           EXTREMITE = (10.0   , -50.0),
                                           ),
                       PRECISION=1.E-4,);

COUPE3 = INTE_MAIL_2D ( MAILLAGE = MAIL ,
                       INFO = 1 ,
                       DEFI_SEGMENT = F( ORIGINE   = (0.89 , -51.27),
                                           EXTREMITE = (5.74   , -58.19),
                                           ),
                       PRECISION=1.E-4,);

COUPE4 = INTE_MAIL_2D ( MAILLAGE = MAIL ,
                       INFO = 1 ,
                       DEFI_SEGMENT = _F( ORIGINE   = (-0.89 , -48.73),
                                           EXTREMITE = (-3.44   , -45.09),
                                           ),
```

Appendix F. Command file of the 2D tunnel analysis

```
        ),
        PRECISION=1.E-4,);

COUPE2 = INTE_MAIL_2D ( MAILLAGE = mail0 ,
                        INFO = 1 ,
                        DEFI_SEGMENT = _F( ORIGINE = (1.5 , -50.),
                                           EXTREMITE = (10.0 , -50.0),
                                           ),
                        PRECISION=1.E-4,);

# =====
# POST PROCESSING - EXTRACTION OF RESULTS FROM CUTLINES
# =====

POSTP1=POST_RELEVE_T(ACTION=(
                    _F(INTITULE='PROFIL VARI',
                       PRECISION=1.E-4,
                       CHEMIN = COUPE1,
                       RESULTAT=RESU1,
                       NOM_CHAM='VARI_NOEU',
                       NOM_CMP='V3',
                       OPERATION='EXTRACTION',),
                    ),
);

POSTP3=POST_RELEVE_T(ACTION=(
                    _F(INTITULE='PROFIL VARI',
                       PRECISION=1.E-4,
                       CHEMIN = COUPE3,
                       RESULTAT=RESU1,
                       NOM_CHAM='VARI_NOEU',
                       NOM_CMP='V3',
                       OPERATION='EXTRACTION',),
                    ),
);

POSTP4=POST_RELEVE_T(ACTION=(
                    _F(INTITULE='PROFIL VARI',
                       PRECISION=1.E-4,
                       CHEMIN = COUPE4,
                       RESULTAT=RESU1,
                       NOM_CHAM='VARI_NOEU',
                       NOM_CMP='V3',
                       OPERATION='EXTRACTION',),
                    ),
);
```

Appendix F. Command file of the 2D tunnel analysis

```
POSTP2=POST_RELEVE_T(ACTION=(
    _F(INTITULE='PROFIL DEPL',
    PRECISION=1.E-4,
    CHEMIN = COUPE2,
    RESULTAT=CH_LI,
    NOM_CHAM='DEPL',

    NOM_CMP='PRE1',
    OPERATION='EXTRACTION',),),
);

# =====
# POST PROCESSING - DISPLACEMENT AT ALL NODES OF TUNNEL WALLS
# =====

DEP1 = POST_RELEVE_T( ACTION = _F( INTITULE = 'DEPLACEMENT',
    RESULTAT = RESU1,
    GROUP_NO = 'tunnel1',
    NOM_CHAM = 'DEPL',
    TOUT_CMP = 'OUI',
    OPERATION = 'EXTRACTION',),),);

# =====
# POST PROCESSING - DISPLACEMENTS FOR COMPARISON (P1-P5)
# =====

DEX1 = POST_RELEVE_T( ACTION = _F( INTITULE = 'DISPOPT',
    RESULTAT = RESU1,
    NOEUD = 'N389',
    NOM_CHAM = 'DEPL',
    TOUT_CMP = 'OUI',
    OPERATION = 'EXTRACTION',),),);

DEX2 = POST_RELEVE_T( ACTION = _F( INTITULE = 'DISPOPT',
    RESULTAT = RESU1,
    NOEUD = 'N373',
    NOM_CHAM = 'DEPL',
    TOUT_CMP = 'OUI',
    OPERATION = 'EXTRACTION',),),);

DEX3 = POST_RELEVE_T( ACTION = _F( INTITULE = 'DISPOPT',
    RESULTAT = RESU1,
    NOEUD = 'N357',
    NOM_CHAM = 'DEPL',
    TOUT_CMP = 'OUI',
    OPERATION = 'EXTRACTION',),),);
```

Appendix F. Command file of the 2D tunnel analysis

```
                                OPERATION='EXTRACTION',,),,);

# =====
# POST PROCESSING - PRINTING RESULTS IN .csv FORMAT
# =====

IMPR_TABLE (TABLE=POSTP1, FORMAT='TABLEAU', SEPARATEUR=',',,);
IMPR_TABLE (TABLE=POSTP2, FORMAT='TABLEAU', SEPARATEUR=',',,);
IMPR_TABLE (TABLE=DEP1, FORMAT='TABLEAU', SEPARATEUR=',',,);

IMPR_TABLE (TABLE=DEX1, FORMAT='TABLEAU', SEPARATEUR=',',,);
IMPR_TABLE (TABLE=DEX2, FORMAT='TABLEAU', SEPARATEUR=',',,);
IMPR_TABLE (TABLE=DEX3, FORMAT='TABLEAU', SEPARATEUR=',',,);
IMPR_TABLE (TABLE=DEX4, FORMAT='TABLEAU', SEPARATEUR=',',,);
IMPR_TABLE (TABLE=DEX5, FORMAT='TABLEAU', SEPARATEUR=',',,);

IMPR_TABLE (TABLE=HSX, FORMAT='TABLEAU', SEPARATEUR=',',,);
IMPR_TABLE (TABLE=HDX, FORMAT='TABLEAU', SEPARATEUR=',',,);
IMPR_TABLE (TABLE=VTP, FORMAT='TABLEAU', SEPARATEUR=',',,);
IMPR_TABLE (TABLE=VBT, FORMAT='TABLEAU', SEPARATEUR=',',,);

IMPR_TABLE (TABLE=PPA2, FORMAT='TABLEAU', SEPARATEUR=',',,);
IMPR_TABLE (TABLE=PPA3, FORMAT='TABLEAU', SEPARATEUR=',',,);
IMPR_TABLE (TABLE=PPA4, FORMAT='TABLEAU', SEPARATEUR=',',,);
IMPR_TABLE (TABLE=PPA5, FORMAT='TABLEAU', SEPARATEUR=',',,);
IMPR_TABLE (TABLE=PPA6, FORMAT='TABLEAU', SEPARATEUR=',',,);
IMPR_TABLE (TABLE=PPA7, FORMAT='TABLEAU', SEPARATEUR=',',,);

IMPR_TABLE (TABLE=POSTP3, FORMAT='TABLEAU', SEPARATEUR=',',,);
IMPR_TABLE (TABLE=POSTP4, FORMAT='TABLEAU', SEPARATEUR=',',,);

FIN();
```

Appendix G. Summary of model parameters calibration

We report in the following a detailed summary of the model parameters calibration. The constitutive model is MS3, while the parameters are the ones used in the 2D tunnel analysis of Chapter 7 and reported in Table 7-2. This is intended as a sort of “guide manual” to the parameters calibration. The full procedure for each parameter was presented in different chapters and sections, while in here is reported a synopsis with proper cross references. As the calibration of the elastic parameters (Young’s modulus and Poisson’s ratio) does not present particular difficulties, they will not be discussed here.

The five parameters characterizing the final failure surface are the friction coefficient β , the cohesive component $\hat{\gamma}$, the fabric tensor eigenvalue Ω , the first anisotropic parameter d_1 and the second anisotropic parameter d_2 . Their determination is performed with the aid of MATLAB[®] function `lsqcurvefit` (The MathWorks, 2011a). The input variables are the state of stress in terms of mean and deviatoric stress invariants and the relative orientation angle. Specific details on the calibration procedure can be found in Section 5.6.2. The values of these parameters in Table 7-2 were obtained in the calibration performed in Section 5.6.2 for the Shaly facies of Opalinus Clay and are based on the experimental results reported in Gräsle and Plischke (2010).

The yield parameter α calibration is illustrated in detail in Section 4.6, while its value is in this case postulated to be equal to the one calibrated for the Sandy facies and reported in Section 4.7. It is worth noticing that, given the fact that this parameter controls the curvature of the plastic onset, its value becomes relevant for Opalinus Clay at higher mean effective stresses (close to the cap surface).

The scaling friction parameter δ is set to be equal to one in this case, so that the friction coefficient (and therefore the friction angle) remains constant during plastic hardening. Its full calibration is also given in detail in Section 4.6. The initial bounding surface parameter r_{ha0} is set to 0.7.

The true triaxial parameter β_θ could not be calibrated for Opalinus Clay, as no true triaxial tests exist for this material. The value of 0.674 was chosen so that the available strength in triaxial extension is roughly 70% of the strength in triaxial extension. It is worth noticing that, for sedimentary materials such as Shirahama Sandstone and Yuubari Shale, its value is, respectively, of 0.673 and 0.637. The full calibration is also based on the utilization of the MATLAB[®] function `lsqcurvefit` (The MathWorks, 2011a), and more details are given in Section 5.6.1.

Globally, the procedure for the determination of the full set of parameters involved in the plastic yield surface suggested is to start with an isotropic calibration as specified in Section 4.6, and then extend the calibration toward anisotropy by following the procedure illustrated in Section 5.6.2.

The plastic compressibility parameter χ_h is in this case taken equal to the one calibrated for the Sandy facies in Section 4.7. The calibration procedure is illustrated in Section 4.6.

The residual damage parameter $0 \leq \beta_d \leq 1$ is taken equal to the value calibrated for the Sandy facies in Section 4.7 and the procedure for the calibration, along with an example, can be found in Section 4.6.

The damage steepness α_d and the dilatancy parameter ψ_h are, for the 2D tunnel analysis, calibrated in order to obtain a localization length that is in the order of the EDZ (roughly 1 m). The classical procedure to calibrate these two parameters can be found once again in Section 4.6. Chapter 6, dedicated to the localization and regularization of inelastic strains, showed that both parameters have a strong influence in the final size of the localized zone. For this reason, both parameters were modified for the tunnel analysis and their values in Table 7-2 is the results of numerical fitting performed to obtain a localization band width as shown in Figure 7-9, which is representative of the EDZ.

The values of hydraulic conductivity and Biot's coefficient are taken after literature, and the hydraulic conductivity later adjusted to better represent observed experimental behavior as discussed in Section 7.5.

In Table G-1 are listed the material parameters of model MS3 along with units, admissible ranges, calibration method (suggested) and reference to the chapters or sections in which the calibration method was discussed. Analytical calibration methods imply that the values of the parameter can be obtained with algebraic procedure. For the numerical fitting, the MATLAB[®] function `lsqcurvefit` is here employed.

Appendix G. Summary of model parameters calibration

Table G-1: List of parameters of the constitutive model MS3 with ranges, units, calibration method and reference inside the manuscript for the calibration procedure.

Name	Parameter	Ranges	Unit	Calibration method	Reference for calibration
<i>Youngs' modulus</i>	E	>0	MPa	Analytical	-
<i>Poisson's ratio</i>	ν	$0 < \nu < 0.5$	-	Analytical	-
<i>Yield par.</i>	α	≤ 0	MPa ⁻¹	Analytical	Section 4.6
<i>Friction coefficient</i>	β	>0	-	Numerical (lsqcurvefit)	Section 5.6.2
<i>Cohesive coefficient</i>	γ	>0	MPa	Numerical (lsqcurvefit)	Section 5.6.2
<i>Scaling friction</i>	δ	>0	-	Analytical	Section 4.6
<i>Initial bounding surface</i>	r_{ha0}	$0 < r_{ha0} < 1$	-	Analytical	Section 4.6
<i>Plastic compressibility</i>	χ_h	>0	-	Analytical	Section 4.6
<i>Dilatancy parameter</i>	ψ_h	>0	-	Analytical	Section 4.6/6.5
<i>Fabric tensor eigenvalue</i>	Ω_l	-	-	Numerical (lsqcurvefit)	Section 5.6.2
<i>Anisotropic parameter 1 (Polynomial coefficient)</i>	$d1$	-	-	Numerical (lsqcurvefit)	Section 5.6.2
<i>Anisotropic parameter 2 (Polynomial coefficient)</i>	$d2$	-	-	Numerical (lsqcurvefit)	Section 5.6.2
<i>True triaxial parameter</i>	β_{θ}	$0 \leq \beta_{\theta} \leq 0.7925$	-	Numerical (lsqcurvefit)	Section 5.6.2
<i>Damage steepness</i>	α_d	>0	-	Analytical	Section 4.6/6.5
<i>Residual damage</i>	β_d	$0 \leq \beta_d \leq 1$	-	Analytical	Section 4.6
<i>Hydraulic conductivity</i>	k	>0	m/s	Analytical	Section 7.5
<i>Biot's coefficient</i>	b	$0 \leq b \leq 1$	-	Analytical	Section 4.7

References

- Gräsle, W., Plischke, I., 2010. Laboratory Testing (LT) Experiment: Mechanical Behavior of Opalinus Clay, Final report from Phases 6 – 14. Mont Terri Technical Note TN 2009-07.
- The MathWorks Inc., 2011a, MATLAB and Statistics Toolbox Release, Natick, Massachusetts, United States.

Curriculum Vitae

Mr. Francesco Parisio

Email: francesco.parisio@yahoo.com
<https://ch.linkedin.com/in/francesco-parisio-b1b53844>
Telephone: +49 152 5391 0506
+39 345 180 7889

EDUCATION

- Aug 2012 – May 2016:** PhD Geomechanics, *Ecole Polytechnique Fédérale de Lausanne, Switzerland*.
Supervisor: Prof. L. Laloui
- Sep 2009 – Dec 2011:** MSc Civil Engineering, *Politecnico di Torino, Italy*.
Final grade: 110/110 Cum Laude.
- Sep 2005 – Jul 2009:** BSc Civil Engineering, *Politecnico di Torino, Italy*.
Final grade: 90/110.

PUBLICATIONS

International Journals:

- Parisio F.**, Samat S. and Laloui L. (2015) Constitutive analysis of shale: a coupled damage plasticity approach, *International Journal of Solids and Structures* (75-76): 88-98.
- Vilarrasa V., **Parisio F.** and Laloui L. (2015) Strength evolution of geomaterials in the octahedral plane under non-isothermal and unsaturated conditions, *International Journal of Geomechanics (Under review)*.

Conference Papers:

- Parisio F.**, Samat S. and Laloui L. (2014) An elasto-plastic-damage model for quasi-brittle shales. *48th US Rock Mechanics / Geomechanics Symposium 2014*.
- Parisio F.**, Samat S. and Laloui L. (2014) On plasticity-damage modeling of shales. *14th International Conference of the ICAMAG 2014*.
- Laloui L., Ferrari A., Favero V., Minardi A. and **Parisio F.** (2015) Multiphysical behaviour of shales. *International Symposium on Energy Geotechnics (1st.: 2015: Barcelona). Universitat Politècnica de Catalunya. Departament d'Enginyeria del Terreny, Cartogràfica i Geofísica, 2015*.

Laloui L., Ferrari A., Favero V., **Parisio F.** and Minardi A. (2016) Geomechanical behavior of shales. *Workshop on geotechnical fundamentals in the face of new world challenges, NSF, Arlington, Virginia, January 24 - 26, 2016.*

Conference Abstracts:

Laloui L. and **Parisio F.** (2015) Modeling quasi-brittle failure using coupled damage-plasticity approach. *CERMODEL 2015, Modelling and Simulation Meet Innovation in Ceramics Technology, Trento.*

Vilarrasa, V., Carpaij, R., **Parisio, F.** and Laloui., L., 2016. 3D numerical model of the FE experiment: tunnel excavation and preliminary results. *Technical Discussion TD-292: FE Experiment, Saint Ursanne, Switzerland, 9 February 2016.*

INVITED TALKS AND SEMINARS

Elasto-plastic-damage constitutive modeling for shales, 1st EDME (Ecole Doctorale Mécanique) PhD Symposium, Ecole Polytechnique Fédérale de Lausanne, Switzerland, December 12 2013

Anisotropic coupled plastic damage model for shale, 1st Joint Workshop Masdar-EPFL, Ecole Polytechnique Fédérale de Lausanne, Switzerland, April 23 2015

Influence of confinement in the anisotropic behavior of shale, LMS-EPFL Modeling Seminar, Ecole Polytechnique Fédérale de Lausanne, Switzerland, June 9 2015

Constitutive and numerical modeling of shale with applications to Opalinus Clay, Workshop on geomechanical aspects of Opalinus Clay, Ecole Polytechnique Fédérale de Lausanne, Switzerland, January 12 2016

AWARDS

Awarded to the participation of the Veolia Summer School 2011, Veolia Environnement (Paris, 3-11 Jul 2011)

MASTER STUDENT SUPERVISION

Apr 2013 – Sep 2013: Supervision of master student Thibaut LeGac on a final master project entitled: *Large scale 3D hydro-mechanical modelling of Mont Terri underground research laboratory*

TEACHING

Teaching assistant:

Geomechanics, EPFL, Prof. Prof. L. Laloui and Dr. Azad Koliji (Fall 2013 and 2014)

Mécanique des Sols et Écoulements Souterrains, EPFL, Prof. L. Vulliet and Prof. L. Laloui (Spring 2013, 2014, 2015)

Physique III, EPFL, Prof. H. Rönnow (Spring 2014)

Probabilités et Statistique, EPFL, Prof. J.M. Helbling (Fall 2012)

PROFESSIONAL EXPERIENCE

Aug 2012 – Aug 2015: Research assistant/PhD student, *Ecole Polytechnique Fédérale de Lausanne, Switzerland*.

Teaching assistant, numerical modeling for nuclear waste repository solutions.

Feb 2012 – Aug 2012: Hydroelectric Project Engineer, *Hydrodata SpA, Torino, Italy*.

Design engineer of hydroelectric power plants.

Nov 2008 – Feb 2009: Tunnelling Assistant, *Maire Technimont SpA, Torino, Italy*.

TBM engineer assistant.

SKILLS

Numerical methods: Finite element method, finite difference method, computational inelasticity.

Modeling: Geomechanics, damage and regularization, structures, transient analyses, coupled poro-mechanics, thermo-hydro-mechanics of porous continua, thermodynamics and thermomechanics of continua.

Engineering: Structures and infrastructures design, civil works accounting, public works.

Programming: FORTRAN 90, Matlab.

CAD softwares: Autocad 3D, Autocad Civil 3D, Autocad Structural Detailing.

Numerical Softwares: *Code_Aster*, FLAC3D, TNO Diana.

LANGUAGE SKILLS

Italian: Native speaker
English: Professional working knowledge (IELTS 7.0)
French: Professional working knowledge

